NAVAL POSTGRADUATE SCHOOL

MONTEREY, CALIFORNIA

DISSERTATION

ENSEMBLE SENSITIVITY ANALYSIS OF A SEVERE DOWNSLOPE WINDSTORM IN COMPLEX TERRAIN: IMPLICATIONS FOR FORECAST PREDICTABILITY SCALES AND TARGETED OBSERVING NETWORKS

by

Paul B. Homan

September 2013

Dissertation Supervisor: Joshua P. Hacker

Approved for public release; distribution is unlimited

REPORT DOCUMENTATION PAGE	*Form Approved OMB No. 0704–0188*

1. AGENCY USE ONLY *(Leave blank)*	**2. REPORT DATE** September 2013	**3. REPORT TYPE AND DATES COVERED** Dissertation

4. TITLE AND SUBTITLE ENSEMBLE SENSITIVITY ANALYSIS OF A SEVERE DOWNSLOPE WINDSTORM IN COMPLEX TERRAIN: IMPLICATIONS FOR FORECAST PREDICTABILITY SCALES AND TARGETED OBSERVING NETWORKS	**5. FUNDING NUMBERS**
6. AUTHOR(S) Paul B. Homan	
7. PERFORMING ORGANIZATION NAME(S) AND ADDRESS(ES) Naval Postgraduate School Monterey, CA 93943–5000	**8. PERFORMING ORGANIZATION REPORT NUMBER**
9. SPONSORING /MONITORING AGENCY NAME(S) AND ADDRESS(ES) N/A	**10. SPONSORING/MONITORING AGENCY REPORT NUMBER**

11. SUPPLEMENTARY NOTES The views expressed in this thesis are those of the author and do not reflect the official policy or position of the Department of Defense or the U.S. Government. IRB Protocol number ____N/A ____.

12a. DISTRIBUTION / AVAILABILITY STATEMENT Approved for public release; distribution is unlimited	**12b. DISTRIBUTION CODE**

13. ABSTRACT (maximum 200 words)

Multiple mesoscale numerical weather simulations are conducted to evaluate whether Ensemble Sensitivity Analysis (ESA) is a useful tool determining the sensitivity of a severe downslope windstorm (DSWS) in complex terrain to initial conditions and assimilated observations. A 96-member ensemble is implemented with 1.33 km grid spacing. Sensitive regions are found both upstream and downstream, based on a new forecast metric that indicates the potential for turbulence and strong winds reaching the Earth's surface. Approximating the effects of assimilating a perfect observation at these sensitivity locations, then executing non-linear ensemble forecasts, shows the linear approximations in ESA are reasonable. We analyze the roles of upstream wind and stability structures, and leeside conditions, in determining the strength and propagation of winds down the mountain slope and onto the adjacent plains. Results suggest that ESA is a viable method to identify observation locations to improve forecasts of fine-scale, non-linear, high-impact events such as DSWS. Also, 14 severe DSWS identified by the High Wind Alert System located at the USAF Academy, CO are modeled utilizing a deterministic WRF configuration. Analysis shows that non-wave breaking events account for the strongest DSWS and propagate further away from the mountains than breaking events at this location.

14. SUBJECT TERMS Ensemble Sensitivity Analysis, Downslope Windstorm, Complex Terrain, Numerical Weather Prediction, Flow Separation, Breaking Waves, Vertically Propagating Waves, Trapped Waves, Data Assimilation, Targeted Observing, Forecast Predictability, Bulk Richardson Number, Mesoscale, Mesonet, Observing System Simulation Experiment, WRF, Mountain Waves.	**15. NUMBER OF PAGES** 181
	16. PRICE CODE

17. SECURITY CLASSIFICATION OF REPORT Unclassified	**18. SECURITY CLASSIFICATION OF THIS PAGE** Unclassified	**19. SECURITY CLASSIFICATION OF ABSTRACT** Unclassified	**20. LIMITATION OF ABSTRACT** UU

THIS PAGE INTENTIONALLY LEFT BLANK

ENSEMBLE SENSITIVITY ANALYSIS OF A SEVERE DOWNSLOPE WINDSTORM IN COMPLEX TERRAIN: IMPLICATIONS FOR FORECAST PREDICTABILITY SCALES AND TARGETED OBSERVING NETWORKS

Paul B. Homan
Major, United States Air Force
B.S., United States Air Force Academy, 2002
M.S., Naval Postgraduate School, 2007

Submitted in partial fulfillment of the
requirements for the degree of

DOCTOR OF PHILOSOPHY IN METEOROLOGY

from the

NAVAL POSTGRADUATE SCHOOL
September 2013

Author: Paul B. Homan

Approved by:

Joshua Hacker Professor of Meteorology Dissertation Supervisor	Wendell Nuss Professor of Meteorology
James Doyle Ph.D. Meteorology	Gregory Hakim Professor of Meteorology
Patrick Harr Professor of Meteorology	Rebecca Stone Professor of Oceanography

Approved by: Wendell Nuss, Chair, Department of Meteorology

Approved by: Douglas Moses, Vice Provost for Academic Affairs

THIS PAGE INTENTIONALLY LEFT BLANK

ABSTRACT

Multiple mesoscale numerical weather simulations are conducted to evaluate whether Ensemble Sensitivity Analysis (ESA) is a useful tool determining the sensitivity of a severe downslope windstorm (DSWS) in complex terrain to initial conditions and assimilated observations. A 96-member ensemble is implemented with 1.33 km grid spacing. Sensitive regions are found both upstream and downstream, based on a new forecast metric that indicates the potential for turbulence and strong winds reaching the Earth's surface. Approximating the effects of assimilating a perfect observation at these sensitivity locations, then executing non-linear ensemble forecasts, shows that the linear approximations in ESA are reasonable. We analyze the roles of upstream wind and stability structures, and leeside conditions, in determining the strength and propagation of winds down the mountain slope and onto the adjacent plains. Results suggest that ESA is a viable method to identify observation locations to improve forecasts of fine-scale, non-linear, high-impact events such as DSWS. Also, fourteen severe DSWS identified by the High Wind Alert System located at the USAF Academy, CO are modeled utilizing a deterministic WRF configuration. Analysis shows that non-wave breaking events account for the strongest DSWS and propagate further away from the mountains than breaking events at this location.

TABLE OF CONTENTS

I. INTRODUCTION..1
- A. MOTIVATION 4

II. BACKGROUND 7
- A. ENSEMBLE SENSITIVITY ANALYSIS 7
  - 1. Overview 7
  - 2. Derivation from Linear Regression..8
- B. DOWNSLOPE WINDSTORMS 10
  - 1. Overview 10
  - 2. Leeside Conditioning 13
    - *a. Downslope Windstorm Leeside Conditioning........................14*
    - *b. Leeside Conditioning Due to Rotor and Flow Separation 15*
- C. CLIMATOLOGY – SEVERE DOWNSLOPE WINDSTORMS AT USAFA 19
- D. CASE STUDY: SEVERE DOWNSLOPE WINDSTORM—DECEMBER 30, 2008 22
  - 1. HWAS Characterization of 30 December 2008 Downslope Windstorm 22
  - 2. Synoptic Conditions of 30 December 2008 Downslope Windstorm 26
  - 3. Modeling Study of the 30 December 2008 Downslope Windstorm 30

III. DATA AND METHODOLOGY 37
- A. OVERVIEW...37
- B. MODEL DESIGN AND SETUP 37
  - 1. Truth Run..38
  - 2. Ensemble System..39
- C. FORECAST METRIC (*J*)—GAUSSIAN TESTS 39
  - 1. Lilliefors Test...40
  - 2. Choosing a Forecast Metric (*J*)...41
    - *a. Forecast Metric—Modified Bulk Richardson Number.........42*
- D. ENSEMBLE SENSITIVITY ANALYSIS USING MODIFIED BULK RICHARDSON AS FORECAST METRIC (*J*) 47
  - 1. Addressing Statistical Sampling Error 47
    - *a. Statistical Significance—Confidence Test............................47*
  - 2. ESA Calculation 48
- E. PERTURBATION TESTS...49
  - 1. Perturbation Method 50
- F. DATA ASSIMILATION METHODS..51
  - 1. Covariance Localization...51
  - 2. Observation Assimilation 51

IV. ESA RESULTS..53

- A. OVERVIEW 53
  - 1. Linearity 55
  - 2. Atmospheric Structure 55
  - 3. Forecast Certainty and Ensemble Spread 59
- B. FORECAST METRIC IMACT 68
  - 1. P1 Ensemble Run 68
  - 2. P2 Ensemble Run 74
  - 3. DA1 Ensemble Run 77
  - 4. DA2 Ensemble Run 82
  - 5. DAJ Ensemble Run 83
- C. PERTURBATION IMPACT BEYOND THREE HOURS 86
- D. METHOD FOR TESTING LINEARITY WITH FEWER MEMBERS 91

V. OBSERVATIONAL, MODELING, AND FREQUENCY ANALYSIS OF FOURTEEN SEVERE DOWNSLOPE WINDSTORMS AT USAFA 95
- A. OVERVIEW 95
- B. BACKGROUND 95
- C. DATA AND METHODOLOGY 97
- D. RESULTS 100
  - 1. Strength Score Analysis 100
  - 2. Composite Upstream Soundings 101
  - 3. Fourier Analysis 103
- E. SUMMARY AND DISCUSSION 106

VI. CONCLUSIONS AND FUTURE WORK 111
- A. SUMMARY 111
- B. OUTCOMES AND BROADER IMPLICATIONS 112
- C. FUTURE WORK 115
  - 1. ESA Testing 115
  - 2. Initial Condition Impacts on Downslope Windstorms 116

APPENDIX A 119
- A. USAFA GEOGRAPHY 119
- B. HIGH WIND ALERT SYSTEM (HWAS) DESCRIPTION 121

APPENDIX B 125
- A. PERFECT MODEL—“TRUTH RUN” FIGURES 125

APPENDIX C 135
- A. FIGURES OF WRF MODEL RUNS FOR FOURTEEN SEVERE DOWNSLOPE WINDSTORMS AT USAFA 135

LIST OF REFERENCES 151

INITIAL DISTRIBUTION LIST 157

LIST OF FIGURES

Figure 1. Total number of severe DSWS broken down by month as recorded by HWAS sensors at USAFA from 2004 to 2012. 5

Figure 2. Results of the ESA performed by Hakim and Torn, showing that the sensitivity of 24 hour precipitation in a box over western Washington State is most sensitive to changes in SLP in the darkest regions west of the box. After Hakim and Torn 2008..8

Figure 3. Schematic diagram of flow pattern over mountain range. From Kuettner 1959..16

Figure 4. Streamlines and horizontal wind speed (m s^{-1}) for simulations using (a) free-slip and (b) no-slip lower boundary conditions. Horizontal wind speed contours less than zero are shaded (from Doyle and Durran 2002).................17

Figure 5. Distance to flow separation (solid, non-dimensional) and pressure drag (dashed) as a function of surface roughness length (from Doyle and Durran 2002). 18

Figure 6. Annual frequency of severe DSWS broken down by month as recorded by HWAS sensors at USAFA from 2004 to 2012. 21

Figure 7. Time series of winds, wind direction, temperature, dewpoint, and MSLP at the Rampart sensors during a severe DSWS on 30 December 2008. 22

Figure 8. Time series winds, wind direction, temperature, dewpoint, and MSLP at the Community Center sensor during a severe DSWS on 30 December 2008..23

Figure 9. Time series winds, wind direction, temperature, dewpoint, and MSLP at the Airfield sensor during a severe DSWS on 30 December 2008. 24

Figure 10. Time series winds, wind direction, temperature, dewpoint, and MSLP at the Pine Creek sensor during a severe DSWS on 30 December 2008. 24

Figure 11. Time series of steady state wind (kt) at the Rampart, Community Center and Airfield sensors during a severe DSWS on 30 December 2008 overlaid with "Truth" run forecasts from WRF simulation. Forecast metric (*J*) from "Truth" run shown with yellow circles and corresponds to scale on right axis..26

Figure 12. Time series of temperature (°C) at the Rampart, Community Center and Airfield sensors during a severe DSWS on 30 December 2008. 27

Figure 13. Upstream sounding from Grand Junction, CO during a severe DSWS on 00Z 30 December 2008...28

Figure 14. a) 200 mb geopotential height (00Z), b) 200 mb windspeed (00Z), c) sea level pressure (00Z), d) sea level pressure (12Z) on 30 December 2008. 29

Figure 15. Water vapor satellite image from 1645Z on 30 December 2008. 29

Figure 16. Model terrain height in meters for innermost domain. Solid black line indicates location of cross section shown in Figure 17...................................31

Figure 17. Cross section of *x*-wind component (shaded) and potential temperature (contoured) from west to east across Colorado at the gridline of the HWAS Rampart sensor for the 30 December 2008 00Z ensemble mean

unperturbed analysis. The horizontal axis is scaled to the number of grid points from the innermost domain with a resolution of 1.33 km. The HWAS sensors and USAFA are along the lee of the Rampart Range just to the east of point F. The black box indicates the area shown in the cross section in Figure 18. 32
Figure 18. Cross section of *x*-wind component (shaded) and potential temperature (contoured) from west to east across the Rampart Range and adjacent plains at the gridline of the HWAS Rampart sensor for the 30 December 2008 00Z ensemble mean unperturbed analysis. The horizontal axis is scaled to the number of grid points from the innermost domain with a resolution of 1.33 km. Approximate locations of four HWAS sensors are marked by circles. The red arrow indicates the horizontal circulation or rotor suggested by the cross section. 33
Figure 19. Cross section of *x*-wind component (shaded) and potential temperature (contoured) from west to east across the Rampart Range and adjacent plains at the gridline of the HWAS Rampart sensor for the 30 December 2008 ensemble mean unperturbed three hour forecast valid at 03Z. The horizontal axis is scaled to the number of grid points from the innermost domain with a resolution of 1.33 km. Approximate locations of four HWAS sensors are marked by circles. 34
Figure 20. WRF nesting configuration used in this study. The star defines the location of Colorado Springs. 38
Figure 21. Cross section of *x*-wind component (shaded) and potential temperature (contoured) from west to east across the Rampart Range and adjacent plains at the gridline of the HWAS Rampart sensor for the 30 December 2008 ensemble mean NP run (unperturbed) three hour forecast valid at 03Z. The horizontal axis is scaled to the number of grid points from the innermost domain with a resolution of 1.33 km. Stars denote location of points where forecast metric *J* is calculated using a modified Bulk Richardson number. 44
Figure 22. a) Histogram of the forecast metric (*J*) for 96-member NP (unperturbed) WRF ensemble at 03Z 30 December 2008, b) scatterplot of $\bar{\theta}$ vs. $(\theta_2 - \theta_1)$, c) scatterplot of $(U_2 - U_1)^2$ vs. $\bar{\theta}$, d) $(\theta_2 - \theta_1)$ vs. $(U_2 - U_1)^2$. The magnitude of the forecast metric (*J*) is shaded in the scatterplots. All plots are valid at 03Z 30 December 2008. 45
Figure 23. Scatterplots of 10-m *x*-wind component from the 03Z forecast of the WRF ensemble and the forecast metric (left) and 2-m potential temperature (right). 46
Figure 24. ESA results for modified Bulk Richardson forecast metric (*J*) at model level 13 for 03Z 30 December 2008. Results for x^a = Potential Temperature are on the left and x^a = Specific Humidity are on the right. The full sensitivity field is shown on the upper plots and the filtered sensitivity by a confidence test at a 95% confidence interval is shown in the lower plots. Perturbation and observation assimilation points are

identified within regions A and B. Locations given for reference are identified in Figure 16...48
Figure 25. Plot of expected δJ (x-axis) vs. actual δJ (y-axis) for each ensemble run at the forecast time of 03Z 30 December 2008. The red line is a perfect 1 to 1 relationship for reference. This plot corresponds to the data given in Table 5...54
Figure 26. Vertical profiles by model level at point 1 (top) of a) Potential Temperature (K), b) Brunt-Väisälä frequency (s^{-1}), c) *x*-wind component (m s^{-1}), d) Scorer parameter and at point 2 (bottom) of e) Potential Temperature (K), f) Brunt-Väisälä frequency (s^{-1}), g) *x*-wind component (m s^{-1}), h) Scorer parameter. These plots are from the NP ensemble mean valid at 00Z 30 December 2008..57
Figure 27. Cross section from west to east (grid points 300–500) at the gridline of point 1, showing ensemble mean potential temperature from the NP run analysis. Black arrow denotes the location of the introduced perturbation (point 1)...58
Figure 28. Cross section from west to east at the gridline of point 2 (grid points 150–375), showing ensemble mean potential temperature from the NP run analysis. Black arrow denotes the location of the introduced perturbation (point 2)...59
Figure 29. Histograms of perturbation potential temperature at point 1from the analysis for the a) NP run, b) P1 run, c) DA1 run, and d) DAJ run................60
Figure 30. Histograms of perturbation potential temperature at point 2 from the analysis for the a) NP run, b) P2 run, c) DA2 run, and d) DAJ run................61
Figure 31. Cross Sections of $\sigma_{DA2} - \sigma_{NP}$ from west to east at the gridline of the Rampart sensor (grid points 150–375) for a) analysis potential temperature, b) 03Z forecast of potential temperature, c) analysis *x*-wind component, d) 03Z forecast of *x*-wind component. The arrow denotes the longitude of the observation insertion (point 2), and the star denotes the location of USAFA and the forecast metric *J*...63
Figure 32. Cross Sections of $\sigma_{DA1} - \sigma_{NP}$ from west to east at the gridline of the Rampart sensor (grid points 300–500) for a) analysis potential temperature, b) 03Z forecast of potential temperature, c) analysis *x*-wind component, d) 03Z forecast of *x*-wind component. The arrow denotes the longitude of the observation insertion (point 1), and the star denotes the location of USAFA and the forecast metric *J*...64
Figure 33. Cross Sections of $\sigma_{DAJ} - \sigma_{NP}$ from west to east at the gridline of the Rampart sensor (grid points 300–500) for a) analysis potential temperature, b) 03Z forecast of potential temperature, c) analysis *x*-wind component, d) 03Z forecast of *x*-wind component. The arrow denotes the longitude of the observation insertion (point 1), and the star denotes the location of USAFA and the forecast metric *J*...65
Figure 34. Cross sections of *x*-wind component (shaded) and potential temperature (contoured) from west to east across the Rampart Range and adjacent

plains at the gridline of the Rampart sensor for the 30 December 2008 ensemble mean NP run (top left), P1 run (top right), and difference between P1 and NP (bottom) for the three hour forecast valid at 03Z. 67
Figure 35. a) Histogram of the forecast metric (J) for P1 96-member WRF ensemble at 03Z 30 December 2008, b) scatterplot of $\overline{\theta}$ vs. $(\theta_2 - \theta_1)$, c) scatterplot of $(U_2 - U_1)^2$ vs. $\overline{\theta}$, d) $(\theta_2 - \theta_1)$ vs. $(U_2 - U_1)^2$. The magnitude of the forecast metric (J) is shaded in the scatterplots. All plots are for 03Z 30 December 2008. 68
Figure 36. a) Histogram for the difference in the forecast metric (J) between P1 and NP runs, b) scatterplot of the difference between the P1 and NP runs for $\overline{\theta}$ vs. $(\theta_2 - \theta_1)$, c) scatterplot of the difference between the P1 and NP runs for $(U_2 - U_1)^2$ vs. $\overline{\theta}$, d) scatterplot of the difference between the P1 and NP runs for $(\theta_2 - \theta_1)$ vs. $(U_2 - U_1)^2$. The magnitude of the difference between the P1 and NP runs for the forecast metric (J) is shaded in the scatterplots. All plots are valid for 03Z 30 December 2008. 69
Figure 37. Perturbation of, a) potential temperature and, b) specific humidity from the P1 run analysis at point 1 as function of model level (x-axis). 71
Figure 38. Cross section of potential temperature difference between the P1 and NP run analysis from west to east at the gridline of point 1 (grid points 300–500). Black arrow denotes the location of the introduced perturbation (point 1). 72
Figure 39. a) Histogram of the forecast metric (J) for P2 96-member WRF ensemble at 03Z 30 December 2008, b) scatterplot of $\overline{\theta}$ vs. $(\theta_2 - \theta_1)$, c) scatterplot of $(U_2 - U_1)^2$ vs. $\overline{\theta}$, d) $(\theta_2 - \theta_1)$ vs. $(U_2 - U_1)^2$. The magnitude of the forecast metric (J) is shaded in the scatterplots. All plots are valid for 03Z 30 December 2008. 73
Figure 40. a) Histogram for the difference in the forecast metric (J) between P2 and NP runs, b) scatterplot of the difference between the P2 and NP runs for $\overline{\theta}$ vs. $(\theta_2 - \theta_1)$, c) scatterplot of the difference between the P2 and NP runs for $(U_2 - U_1)^2$ vs. $\overline{\theta}$, d) scatterplot of the difference between the P2 and NP runs for $(\theta_2 - \theta_1)$ vs. $(U_2 - U_1)^2$. The magnitude of the difference between the P2 and NP runs for the forecast metric (J) is shaded in the scatterplots. All plots are valid for 03Z 30 December 2008. 74
Figure 41. Perturbation of a) potential temperature and b) specific humidity for the P2 run analysis at point 2 as function of model level (x-axis). 75
Figure 42. Cross section of ensemble mean potential temperature difference between the analysis for the P2 and NP runs from west to east at the gridline of point 2 (grid points 150–375). The black arrow denotes the location of the introduced perturbation (point 2). 76
Figure 43. Cross sections of x-wind component (shaded) and potential temperature (contoured) from west to east across the Rampart Range and adjacent

plains at the gridline of the Rampart sensor for the 30 December 2008 ensemble mean NP run (top left), DA1 run (top right), and difference between DA1 and NP (bottom) for the three hour forecast valid at 03Z. All plots are valid at 03Z 30 December 2008. 78

Figure 44. a) Histogram of the forecast metric (J) for DA1 96-member WRF ensemble at 03Z 30 December 2008, b) scatterplot of $\overline{\theta}$ vs. $(\theta_2 - \theta_1)$, c) scatterplot of $(U_2 - U_1)^2$ vs. $\overline{\theta}$, d) $(\theta_2 - \theta_1)$ vs. $(U_2 - U_1)^2$. The magnitude of the forecast metric (J) is shaded in the scatterplots. All plots are valid at 03Z 30 December 2008. 79

Figure 45. a) Histogram for the difference in the forecast metric (J) between DA1 and NP runs, b) scatterplot of the difference between the DA1 and NP runs for $\overline{\theta}$ vs. $(\theta_2 - \theta_1)$, c) scatterplot of the difference between the DA1 and NP runs for $(U_2 - U_1)^2$ vs. $\overline{\theta}$, d) scatterplot of the difference between the DA1 and NP runs for $(\theta_2 - \theta_1)$ vs. $(U_2 - U_1)^2$. The magnitude of the difference between the DA1 and NP runs for the forecast metric (J) is shaded in the scatterplots. All plots are valid at 03Z 30 December 2008........80

Figure 46. Perturbation of a) potential temperature and b) specific humidity for the DA1 run analysis at point 2 as function of model level (x-axis). 81

Figure 47. Cross section of potential temperature difference between the analysis for the DA1 and NP runs from west to east at the gridline of point 1 (grid points 300–500). The black arrow denotes the location of the introduced perturbation (point 1). 82

Figure 48. a) Histogram of the forecast metric (J) for DA2 96-member WRF ensemble at 03Z 30 December 2008, b) scatterplot of $\overline{\theta}$ vs. $(\theta_2 - \theta_1)$, c) scatterplot of $(U_2 - U_1)^2$ vs. $\overline{\theta}$, d) $(\theta_2 - \theta_1)$ vs. $(U_2 - U_1)^2$. The magnitude of the forecast metric (J) is shaded in the scatterplots. All plots are valid at 03Z 30 December 2008. 83

Figure 49. a) Histogram for the difference in the forecast metric (J) between DA2 and NP runs, b) scatterplot of the difference between the DA2 and NP runs for $\overline{\theta}$ vs. $(\theta_2 - \theta_1)$, c) scatterplot of the difference between the DA2 and NP runs for $(U_2 - U_1)^2$ vs. $\overline{\theta}$, d) scatterplot of the difference between the DA2 and NP runs for $(\theta_2 - \theta_1)$ vs. $(U_2 - U_1)^2$. The magnitude of the difference between the DA2 and NP runs for the forecast metric (J) is shaded in the scatterplots. All plots are valid at 03Z 30 December 2008........84

Figure 50. a) Histogram of the forecast metric (J) for DAJ 96-member WRF ensemble at 03Z 30 December 2008, b) scatterplot of $\overline{\theta}$ vs. $(\theta_2 - \theta_1)$, c) scatterplot of $(U_2 - U_1)^2$ vs. $\overline{\theta}$, d) $(\theta_2 - \theta_1)$ vs. $(U_2 - U_1)^2$. The magnitude of the forecast metric (J) is shaded in the scatterplots. All plots are valid for 03Z 30 December 2008. 85

Figure 51. a) Histogram for the difference in the forecast metric (J) between DAJ and NP runs, b) scatterplot of the difference between the DAJ and NP runs for $\bar{\theta}$ vs. $(\theta_2 - \theta_1)$, c) scatterplot of the difference between the DAJ and NP runs for $(U_2 - U_1)^2$ vs. $\bar{\theta}$, d) scatterplot of the difference between the DAJ and NP runs for $(\theta_2 - \theta_1)$ vs. $(U_2 - U_1)^2$. The magnitude of the difference between the DAJ and NP runs for the forecast metric (J) is shaded in the scatterplots. All plots are valid at 03Z 30 December 2008........86

Figure 52. Kinetic, available potential, and total energy perturbation for domain 3 by forecast hour for each ensemble run from 00Z 30 December to 00Z 31 December 2008. Units for the vertical axis are Joules. The y-axis scales are different for each plot..89

Figure 53. Total energy perturbation for domain 3 divided into the western and eastern portions of the domain by forecast hour for each ensemble run from 00Z 30 December to 00Z 31 December 2008. Units for the vertical axis are Joules. The y-axis scales are different for each plot...........................90

Figure 54. Kinetic, available potential, and total energy perturbation for a 40 grid point by 40 grid point box centered over USAFA from domain 3 by forecast hour for each ensemble run from 00Z 30 December to 00Z 31 December 2008. Units for the vertical axis are joules. The y-axis scales are different for each plot...91

Figure 55. Summed differences of the forecast metric J between ensemble runs and the NP run (y-axis) for ranked ensemble sizes 1–90 (x-axis)..........................93

Figure 56. Cross section of *x*-wind component (shaded) and potential temperature (contoured) from west to east across Colorado (top) at the gridline of the Rampart sensor from the WRF deterministic run valid 23Z 18 December 2008. The black box indicates the area shown in the cross section in the bottom part of the figure. The horizontal axis is scaled to the number of grid points from the innermost domain with a resolution of 1.33 km. Approximate locations of four HWAS sensors are marked by circles. 98

Figure 57. Composite vertical soundings by model level at Grand Junction, CO for all non-breaking events (top) and breaking events (bottom). Valid three hours prior to strongest winds at USAFA. Shown is Potential temperature (K) in plots a and e, *x*-wind component (m s^{-1}) in plots b and f, Brunt-Väisälä frequency in plots c and g, and Scorer parameter in plots d and h. 101

Figure 58. Upstream *z*-wind component at the gridline of the Rampart sensor during time of maximum winds at USAFA from model level 10 for the truth run valid 12Z December 2008..102

Figure 59. Frequency spectrum of upstream *z*-wind component during time of maximum winds at USAFA from model level 10 for the truth run valid 12Z December 2008...103

Figure 60. Frequency spectrum of upstream terrain overlaid with wavelength of the fourteen severe DSWS as given in Table 7. A "*" denotes the wavelength of a non-wave breaking event and a "#" denotes the wavelength of a wave breaking event...105

Figure 61. Frequency spectrum of upstream terrain (green) and composite frequency spectrums for the non-wave breaking (blue) and wave breaking (red) severe DSWS. 106
Figure 62. Composite vertical soundings by model level at downstream sensitivity location (point 1) for six non-breaking severe DSWS. Valid three hours prior to strongest winds at USAFA. Shown is a) potential temperature (K), b) *x*-wind component (m s^{-1}), c) Brunt-Väisälä frequency, and d) Scorer parameter....................109
Figure 63. Image showing mountain ranges, terrain and geography of Colorado. Image taken after first snowfall in 2002. (After Descloitres, 2002). 120
Figure 64. Map of locations of HWAS sensors. Green shaded regions indicate areas covered by forest. 123
Figure 65. Terrain height in meters for innermost domain centered over Colorado. Solid black line indicates location of cross sections shown in upper plots of figures that follow at the gridline of the Rampart sensor. 125
Figure 66. Top: Cross section of *x*-wind component (shaded) and potential temperature (contoured) from west to east along solid black line in previous figure for the 12/30/2008 00Z truth run. Black inset box indicates location of zoomed in cross section depicted at bottom half of figure. The horizontal axis is scaled to the number of grid points from the innermost domain with a resolution of 1.33 km. Approximate locations of four HWAS sensors are marked by circles. 126
Figure 67. Truth run for 12/30/2008 03Z. Description follows previous figure. 127
Figure 68. Truth run for 12/30/2008 06Z. Description follows previous figure. 128
Figure 69. Truth run for 12/30/2008 09Z. Description follows previous figure. 129
Figure 70. Truth run for 12/30/2008 12Z. Description follows previous figure. 130
Figure 71. Truth run for 12/30/2008 15Z. Description follows previous figure. 131
Figure 72. Truth run for 12/30/2008 18Z. Description follows previous figure. 132
Figure 73. Truth run for 12/30/2008 21Z. Description follows previous figure. 133
Figure 74. Truth run for 12/31/2008 00Z. Description follows previous figure. 134
Figure 75. Top: Cross section from west to east as depicted by solid black line in Figure 16 for the 11/03/2005 17Z WRF run. Black inset box indicates location of zoomed in cross section depicted at bottom half of figure. The *x*-wind component is shaded in color and theta is contoured with solid black lines. The horizontal axis is scaled to the number of grid points from the innermost domain with a resolution of 1.33 km. Approximate locations of four HWAS sensors are marked by circles. 136
Figure 76. WRF run for 03/06/2004 18Z. Description follows previous figure. 137
Figure 77. WRF truth run for 12/30/2008 12Z. Description follows previous figure. 138
Figure 78. WRF run for 01/19/2012 04Z. Description follows previous figure. 139
Figure 79. WRF run for 12/20/2010 05Z. Description follows previous figure. 140
Figure 80. WRF run for 11/12/2011 18Z. Description follows previous figure. 141
Figure 81. WRF run for 12/18/2008 23Z. Description follows previous figure. 142
Figure 82. WRF run for 01/05/2008 15Z. Description follows previous figure. 143
Figure 83. WRF run for 02/21/2012 12Z. Description follows previous figure. 144

Figure 84. WRF run for 02/23/2012 03Z. Description follows previous figure. 145
Figure 85. WRF run for 10/02/2007 09Z. Description follows previous figure. 146
Figure 86. WRF run for 11/13/2011 07Z. Description follows previous figure. 147
Figure 87. WRF run for 06/07/2007 13Z. Description follows previous figure. 148
Figure 88. WRF run for 04/15/2006 13Z. Description follows previous figure. 149

LIST OF TABLES

Table 1. Physics processes used in the WRF system 38

Table 2. Model grid point location, latitude, longitude and sensitivity (*dJ/dx*) for point 1 and point 2. The units for *dJ/dx* are per Kelvin. 49

Table 3. Potential temperature (K) at points 1 and 2 from the ensemble mean of the NP run and from the truth run valid at 00Z 30 December 2008. The difference between the truth run and NP mean is shown in the far right column as δx. 53

Table 4. Temperature (K) at points 1 and 2 from the ensemble mean of the NP run and from the truth run valid at 00Z 30 December 2008. The corresponding perturbation in potential temperature after assimilation between the truth run and NP mean is shown in the far right column as δx. 53

Table 5. The mean, standard deviation, expected change, actual change and percent of predicted change of the forecast metric *J* for each of the WRF ensemble runs. All values are valid at the forecast time of 03Z 30 December 2008.......54

Table 6. Table showing the mean and standard deviation of perturbation potential temperature at points 1 and 2 from the analysis for every ensemble run. 61

Table 7. Table summarizing fourteen severe DSWS analyzed and modeled at USAFA. Six non-wave breaking (NWB) and eight wave breaking (WB) storms are shown...97

Table 8. HWAS sensors longitude/latitude and elevation. 121

THIS PAGE INTENTIONALLY LEFT BLANK

LIST OF ACRONYMS AND ABBREVIATIONS

AGL	above ground level
ARW	Advanced Research WRF
CA	California
CFSR	Climate Forecast System Reanalysis
CO	Colorado
DA	data assimilation
DART	Data Assimilation Research Testbed
DSWS	downslope windstorm
EnKF	Ensemble Kalman Filter
ERDC	United States Army Engineer Research and Development Center
ESA	Ensemble Sensitivity Analysis
FFT	Fast Fourier Transform
HWAS	High Wind Alert System
LTZ	lower turbulent zone
MSL	mean sea level
MSLP	mean sea level pressure
NCAR	National Center for Atmospheric Research
NCEP	National Centers for Environmental Prediction
NWB	non-wave breaking
NWP	numerical weather prediction
NWS	National Weather Service
OSSE	observing system simulation experiment
PDF	probability distribution function
TREX	Terrain-Induced Rotor Experiment
UAS	unmanned aerial system
UAV	unmanned aerial vehicle
USAFA	United States Air Force Academy
WB	wave breaking
WRF	Weather Research and Forecasting Model

THIS PAGE INTENTIONALLY LEFT BLANK

ACKNOWLEDGMENTS

I am extremely grateful to my advisor, Dr. Joshua Hacker, who poured countless hours into this project and always seemed to have an answer or suggestion whenever I hit a bump in the road. I thank him with my sincerest gratitude for mentoring me and helping me learn how to become a better researcher and more critical thinker.

Thanks also goes to the rest of my committee, including Dr. Wendell Nuss, Dr. James Doyle, Dr. Gregory Hakim, Dr. Patrick Harr, and CAPT Rebecca Stone for their commitment to me and my research. The insight, suggestions, and experience you brought to the research were incalculable. A special big thanks goes to Bob Creasy for always finding ways to store just a little more model data, and Mary Jordan for her help troubleshooting code and getting me back on track. Thanks to many others at NPS who were always there to answer a question or help me conquer the next obstacle. These include my officemate Lt Col Jack Evans, Andy Penny, Heather Archambault, Maj Bill Ryerson, LCDR Heather Hornick, CDR Joel Feldmeier, and many others.

I would also like to thank the faculty and staff at the United States Air Force Academy who granted me this opportunity, provided counsel and sound advice, and who aided me in collecting the HWAS data over many years. Particularly, I would like to thank Dr. Tom Koehler, Lt Col Mike Gauthier, Dr. Kurt Brueske, and Col Rex Kiziah. Without your help, none of this would be possible.

A special thanks and remembrance goes to my father, John Homan, who gave me and fostered my desire to learn, taught me perseverance, integrity, and that "godliness with contentment is great gain." I wish you were here to see this to completion.

Many thanks go to my mother, Teresa Homan; my brothers and sisters; my in-laws Dave and Joni; and all of my extended family for your constant love and support.

Finally, to my incredible wife, Janee, thank you for your unwavering commitment to me and for shouldering the "joy" of raising our kids while I finished this work. Thanks to Ben, Emily, and Matthew for being the best kids a dad could ever hope for. I love you all and look forward to our many adventures ahead!

THIS PAGE INTENTIONALLY LEFT BLANK

I. INTRODUCTION

Downslope windstorms (DSWS) in regions of complex terrain are well-documented, but also notoriously difficult to forecast for individual locations due to dramatic differences in observed wind intensity that can occur over very short spatial and temporal scales. During certain seasons in regions of complex terrain, high winds are often the most disruptive meteorological variable to military operations. In particular, aviation missions can be severely hampered by high winds and associated waves, rotors, and turbulence. One such location is at the United States Air Force Academy (USAFA) just north of Colorado Springs, Colorado. In response to the disruptive nature of high winds to military operations at USAFA, a meso-net of twelve automated meteorological observing stations was deployed in various locations along the Front Range of the Rocky Mountains in and around USAFA in 2004. This network was aptly named the High Wind Alert System (HWAS).

It is of the utmost importance to the military to determine if the deployment of similar observation networks into the forward battlespace can increase the forecast skill of high resolution Numerical Weather Prediction (NWP) models in complex terrain, especially in data-denied or data-sparse regions. As the technology and delivery platforms such as drones or UAV/UAS's for these automated forward deployed systems are developed, an important cost analysis process will need to occur. A better understanding of the usefulness of these observations for characterizing the battlespace, and understanding these observations impact on numerical forecasts in complex terrain is paramount.

A tool that can potentially assess the impact of observations to NWP forecasts is Ensemble Sensitivity Analysis (ESA). ESA is emerging as a viable alternative to adjoint sensitivity and its potential has recently been demonstrated by several studies (Ancell and Hakim 2007; Torn and Hakim 2008, 2009; Torn 2010). ESA can potentially identify forecast sensitivity to initial condition and parameter changes. Combined with an ensemble data assimilation system, ESA can help evaluate existing and proposed observation network designs. Most previous work focused on synoptic scales, and much less is known about ESA for mesoscale predictions with grid spacing of a few km. Because ESA relies on an ensemble to sample initial condition and forecast PDFs, it is subject to sampling error and an assumption of linear statistics. The validity of the linearity assumptions, and the role of sampling error associated with potentially weak correlations, are largely unknown for smaller spatial and faster temporal scales. Because mesoscale predictability varies according to the phenomenon of interest and forecast metric, the performance and potential of ESA will be a function of both phenomenon and metric.

For decades it has been widely accepted within the meteorological community that the forecast accuracy of NWP models is inextricably linked to the accuracy of the initial conditions of the forecast model. In response to this relationship, one area of focus in research to improve NWP forecasts has emphasized the importance of robust data assimilation (DA) systems for NWP models. The goal of most DA systems is to combine previous model forecasts, current observations, and the error statistics of both to produce the most accurate analysis of the current state of the atmosphere. Although not always true, the governing assumption in NWP is that the more accurate the analysis, the more skillful a forecast will be.

In response to the notion that a more accurate analysis of the atmosphere is needed, an immense amount of research has gone into producing new DA systems that can handle the myriad of different observation types. In addition, research has addressed the question of what type, and where, observations are needed in the first place to improve analysis accuracy. From this notion emerged what is now known as targeted, or adaptive, observing aimed at improving forecasts by taking observations in regions where analysis errors are likely to be large and to grow rapidly, and to which some specified measure of forecast error is sensitive (Snyder 1996; Lorenz and Emmanuel 1998; Berliner et al. 1999). Movable observing platforms such as unmanned aircraft are one approach. Targeted observing motivates the question: If the atmosphere could be observed at any place and time, where and what measurements are needed to improve the forecast? Although there has been much progress in this area in global and regional models, many unresolved questions remain about the impact of observations on the predictive skill at fine scale resolutions of less than 4 km.

One fundamental question that has to be addressed in targeted observing research is: what is the impact of a particular observation on the analysis and thus the forecast? If adding a new observation to the DA scheme either doesn't change the analysis or if the new observation changes the analysis but doesn't change the forecast of the NWP model, then why add the observation in the first place? In the most general sense, if a forecast is highly sensitive to initial conditions, then the forecast is inherently less predictable. If a forecast is not affected by inaccurate or varied initial conditions, then that forecast is more stable and thus much more predictable.

This idea of sensitivity to initial conditions and the relation of the stability of the system to the limits of predictability was linked to the ideas of chaos and explored by Lorenz (Lorenz 1963, 1969). In NWP, much progress has been made through the realization that the chaotic behavior of the atmosphere requires the replacement of single deterministic forecasts by ensembles of forecasts with differences in the initial conditions (Kalnay 2009). In addition, for an ideal ensemble that accurately accounts for all sources of forecast uncertainty, the verifying truth should be indistinguishable from the members of the forecast ensemble. Also, the spread of such an ideal forecast ensemble ought to be correlated to the forecast uncertainty where cases with large (small) ensemble spread are associated with large (small) forecast uncertainty (e.g. Grimit and Mass 2007).

Our research aims to further the exploration of forecast sensitivity and forecast uncertainty in the context of a strongly forced mesoscale phenomena with non-linear dynamics by:

- Evaluating the potential of ESA as an analysis tool for determining the sensitivity of a severe DSWS in complex terrain to initial conditions and assimilated observations.
- Using ESA to determine the leeside conditioning versus upstream synoptic forecast sensitivities for a DSWS to the initial conditions in a mature ensemble forecasting system.
- Evaluating the potential of ESA to determine a priori where and when targeted observations can add value to a forecast by reducing ensemble spread and thus increasing the reliability of the forecasts.

A. MOTIVATION

DSWS have been well documented and modeled for decades. However, many of these studies have occurred at Boulder, CO or in the Owens Valley, CA in the lee of the Sierras. These locations lend themselves to test and model theories in nature, yet in an environment that are similar to idealized two-dimensional ridges used to develop much of the theory. The geography in and around the Pikes Peak region is more three-dimensional relative to most of the previous studies, and it follows that the wind storm characteristics are likely more three dimensional as well.

For the purposes of this study, a severe DSWS is defined as westerly wind gusts of 50 kt or greater (NWS severe criteria) recorded by at least two HWAS sensors. Severe DSWS have been recorded regularly using the HWAS network at USAFA since its installation in 2004. A careful examination of these events reveals downslope storms that are produced frequently and on the same order of magnitude as found in Boulder and Ft Collins, CO to the north. A total of 110 severe DSWS (Figure 1) have been recorded by HWAS over an eight year period from 2004 to 2012 (2009 excluded due to data outages) with frequent gusts observed greater than 70 kt (36 m s^{-1}).

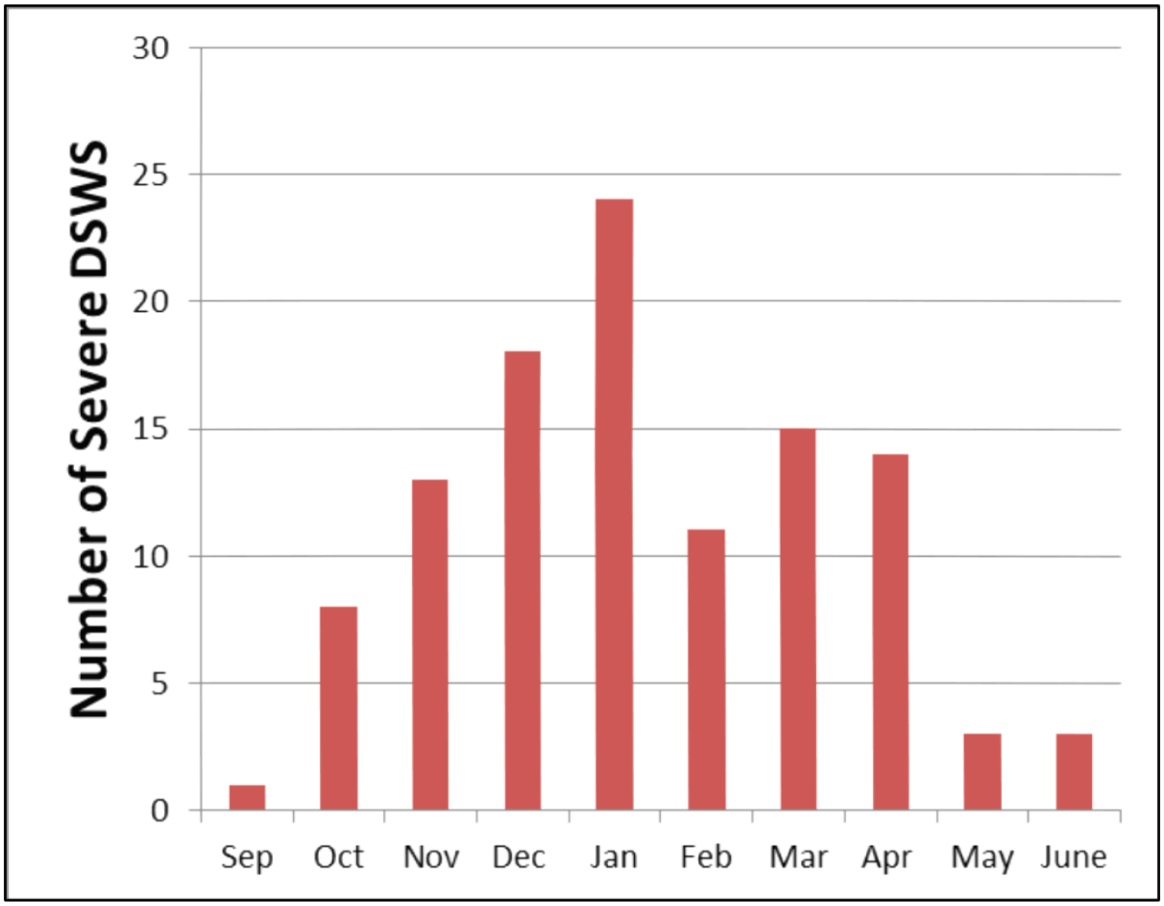

Figure 1. Total number of severe DSWS broken down by month as recorded by HWAS sensors at USAFA from 2004 to 2012.

While the initiation, upstream conditions, and synoptic setup for severe downslope wind storms has been thoroughly examined in research over the past several decades, less work has been done on defining the conditions that promote the propagation of strong winds down the slope and away from the mountains into the valleys or plains. In addition, often severe downslope winds caused by mountain waves are accompanied by leeside trapped waves, low-level vortices or rotor, and flow separation (Doyle 2002; Hertensteirn and Kuettner 2005; Vosper et al. 2006; Jiang et al. 2007). Even less work has been done on describing the impact these leeside features have on the propagation of the strong downslope winds away from the slope and into the valleys or plains.

We use the term “leeside conditioning” in our study to describe the conditions prior to and during the onset of high winds lee of the mountain slope in the region where downslope winds are observed that play a role in determining the distance strong winds will move down the slope. Leeside conditioning can consist of the thermal structure, stability profiles, surface pressure distributions, wave structures, and boundary layer characteristics which lend themselves to strong wind events at lower elevations separated from the mountain slope. Leeside conditioning is often a mesoscale feature that is related to or aided by larger synoptic scales, but can vary at fine spatial and temporal scales driven by the mesoscale details.

Recent studies have examined the sensitivity of mountain waves to topography and upstream conditions using an adjoint (Doyle 2007) and ensemble sensitivities (Reinecke and Durran 2009), but do not focus on leeside conditioning and its role in the spatial extent of strong downslope winds. Additionally, studies have examined leeside boundary layer flow separations (Jiang et al. 2007), the influence of inversions (Vosper et al. 2006; Hertenstein 2009), surface friction (Doyle and Durran 2002), and wind profiles (Hertenstein and Kuettner 2005) on trapped waves and rotors. However, almost all these studies cite the need for further examination of these features in irregular terrain and with the aid of a model capable of performing full three-dimensional simulations. In summary, the full exploitation of ESA to examine the sensitivity of a forecast to initial conditions and assimilated observations has yet to be accomplished for a DSWS, and the associated leeside conditioning, in more three-dimensional terrain. Here we address these issues.

II. BACKGROUND

A. ENSEMBLE SENSITIVITY ANALYSIS

1. Overview

A method that has shown promise in identifying locations of initial condition sensitivity is Ensemble Sensitivity Analysis (ESA). ESA, as proposed by Hakim and Torn (2008), computes the sensitivity of a forecast metric (J) with respect to the model initial conditions ($\overrightarrow{x^a}$) by utilizing the statistics of the ensemble. Hakim and Torn used ESA to diagnose relationships between the minimum central pressure of a mid-latitude cyclone and initial condition fields such as geopotential height and wind speed.

ESA was also explored by Ancell and Hakim (2007), where they relate and show the equivalence of ensemble sensitivity to adjoint sensitivity. Furthermore, Torn and Hakim (2008) illustrated how ensemble sensitivity for synoptic-scale forecasts can be used to determine climatological sensitivity. Their experiment demonstrated that forecasts of sea-level pressure and rainfall over western Washington were sensitive to the upstream mass and temperature fields (Figure 2). Their results suggest that ESA provides an attractive alternative to adjoint sensitivity analysis and may be useful for observation thinning and observation targeting.

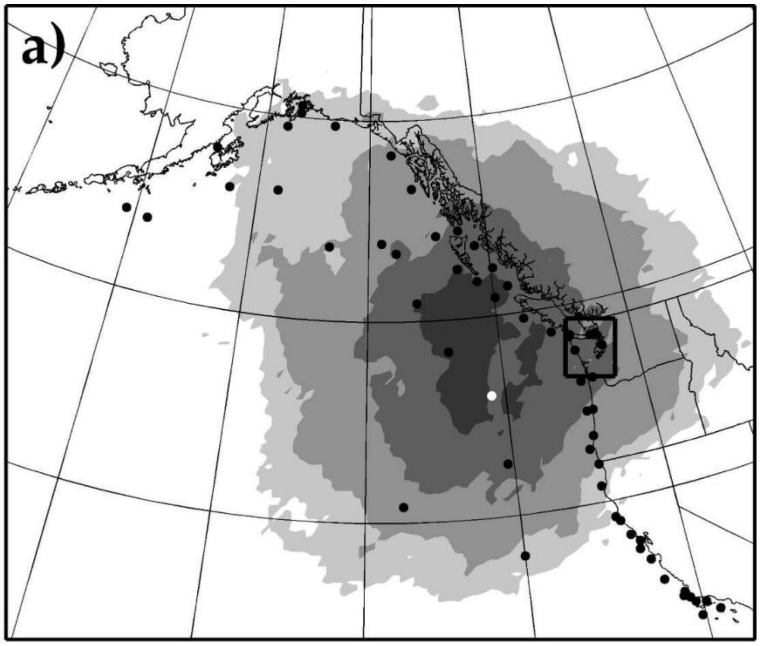

Figure 2. Results of the ESA performed by Hakim and Torn, showing that the sensitivity of 24 hour precipitation in a box over western Washington State is most sensitive to changes in SLP in the darkest regions west of the box. After Hakim and Torn 2008.

Derivation from Linear Regression

A scalar approximation to the full ESA can be derived. Given a bivariate dataset of observations, linear regression finds the straight line that explains the linear relationship of the sample. This line is given by the equation $y = mx + b$ where y is the dependent variable, x is the independent variable, m is the slope of the line, and b is the y-intercept. This line minimizes the sum of squared differences between observed values (the y values) and predicted values given by the line. Linear regression is most appropriate when both the x and y values are normally distributed, meaning the marginal distributions are symmetric and have a single mode. The slope of this best fit line (m) can be expressed by $\frac{\Delta y}{\Delta x}$. It can be shown by using any bivariate sample that the slope of this best fit line can be represented by:

$$\frac{\Delta y}{\Delta x} = \frac{\mathrm{cov}(x, y)}{\mathrm{var}(x)}. \tag{2.1}$$

This expression can be simplified to:

$$\frac{\Delta y}{\Delta x} = \frac{r\,\sigma_y}{\sigma_x} \tag{2.2}$$

where r is the correlation coefficient between x and y, σ_y is the standard deviation of y, and σ_x is the standard deviation of x.

ESA in its most basic scalar form performs linear regression to find the best fit line between two samples where the sensitivity is the slope of this line. For an ensemble size M, the sensitivity of a scalar forecast metric derived from the ensemble mean forecast (J_e) to an analysis state variable (x^a) is equivalent to Eq. (1) in Torn and Hakim (2008):

$$\frac{\delta J_e}{\delta x^a} = \frac{\mathrm{cov}(\ J\ ,\ x)}{\mathrm{var}(x)}\ . \tag{2.3}$$

ESA uses samples of the state at the initial and forecast time to estimate statistically (probabilistically) how changes in the initial conditions affect the forecast metric J. Here J and x are 1 x M ensemble estimates of the state variable (independent variable) at an analysis grid point and forecast metric (dependent variable) at a defined location and time. ESA is shown to approximate the adjoint ($\frac{\partial J}{\partial \boldsymbol{x^a}}$) given that as the limit of δJ_e and δx^a approaches zero:

$$\frac{\delta J_e}{\delta x^a} = \frac{\partial J_e}{\partial x^a} = \frac{\partial J}{\partial x^a}\,. \tag{2.4}$$

Switching from a scalar form to matrix form, ESA can be performed at every grid point and every state variable represented by $\boldsymbol{x^a}$ that is a N x M matrix where N is the number of state variables and M is the number of ensemble members.

To determine the impact of hypothetical observations, Ancell and Hakim (2007) propose in their Eq. (26) to use the analysis increment and an ensemble Kalman filter (EnKF) to assimilate observations 1..i, and can be written as:

$$\delta \boldsymbol{x^a} = \boldsymbol{x}_{i+1}^{a} - \boldsymbol{x}_{i}^{a} = \mathbf{K}_i(y_{i+1}^{o} - \mathbf{H}\boldsymbol{x}_i^a) \tag{2.5}$$

where

$$\mathbf{K} = \ \mathbf{P}_i^{\mathbf{a}}\ \mathbf{H}^{\mathbf{T}}(\mathbf{H}\mathbf{P}_i^{\mathbf{a}}\mathbf{H}^{\mathbf{T}} + \mathbf{R})^{-1} \tag{2.6}$$

and $\mathbf{P}_i^{\mathbf{a}}$ is the n x n ensemble-estimated analysis error covariance, $\mathbf{H}$ is the n-length row vector containing a linearized forward operator, and $\mathbf{R}$ is the p x p observation error variance. It is important to note that the analysis increment from the EnKF is consistent with ensemble statistics only for the same EnKF and model. Here the perturbation to the analysis $\delta\boldsymbol{x^a}$ is due to the assimilation of a new observation (y_{i+1}^{o}). To determine how this perturbation relates to the forecast metric J, Eq. (2.5) is solved for $\delta\boldsymbol{x^a}$ substituted into a matrix form of Eq. (2.1) yielding:

$$\delta J = \left(\frac{\partial J}{\partial \boldsymbol{x^a}} \right)^T \mathbf{K}_i (y_{(i+1)}^{o} - Hx_i^a). \qquad (2.7)$$

The implications of Eq. (2.7) are significant as it allows, within the sampling and assumptions of ESA, an a priori assessment of how a hypothetical observation would affect an ensemble mean and ensemble spread of a forecast given a particular model, and data assimilation system. Within the framework presented, ESA is able to not only predict regions of sensitivity to initial conditions but also allows for the evaluation of potential targeted observations or network design without taking or assimilating real observations. This capability is of the utmost value for military contingency operations and planning in data denied or data sparse regions where accurate forecasts and assessment of forecast reliability are strongly desired.

B. DOWNSLOPE WINDSTORMS

1. Overview

DSWS have received much attention by the meteorological community over the past several decades. Downslope winds are produced when stably stratified air encounters a mountain barrier that generates gravity waves to produce strong winds under certain conditions in the lee of the mountain barrier. Generally, upstream conditions favorable for strong downslope winds include the existence of a stable layer near or above mountain top and a less stable layer above. Winds can be high at the level of the stable layer, but strong winds in the upper-troposphere are not necessary (Brinkman 1974). DSWS have been given many names in different locations across the globe and are generally classified into two types of winds; foehn winds or warming winds and bora winds or cooling winds.

The Rocky Mountain region with its chinook winds is perhaps the most studied and well known location for these events. A chinook is a foehn wind phenomenon along the eastern slopes of the Rocky Mountains. These winds are much more frequent and stronger in the winter than in the summer. The onset of a chinook is easily recognized by a sharp increase in temperature, a drop in relative humidity, the development of strong westerly surface winds, the existence of a dry-adiabatic lapse rate, and often the appearance of wave cloud features (Oard 1993). For a long time, severe downslope winds along the eastern slopes of the Rocky Mountains were only attributed to chinook type events. However, it has been documented that katabatic flows similar to the bora of Europe have been responsible for many of the wind events along the Colorado Front Range (Brinkman 1974). Some of Boulder's windstorms have caused temperature rises of 15–20°C while others have resulted in temperature drops of up to 15°C. Despite the difference in the evolution of surface temperature lee of the slope, there does not appear to be any significant dynamical distinction between the processes responsible for the development of high winds in cold or warm events (Durran 2003). Regardless of their classification, these downslope wind events can be intense, damaging to property, forests, vegetation, military and aviation operations, and human life. Wind intensities can vary upon small-scale terrain effects, exposure, the synoptic weather patterns and the atmospheric dynamics present.

Several theories explaining the dynamic forcing of these storms have been published throughout the years, with some disagreement. Scorer and Klieforth (1959), and Aaneson (1965) proposed that the generation of strong downslope winds were primarily attributed to rather short (generally < 20 km wavelength) quasi-periodic lee waves that propagate downstream of a mountain range under conditions that allow trapping of wave energy to create strong windstorms. These waves form under conditions most notably when the wind speed increases rapidly with height. According to Klemp and Lilly (1975), this theory proved insufficient to describe the dynamics of a DSWS as observations of DSWS around Boulder, Colorado indicated that the horizontal wavelength of waves associated with downslope winds storms are on the order of 50–100 km and vertically propagate freely, leading to the conclusion that trapped resonant waves do not play an important role in this phenomenon.

Eliassen and Palm (1960) demonstrated that when an upward propagating gravity wave encounters a region in which the Scorer parameter changes rapidly, some of this wave energy can be directed back into a downward propagating wave. The Scorer parameter is defined as:

$$l^2 = \frac{N^2}{U^2} - \frac{1}{U}\frac{d^2U}{dz^2} \tag{2.8}$$

where $U(z)$ is the flow of the background state and $N(z)$ is the Brunt-Väisälä or buoyancy frequency. Extending the work of Eliassen and Palm (1960), Klemp and Lilly (1975) suggest that strong downslope winds occur when the atmosphere has a multilayer structure that produces an optimal superposition of upward and downward-propagating waves. They found that this most often occurs when the tropopause is located one-half vertical wavelength above the ground.

Clark and Peltier (1977) further explored this idea using a numerical model and suggested that large-amplitude waves and downslope winds are produced after a vertically propagating wave breaks; the energy in the upward propagating wave is trapped beneath its own level of “supercritical steepening,” producing a substantial increase in the wave amplitude. A series of studies ensued (Clark and Peltier 1984; Peltier and Clark 1979, 1984; Clark and Farley 1984) that suggested that after increasing in amplitude and breaking, the wave breaking region was characterized by strong mixing and a wind reversal in the cross-mountain flow. This wave induced critical level provides a top to a resonant layer that reflects upward propagating waves back toward the mountain leading to very strong surface winds. Additional numerical studies have repeatedly verified the importance of wave breaking in the development of strong surface winds (Durran 1990).

The dynamics governing the development of strong downslope winds in the atmosphere are similar to those governing the rapid increase in speed that occurs when water flowing over a rock in a river undergoes a transition from a relatively slow velocity upstream to a thin layer of high-velocity fluid over the downstream face. In such circumstances, a turbulent hydraulic jump often develops downstream of the rock at the point where the high-speed flow decelerates back to the ambient velocity of the river (Durran 2003). This notion has led researchers to describe the DSWS on the basis of hydraulic jump theory, assuming the atmosphere can be modeled as two or more neutrally stratified layers with sharp inversions at each layer interface (Long 1953a; Kuettner 1959; Houghton and Isaacson 1968). Additional work was done in this area proposing that strong winds will occur along the lee slope when a fluid undergoes a transition from subcritical flow upstream to supercritical flow over the mountain (Smith 1977; Durran 1986; Durran and Klemp 1987). However, it has been suggested that the hydraulic analog is best applied to the atmosphere in a qualitative, rather than a quantitative, manner (Durran 2003), as quantitative application is made difficult by defining a dynamically meaningful Froude number in vertically unbounded continuously stratified flow as hydraulic theory bounds the flow by a free surface and hydrostatic balance (Durran 1990; Reinecke and Durran, 2008).

2. Leeside Conditioning

While upstream synoptic forcing is necessary for the creation of mountain waves and DSWS, often the local conditions in the lee of the mountain barrier can determine the severity, impact, and propagation of the downslope wind storm down the slope to the adjacent valleys or plains. We use the term “leeside conditioning” in our study to describe the conditions prior to and during the onset of high winds lee of the mountain slope in the region where downslope winds are observed, and which may play a role in determining the distance strong winds will move down the slope. Leeside conditioning can consist of the thermal structure, stability profiles, surface pressure distributions, wave structures, and boundary layer characteristics which lend themselves to strong wind events at lower elevations separated from the mountain slope. Leeside conditioning is often a mesoscale feature that varies at very fine spatial and temporal scales, but can be influenced or aided by larger synoptic scales.

a. Downslope Windstorm Leeside Conditioning

While several studies have considered leeside conditioning during severe DSWS, the topic is less studied than the upstream conditions which are thought to be important for the development or initiation of DSWS. Brinkman (1974) analyzed 20 Boulder windstorms and assessed the role of mean deviations from normal station pressure lee of the mountain slope. During chinook (warm) events he found that lee-side pressure drops twice as rapidly as upstream stations; but in cold or bora cases pressures rise twice as fast in the upstream stations than in the lee. Brinkman concludes that a strong local pressure minimum is observed beneath a warm region caused by adiabatic compression. Because this pressure minimum is caused by the windstorm, it would have little predictive value and the extent of eastward surface winds would be limited. In addition, Brinkman noted that leeside soundings showed a lower stable layer (inversion) than upstream soundings, and also have a steeper lapse rate for Boulder windstorms.

The depth and strength of surface-based inversions and cold pools has been identified as a primary factor in the strength of surface winds during a downslope event. Pielke (1985) suggested that in the absence of surface heating, cold air lee of a mountain barrier can be flushed out by internal gravity waves that reach sufficient amplitude, and also by shear-induced turbulence at the top of the cold pool. Pielke notes that in nature, both processes are likely to occur simultaneously. In order to test these theories, Lee et al. (1989) investigated the influence of cold pools of air on downslope winds and the flushing of the cold air east of the mountain barrier using a two-dimensional model and idealized terrain. Their results showed that cold pools can determine whether downslope winds make it to the mountain base. They conclude that the top of the cold pool acts very much like terrain with similar shape preventing the penetration of strong winds to the mountain base. In this case, the core of maximum horizontal winds is found at the top of the mountain with less intense winds along the lee slope.

Jiang and Doyle (2008) conducted a series of idealized simulations of modest downslope events in the Owens Valley, CA during the TREX experiment and looked at the effects of diurnal surface heating on leeside conditioning. They concluded that surface heating after sunrise weakens the downslope winds by destratifying the downslope flow, and eventually leads to the decoupling of the valley air from the westerlies above the mountaintop by local noon. Their simulations showed that a shallow penetration depth down the slope into the valley exists in the absence of surface heating. Furthermore, they stated that surface heating in the lee plays a dual role; it tends to weaken the downslope flow by reducing its stratification and enhance it by creating a leeside surface low.

b. Leeside Conditioning Due to Rotor and Flow Separation

Rotor is defined as the circulation of flow about a horizontal or nearly horizontal axis that is usually associated with flow over the lee side of a barrier, such as a mountain range (Glickman 2000). Rotors are often found in the lee of a mountain ridge in conjunction with high amplitude mountain waves (Holmboe and Kleforth 1957; Kuettner 1959; Lester and Fingerhut 1974). Because a rotor can exist in the lee of mountains without the presence of severe downslope winds, leeside trapped waves, rotor, and flow separation are often treated in the literature as separate phenomena from DSWS. However, the two phenomena are linked by their fundamental forcing, stratified flow over a terrain barrier. This delineation in most of the literature has led to very little research or linkage between the convergence zone between the downslope winds and the low-level rotor region.

Kuettner (1959) was probably the first to thoroughly document and research leeside rotors after experiencing its effects during many glider flights. He summarized the structure he observed and proposed in a diagram shown in Figure 3. Lester and Fingerhut (1974) named this rotor region the Lower Turbulent Zone (LTZ) and defined it as a highly turbulent region of nearly neutral stability found immediately to the lee of the mountains between the ground and an elevated stable layer in which the mountain wave motion is occurring. Based upon the observations from this study and modeling efforts (Hertenstein and Kuettner 2005), leeside rotors have been classified into two main types; lee-wave type and jump type. In lee wave types, the rotor is located below lee waves and contains moderate to severe turbulence. Jump-type rotors extend well above the upstream inversion and contain severe turbulence. Lester and Fingerhut (1974) documented the varying distances the first lee trough can set up from the ridge line giving a distance ranging from 5 to ~50 km. While much further research has been conducted on understanding the strength, size, internal dynamics, and relation to boundary layer flow separation for rotors, almost no progress has been made on determining where the first rotor in the lee of the ridge line sets up.

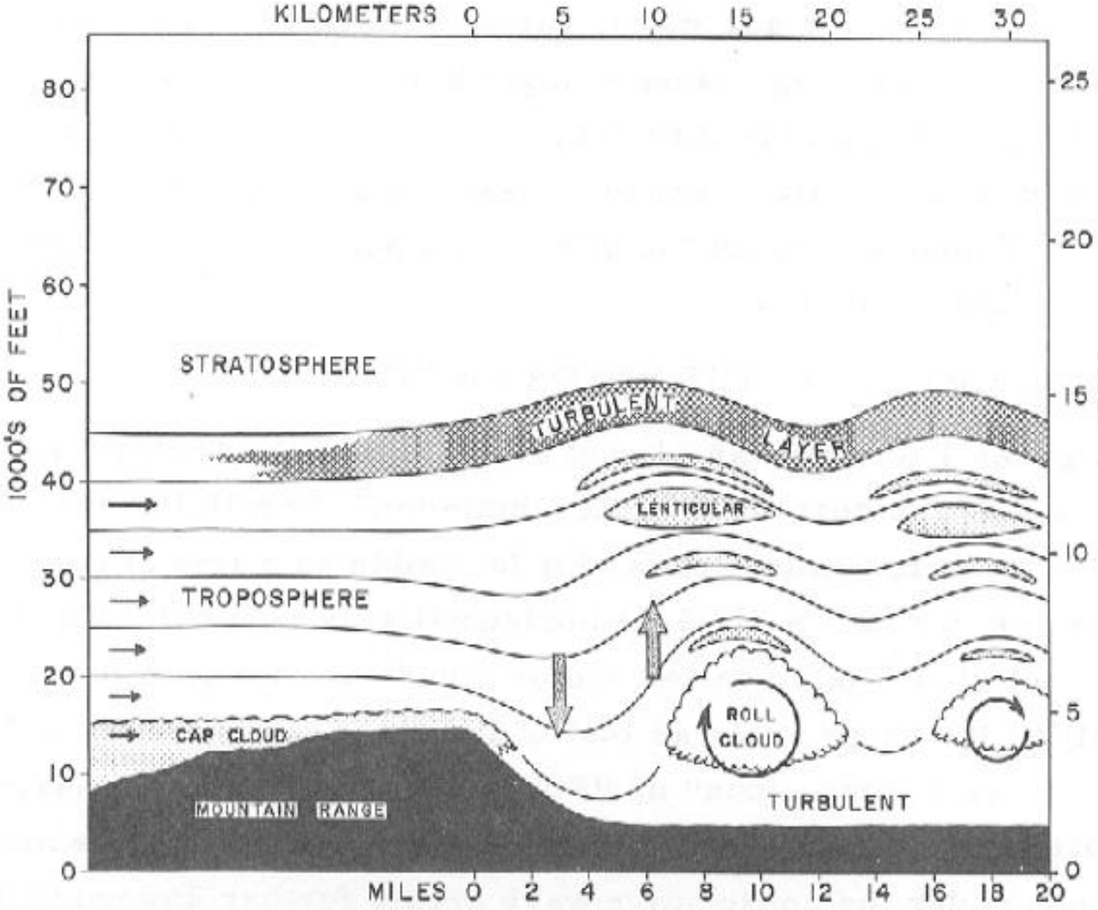

Figure 3. Schematic diagram of flow pattern over mountain range.
From Kuettner 1959

Doyle and Durran (2002) linked the importance of lee waves in the formation of rotors. In a series of two-dimensional numerical simulations they documented that the existence of rotors depends on the amount of surface friction; and that sufficiently high wave amplitude can induce a pressure gradient that can lead to boundary-layer flow separation. Regions of recirculation or upstream flow underneath the wave crests can exist as shown in Figure 4. Figure 5, from Doyle and Durran (2002), shows that as surface friction increases the distance to flow separation decreases. However, no further discussion was given on what factors other than surface friction might play a role in the locations of flow separation and rotor formation.

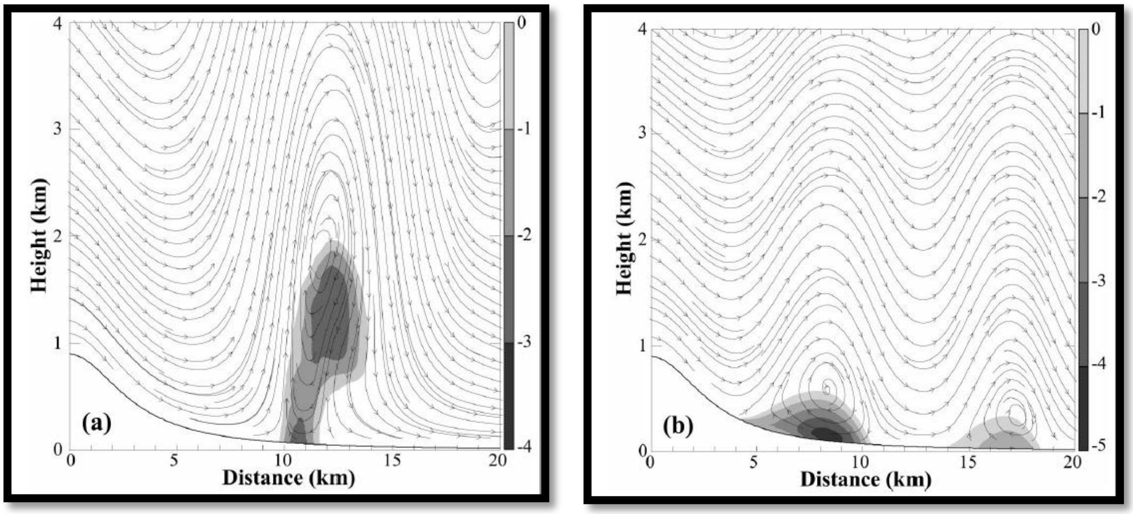

Figure 4. Streamlines and horizontal wind speed (m s^{-1}) for simulations using (a) free-slip and (b) no-slip lower boundary conditions. Horizontal wind speed contours less than zero are shaded (from Doyle and Durran 2002).

Doyle and Durran (2002) also discussed the relationship between the strength of downslope winds and the formation of lee waves and rotors. They note that an increase in rotor strength is often accompanied by an increase in the downslope winds along the lee slope. However, they conclude that it is the lee-wave amplitude that most closely correlates with rotor intensities, rather than downslope wind strength. The increase in the downslope wind speed is much smaller than the increase in the lee-wave induced pressure gradient. Furthermore, in one of their experiments the downslope winds were so strong (exceeding 60 m s^{-1}) that no rotors or reversed flow were able to develop. They conclude that in the absence of significant lee wave activity, rotors do not need to develop even when the winds are very high, but large-amplitude lee-waves can produce very strong rotors even when the downslope winds are relatively modest.

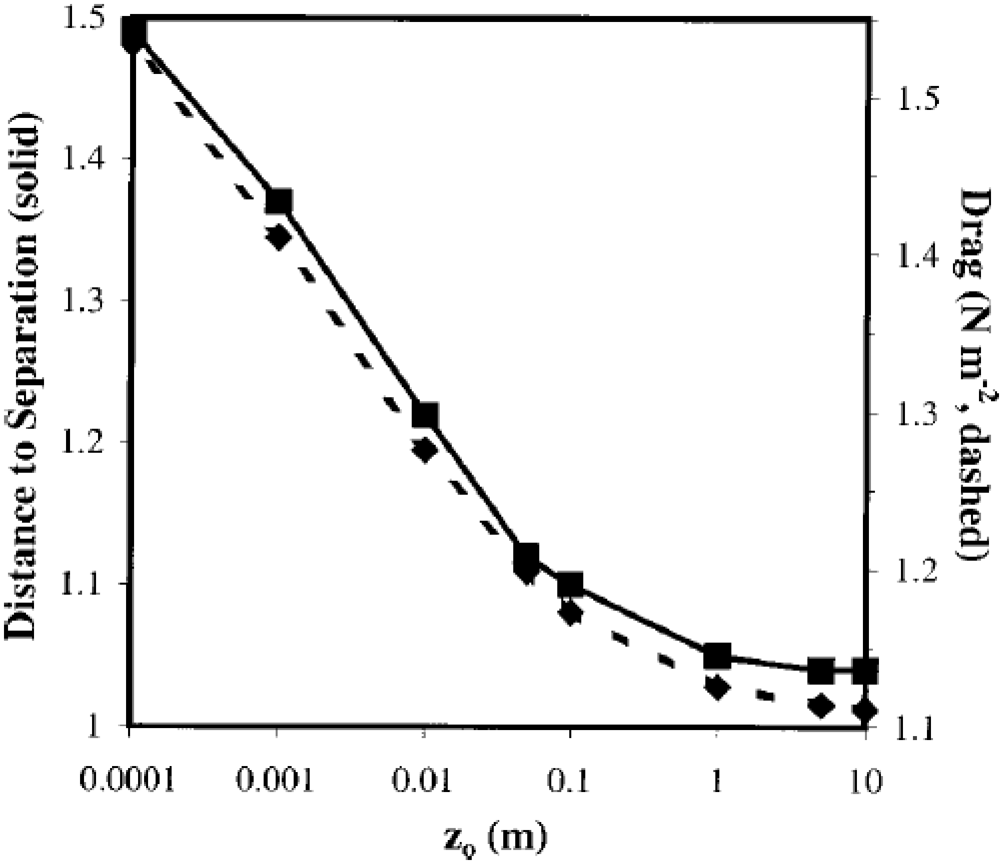

Figure 5. Distance to flow separation (solid, non-dimensional) and pressure drag (dashed) as a function of surface roughness length (from Doyle and Durran 2002).

Jiang et al. (2007) investigated the relationship between winds in the lee of topography, trapped waves, and boundary-layer separation. They defined boundary- layer separation as the separation of the boundary layer from the lee slope under the influence of an adverse pressure gradient. They described further that at the separation point, the lowest streamline is lifted of the surface with a recirculation region located between the separation points. They connect this study with previous studies, noting that the recirculation region is also known as a rotor. Using a two-dimensional numerical model, Jiang et al. studied the effects of stability, trapped waves, wave breaking, and elevated inversions on boundary flow separation lee of topography.

Contrary to previous studies, such as Doyle and Durran (2002) and Vosper (2004), Jiang et al. conclude that while bottom friction plays a role in rotor formation, surface wind speed down the slope of the terrain is the most relevant boundary-layer property that determines boundary-layer separation. Their study suggests that in the presence of trapped waves, boundary-layer separation occurs where the wave-induced adverse pressure gradient and the negative horizontal wind perturbation reach a maximum and that boundary layers separation forced by trapped waves is governed by a normalized ratio of the vertical-velocity maximum to the surface wind speed. Put in a different way, the stronger the surface wind speed, the stronger the wave forcing needs to be to induce boundary layer separation. While this study further enhanced the understanding of the conditions during which boundary layer separation occurs, no discussion was given on what determines the distance from the upstream terrain that the first flow separation point occurs.

C. CLIMATOLOGY – SEVERE DOWNSLOPE WINDSTORMS AT USAFA

A study of the climatology of severe DSWS at USAFA is conducted analyzing the HWAS dataset from 2004 through 2012 (2009 excluded due to data outages). A study of this type is useful to determine how the frequency, intensity, and seasonal variation of the storms at USAFA compare to other commonly studied locations. A severe DSWS is defined as westerly wind gusts of 50 kt or greater (NWS severe criteria) recorded by at least two HWAS sensors for the purposes of this study. A total of 110 severe events are identified with an average of 17 severe events per year (Figure 1). Severe low-level winds also occur several times per year due to thunderstorm outflow or strong pressure gradients with winds parallel to the mountains (winds not out of the west) and these events are excluded for the purposes of this study. The complexity of the terrain surrounding USAFA is described in detail in Appendix A. Cross sections from the

“Truth” simulation (described in Chapter III) are given in Appendix B for the entirety of the 30 December 2008 event used as a case study and described in section D.

Severe DSWS at USAFA are most common during the winter months. Peak frequency of occurrence is in November and December, with a second peak in the months of March and April (Figure 6). The second peak in March and April coincides with the frequent strong leeside cyclogenesis that occurs in this region during the early spring months, which may play a role in the development of leeside troughing that often accompanies severe events by increasing the cross mountain pressure gradient in this region. As shown in Figures 1 and 6, severe DSWS occur at almost any time of the year, with the exception of July and August where a severe event has yet to be recorded.

The winter of 2011/12 was particularly active for severe DSWS at USAFA. HWAS recorded 26 between the months of November to May, with 24 of the 26 events recorded between the months of November through March. An average of only 6.3 days existed between severe events during this period. The peak during this season was in January with six events.

Of the 110 severe DSWS identified, only eight of these events were recorded on ten or more of the twelve sensors and only two events were recorded by all twelve sensors including the December 30, 2008 event used as a case study for this research. The average peak gust recorded by HWAS for these eight widespread events is 70 kt (36 m s^{-1}), with the highest gust of 79 kt (41 m s^{-1}) recorded at the Rampart sensor at 1708Z on December 30, 2008. This event is discussed in detail in the next section and is the basis for our ESA studies.

HWAS additionally reveals that the highest winds are predominantly confined to the higher elevations and along the western-most portions of USAFA that lie closest to the steep slopes of the Rampart Range. The Rampart sensor is by far the most wind-prone sensor; most every severe event was recorded by this sensor except for a few when this sensor had a data outage. Many more severe events were recorded by this sensor than are included in the 110 events cited in this study as these additional events were only recorded by the Rampart sensor and not by any of the other HWAS sensors.

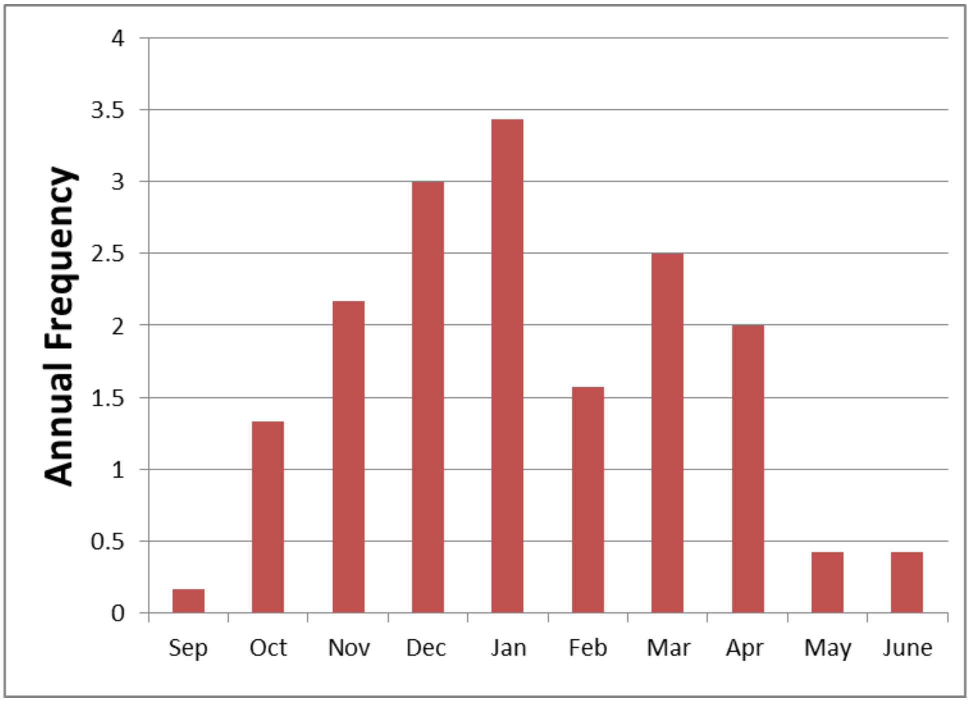

Figure 6. Annual frequency of severe DSWS broken down by month as recorded by HWAS sensors at USAFA from 2004 to 2012.

For the purposes of this research, the Airfield sensor is selected to represent a valley location separated from the slopes of the Rampart Range. This sensor's selection is based upon its downstream location almost directly east of the higher Rampart sensor, and because of the importance of forecasting winds at this location in support of aviation activities. An examination of the Airfield sensor reveals that only 24 of the 110 severe events (21.8%) are recorded at the Airfield sensor, or approximately three events per year. These events, although less frequent, can still be intense with gusts as high as 64 kt (33 m s^{-1}). It is a primary goal of this research to determine if ESA can be used as a tool to identify what initial conditions these events are sensitive to, leading to insight about the structure of these events and why 78% of severe DSWS observed by HWAS never propagate away from the mountain slope and move out into the adjacent valleys and plains.

D. CASE STUDY: SEVERE DOWNSLOPE WINDSTORM—DECEMBER 30, 2008

1. HWAS Characterization of 30 December 2008 Downslope Windstorm

The strongest DSWS recorded during the period of study by HWAS was on December 30, 2008. This event was recorded by all twelve HWAS sensors and included the strongest gusts ever recorded by five of the twelve sensors. This severe event caused widespread damage across Colorado Springs and the Front Range of Colorado and is the fourth most costly wind event in Colorado history with an estimated $7 million in insured damage (Rocky Mountain Insurance Information Association 2009). Time series of winds, wind direction, temperature, dewpoint, and MSLP are shown for the Rampart, Community Center, Airfield, and Pine Creek HWAS sensors in Figures 7–11, showing the west to east progression during this severe DSWS. This event lasted approximately 24 hours with winds ramping up at the Rampart sensor at 18Z on the 29th and continuing until around 18Z on the 30th (Figure 7). At the Rampart sensor, severe gusts (greater than 50 kt) were observed for sixteen straight hours from approximately 03Z to 19Z on the 30th with a max peak gust of 79 kt at around 17Z.

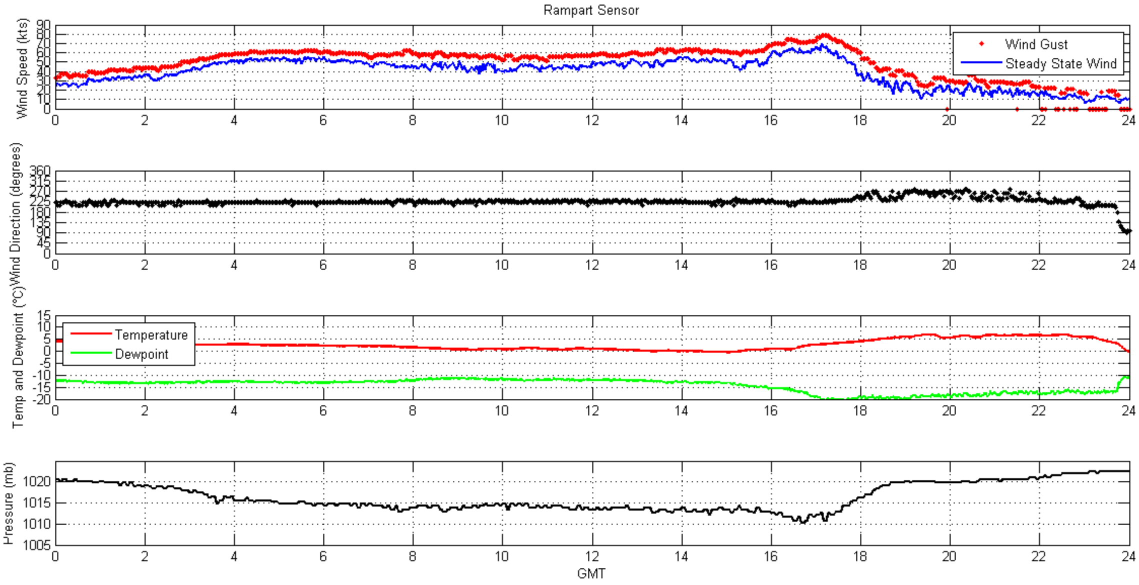

Figure 7. Time series of winds, wind direction, temperature, dewpoint, and MSLP at the Rampart sensors during a severe DSWS on 30 December 2008.

Two distinct maxima are shown in Figure 11, with the first maximum gust of 62 kt at 05Z (Figure 7). After a relative lull, a second maximum of 79 kt (41 m s^{-1}) followed. Strong gusts increased at the Community Center sensor at the base of the slope at 03Z, corresponding to the beginning of the first maximum at the Rampart sensor (Figure 11). Severe gusts were observed intermittently at the Community Center sensor from approximately 04Z to 18Z with the highest gusts of 68 kt (35 m s^{-1}) occurring about 1530Z (Figure 8). A comparison of the observed steady state winds and "Truth" run forecasts for the Rampart, Community Center and Airfield sensors is shown in Figure 11. In addition, the forecast metric (*J*) used in the ensemble perturbation experiments is shown for comparison to the evolution of severe DSWS. The design and set-up of the WRF "Truth" run forecasts, and development and calculation of the forecast metric (*J*) are discussed in Chapter III.

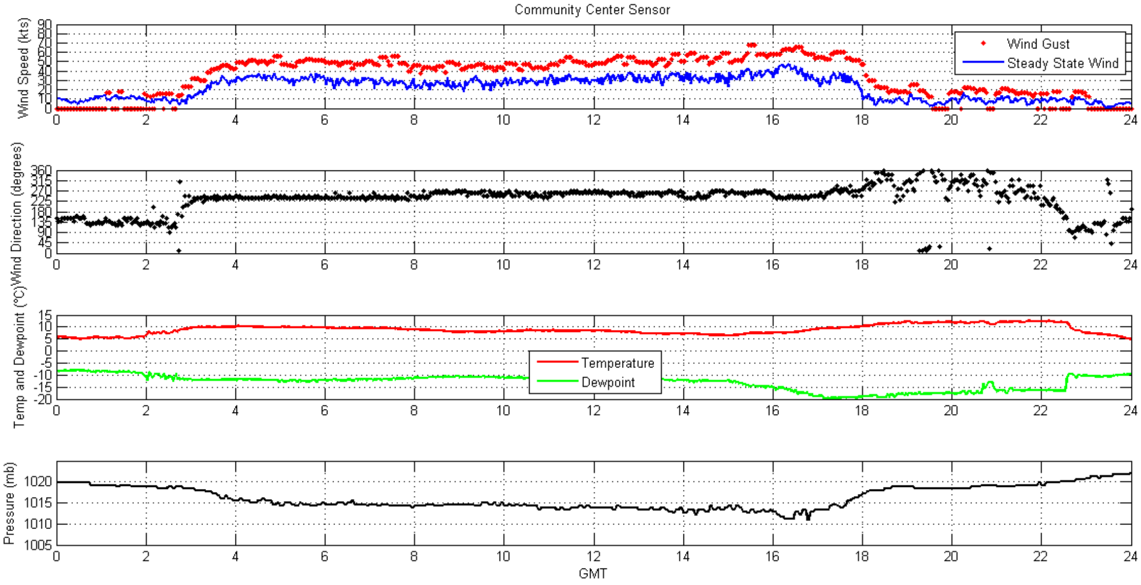

Figure 8. Time series winds, wind direction, temperature, dewpoint, and MSLP at the Community Center sensor during a severe DSWS on 30 December 2008.

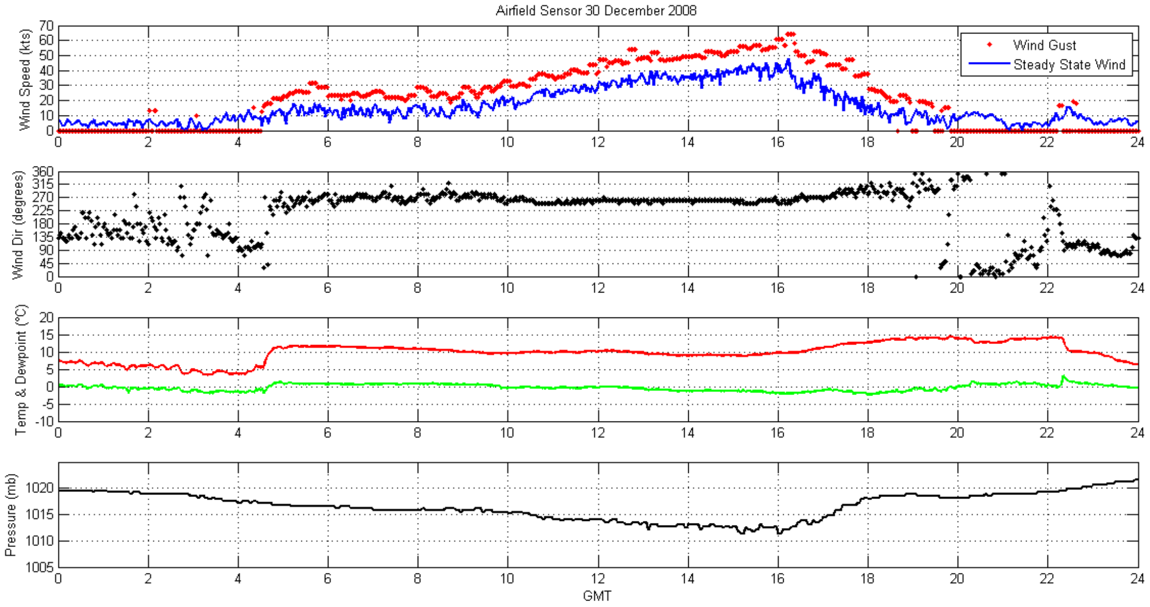

Figure 9. Time series winds, wind direction, temperature, dewpoint, and MSLP at the Airfield sensor during a severe DSWS on 30 December 2008.

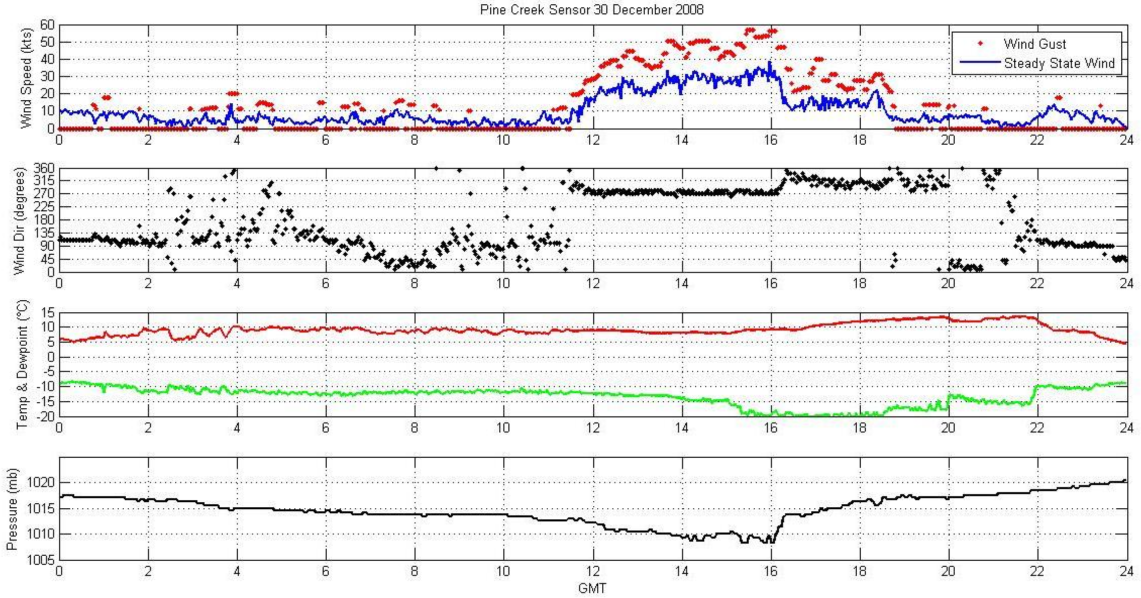

Figure 10. Time series winds, wind direction, temperature, dewpoint, and MSLP at the Pine Creek sensor during a severe DSWS on 30 December 2008.

A strong cold pool was present in the lower elevations from 02Z to 05Z as shown by the 6°C colder temperatures present at the Airfield when compared to the Community Center (Figure 12). As winds increased from the west, adiabatic warming was observed first at the Community Center sensor from 02Z to 04Z while temperatures decreased at the Airfield due to radiational cooling during the nighttime hours. At 04Z the temperature inversion was mixed out as evident from the rapid warming of 8°C in less than one hour at the Airfield corresponding with a winds shifting from light and variable before 04Z to westerly and increased after 04Z (Figure 9). Winds slowly increased at the Airfield, but do not begin to prominently increase until after 10Z with severe winds occurring intermittently between 13Z and 18Z as shown in Figure 9. Severe winds steadily work to the east as winds increase rapidly from the west at 1130Z at the Pine Creek Sensor with maximum severe gusts of 57 kt occurring at 16Z (Figure 10). In addition, a 10 mb decrease in MSLP is observed during this event at all four sensors with the minimum pressure occurring between 16Z and 17Z corresponding to the period of strongest winds at all four sensors (Figures 7,8,9, and 10).

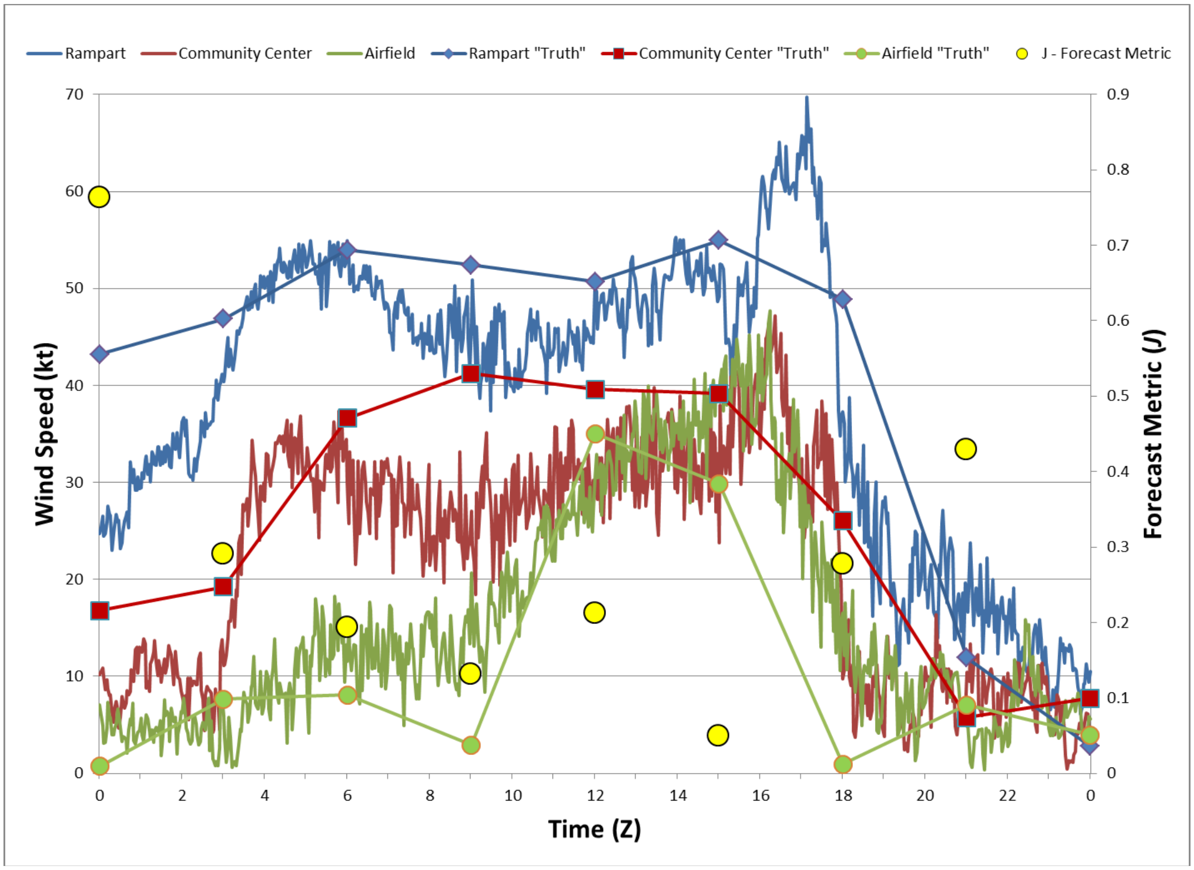

Figure 11. Time series of steady state wind (kt) at the Rampart, Community Center and Airfield sensors during a severe DSWS on 30 December 2008 overlaid with “Truth” run forecasts from WRF simulation. Forecast metric (*J*) from “Truth” run shown with yellow circles and corresponds to scale on right axis.

2. Synoptic Conditions of 30 December 2008 Downslope Windstorm

Synoptically this event is characterized by moderate westerly flow aloft with the Grand Junction sounding showing upstream winds generally between 50 – 80 kt above 500 mb, and between 20 – 30 kt between 700 and 500 mb (Figure 13). This sounding shows a relatively high tropopause and jet for this time of the year at around 200 mb. The polar- front jet axis lies to the north and dips south (Figure 14b) as part of an upper-level trough over Idaho and northern Utah evident in the 200 mb geopotential height field (Figure 14a) that extends down to 500 mb (not depicted). A jet maximum of 110 kt lies along the Utah/Idaho border at 200 mb. The upper-level trough supports a surface low in southern Montana at 00Z, which moves rapidly over the Dakota’s by 12Z. This low-pressure system, combined with a strong high pressure center over the four-corners region, produces a strong cross-mountain surface pressure gradient over Colorado during this period (Figure 14c and 14d). In addition, a deep inversion (most likely due to subsidence) is observed in the Grand Junction sounding from the surface up to 650 mb (Figure 13).

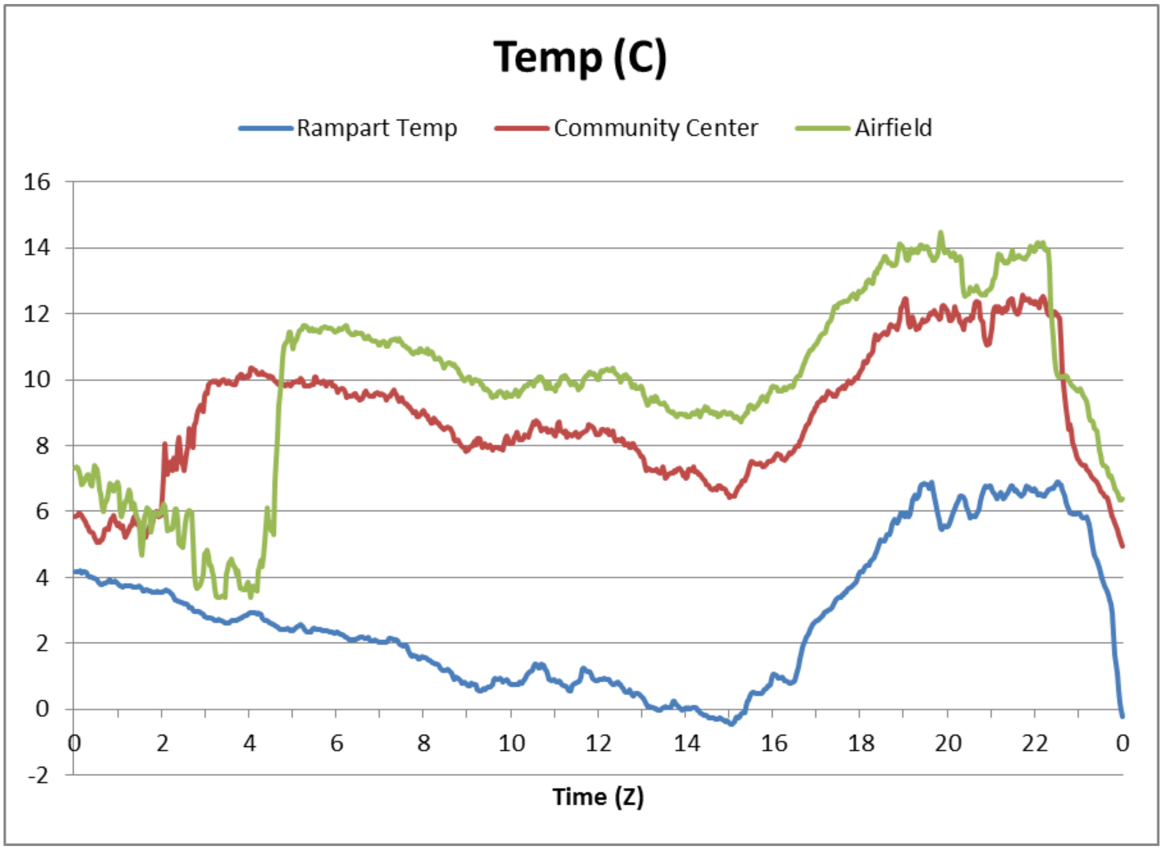

Figure 12. Time series of temperature (°C) at the Rampart, Community Center and Airfield sensors during a severe DSWS on 30 December 2008.

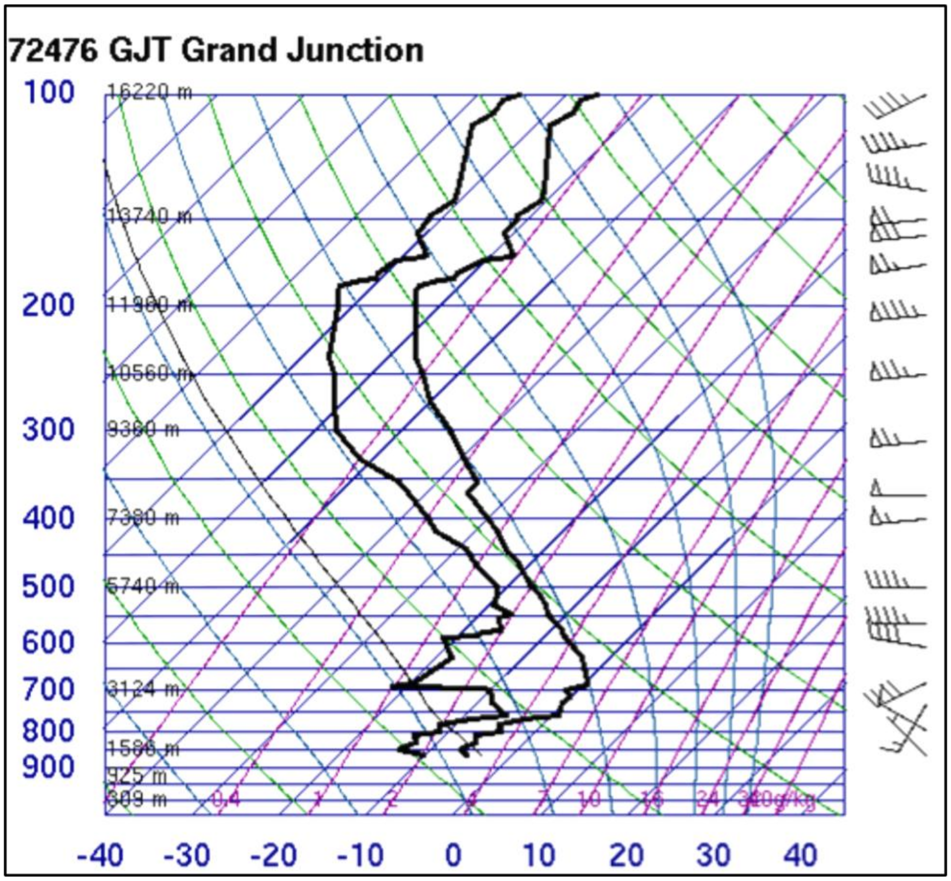

Figure 13. Upstream sounding from Grand Junction, CO during a severe DSWS on 00Z 30 December 2008.

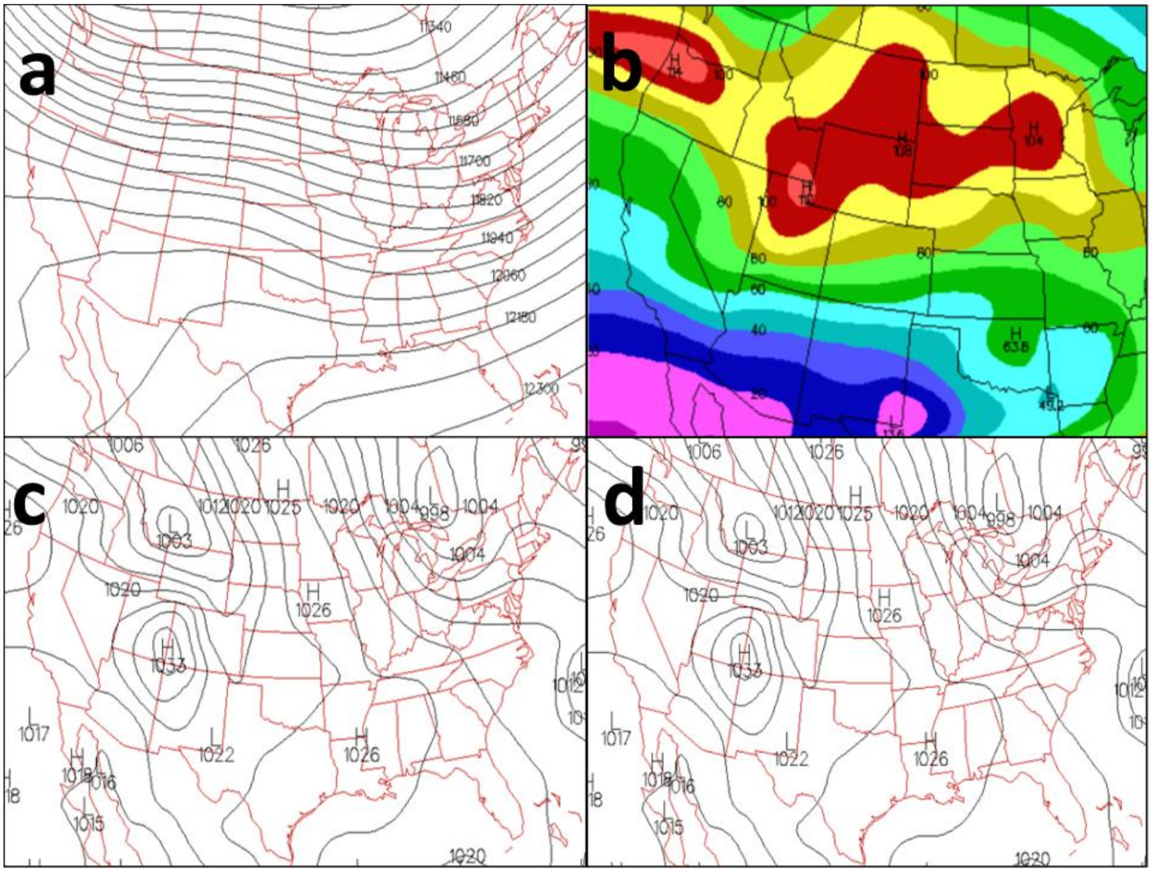

Figure 14. a) 200 mb geopotential height (00Z), b) 200 mb windspeed (00Z), c) sea level pressure (00Z), d) sea level pressure (12Z) on 30 December 2008.

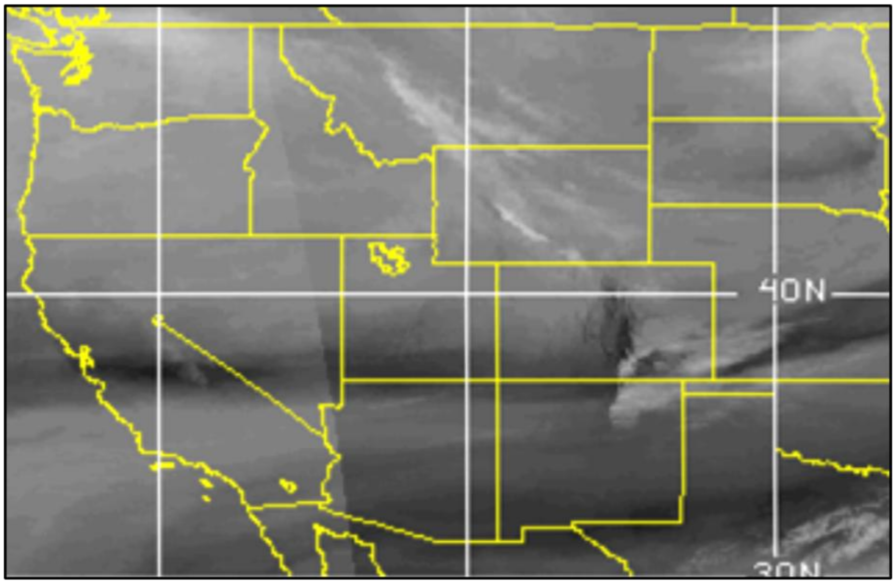

Figure 15. Water vapor satellite image from 1645Z on 30 December 2008.

3. Modeling Study of the 30 December 2008 Downslope Windstorm

Multiple model runs are performed for the 30 December 2008 DSWS, and add insight and detail to the three-dimensional structure and HWAS observations. Two different types of model runs are used for this case: a WRF ensemble run with 96 members and multiple runs of a WRF deterministic model. All models are run with the Advanced Research version 3.3.1 of the WRF (ARW; Skamarock et al. 2008). Over 100 deterministic runs are performed in this study, with the primary goal of ascertaining which configuration of physics packages, number of vertical levels, time step needed, and initialization time needed to most accurately simulate this DSWS. Simple verification metrics for these runs included the root mean square error with the HWAS observations at the Rampart, Community Center, and Airfield sensors. The information obtained from these runs is primarily used to determine a skillful configuration for the WRF ensemble runs, but also reveals information about the three-dimensional structure and dynamics of this DSWS.

Examination of the model runs shows that a trapped wave in the lee of the highest terrain of the Colorado continental divide is most likely responsible for the strong downslope winds observed at USAFA on 30 December 2008. A detailed examination of the characteristics of trapped wave events of this type is given in Chapter V. The highly variable and complex terrain that separates the Front Range (Rampart Range) and the continental divide 135 km to the west plays a significant role in the flow in this region. The downslope flow separates from the surface over the adjacent valley, showing a large-amplitude rotor and easterly flow reversal back into a convergence zone between the downslope winds, rotor, and easterly flow under the rotor. This is clearly depicted by Figures 18 and 19.

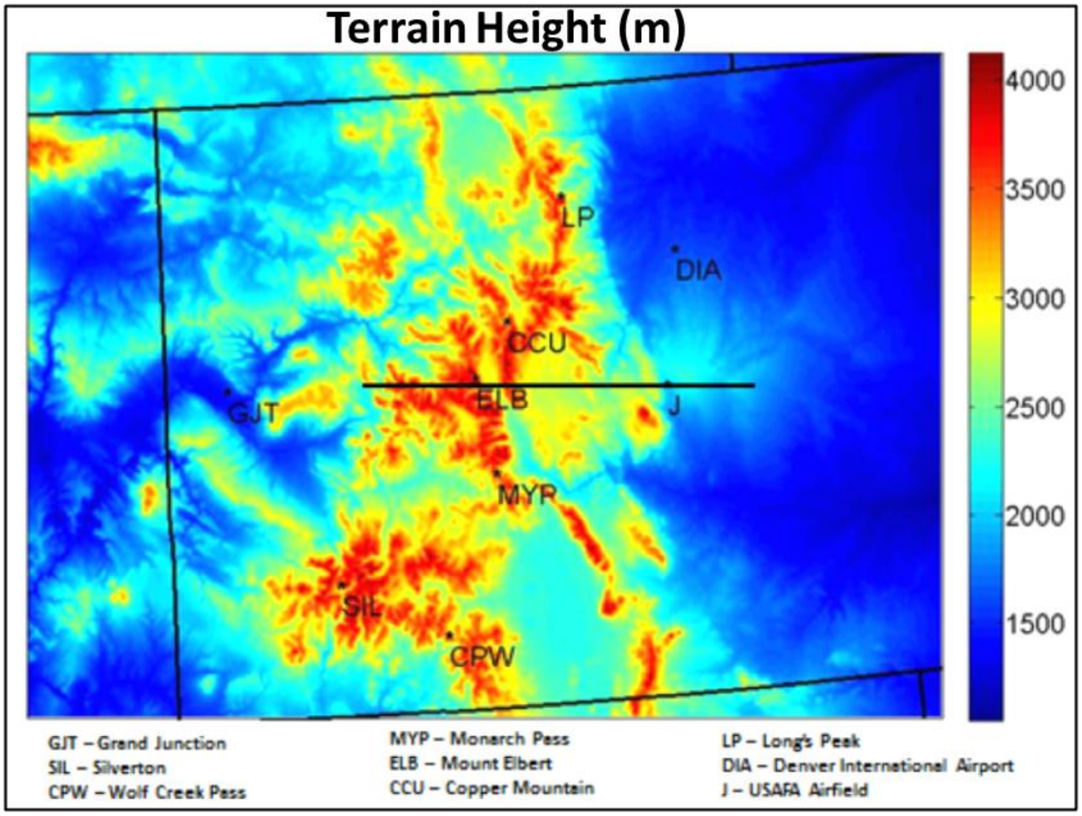

Figure 16. Model terrain height in meters for innermost domain. Solid black line indicates location of cross section shown in Figure 17.

Initially at 00Z on 30 December 2008, the WRF ensemble mean contains moderate westerly flow that interacts with the high terrain of the continental divide, but the width and orientation of the terrain in the Elk and Sawatch Mountains do not initiate a strong wave response. The Mosquito Range initiates a large trapped wave that propagates east and is strongest at heights ranging from 4 to 6 km above MSL in height across the high mountain valley of South Park, and toward the Rampart Range. This is shown by the higher wind speeds and tight theta gradient in this area shown in Figure 17. The mean wavelength is closely linked with the dominant wavelength of complex terrain beneath and culminates with a downward branch along the Front Range adjacent to USAFA. Instead of the terrain and low-level inversions reflecting the wave back upward as is the case to the west of the Rampart Range, the wave dives downward and accelerates in the lee bringing strong winds to the HWAS sensors and USAFA.

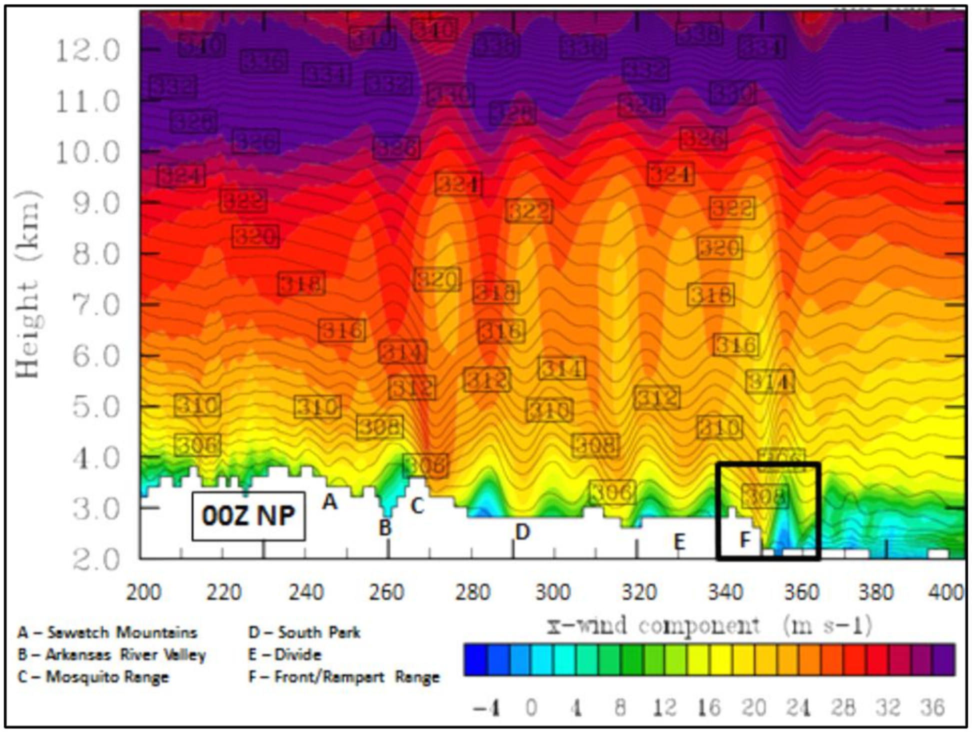

Figure 17. Cross section of *x*-wind component (shaded) and potential temperature (contoured) from west to east across Colorado at the gridline of the HWAS Rampart sensor for the 30 December 2008 00Z ensemble mean unperturbed analysis. The horizontal axis is scaled to the number of grid points from the innermost domain with a resolution of 1.33 km. The HWAS sensors and USAFA are along the lee of the Rampart Range just to the east of point F. The black box indicates the area shown in the cross section in Figure 18.

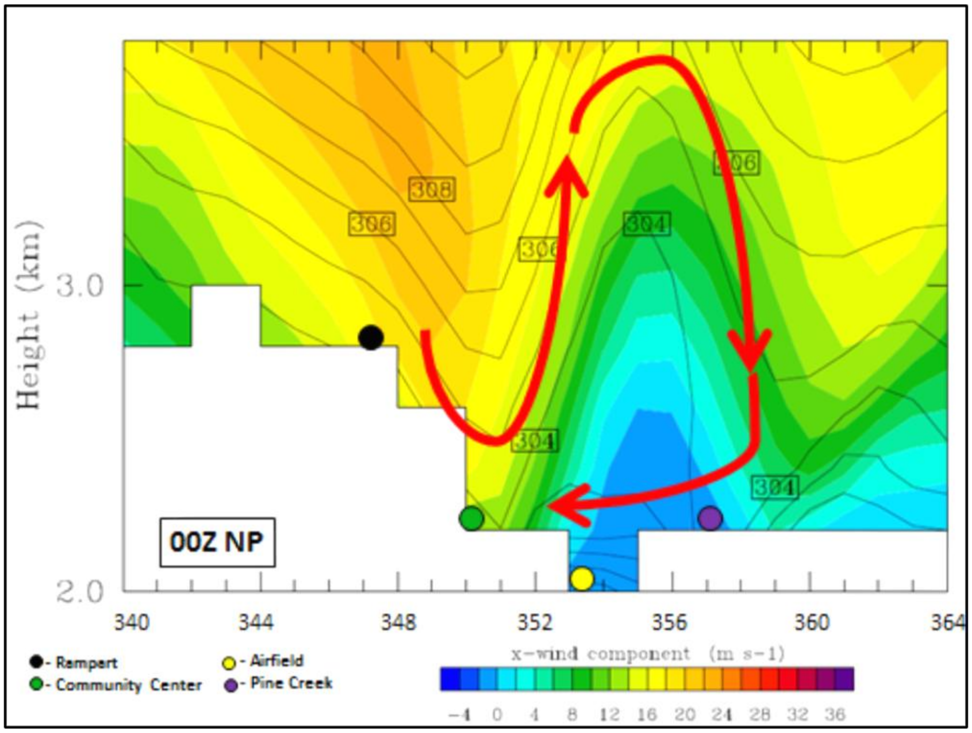

Figure 18. Cross section of *x*-wind component (shaded) and potential temperature (contoured) from west to east across the Rampart Range and adjacent plains at the gridline of the HWAS Rampart sensor for the 30 December 2008 00Z ensemble mean unperturbed analysis. The horizontal axis is scaled to the number of grid points from the innermost domain with a resolution of 1.33 km. Approximate locations of four HWAS sensors are marked by circles. The red arrow indicates the horizontal circulation or rotor suggested by the cross section.

The strong downward motion along the Rampart Range causes adiabatic warming and pressure falls in the lee. The localized pressure minimum causes a reverse pressure gradient to the east of the Rampart Range, and easterlies that flow toward the pressure minimum are initiated. The combination of the upward motion due to the trapped wave, and the convergence of the westerlies with the easterlies, creates a strong upward branch of the wave and boundary layer flow separation between the Community Center and Airfield at 00Z (Figure 18). The flow separation is shown by the potential temperature contours that follow the surface or terrain upstream of the Community Center that separate from the surface and reorient in the atmosphere at a level above the surface. The flow separation is associated with a large rotor that extends several km upward in the

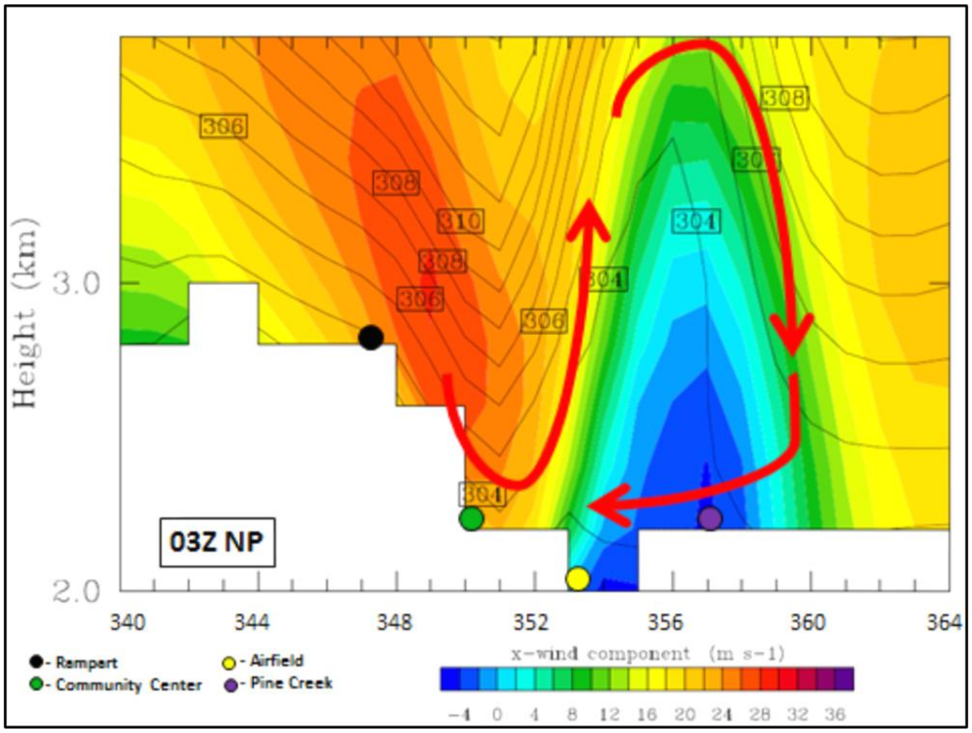

Figure 19. Cross section of *x*-wind component (shaded) and potential temperature (contoured) from west to east across the Rampart Range and adjacent plains at the gridline of the HWAS Rampart sensor for the 30 December 2008 ensemble mean unperturbed three hour forecast valid at 03Z. The horizontal axis is scaled to the number of grid points from the innermost domain with a resolution of 1.33 km. Approximate locations of four HWAS sensors are marked by circles.

atmosphere with easterlies underneath the rotor at the surface and lowest levels. The flow separation reconnects with the surface to the east of Pine Creek where weak westerlies at the surface resume. The 1.33 km resolution of this simulation is not sufficient to capture the detailed structures of the rotor and flow separation and only the gross characteristics of these features are resolved by the simulation in this study.

The strong downslope winds continue to strengthen from 00Z until approximately 12Z and their eastward extent slowly propagates at the surface as shown in Appendix B. The convergence zone where westerlies and easterlies come together, and boundary layer separation occurs, is just west of the Airfield at 03Z (Figure 19). It moves west of the Airfield by 06Z, just to the east of Pine Creek by 09Z, and just west of Pine Creek by 12Z. It can be clearly seen in Figures 18 and 19 that as the strength of the downslope flow increases, the strength of the reversed flow under the rotor also increases similar to results shown in Jiang et al. 2007.

After 12Z, the strongest winds begin to retreat back toward the mountains. The strongest winds occur just east of Pine Creek and over the Airfield at 15Z, and easterlies replacing westerlies at all but the highest terrain are depicted by 18Z. A cold front passes through the area bringing an end to the strong westerly wave activity and reorients the flow from the northeast with cold air building at the lower elevations at 21Z and deepening to the top of the Rampart Range by 00Z on 31 December.

The results from this ensemble modeling simulation suggest that the location of the boundary layer flow separation is critical in determining the westward extent of the severe DSWS. If an observation location is east of the flow separation and west of the reattachment point, generally weak winds are found at the surface underneath the lee wave. Winds reverse under the rotor and are generally light and variable out of the east. This modeling simulation is in good agreement with the HWAS observations taken during this event. Therefore, identifying the factors that determine the distance from the upstream ridge that flow separation occurs is paramount to determining the eastward extent of the severe winds. A process for determining these sensitivities using ESA is presented in Chapter III with results given in Chapter IV.

THIS PAGE INTENTIONALLY LEFT BLANK

III. DATA AND METHODOLOGY

A. OVERVIEW

A 96-member WRF ensemble system is implemented for the 30 December 2008 DSWS recorded by the HWAS sensors. Details and characteristics of this ensemble system are given in section B. Diagnosis of the structure and detail of this event from the ensemble and HWAS observations leads to the development of a forecast metric (*J*) to be used in the ESA calculations. The process used to develop the forecast metric is given in section C. The forecast metric is tested for Gaussian properties as described in section C. The ESA calculation is performed as described in Chapter II. The results of the ESA calculations are used to identify sensitive locations to perturb the model and assimilate observations. Methods for perturbing the ensemble and assimilating observations are outlined in section E and section F. Results from these perturbations and assimilated observations are given in Chapter IV.

B. MODEL DESIGN AND SETUP

The 96-member ensemble system used in this research uses the Advanced Research version 3.3.1 of the WRF (ARW; Skamarock et al. 2008). The WRF ensemble is run on Cray XE6 supercomputers at the U.S. Army Engineer Research and Development Center (ERDC) in Vicksburg, Mississippi. Each domain in the model contains 60 vertical η-levels (mass) with the model top boundary condition at 5 mb. The time step is 60 seconds for the outermost domain. The outermost grid domain (Figure 20) uses 12 km horizontal grid spacing, the middle domain uses 4 km horizontal grid spacing, and the inner domain uses 1.33 km grid spacing and has a grid size of 363 x 501 (north/south x east/west). The ensemble uses the parameterized physics configuration shown in Table 1. Prior to the ensemble experiment, over 100 deterministic runs are analyzed to test and determine the physics suite, number of vertical levels, and time step.

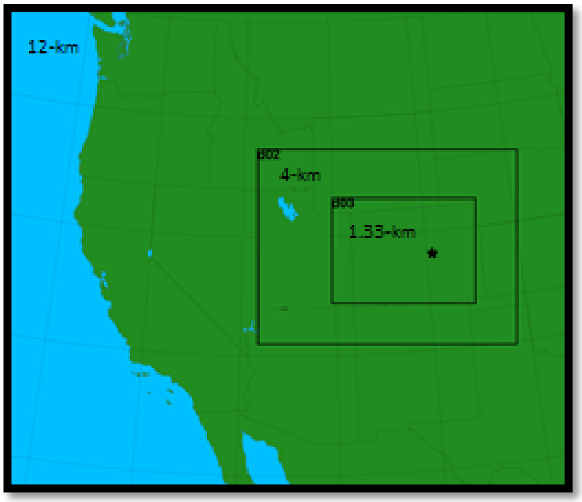

Figure 20. WRF nesting configuration used in this study. The star defines the location of Colorado Springs.

Land Surface	PBL	Microphysics	Cumulus	Longwave	Shortwave
MM5	YSU	WSM5	Kain-Fritsch	RRTM	Dudhia

Table 1. Physics processes used in the WRF system

1. Truth Run

To recreate the conditions that supported this severe downslope wind event, an observing system simulation experiment (OSSE) is conducted. The experiment begins with a single “Truth” WRF 5-day simulation run from 26–31 December 2008. The WRF truth simulation is initialized at 0000 UTC on 26 December 2008 using initial and lateral boundary conditions provided by the Climate Forecast System Reanalysis (CFSR) (Saha et al. 2010). The top pressure level from the CFSR data is ~.2 mb. Forecast winds at three HWAS sensors from this truth simulation for the severe DSWS are shown in Figure 11. Boundary conditions and soil conditions are updated every three hours with CFSR data. Cross sections from this truth simulation depicting the severe DSWS at USAFA are shown in Appendix B.

2. Ensemble System

Conditioning of the WRF ensemble system began at 00Z on 26 December 2008. Synthetic observations are produced by interpolating the truth run to locations of real observations available in the archived National Centers for Environmental Prediction (NCEP) PrepBUFR data-stream. An ensemble is produced by assimilating these synthetic observations with the Data Assimilation Research Testbed (DART). DART, developed and maintained at the National Center for Atmospheric Research (NCAR) is an open-source community resource that provides well-documented software tools for data assimilation education, research and development (Anderson et al. 2009).

Initialization of the ensemble spread is completed by adding spatially consistent, but random, perturbations drawn from the default static WRF-Var error covariance. Assimilations proceed every three hours. By the experiment period beginning 00Z 30 December, the ensemble initial conditions are independent from the random perturbations and instead reflect the assimilated synthetic observations. To ensure that uncertainty continues to enter the domain, perturbations applied to lateral boundary conditions are also drawn from the WRF-Var static covariance, following Torn et al. (2006).

An ensemble simulation is initiated for the forecast period beginning at 00Z on 30 December running for 24 hours through 00Z on 31 December 2008. This simulation is the control forecast for all ESA experiments. It is referred to as the no-perturbation (NP) run as it is the control run without perturbations and is the base state of the system. In other experiments, perturbations are applied to the base state to test the sensitivity and response of the ensemble system. The process for determining where the ensemble analysis is perturbed and details of how perturbations are performed are found in sections D and E. Forecasts for all 96 members are generated every three hours.

C. FORECAST METRIC (*J*)—GAUSSIAN TESTS

As described in Chapter II, the ESA calculation is a linear regression between the forecast metric (J) and the initial conditions (x^a) of an ensemble. The underlying assumptions of linear regression require all variables to be normally distributed, which implies they are symmetric and have a single mode. The spread of a normal distribution is given by its standard deviation (σ). As shown in Eq. (2.2), ESA utilizes the properties of normal distributions, their standard deviations, and correlations. Therefore, when using ESA, finding forecast metrics (*J*) that have normal or Gaussian distributions is a requirement for the linear regression assumptions to not be violated. The following section describes the Gaussian tests for normal distributions that are used to help choose the forecast metric (*J*).

1. Lilliefors Test

A Lilliefors test is a modified Kolmogorov-Smirnov test that determines if sample data can be reasonably fit by a normal distribution. Lilliefors (1967) showed that the standard Kolmogorov-Smirnov test no longer applies when certain parameters such as the mean or variance are not specified and must be estimated from the sample data. A Lilliefors test is a two-sided non-parameter goodness-of-fit test. This is in contrast to the standard parameter Kolmogorov-Smirnov test, which is a one-sample test that requires the null distribution be completely specified. The Lilliefors test statistic is defined as:

$$\mathrm{T} = max_x \left| F\left(x\right) - S(x) \right| \tag{3.1}$$

where $F(x)$ is the hypothesized cumulative normal distribution function with a mean and standard deviation equal to the mean and standard deviation of the sample and $S(x)$ is the sample cumulative distribution function. A table of critical values derived from a Monte Carlo simulation for sample sizes less than 1000 gives criteria for goodness of fit. If the value of T exceeds the critical value from the table for a distribution with sample size N, and a given level of significance (α), then the hypothesis that the sample is from a normal distribution is rejected. In other words, the number of observed values in a specified bin of the hypothesized distribution is far from what would be expected of the data for the hypothesized distribution. Hypothesis rejection corresponds to a p-value less than the specified alpha (α). Alpha is set at .05 for all experiments in this research, unless explicitly stated otherwise. The Lilliefors test here is thus applied as a 1- α = .95 confidence interval test.

2. Choosing a Forecast Metric (*J*)

A Lilliefors test for normality was performed on all potential candidates for the forecast metric *J*. Several forecast metrics were initially evaluated at single locations before being rejected in favor of the more complex Bulk Richardson metric described in the next section. These initial locations are at two HWAS sensor locations; the Rampart and Airfield sensors. These locations were chosen as Rampart is a high mountain location above all cold pools and influences of the valley, flow separation, and rotor below and to the east. The Airfield sensor is located below surface-based inversions before the severe DSWS. It is in the rotor east of the flow-separation point initially, yet still experiences severe criteria winds for multiple hours on 30 December 2008. The exact location of these sensors is shown in Table 2 and Figure 51 in Appendix A.

The first forecast metric tested at the Rampart sensor was three-dimensional wind speed (*u*, *v*, and *w* components). As shown in Figure 7, the wind direction changes very little at the Rampart sensor during this event, allowing a simple wind speed calculation to adequately capture the onset, duration, and intensity of this severe DSWS at the Rampart sensor.

The winds and temperatures at the Airfield are far more varied than at Rampart prior to the DSWS, thus making the selection of *J* much more complicated at this location. The presence of a cold pool, inversion, rotor, and flow separation allowed easterly winds to persist until the inversion broke just after 04Z, when westerly winds began to increase. Therefore, the *u* wind component is selected as the forecast metric at the airfield to account for this transition from weak easterlies to strong westerlies.

The three-dimensional grid region over which the forecast metric *J* is defined is referred to as the "*J* box." A *J* box is specified over each sensor by the number of grid points east to west, north to south, and vertically to calculate *J* on the finest model domain. The function used to calculate the forecast metric is the average of wind speed (Rampart) or *u* wind component (Airfield) at all points specified in a particular *J* box. Various *J* box sizes are tested at both Rampart and the Airfield locations, and a Lilliefors test for Gaussianity is performed at each *J* box configuration. *J* box configurations are tested for each forecast hour (three hour increments) for the 00Z 30 December NP ensemble run at both the Rampart and Airfield locations.

While these forecast metrics are viable candidates for sensitivity testing due to their high standard deviations and strong Gaussianity, they lack information about the complexity of the flow characteristics that may determine the onset of high winds. Thus, we opt to seek a forecast metric based on a more complete description of the relevant physics and dynamic relationships in the proximity of the strong downslope winds. These additional characteristics include wind shear and thermal stability.

a. Forecast Metric—Modified Bulk Richardson Number

A forecast metric is developed with the goal of capturing the relevant physics and structure of the downslope winds along the lee slope, rotor with reversed surface flow to the east, and flow separation with a convergence zone between these features. A modified Bulk Richardson number is used as the metric to sample these relationships.

The Bulk Richardson number is a dimensionless quantity that uses finite differences between levels to calculate the ratio of the vertical stability to the vertical shear of the flow. It is given by the equation:

$$R_B = \frac{g(\Delta\overline{\theta_v})(\Delta z)}{\overline{\theta_v}[(\Delta\overline{U})^2 + (\Delta\overline{V})^2]}, \qquad (3.2)$$

where g is the gravitational acceleration, $\Delta\overline{\theta_v}$ is the virtual potential temperature difference across a layer of thickness Δz, $\overline{\theta}_v$ is the mean virtual temperature across the layer, and $\Delta\overline{U}$ and $\Delta\overline{V}$ are the changes in horizontal wind components across the same layer (Stull 1988).

The geometry of the DSWS, and in particular the angle of flow separation from horizontal, leads to a modified form of the Bulk Richardson number. It samples near-surface buoyancy and wind shear across the flow separation, convergence zone, and strong potential temperature gradient that existed at 03Z on 30 December 2008 between the Rampart and Airfield locations. This forecast metric for the ensemble mean NP (unperturbed) run is depicted in Figure 21 and given by

$$J = R_B = \frac{g(\theta_2 - \theta_1)\Delta z}{\bar{\theta}(U_2 - U_1)^2}, \tag{3.3}$$

where θ is the 2-m potential temperature, $\bar{\theta}$ is the 2-m mean layer potential temperature, U is the 10 m *x*-wind component, and Δz is the distance between the upper and lower modeled terrain height. Points 1 and 2 are determined by the ensemble mean, with point 2 being the location with the highest local positive *U* wind at 10 meters and point 1 being the location with the highest local negative *U* wind at 10 meters. At 03Z, points 1 and 2 roughly correspond to the locations of the HWAS Rampart sensor and a location east of the Airfield sensor, but west of the Pine Creek sensor. A histogram of the ensemble members for the forecast metric *J* valid at 03Z for the ensemble mean NP (unperturbed) run is given in Figure 22. A Lilliefors test is performed on *J* at this valid time and confirms that the metric is normally distributed.

This modified Bulk Richardson number relates well to the strength of a severe DSWS. This is revealed in Figure 11, which shows a time series of the steady state winds at the Rampart, Community Center, and Airfield HWAS sensors during the severe DSWS, the corresponding forecast from the truth run at these sensors, and the forecast metric (*J*) as calculated from the truth run. This plot reveals an inverse relationship between the strength of the wind event and the value of the Bulk Richardson number. The Bulk Richardson number steadily decreases in magnitude as winds increase and move from the higher terrain down the slope and to the adjacent plains. The smallest Bulk Richardson value (.0492) is calculated at 15Z, which corresponds to the strongest winds moving down the lee slope and out over the plains. The Bulk Richardson value quickly increases as the wind event begins to subside at 18Z and beyond.

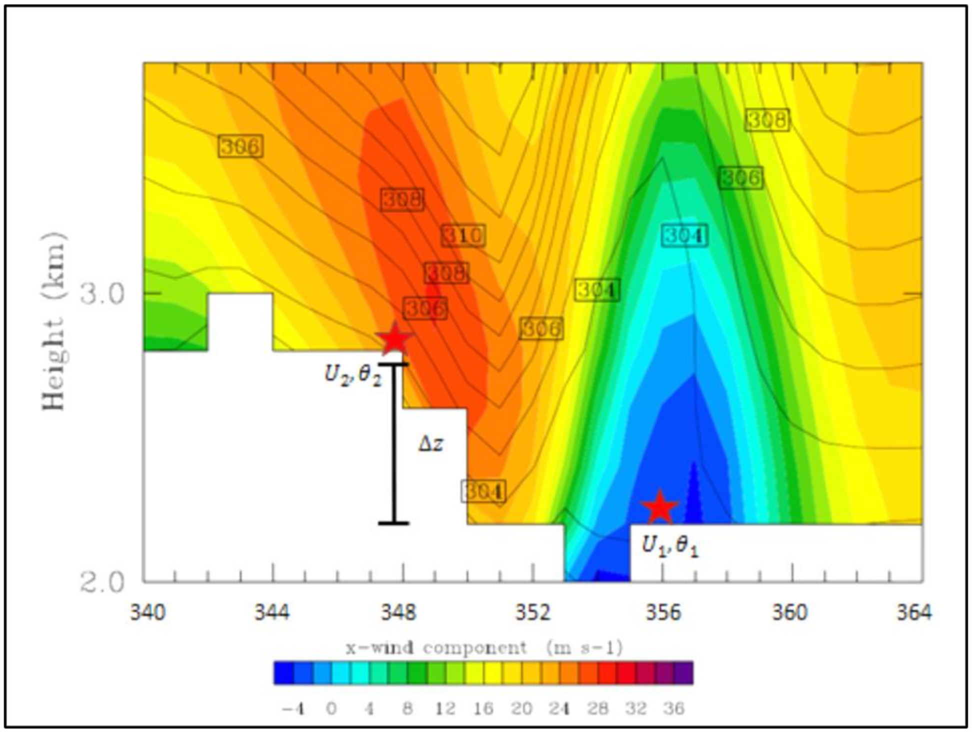

Figure 21. Cross section of *x*-wind component (shaded) and potential temperature (contoured) from west to east across the Rampart Range and adjacent plains at the gridline of the HWAS Rampart sensor for the 30 December 2008 ensemble mean NP run (unperturbed) three hour forecast valid at 03Z. The horizontal axis is scaled to the number of grid points from the innermost domain with a resolution of 1.33 km. Stars denote location of points where forecast metric *J* is calculated using a modified Bulk Richardson number.

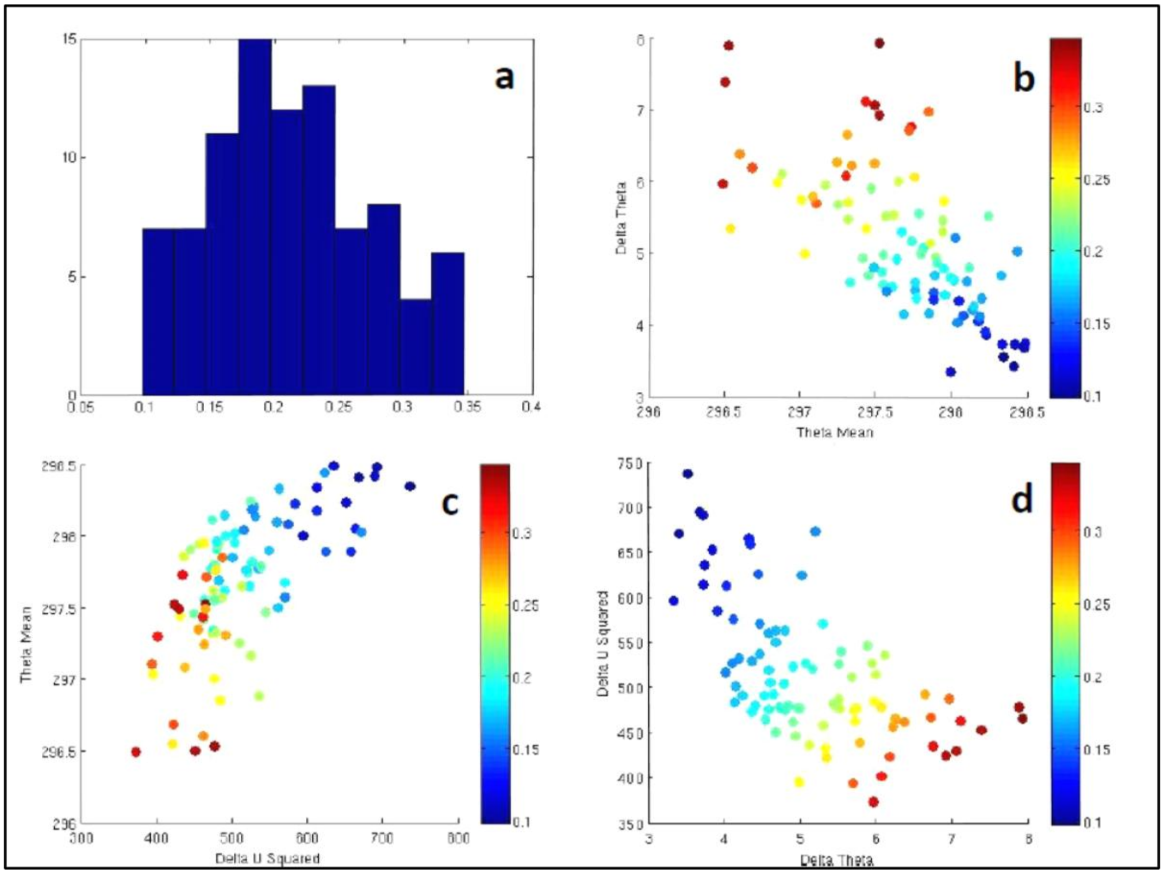

Figure 22. a) Histogram of the forecast metric (J) for 96-member NP (unperturbed) WRF ensemble at 03Z 30 December 2008, b) scatterplot of $\overline{\theta}$ vs. $(\theta_2 - \theta_1)$, c) scatterplot of $(U_2 - U_1)^2$ vs. $\overline{\theta}$, d) $(\theta_2 - \theta_1)$ vs. $(U_2 - U_1)^2$. The magnitude of the forecast metric (J) is shaded in the scatterplots. All plots are valid at 03Z 30 December 2008.

The scatterplots in Figure 22 show that the forecast metric (J) can be interpreted in the traditional Bulk Richardson manner. The highest values of J are associated with a strong horizontal potential temperature gradient and weaker wind shear across the flow separation and convergence zone. The result is that stability dominates over wind shear and the likelihood of turbulence is minimized. Conversely, low values of J are associated with strong wind shear and weak stability; shear dominates over stability and the likelihood of turbulence is maximized.

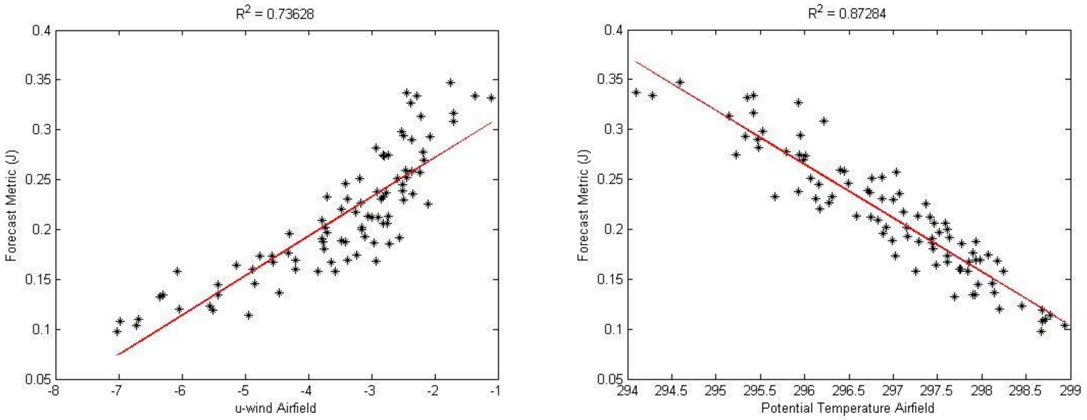

Figure 23. Scatterplots of 10-m *x*-wind component from the 03Z forecast of the WRF ensemble and the forecast metric (left) and 2-m potential temperature (right).

In the context of the downslope winds, flow separation, and rotor with return flow in the lower-levels, low values of *J* represent flow situations where stronger easterlies and higher potential temperatures are observed at the Airfield. Conversely, high values of *J* correspond to weak easterlies at the Airfield and lower potential temperature. This is revealed in two ways. First, it is deduced from the relationships shown by the scatterplots in Figure 22, and secondly, from the fact that the standard deviation for both potential temperature and the *x*-wind component is larger at the Airfield than at Rampart. Thus, the majority of the variation of *J* is explained by variations at the Airfield. This relationship is also seen in the scatterplots of *J* vs. U_2 and *J* vs. θ_2 shown in Figure 23, and is further confirmed by the large coefficient of determination between these parameters (0.73628 and 0.87284, respectively).

In summary, the modified Bulk Richardson number that is developed as a forecast metric to sample the relevant physics and dynamic relationships between the strength of the winds down the slope, the reverse flow under the induced rotor, and flow separation is determined to be Gaussian and behaves in a manner that allows for physically consistent interpretation.

D. ENSEMBLE SENSITIVITY ANALYSIS USING MODIFIED BULK RICHARDSON AS FORECAST METRIC (*J*)

The forecast metric as described and calculated in the previous section is now utilized to perform the ESA calculation and test for sensitivities in the ensemble initial conditions.

1. Addressing Statistical Sampling Error

a. Statistical Significance—Confidence Test

Given that the ESA calculation draws from a finite ensemble, sampling error is naturally introduced. In order to test for statistical significance of the forecast metric (*J*), a *t* test is performed at a 95% confidence interval. The null hypothesis is that changes to input variable x^a do not change the forecast metric *J*. We reject this hypothesis if the absolute value of the correlation coefficient between x^a and *J* exceeds the 95% confidence bounds approximated for the sample formed by the 96-member ensemble (Torn and Hakim 2008).

Probability values (p-values), $\mathrm{p}[J, x^a]$ associated with each correlation coefficient, $R[J, x^a]$ are computed and used in the confidence test. The p-value is the probability of getting a correlation as large as the observed value by random chance when the true correlation is zero (Wilks 2006). P-values are computed by transforming the correlation to create a t-statistic having n-2 degrees of freedom. These values are then used for testing the null hypothesis of no significant correlation. When using a 95% confidence interval and if $\mathrm{p}[J, x^a]$ is small (less than 0.05), then we consider the $R[J, x^a]$ to be significant and we can reject the null hypothesis (Wilks 2006). Locations with correlation coefficients that fail the statistical significance test are rejected and data provided from these points is withheld from the sensitivity fields.

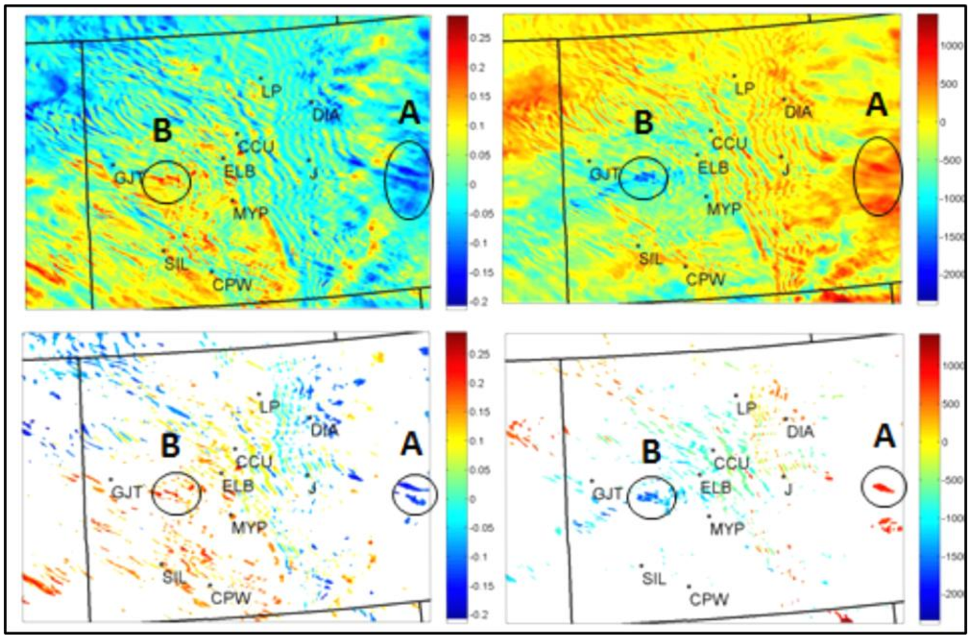

Figure 24. ESA results for modified Bulk Richardson forecast metric (*J*) at model level 13 for 03Z 30 December 2008. Results for x^a = Potential Temperature are on the left and x^a = Specific Humidity are on the right. The full sensitivity field is shown on the upper plots and the filtered sensitivity by a confidence test at a 95% confidence interval is shown in the lower plots. Perturbation and observation assimilation points are identified within regions A and B. Locations given for reference are identified in Figure 16.

2. ESA Calculation

The ESA calculation as given in eq. 2.3 is performed for the WRF state variables *u*, *v*, *w*, *T*, *QVAPOR*, and *PSFC* for each level and every grid point in the 1.33 km inner domain for three hour forecast valid at 03Z 30 December 2008. Viable candidates for ensemble perturbation or observation assimilation are sought from the ESA results. The sensitivity fields are analyzed level by level and grid points are rank ordered from the highest sensitivity values to the lowest. The confidence test defined in the previous section is performed for each sensitivity calculation. Locations with correlation coefficients that fail the statistical significance test and locations that fail a Lilliefors Gaussianity test are withheld from the sensitivity fields. Locations where sensitivity patterns are found in multiple variables are given stronger consideration as potential candidates for further testing. In addition, coherent structures in both the horizontal and vertical are sought in the sensitivity fields, as sensitivities that are linked to detectible atmospheric features are desired, not spurious noise due to a high statistical correlation. In addition, a strong sensitivity upstream and one downstream of USAFA is sought to test the response of the forecast to perturbations and observations assimilated both upstream and downstream of the severe DSWS.

Two regions of high sensitivity are selected from the criteria previously described, and are shown in Figure 24. These areas of sensitivity are found in several levels in the model but are largest at model level 13 in both the potential temperature and specific humidity ESA fields. Level 13 is approximately 2200 m AGL at both locations with the downstream point at 3600 m MSL and the upstream point at 4150 m MSL. The largest point of sensitivity in the potential temperature in both areas is used as a location for introducing perturbations and assimilating observations. The sensitivity point downstream of USAFA in region A is at location z = 13, x = 468, and y = 172 at a longitude of 38.772 N and longitude of -103.09 W. This point is referred to as point 1 for the remainder of this study. The sensitivity point upstream of USAFA in region B is at location z = 13, x = 182, and y = 162 in the inner most nested domain at a longitude of 38.931 N and longitude of -107.49 W. This point is referred to as point 2 for the remainder of this study. A summary of the location information and sensitivities calculated for points 1 and 2 is given in Table 2.

	z	y	x	lat	lon	dJ/dx
Point 1	13	172	468	38.772	-103.09	-0.20031
Point 2	13	162	182	38.931	-107.49	0.28948

Table 2. Model grid point location, latitude, longitude and sensitivity (*dJ/dx*) for point 1 and point 2. The units for *dJ/dx* are per Kelvin.

E. PERTURBATION TESTS

Perturbation tests are conducted at each sensitivity location to examine whether ESA is skillful at identifying sensitivity locations. Perturbations are introduced in two ways. The first method introduces perturbations at our defined sensitivity points and spreads the perturbation using a linear regression of the ensemble analysis as sampled by the NP ensemble run. The second method utilizes an Ensemble Kalman Filter (EnKF) and assimilates observations using full data assimilation methods. Both methods are implemented in order to compare the effectiveness of one versus the other. The perturbation method is less computationally expensive as it only performs single variable linear regression, and it does not reduce the spread of the analysis, but shifts the distribution in the direction of the perturbation. In contrast, the full data assimilation method is more similar to a full multivariate regression and allows not only a shift of an analysis distribution, but also a reduction in the spread of the ensemble at the points of observation assimilation in the analysis. These distinct differences motivate our decision to test both methods.

1. Perturbation Method

Separate ensemble WRF runs are generated with perturbations introduced first at sensitivity point 1 and then at point 2 in a second ensemble run. These ensemble runs are referred to as P1 (perturbation at eastern/downstream sensitivity point) and P2 (perturbation at western/upstream sensitivity point) for the remainder of this experiment. The perturbation is introduced by increasing the ensemble mean potential temperature value for x^a by a value taken from the WRF truth run at that location. The effect of this perturbation at a single point is spread through to other model variables in the horizontal and vertical through linear regression between the analysis variable at the perturbation point and the analysis variables from the original NP ensemble run. The intent of the linear regression is to reduce model shock in the subsequent analysis. Following Reinecke (2008) and Torn and Hakim (2009) the ensemble mean perturbation to each ith analysis state variable can be written as:

$$x_i^p = x_i^a + \frac{\operatorname{cov}(x_i^a, x_s^a)}{\operatorname{var}(x_s^a)}\alpha \tag{3.4}$$

where x_i^p is the ensemble mean perturbation, x_i^a is the analysis variable from the original unperturbed ensemble, x_s^a is the analysis variable from the perturbation point, and α is the scalar perturbation made at the individual grid point for all i-state variables given by

$$\alpha = x_i^s - \overline{x_s^a} \tag{3.5}$$

where x_i^s is the perturbation variable at the perturbation point from the truth run, and $\overline{x_s^a}$ is the perturbation variable at the perturbation point from the ensemble mean unperturbed analysis (NP run).

This perturbation method ensures the ensemble variability is left unchanged while the mean is shifted. This perturbation is applied to all three domains and then run forward to show a forecast change due to the perturbation. The results of these perturbations are shown in the next chapter.

F. DATA ASSIMILATION METHODS

1. Covariance Localization

Due to sampling error inherent in the ensemble system, it is essential to devise a method to limit the horizontal and vertical magnitude of the covariance between x^a and J. Typically a spatial function ρ weights the data assimilation regression to express confidence in the regression. This spatial function, ρ is typically a compactly supported function similar in shape to a Gaussian, 1.0 at the observation location (Gaspari and Cohn 1999). Decreasing covariance according to ρ is called covariance localization, and helps prevent the creation of spurious covariances at long distances arising from sampling error. While this process can introduce some imbalances to the state (Houtekamer and Mitchell 2001), it is a "practical necessity for EnKF NWP applications" (Hamill 2013).

2. Observation Assimilation

An observation using the temperature from the truth simulation is assimilated using a two part process outlined by Anderson (2003). An update increment is computed for each prior ensemble estimate of the observation variable by applying a scalar ensemble filter. Second, a linear regression of the prior ensemble sample of each state variable on the observation variable is performed to compute update increments for each state variable ensemble member from corresponding observation variable increments.

Equation 2.5 defines how matrix data assimilation can be performed with a single observation. The Kalman gain matrix from eq. 2.5 is now defined as

$$\mathbf{K} = \rho * \mathbf{P}_i^{\mathbf{a}} \ \mathbf{H}^{\mathbf{T}} (\mathbf{H} \rho * \mathbf{P}_i^{\mathbf{a}} \mathbf{H}^{\mathbf{T}} + \mathbf{R})^{-1} \tag{3.6}$$

where ρ represents the covariance localization matrix, $\mathbf{P}_i^{\mathbf{a}}$ the background error variance matrix, $*$ the Hadamard or Schür product between the two arguments, $\mathbf{H}$ the linearized forward operator, and $\mathbf{R}$ the observation error covariance matrix. Equation 2.5 can be written in scalar form for a single scalar additional observation as

$$x_{i+1}^a = x_i^a + \rho_{xy} \left[\frac{\sigma_{xy}^2}{\sigma_{yy}^2} \cdot \frac{\sigma_{yy}^2}{\sigma_{yy}^2 + \sigma_o^2} \right] (y_{i+1}^o - y_i^a) \tag{3.7}$$

with ρ_{xy} representing the localization covariance function between the arguments, σ_{xy}^2 the covariance between the arguments, σ_{yy}^2 the variance between the arguments, σ_o^2 the observation variance, y_{i+1}^o the observation value, and y_i^a the value from the background at the observation location. Anderson (2003) showed that introducing an observation to the analysis in this scalar form is permissible and equivalent to the matrix form because our DART analysis is performed in serial. Assimilating a single observation in this manner yields the same result as if it were included in the observation set at analysis time in the original assimilation. This data assimilation procedure allows for the contribution of one single observation to an analysis and thus a forecast to be measured.

Three separate WRF ensemble runs are performed by 1) assimilating temperature from the WRF truth as an observation only at point 1, 2) assimilating temperature from the WRF truth as an observation only at point 2, and 3) assimilating temperature from the WRF truth at both points 1 and 2 simultaneously. These three ensemble runs are referred to as DA1, DA2, and DAJ, respectively, for the remainder of this study. The results of these runs are presented in the next chapter.

IV. ESA RESULTS

A. OVERVIEW

ESA is performed using the methodology described in Chapter III. Two sensitivity regions are identified (Figure 24), with sensitivity point 1 coming from region A and sensitivity point 2 coming from region B. Five separate ensemble runs are generated (P1, P2, DA1, DA2, DAJ) as described in the previous chapter. The sizes of the perturbations for P1 and P2 are given as δx in Table 3 and the values of the temperature observations from the truth run assimilated for DA1, DA2, and DAJ are given in Table 4.

	Theta Mean NP	Theta Truth	δ
Point 1	307.5800	307.7629	0.1829
Point 2	305.9969	306.1230	0.1261

Table 3. Potential temperature (K) at points 1 and 2 from the ensemble mean of the NP run and from the truth run valid at 00Z 30 December 2008. The difference between the truth run and NP mean is shown in the far right column as δx.

	Temperature Mean NP	Temperature Truth Run	δ (Theta)
Point 1	273.4546	273.6215	0.6118
Point 2	266.3875	266.4537	0.1894

Table 4. Temperature (K) at points 1 and 2 from the ensemble mean of the NP run and from the truth run valid at 00Z 30 December 2008. The corresponding perturbation in potential temperature after assimilation between the truth run and NP mean is shown in the far right column as δx.

	$<J>$	σ_J	**Expected δJ**	**Actual δJ**	**Percent**
NP	0.2130	0.0620	-	-	-
P1	0.1953	0.0639	-0.0366	-0.0177	48.28%
P2	0.2180	0.0586	0.0365	0.0050	13.73%
DA1	0.1928	0.0819	-0.1225	-0.0202	16.47%
DA2	0.2256	0.0609	0.0548	0.0126	23.00%
DAJ	0.1956	0.0766	-0.0687	-0.0174	25.31%

Table 5. The mean, standard deviation, expected change, actual change and percent of predicted change of the forecast metric *J* for each of the WRF ensemble runs. All values are valid at the forecast time of 03Z 30 December 2008.

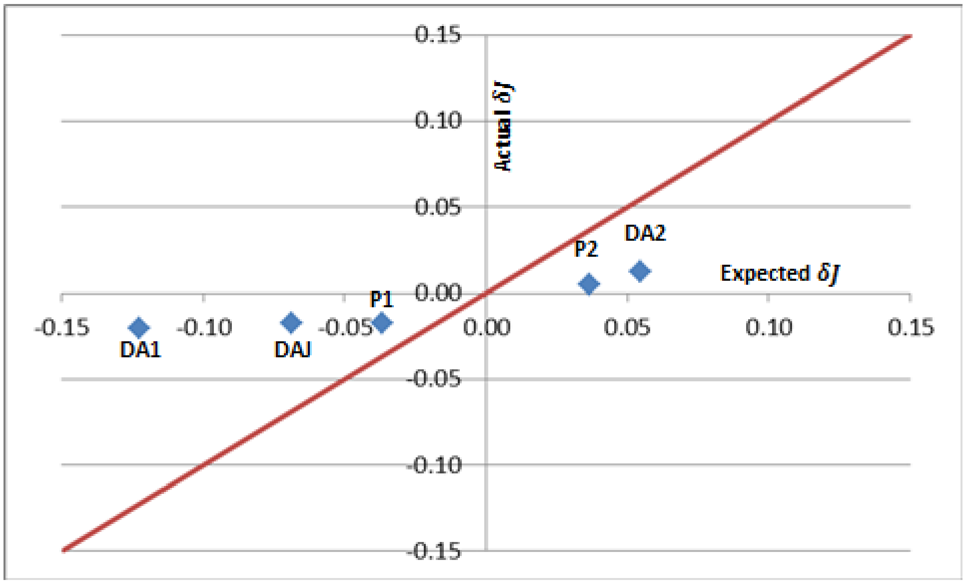

Figure 25. Plot of expected δJ (x-axis) vs. actual δJ (y-axis) for each ensemble run at the forecast time of 03Z 30 December 2008. The red line is a perfect 1 to 1 relationship for reference. This plot corresponds to the data given in Table 5.

ESA identifies two sensitivity regions. While these regions only need a statistical correlation to show sensitivity, a physical interpretation is desired to gain insight into the effects perturbations may have on the physical structures in the atmosphere. This also highlights the utility of ESA to detect these structures from an independent approach (statistical correlation only), possibly leading to the identification and location of important dynamic relationships in the atmosphere that have not been previously identified. In this chapter, tests of the sensitivity points are first presented corresponding to each of the experiments. Then a physical interpretation is offered in section B, a total energy analysis of each experiment is given in section C, and a method for accomplishing linearity tests with fewer ensemble members is given in section D.

1. Linearity

A linearity test is needed to examine responses to perturbations propagated by the non-linear model, compared to the response predicted by the linear ESA. This tests the validity of ESA. Since we are linearizing about the ensemble mean, it is possible for the ensemble to evolve in a non-linear manner, but if the perturbations are sufficiently small, then linearity may hold for a discreet amount of time. All results, unless otherwise noted, are for a verification time for J of 03Z on 30 December 2008. As shown in Table 5 and Figure 25, every experiment moves the ensemble mean for J in the correct direction as predicted by the sensitivity (dJ/dx) given in Table 2 and shown in Figure 24. However, as shown in Figure 25, ESA overestimates the impact of introducing a perturbation or assimilating an observation in every experiment.

In general, experiments at point 1 (downstream) have a larger actual δJ and impact the forecast more than experiments at point 2 (upstream). This is partially due to the larger δx introduced for DA1. The P1 ensemble run moves J as a percentage of actual change to predicted change more than any other perturbation. This P1 run moves J over 48% toward the expected δJ as predicted by the ESA performed using the NP run as shown in Table 5. The expected δJ is calculated by multiplying the sensitivity value (dJ/dx) from a perturbation point by the size of the perturbation (δx) introduced at the same point. While the perturbations introduced are very small, even these small perturbations, identified by ESA, impact the forecast metric J, showing the strong dependence of mountain waves on the initial conditions.

2. Atmospheric Structure

Examination of the perturbation structures imposed by either linear regression, or data assimilation of observations at analysis time, leads to physical insight. In the case at hand, ESA successfully identifies the importance of the vertical structure of atmospheric stability and the vertical wind profile both upstream and downstream of the DSWS. Figure 26 shows the vertical profiles of potential temperature, Brunt-Väisälä frequency, and *x*-wind component at the downstream (top) and upstream points (bottom). These profiles reveal that the sensitivity region identified by ESA at model level 13 is at the top of a stable layer in the atmosphere at both points 1 and 2. The higher values of Brunt-Väisälä frequency just below level 13 in Figure 26 (b and f) clearly show this stable layer. In a physical sense, introducing a perturbation of higher potential temperature, (P1, P2) or temperature (DA1, DA2) at these locations has the effect of sharpening and lowering the top of this stable layer.

Figure 27 shows how the vertical structure of potential temperature changes in the initial conditions of the unperturbed (NP) run from west to east across the downstream point. A strong stable layer, approximately identified by the green colors in the cross section is shallowest just lee of the front range and begins to widen or deepen moving toward the east. A hypothetical increase in potential temperature at the top of this stable layer over the east would lead to a flattening of the potential temperature ridge between 2.5 and 3.5 km in the eastern third of Figure 27 over the eastern plains of Colorado.

Figure 28 shows the vertical structure of potential temperature in the initial conditions of the NP run from west to east across the upstream point. A stable layer, approximately identified by the green colors in the cross section, is just upstream of the central Colorado Rockies. A hypothetical increase in potential temperature at the top of this stable layer, just to the west and roughly at the level of the highest terrain, could modulate the frequency of the wave response downstream. This could be accomplished by decreasing the height of the inversion which could change how much energy is trapped and the frequency at which it oscillates. Different dynamics and locations of the highest winds and wave structures to the east would follow. This bolstered stable layer could lead to an increased trapping effect in this layer of the atmosphere, possibly leading to a stronger trapped response in the wave propagating in the lower atmosphere across the Rockies or downstream across the plains.

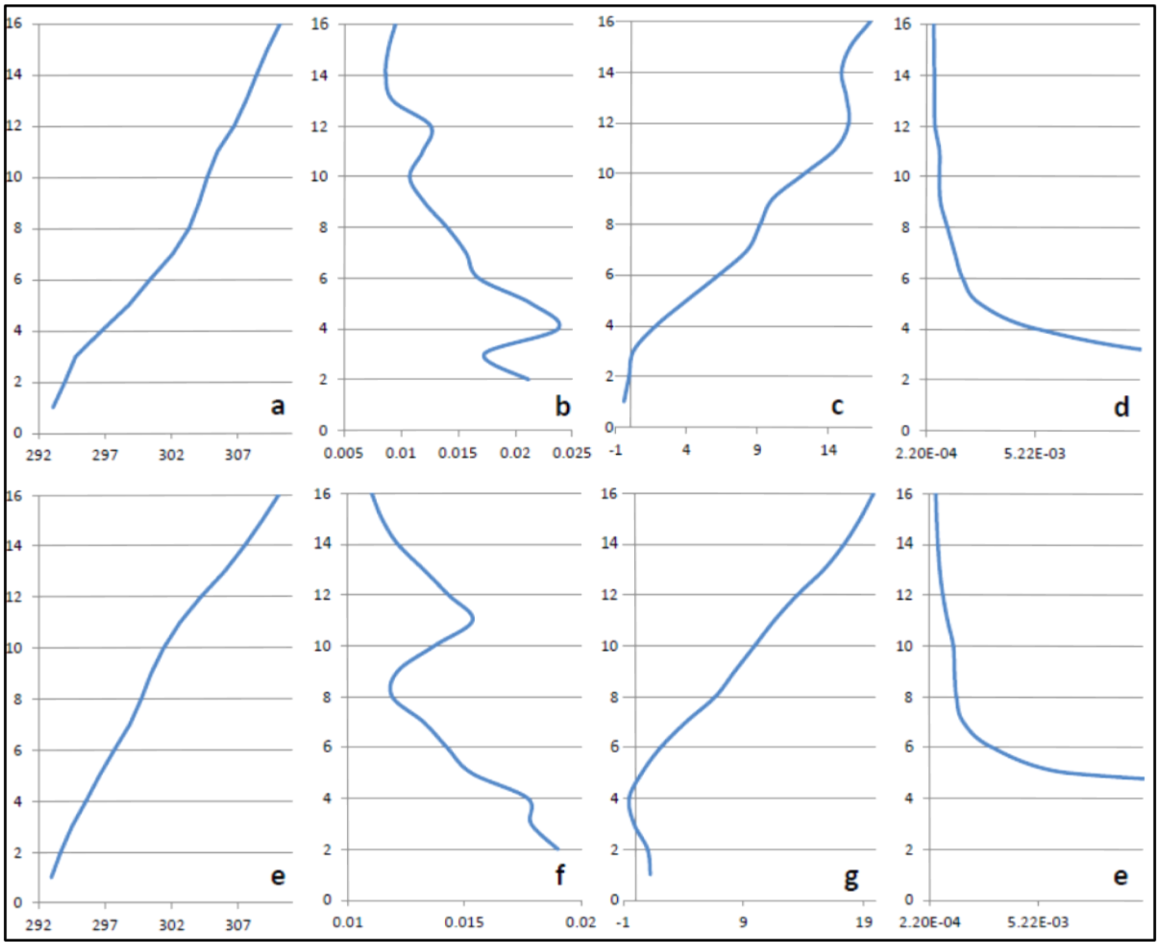

Figure 26. Vertical profiles by model level at point 1 (top) of a) Potential Temperature (K), b) Brunt-Väisälä frequency (s^{-1}), c) *x*-wind component (m s^{-1}), d) Scorer parameter and at point 2 (bottom) of e) Potential Temperature (K), f) Brunt-Väisälä frequency (s^{-1}), g) *x*-wind component (m s^{-1}), h) Scorer parameter. These plots are from the NP ensemble mean valid at 00Z 30 December 2008.

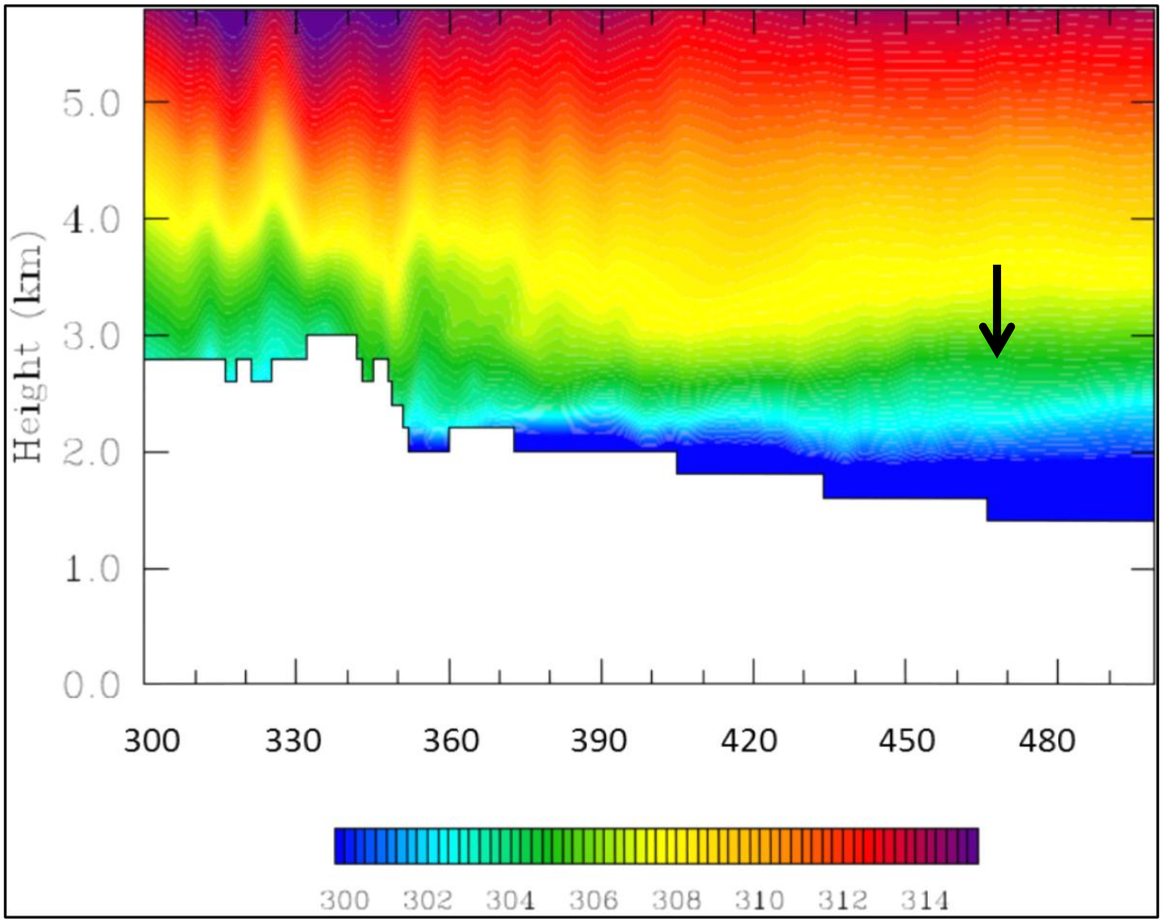

Figure 27. Cross section from west to east (grid points 300–500) at the gridline of point 1, showing ensemble mean potential temperature from the NP run analysis. Black arrow denotes the location of the introduced perturbation (point 1).

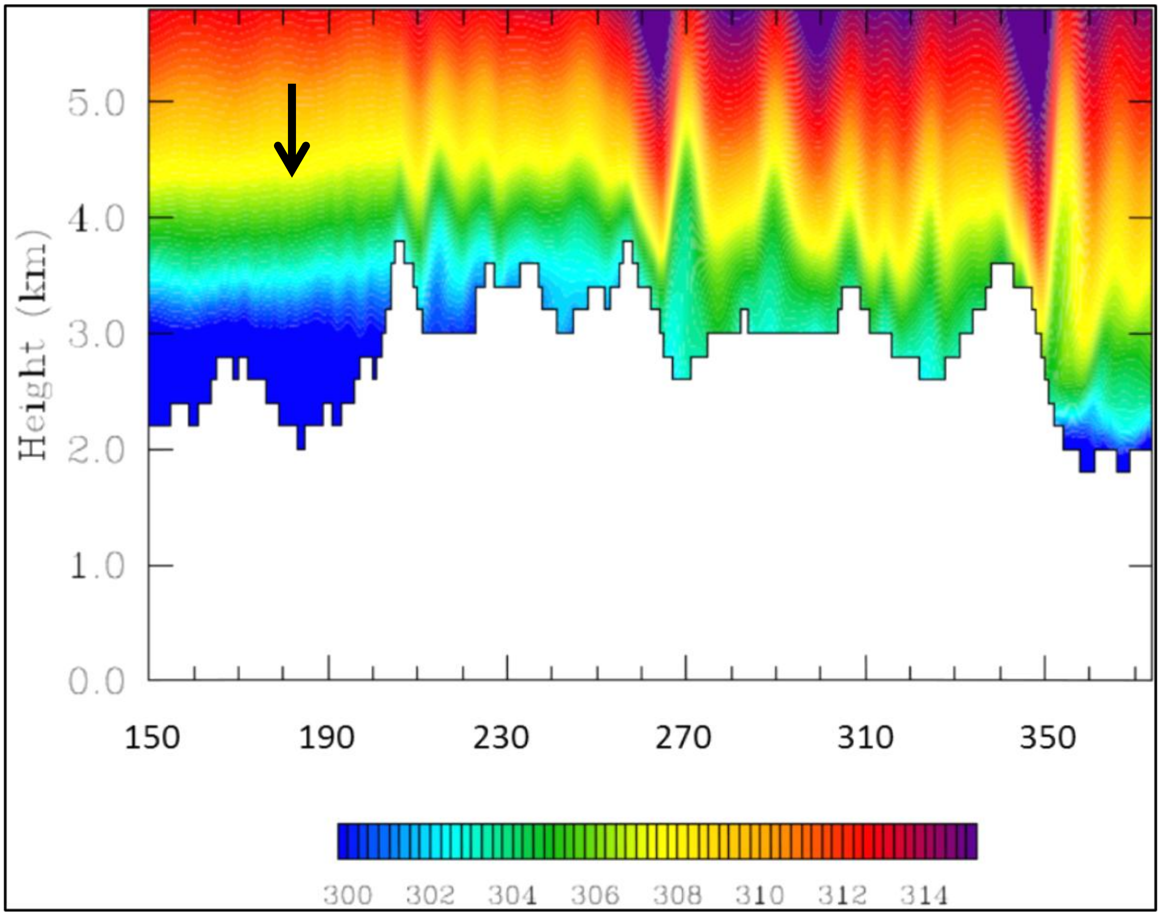

Figure 28. Cross section from west to east at the gridline of point 2 (grid points 150–375), showing ensemble mean potential temperature from the NP run analysis. Black arrow denotes the location of the introduced perturbation (point 2).

3. Forecast Certainty and Ensemble Spread

While it is not a primary goal of the perturbation/data assimilation experiments here to create a more accurate forecast, but rather to test the sensitivity of the ensemble system to changes in initial conditions, it is worthwhile to comment on changes in the certainty of the forecast due to the perturbations/data assimilation. The most likely forecast of a well-developed ensemble system is the ensemble mean for a single mode distribution. The standard deviation of the distribution is often used to access ensemble spread and the certainty of the forecast. If the standard deviation decreases, the forecast is expected to be more certain. If the standard deviation increases, the forecast is expected to be less certain.

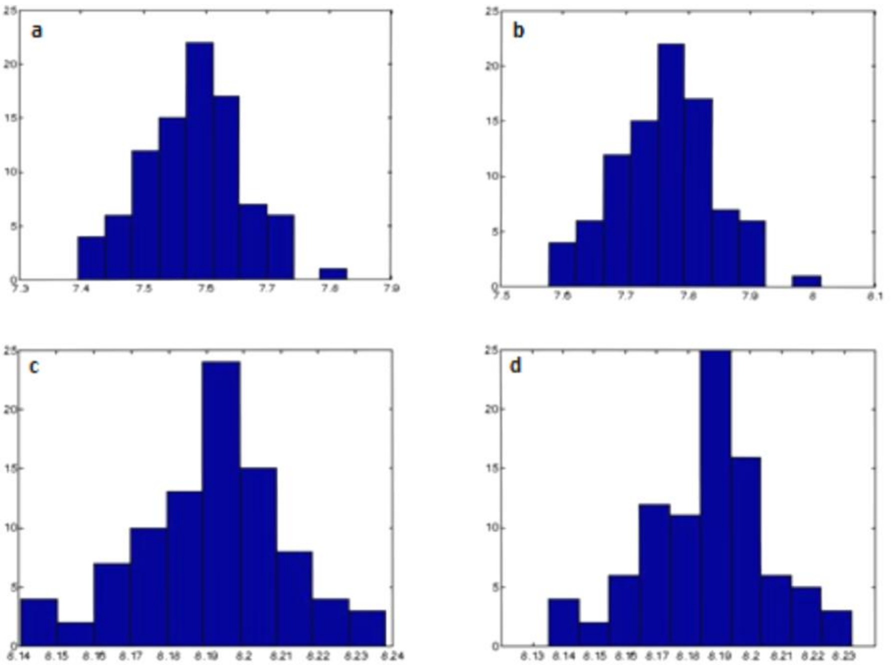

Figure 29. Histograms of perturbation potential temperature at point 1from the analysis for the a) NP run, b) P1 run, c) DA1 run, and d) DAJ run.

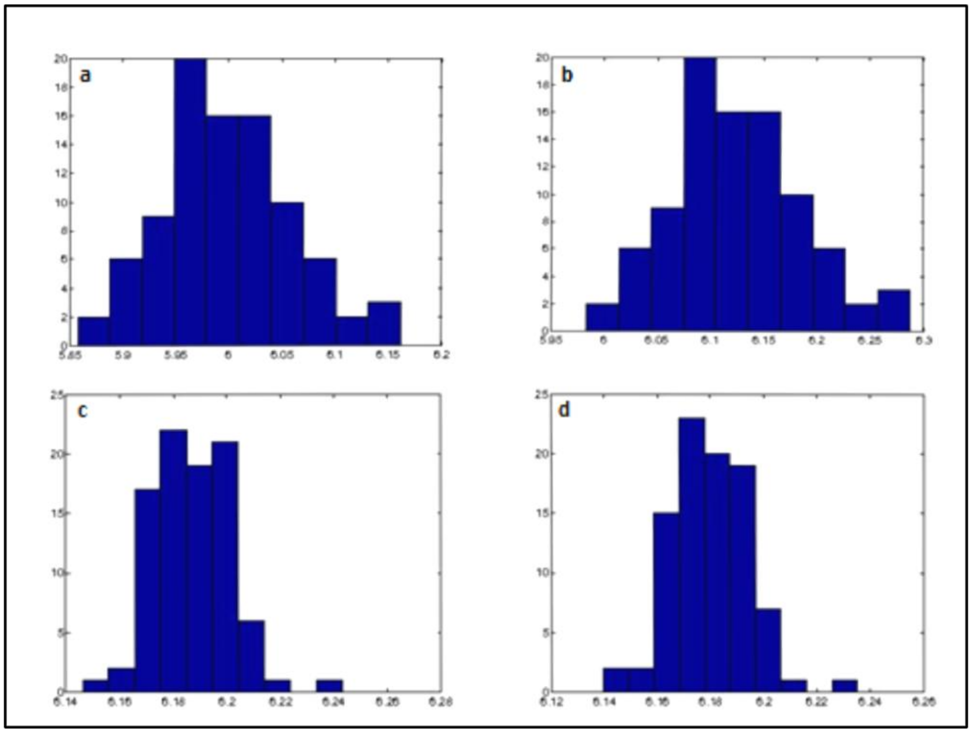

Figure 30. Histograms of perturbation potential temperature at point 2 from the analysis for the a) NP run, b) P2 run, c) DA2 run, and d) DAJ run.

	$<\theta'>$	σ
NP Run Point 1	7.582	0.0789
NP Run Point 2	5.9978	0.0606
P1 Run Point 1	7.7649	0.0789
P2 Run Point 2	6.1239	0.0606
DA1 Run Point 1	8.1913	0.0198
DA2 Run Point 2	6.1863	0.0146
DAJ Run Point 1	8.1857	0.0198
DAJ Run Point 2	6.1791	0.0146

Table 6. Table showing the mean and standard deviation of perturbation potential temperature at points 1 and 2 from the analysis for every ensemble run.

Introducing perturbations and assimilating observations at points 1 and 2 have different effects on the standard deviation at these points in the analysis. The standard deviation and shape of the distribution does not change when introducing a perturbation (P1 and P2 runs). This is seen when comparing histogram A to histogram B in Figures 29 and 30. The standard deviation of each is the same, but the distribution is shifted in the direction of the perturbation. In contrast, the standard deviation decreases and the distributions shift when assimilating an observation (DA1, DA2, and DAJ runs). This is seen when comparing histograms C and D to histogram A in Figures 29 and 30. The data assimilation process decreases the standard deviation at the observation point and shifts the distribution in the direction of the observation. This is caused by assimilating an observation with zero observation error in our experiments. The mean and standard deviation of perturbation potential temperature at the analysis time is shown in Table 6 for every ensemble run and corresponds to the histograms shown in Figures 29 and 30.

It is expected that the decrease in the analysis standard deviation will lead to a decreased standard deviation in *J* at the forecast time. However, this is not always the case for our experiments. After the perturbations/data assimilation, the 03Z forecast standard deviation of *J* increases in all ensemble runs that include the downstream point (P1, DA1, DAJ) and decreases for all runs that include the upstream point (P2, DA2). While run P1 responds with a more accurate change in *J* than any other run, at the same time its spread increases as measured by standard deviation as shown in Table 5. Conversely, runs perturbed at point 2 respond with a less accurate change in *J*, but their spread decreases as measured by standard deviation.

A possible explanation to why the spread of *J* increases at the forecast time, when it is expected to decrease, is that the mean flow advects the atmospheric features containing the lower spread in the analysis downstream as the forecast progresses. This has the effect of moving features with decreased spread toward the location of *J* for the upstream perturbation/assimilation point and moving features farther away from *J* for the downstream perturbation/assimilation point. This is supported by the cross sections shown in Figures 31, 32, and 33.

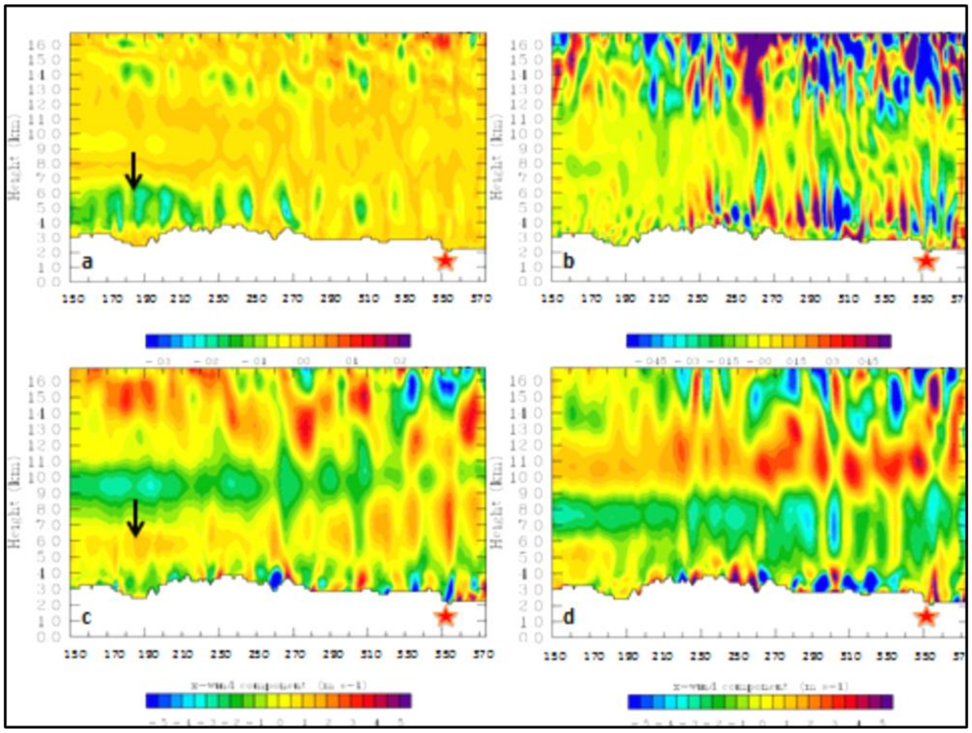

Figure 31. Cross Sections of $\sigma_{DA2} - \sigma_{NP}$ from west to east at the gridline of the Rampart sensor (grid points 150–375) for a) analysis potential temperature, b) 03Z forecast of potential temperature, c) analysis x-wind component, d) 03Z forecast of x-wind component. The arrow denotes the longitude of the observation insertion (point 2), and the star denotes the location of USAFA and the forecast metric J.

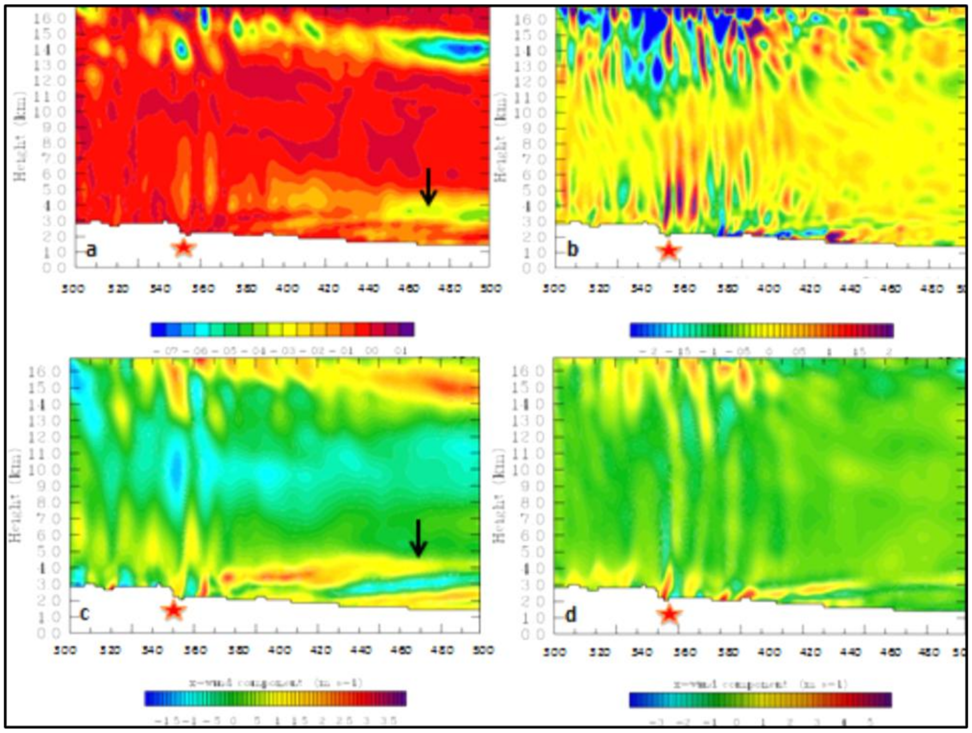

Figure 32. Cross Sections of $\sigma_{DA1} - \sigma_{NP}$ from west to east at the gridline of the Rampart sensor (grid points 300–500) for a) analysis potential temperature, b) 03Z forecast of potential temperature, c) analysis *x*-wind component, d) 03Z forecast of *x*-wind component. The arrow denotes the longitude of the observation insertion (point 1), and the star denotes the location of USAFA and the forecast metric *J*.

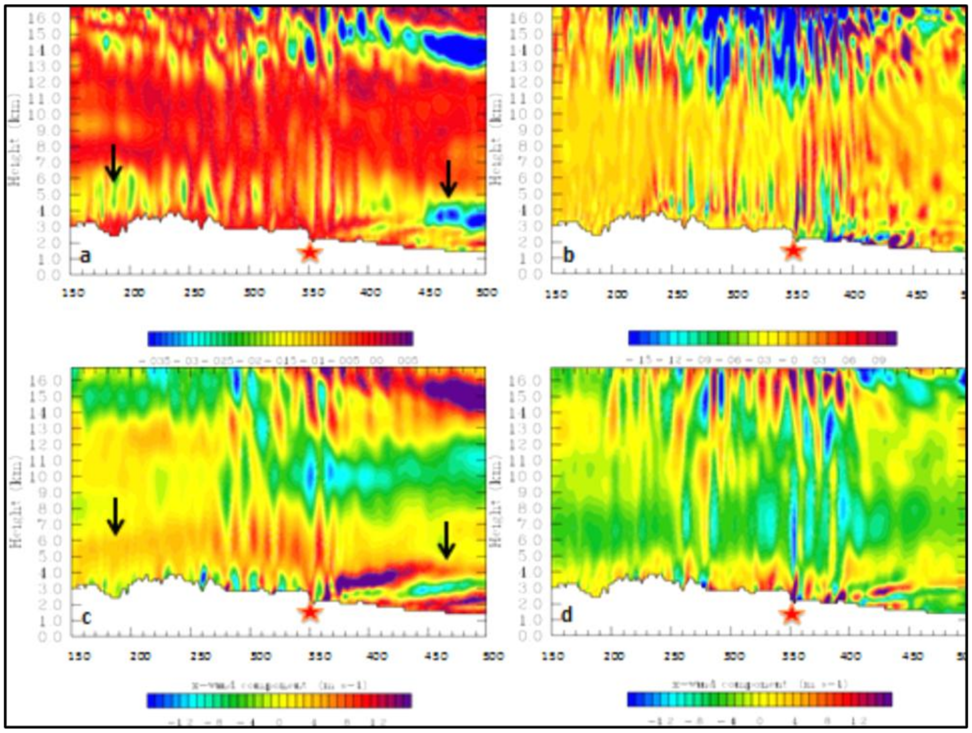

Figure 33. Cross Sections of $\sigma_{DAJ} - \sigma_{NP}$ from west to east at the gridline of the Rampart sensor (grid points 300–500) for a) analysis potential temperature, b) 03Z forecast of potential temperature, c) analysis *x*-wind component, d) 03Z forecast of *x*-wind component. The arrow denotes the longitude of the observation insertion (point 1), and the star denotes the location of USAFA and the forecast metric *J*.

Figure 31 shows a cross section of the difference between the DA2 run standard deviation and the NP run standard deviation ($\sigma_{DA2} - \sigma_{NP}$) for potential temperature (top), *x*-wind component (bottom), at analysis time (left), and at the three hour forecast (right). Figure 31a shows a region of decreased spread in potential temperature associated with the observation location. This area of decreased spread evolves into a complicated wave structure, but clearly moves to the east in the three hour forecast as shown in Figure 31b. Similarly, decreased spread is seen in the *x*-wind component at analysis time just above the observation location and moves to the east by the three hour forecast (Figure 31 bottom).

Figure 32 shows a cross section of the difference between the DA1 run standard deviation and the NP run standard deviation ($\sigma_{DA1} - \sigma_{NP}$) for potential temperature (top), *x*-wind component (bottom), at analysis time (left), and at the three hour forecast (right). Figure 32a shows a region of decreased spread for potential temperature in the analysis associated with the location of the assimilated observation. This region is not observed in the three hour forecast and based on the evidence from the DA2 run of the decreased spread features advecting downstream, it is presumed that the decreased spread regions in DA1 advect to the east and out of the domain. This potentially explains why the standard deviation increases at the forecast time of 03Z for J in each run that has a perturbation/assimilation point downstream of the forecast metric's location. Further evidence for this explanation is presented in section C of this chapter which shows from a total energy perspective that perturbation energy from the downstream location propagates out of the domain more quickly than perturbations introduced at the upstream location. Similar results as shown in the DA1 and DA2 runs are found simultaneously in the DAJ run that is shown in Figure 33.

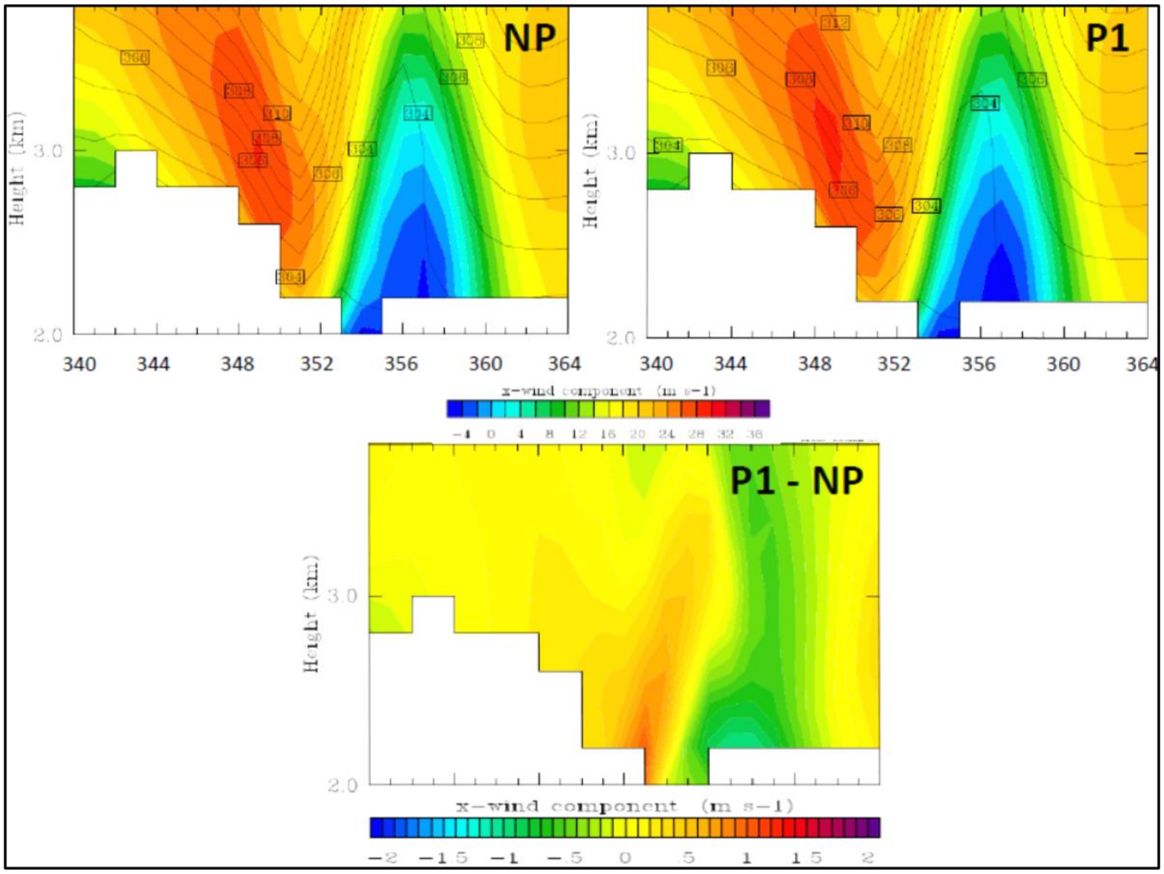

Figure 34. Cross sections of *x*-wind component (shaded) and potential temperature (contoured) from west to east across the Rampart Range and adjacent plains at the gridline of the Rampart sensor for the 30 December 2008 ensemble mean NP run (top left), P1 run (top right), and difference between P1 and NP (bottom) for the three hour forecast valid at 03Z.

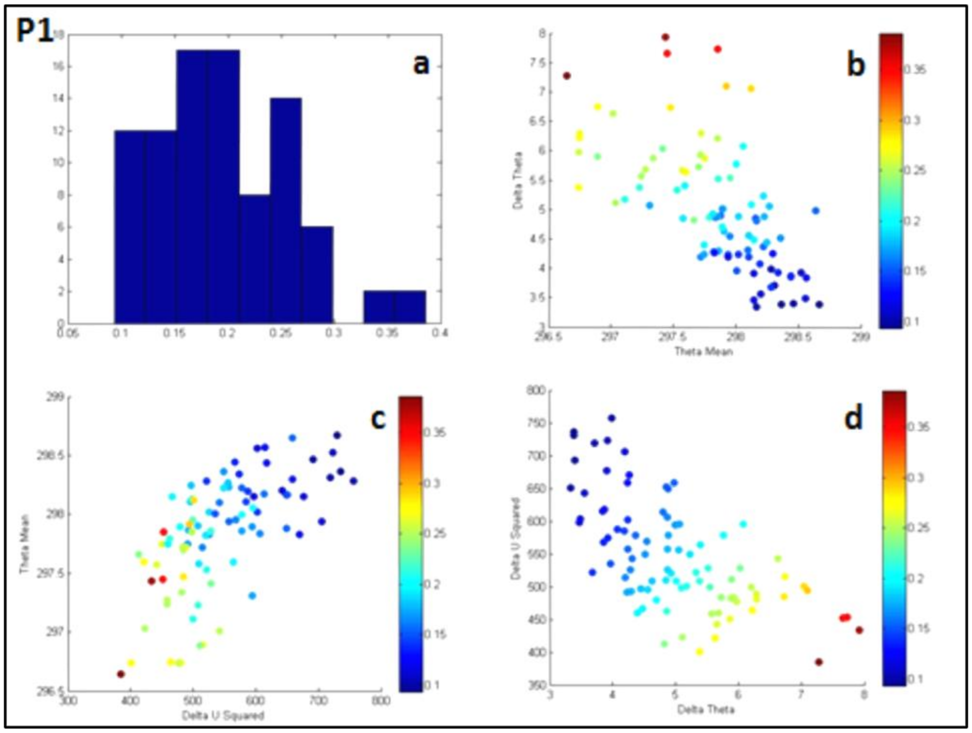

Figure 35. a) Histogram of the forecast metric (*J*) for P1 96-member WRF ensemble at 03Z 30 December 2008, b) scatterplot of $\bar{\theta}$ vs. $(\theta_2 - \theta_1)$, c) scatterplot of $(U_2 - U_1)^2$ vs. $\bar{\theta}$, d) $(\theta_2 - \theta_1)$ vs. $(U_2 - U_1)^2$. The magnitude of the forecast metric (*J*) is shaded in the scatterplots. All plots are for 03Z 30 December 2008.

B. FORECAST METRIC IMACT

1. P1 Ensemble Run

The P1 ensemble run with the downstream perturbation at point 1, over the eastern plains of Colorado, decreases the forecast metric *J* as expected. The sensitivity prediction (*dJ/dx*) correctly indicates that an increase in potential temperature at point 1 corresponds with a decrease in *J*. The magnitude of the shift is over 48% of what ESA predicts (Table 5). As shown in Figure 34, the decrease in *J* is due to a slight increase of the downslope winds and a slightly larger increase in the easterly flow beneath the rotor over the adjacent plains, thus increasing the wind shear acting on the stable layer. In addition, the perturbation of potential temperature causes a slight shift to the east of the flow separation and convergence zone, moving stronger westerlies about 2–3 km further to the east than in the NP run.

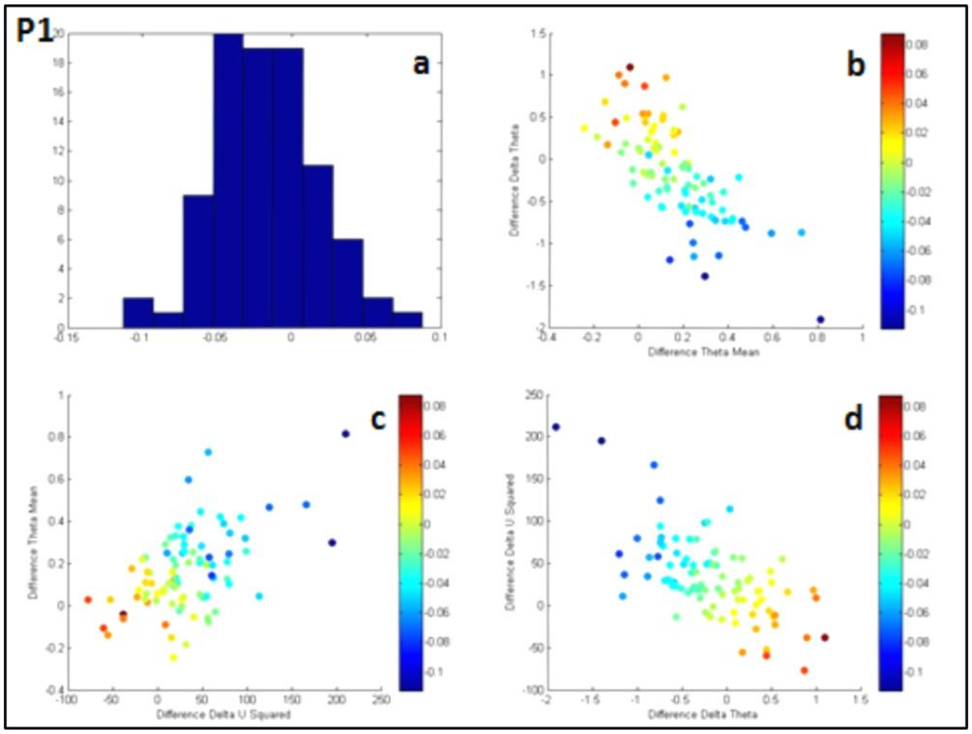

Figure 36. a) Histogram for the difference in the forecast metric (J) between P1 and NP runs, b) scatterplot of the difference between the P1 and NP runs for $\overline{\theta}$ vs. $(\theta_2 - \theta_1)$, c) scatterplot of the difference between the P1 and NP runs for $(U_2 - U_1)^2$ vs. $\overline{\theta}$, d) scatterplot of the difference between the P1 and NP runs for $(\theta_2 - \theta_1)$ vs. $(U_2 - U_1)^2$. The magnitude of the difference between the P1 and NP runs for the forecast metric (J) is shaded in the scatterplots. All plots are valid for 03Z 30 December 2008.

The changes observed in the P1 run are physically consistent in terms of what is expected when J decreases. Since J is a modified Bulk Richardson number, a decrease in J should be due to increased shear and decreased stability causing the likelihood of turbulence to increase. This can be seen in Figures 34, 35, and 36 valid for the three hour forecast. The scatterplots in Figure 35 are consistent with the NP runs in the interpretation of the forecast metric. The distributions of the shear and stability terms in J allow for a consistent physical interpretation of the results. The highest values of J are associated with a strong horizontal potential temperature gradient and weaker wind shear across the flow separation and convergence zone. The result is that stability dominates over wind shear and the likelihood of turbulence is minimized. Conversely, low values of *J* are associated with strong wind shear and weak stability; shear dominates over stability and the likelihood of turbulence is maximized. Figure 36 shows that a majority of members have decreased with respect to *J* due to both increased shear and decreased stability. Some members have an increase with respect to *J* due to decreased shear and increased stability. Their numbers are fewer and their change is smaller compared to the members where *J* decreases. Overall the ensemble mean of *J* decreases.

Figure 37 (top) shows the perturbations introduced in the P1 run at point 1 for all model levels, and shows the small potential temperature increase introduced by adding a perturbation at level 13. The perturbation introduced at level 13 leads to greater changes in potential temperature in the upper-troposphere and lower stratosphere, as also shown by the cross section in Figure 38. This results from a strong covariance between point 1 and the upper-troposphere in the ensemble analysis used for regressing the perturbation. The perturbation is spread in the lower troposphere east to west along the potential temperature ridge (Figure 32), with an effect of flattening this ridge over the eastern third of the cross section and sharpening the vertical transition from more stable to less stable air in this region.

Figure 37 (bottom) reveals an inverse relationship between potential temperature and specific humidity at point 1. The sensitivity analysis shown in Figure 24 suggests that increases in potential temperature should have similar effects as decreasing the specific humidity at the same point. This relationship holds after the perturbation is introduced, as increasing potential temperature has the effect of lowering specific humidity at the downstream point (point 1).

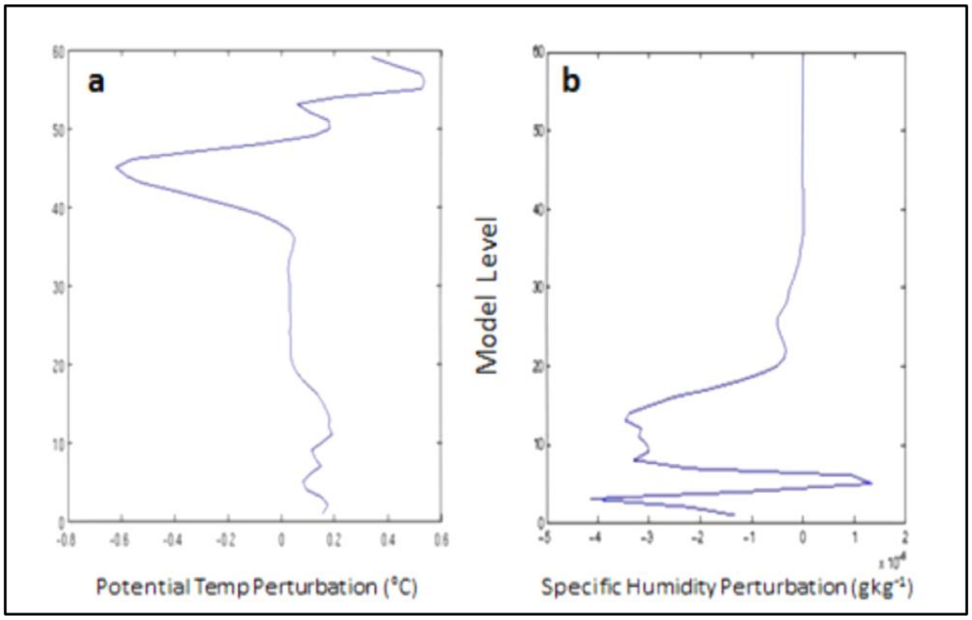

Figure 37. Perturbation of, a) potential temperature and, b) specific humidity from the P1 run analysis at point 1 as function of model level (x-axis).

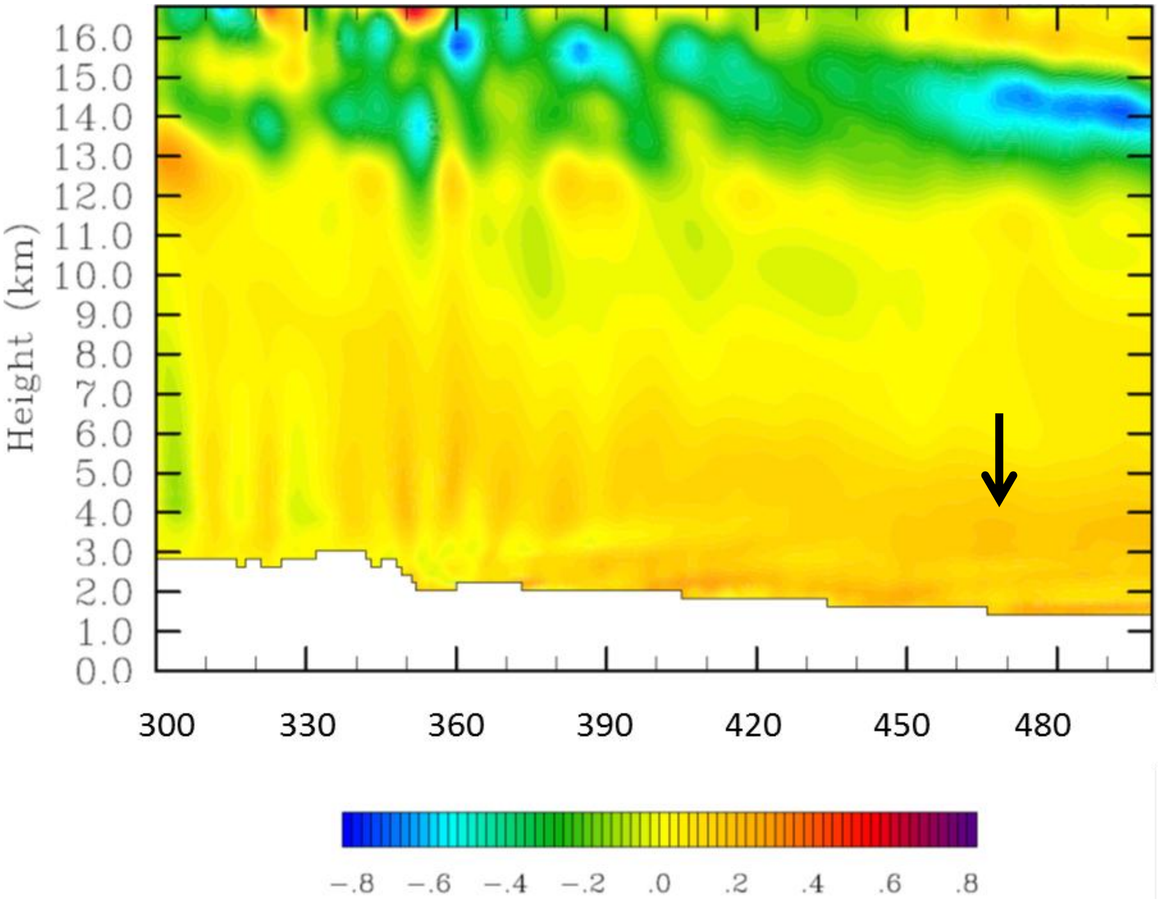

Figure 38. Cross section of potential temperature difference between the P1 and NP run analysis from west to east at the gridline of point 1 (grid points 300–500). Black arrow denotes the location of the introduced perturbation (point 1).

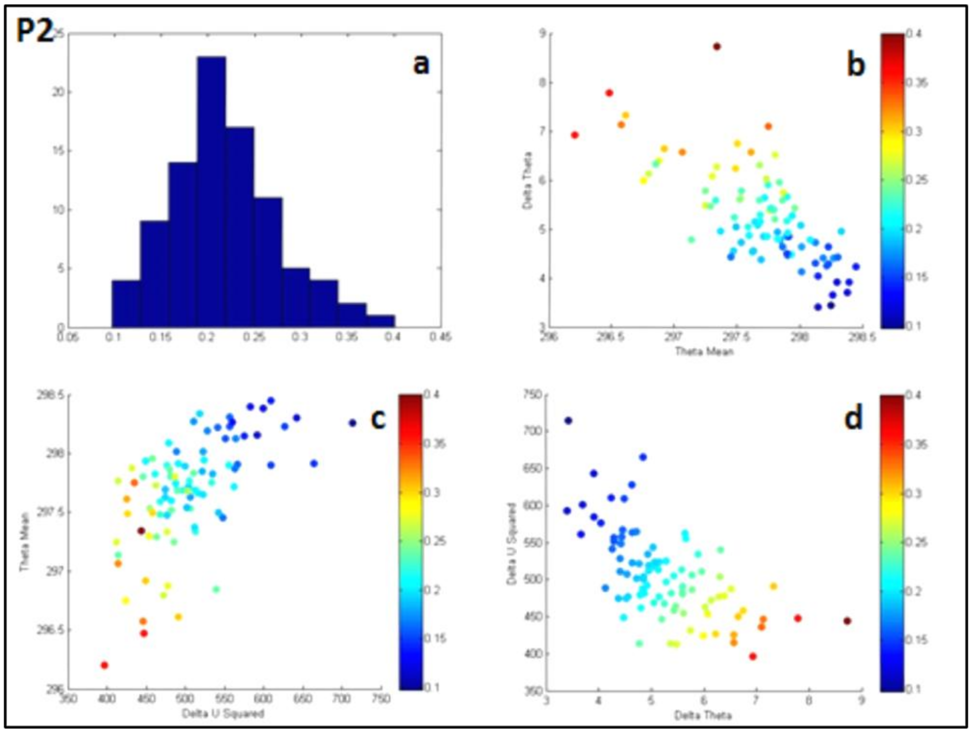

Figure 39. a) Histogram of the forecast metric (J) for P2 96-member WRF ensemble at 03Z 30 December 2008, b) scatterplot of $\overline{\theta}$ vs. $(\theta_2 - \theta_1)$, c) scatterplot of $(U_2 - U_1)^2$ vs. $\overline{\theta}$, d) $(\theta_2 - \theta_1)$ vs. $(U_2 - U_1)^2$. The magnitude of the forecast metric (J) is shaded in the scatterplots. All plots are valid for 03Z 30 December 2008.

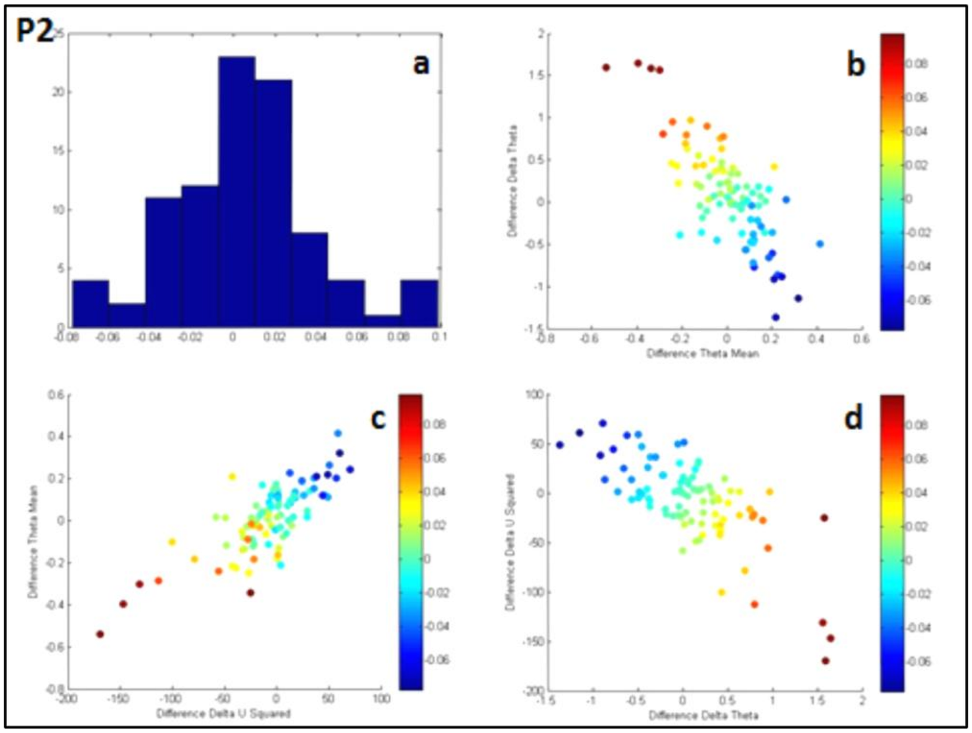

Figure 40. a) Histogram for the difference in the forecast metric (J) between P2 and NP runs, b) scatterplot of the difference between the P2 and NP runs for $\bar{\theta}$ vs. $(\theta_2 - \theta_1)$, c) scatterplot of the difference between the P2 and NP runs for $(U_2 - U_1)^2$ vs. $\bar{\theta}$, d) scatterplot of the difference between the P2 and NP runs for $(\theta_2 - \theta_1)$ vs. $(U_2 - U_1)^2$. The magnitude of the difference between the P2 and NP runs for the forecast metric (J) is shaded in the scatterplots. All plots are valid for 03Z 30 December 2008.

2. P2 Ensemble Run

Changes in P2 due to the introduction of a perturbation of potential temperature from the truth run at the upstream point (point 2) are almost not discernible in the mean statistics. Cross sections comparing the ensemble mean of P2 to NP at the forecast time and location of *J* are virtually identical (not shown). However, changes in the distribution and to individual members are apparent. Figure 40 shows that a majority of members exhibit very little change and the slight increase in the P2 *J* mean is driven by relatively few members that decrease shear and increase in stability. In addition, the inverse relationship between potential temperature and specific humidity predicted by the

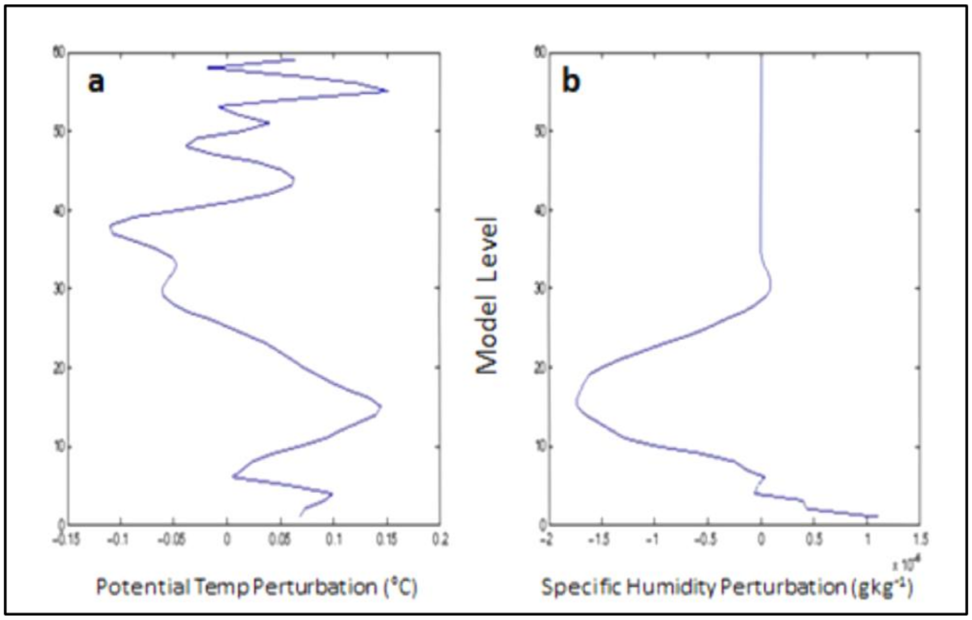

Figure 41. Perturbation of a) potential temperature and b) specific humidity for the P2 run analysis at point 2 as function of model level (x-axis).

sensitivity analysis (Figure 41b) holds true after the introduction of a potential temperature perturbation at point 2.

Figure 41a shows the perturbations introduced in the P2 run in the column through point 2, and shows the small increase in potential temperature introduced by adding a perturbation at level 13. The perturbation introduced at level 13 leads to stronger downward branches of the downstream trapped waves. This is seen by the location of increased potential temperature east of point 2, and also by comparing the location of the waves in Figure 28 and the location of potential temperature increases in Figure 42. The increased sharpness in the upstream stable layer has the effect of increasing reflection downward of the downstream trapped waves in the P2 run.

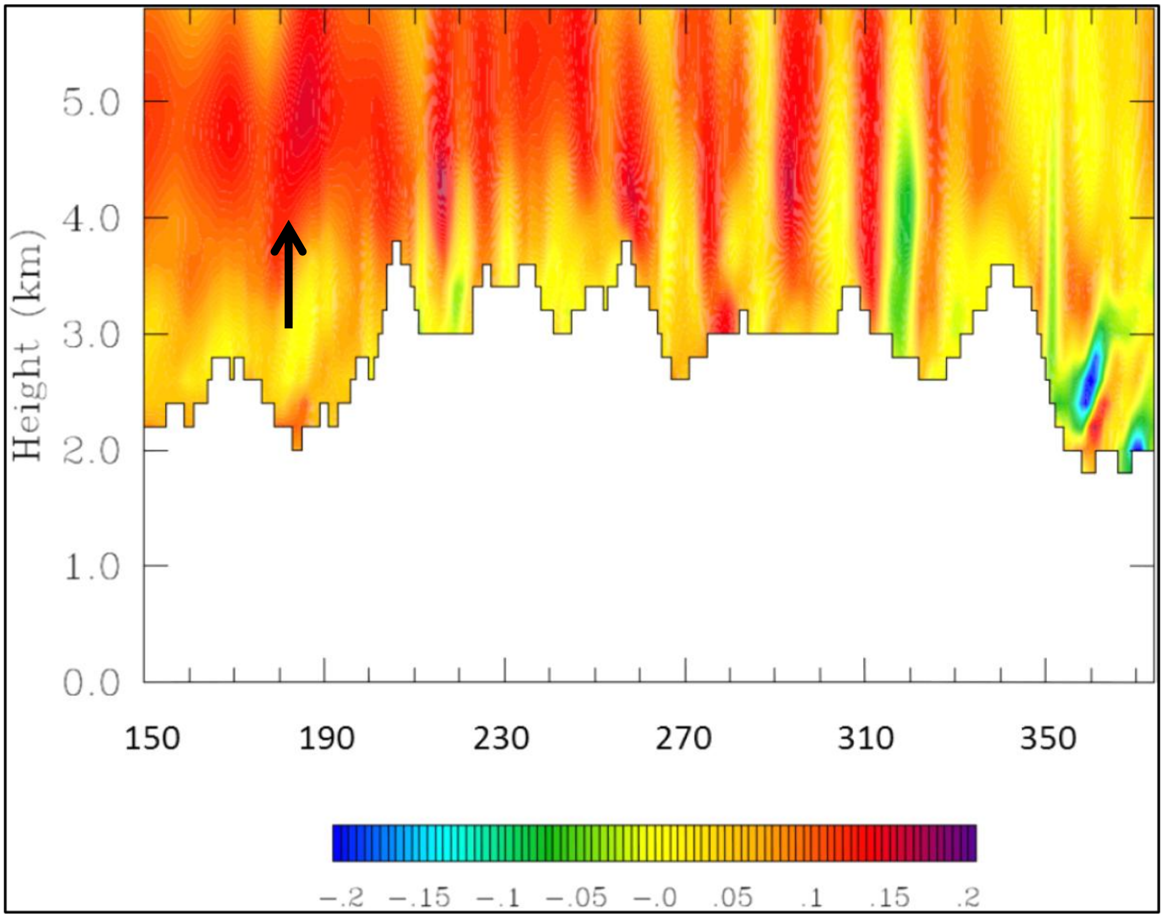

Figure 42. Cross section of ensemble mean potential temperature difference between the analysis for the P2 and NP runs from west to east at the gridline of point 2 (grid points 150–375). The black arrow denotes the location of the introduced perturbation (point 2).

As noted in the overview to this chapter, the spread of *J* as measured by standard deviation decreases in the P2 run (Table 5). This is seen graphically when comparing histograms between Figures 22 and 39 for the NP and P2 runs. The histogram for the P2 run shows a much sharper distribution than the NP histogram, with the highest bar in the plot having more than 20 members in its range. This suggests increased certainty in the forecast of *J* at 03Z in the P2 run.

3. DA1 Ensemble Run

The DA1 ensemble run has the largest change in J of any run due to the large δx introduced through assimilation. However, it only moves J slightly more than 16% of what ESA predicts it should move. ESA indicates that an increased potential temperature at the downstream point causes a decrease in J. This is revealed in the cross section of the ensemble mean in the region of J (Figure 43) and in scatterplots (Figures 44 and 45). The mean of J decreases as the majority of members move in a negative direction. The negative δJ results from increased shear, decreased stability, and increased mean potential temperature. The increase in shear is primarily due to a 2.5 m s^{-1} increase in the easterlies in the return flow under the rotor. Additionally, the westerlies and the region of flow separation shift slightly to the east causing an increase of over 5 m s^{-1} in the region just west of the Airfield between the DA1 and NP runs in the ensemble mean.

Figure 46 (top) shows the perturbations introduced in the DA1 run at point 1, and reveals the potential temperature increase introduced by assimilating the temperature from the truth run at level 13. Assimilating this temperature observation at level 13 also leads to greater potential temperature in the upper-troposphere and lower stratosphere, (also shown by the cross section in Figure 47). The magnitude of the changes from data assimilation is significantly larger in the DA1 than the P1 case, most likely due to a larger δx at point 1 after assimilation of the temperature observation. At most locations the perturbations in DA1 are 2–3 times larger than the P1 run. The implications of this in terms of total energy are explored in the next section. Similar to P1, the perturbation is spread in the lower troposphere east to west along the potential temperature ridge identified in Figure 37. This has the effect of flattening this ridge over the eastern third of the cross section and sharpening the vertical transition from more stable to less stable air in this region. Lastly, Figure 46 (bottom) reveals an inverse relationship between potential temperature and specific humidity at point 1 for the DA1 run, consistent with all other runs and suggested by the original ESA prediction.

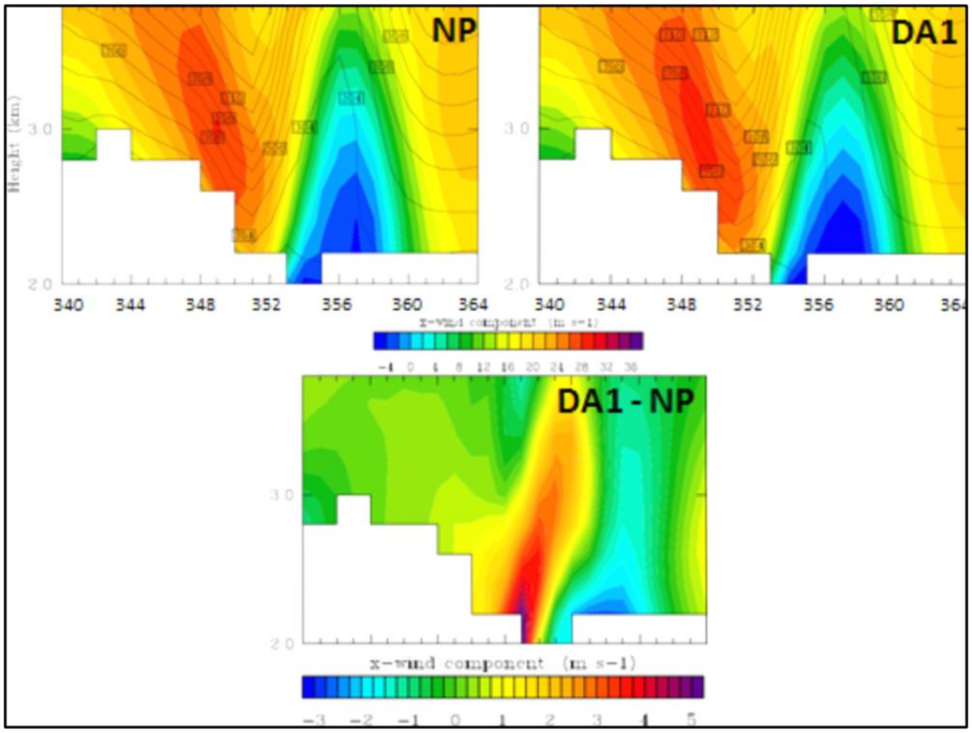

Figure 43. Cross sections of *x*-wind component (shaded) and potential temperature (contoured) from west to east across the Rampart Range and adjacent plains at the gridline of the Rampart sensor for the 30 December 2008 ensemble mean NP run (top left), DA1 run (top right), and difference between DA1 and NP (bottom) for the three hour forecast valid at 03Z. All plots are valid at 03Z 30 December 2008.

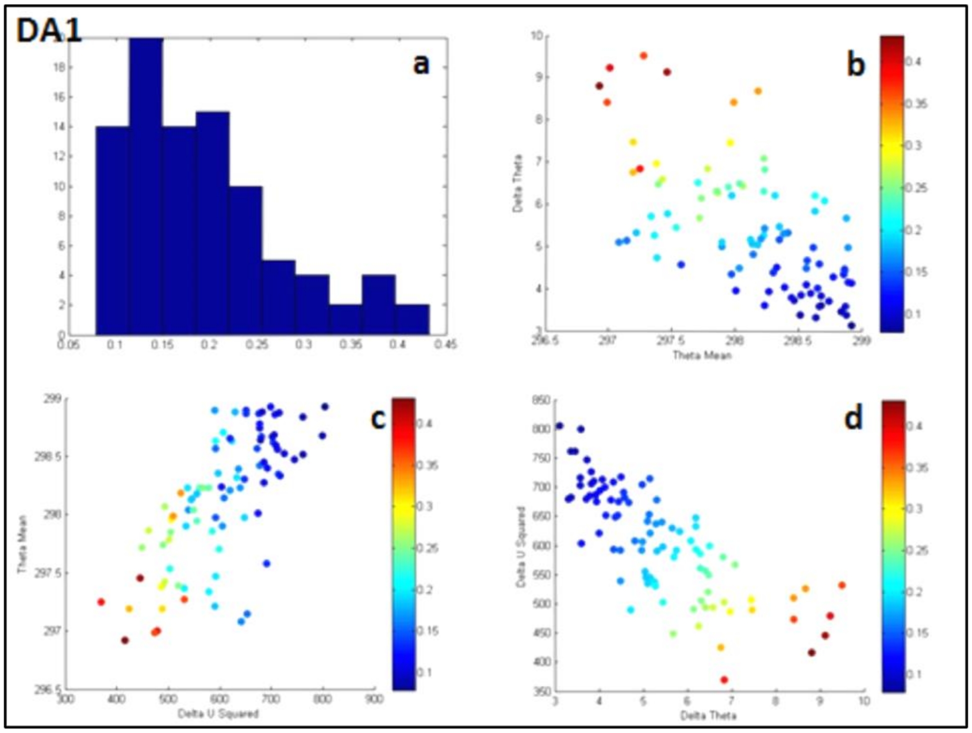

Figure 44. a) Histogram of the forecast metric (J) for DA1 96-member WRF ensemble at 03Z 30 December 2008, b) scatterplot of $\bar{\theta}$ vs. $(\theta_2 - \theta_1)$, c) scatterplot of $(U_2 - U_1)^2$ vs. $\bar{\theta}$, d) $(\theta_2 - \theta_1)$ vs. $(U_2 - U_1)^2$. The magnitude of the forecast metric (J) is shaded in the scatterplots. All plots are valid at 03Z 30 December 2008.

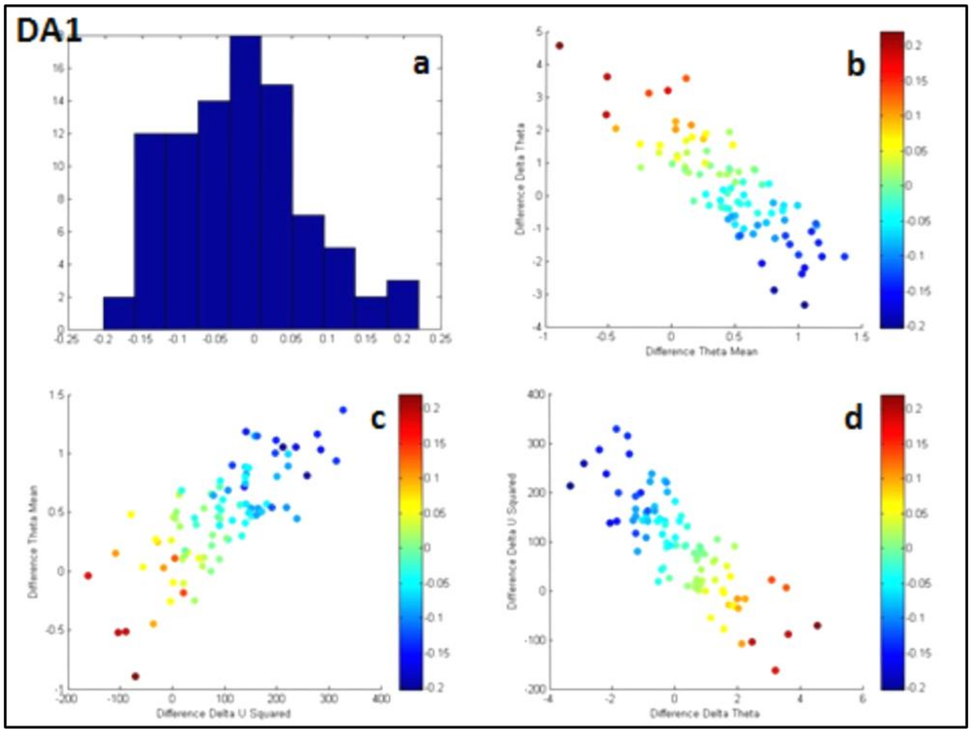

Figure 45. a) Histogram for the difference in the forecast metric (J) between DA1 and NP runs, b) scatterplot of the difference between the DA1 and NP runs for $\overline{\theta}$ vs. $(\theta_2 - \theta_1)$, c) scatterplot of the difference between the DA1 and NP runs for $(U_2 - U_1)^2$ vs. $\overline{\theta}$, d) scatterplot of the difference between the DA1 and NP runs for $(\theta_2 - \theta_1)$ vs. $(U_2 - U_1)^2$. The magnitude of the difference between the DA1 and NP runs for the forecast metric (J) is shaded in the scatterplots. All plots are valid at 03Z 30 December 2008.

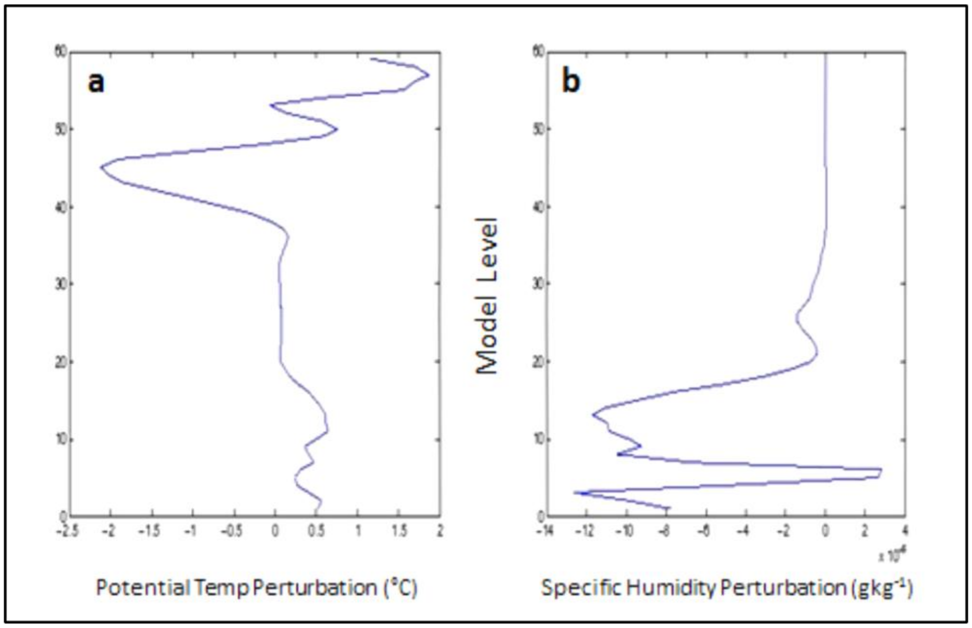

Figure 46. Perturbation of a) potential temperature and b) specific humidity for the DA1 run analysis at point 2 as function of model level (x-axis).

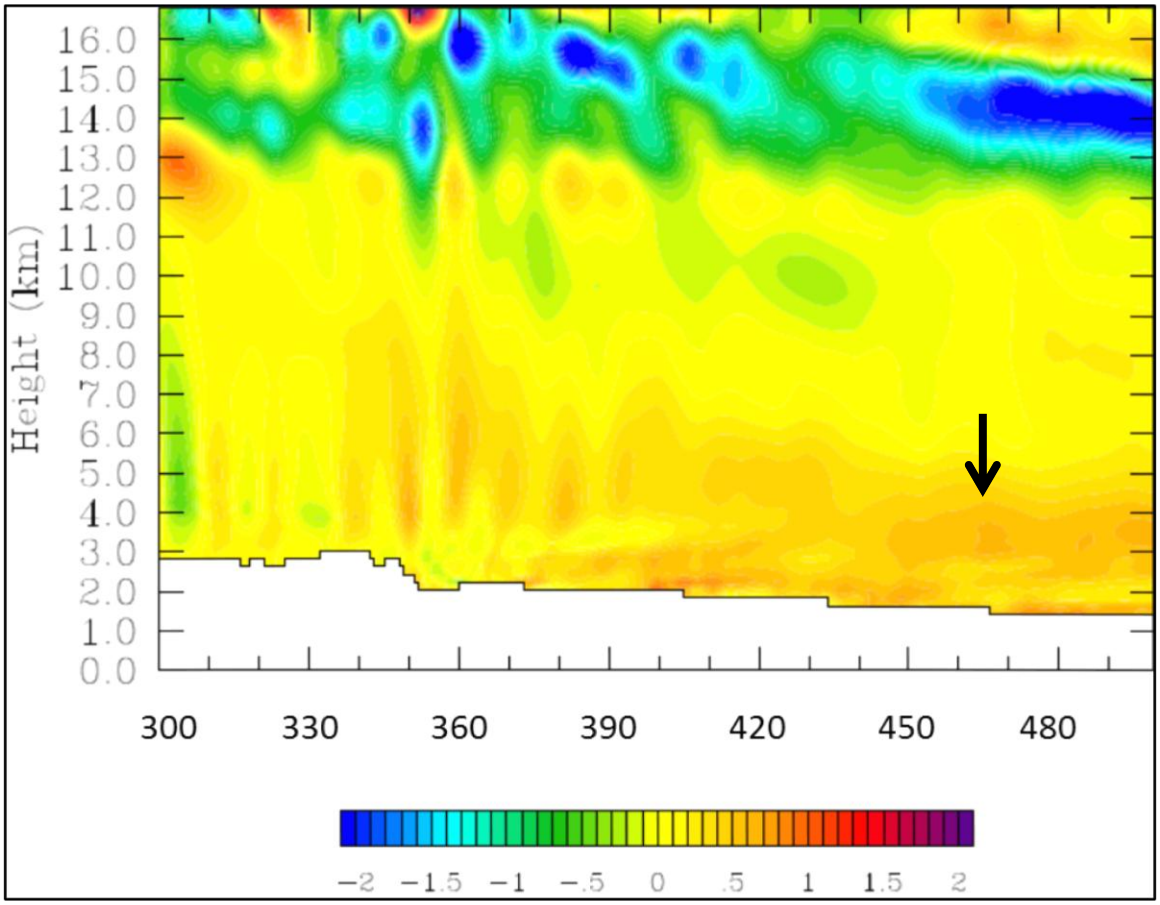

Figure 47. Cross section of potential temperature difference between the analysis for the DA1 and NP runs from west to east at the gridline of point 1 (grid points 300–500). The black arrow denotes the location of the introduced perturbation (point 1).

4. DA2 Ensemble Run

The results of the DA2 run are very similar to the findings in the P2 run, except the magnitude of the changes are greater when comparing DA2 with P2. The DA2 run verifies better than the P2 run in terms of how much *J* actually changes when compared to the predicted change by ESA. Qualitatively the patterns and shifts in the various fields are almost identical for the DA2 run as the P2 run. The shifts in *J* continue to be consistent with the Bulk Richardson reasoning, as the small increase in *J* is caused by both increases in stability and decreases in shear in the majority of the members (Figures 48 and 49).

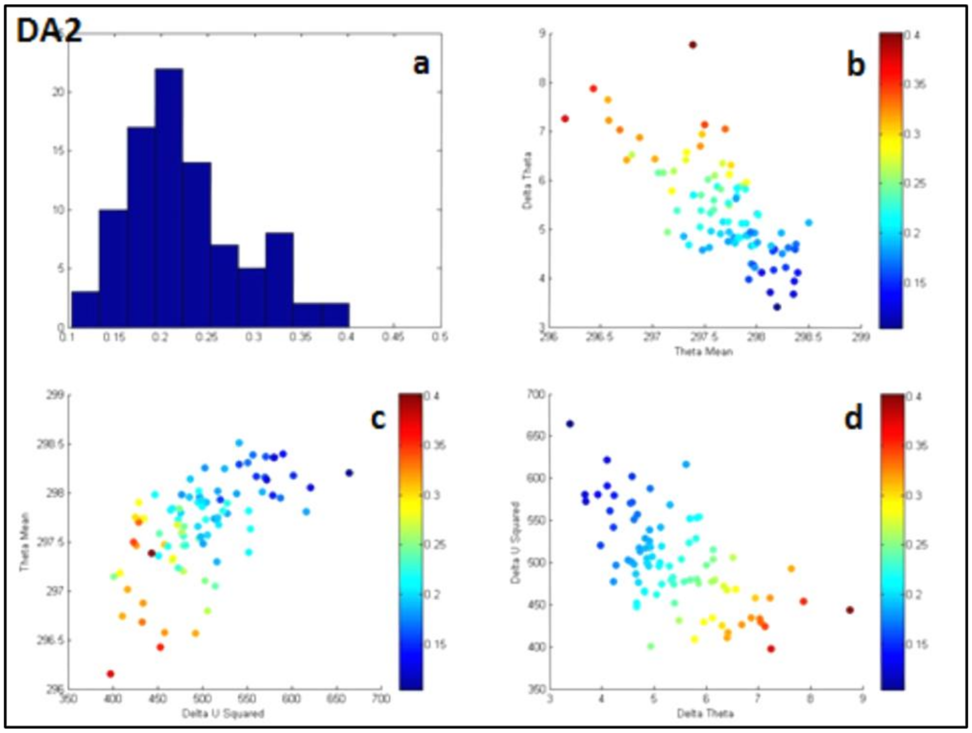

Figure 48. a) Histogram of the forecast metric (J) for DA2 96-member WRF ensemble at 03Z 30 December 2008, b) scatterplot of $\bar{\theta}$ vs. $(\theta_2 - \theta_1)$, c) scatterplot of $(U_2 - U_1)^2$ vs. $\bar{\theta}$, d) $(\theta_2 - \theta_1)$ vs. $(U_2 - U_1)^2$. The magnitude of the forecast metric (J) is shaded in the scatterplots. All plots are valid at 03Z 30 December 2008.

5. DAJ Ensemble Run

The DAJ run has the same temperature observations as assimilated at point 1 in DA1 and point 2 in DA2, but jointly assimilates them into the same run. Overall, the DAJ run resembles very closely the results obtained from the DA1 run. Cross sections from the DAJ run are not shown and the reader is referred to cross sections in section 3 from the DA1 run as the structures are almost identical. The perturbation at point 1 dominates the domain and causes changes to the forecast that are much larger in magnitude than changes caused by the perturbation at point 2, especially in the area in and around the forecast metric J at USAFA. This is due to the perturbation associated with the downstream condition being more linearly related to the downslope winds three hours later. The influence of observation assimilation at point 2 is seen, but mostly upstream over the higher terrain and much smaller than the influences caused by assimilating the temperature observation from the truth run at point1.

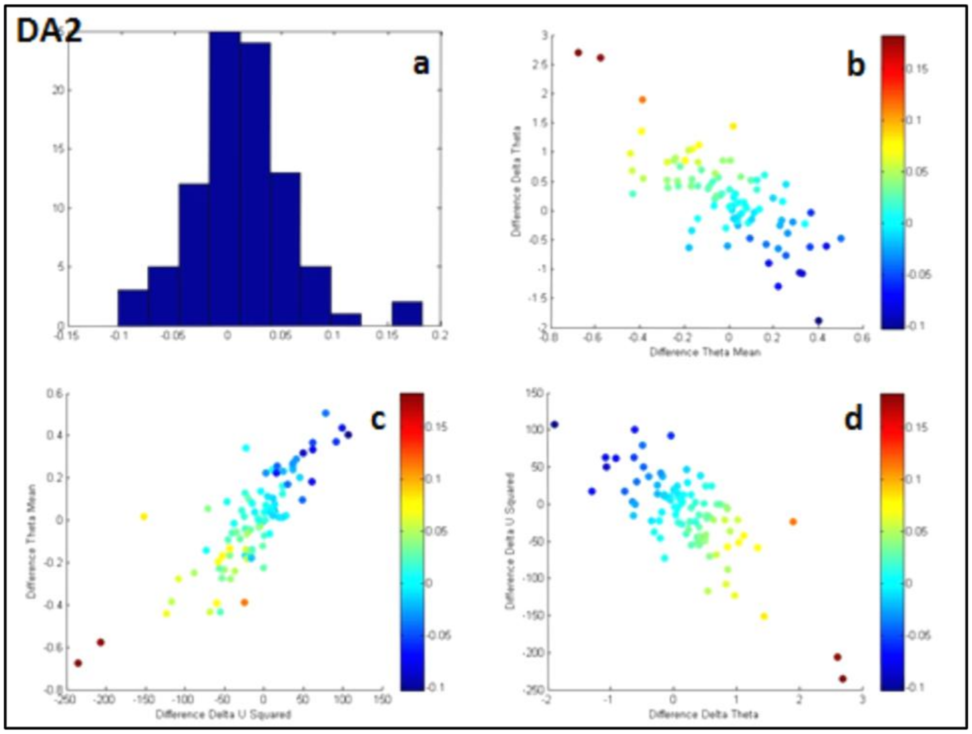

Figure 49. a) Histogram for the difference in the forecast metric (J) between DA2 and NP runs, b) scatterplot of the difference between the DA2 and NP runs for $\bar{\theta}$ vs. $(\theta_2 - \theta_1)$, c) scatterplot of the difference between the DA2 and NP runs for $(U_2 - U_1)^2$ vs. $\bar{\theta}$, d) scatterplot of the difference between the DA2 and NP runs for $(\theta_2 - \theta_1)$ vs. $(U_2 - U_1)^2$. The magnitude of the difference between the DA2 and NP runs for the forecast metric (J) is shaded in the scatterplots. All plots are valid at 03Z 30 December 2008.

As shown in Table 5, DAJ verifies better than DA1 or DA2 as the percent of change between the expected δJ and actual δJ for DAJ is larger for than either DA1 or DA2. This indicates a synergistic effect where the joint assimilation of points 1 and 2 is slightly better than assimilating at any of the single points alone. For the DAJ run, the mean of J decreases as the majority of members move in a negative direction (Figures 50 and 51). This negative shift in J is due increased shear, decreased stability, and increased mean potential temperature. This again shows that J continues to behave in a consistent

Bulk Richardson manner, and a decrease in *J* corresponds to the likelihood of turbulence being increased due to increased shear in the region of the flow separation. The increase in shear is primarily due to a 2.5 m s^{-1} increase in the easterlies in the return flow under the rotor. Additionally, the westerlies and the region of flow separation shift slightly to the east. This causes the ensemble mean in the DAJ run to increase over 5 m s^{-1} in the region just west of the Airfield when compared to the NP run as also seen in the DA1 run (Figure 43).

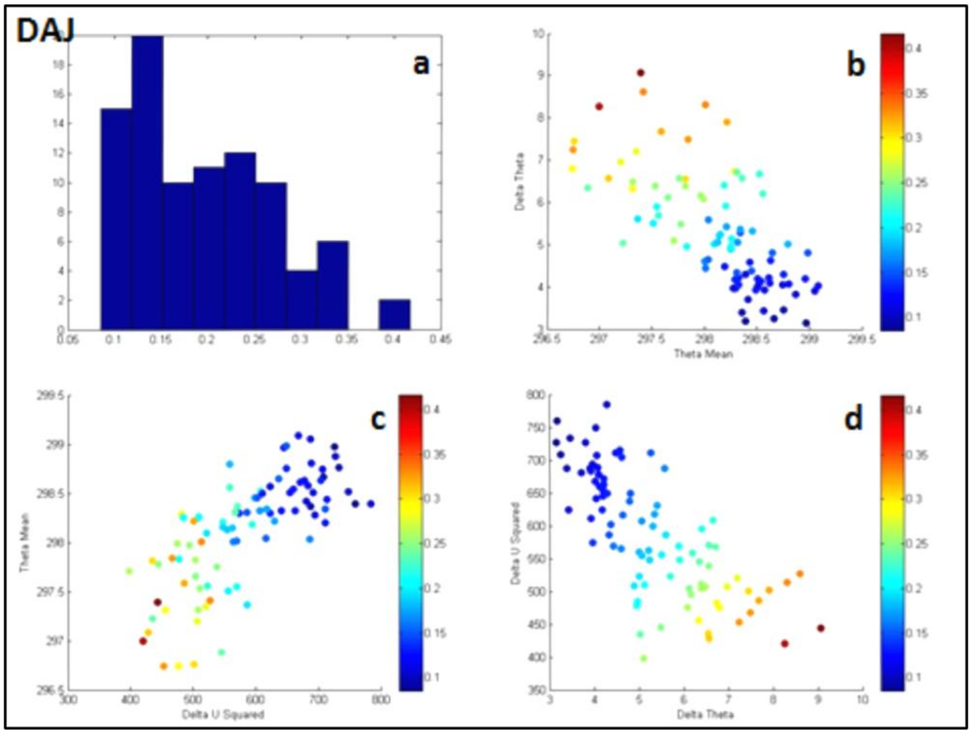

Figure 50. a) Histogram of the forecast metric (J) for DAJ 96-member WRF ensemble at 03Z 30 December 2008, b) scatterplot of $\bar{\theta}$ vs. $(\theta_2 - \theta_1)$, c) scatterplot of $(U_2 - U_1)^2$ vs. $\bar{\theta}$, d) $(\theta_2 - \theta_1)$ vs. $(U_2 - U_1)^2$. The magnitude of the forecast metric (J) is shaded in the scatterplots. All plots are valid for 03Z 30 December 2008.

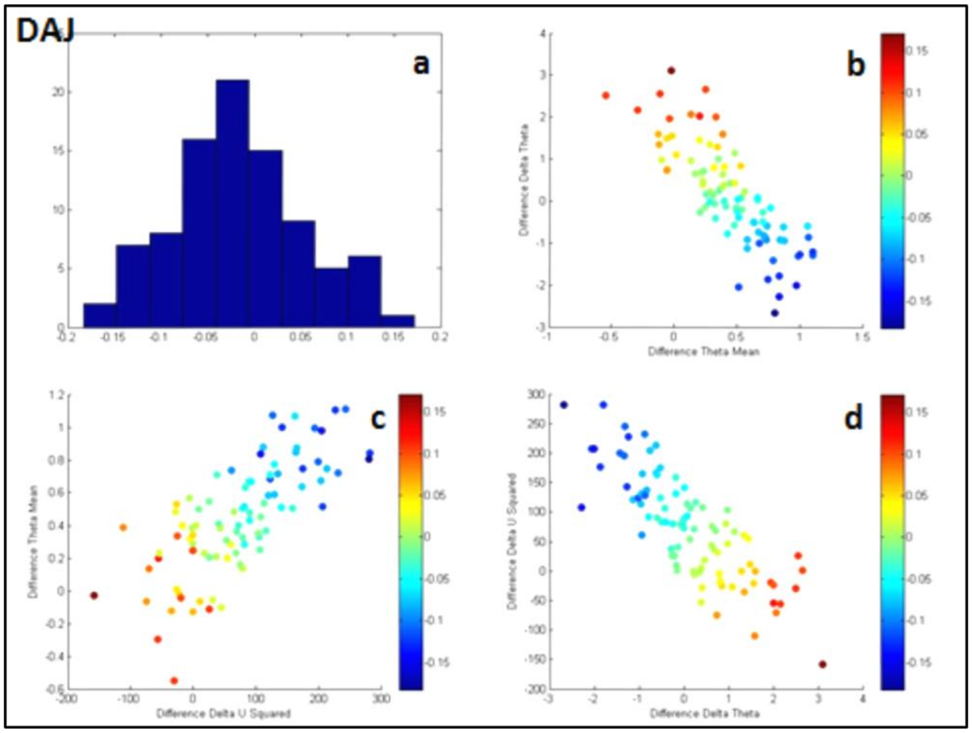

Figure 51. a) Histogram for the difference in the forecast metric (*J*) between DAJ and NP runs, b) scatterplot of the difference between the DAJ and NP runs for $\overline{\theta}$ vs. $(\theta_2 - \theta_1)$, c) scatterplot of the difference between the DAJ and NP runs for $(U_2 - U_1)^2$ vs. $\overline{\theta}$, d) scatterplot of the difference between the DAJ and NP runs for $(\theta_2 - \theta_1)$ vs. $(U_2 - U_1)^2$. The magnitude of the difference between the DAJ and NP runs for the forecast metric (*J*) is shaded in the scatterplots. All plots are valid at 03Z 30 December 2008.

C. PERTURBATION IMPACT BEYOND THREE HOURS

To access the impact each perturbation or data assimilation had on the total energy of the inner-most domain, a calculation of the change in the dry total energy is performed for each ensemble run using the ensemble mean. The purpose of this calculation is to access the impact of the perturbation beyond the three hour point and to gauge the length of time ESA may be useful in our DSWS scenario. The dry total energy is defined according to Zou et al. (1997) and Kim and Jung (2009) as

$$E_d = \int_\sigma \int_x \int_y \frac{1}{2}\left[(u^{'} + v^{'} + w^{'})^2 + \left(\frac{g}{\overline{N}\overline{\theta}} \right)^2 \theta^{'2} + \left(\frac{1}{\overline{\rho} c_s} \right)^2 p^{'2} \right] dy\, dx\, d\sigma, \qquad 4.1$$

where E_d is the total dry energy, $u^{'}$, $v^{'}$, $w^{'}$ are the are the zonal, meridional, and vertical wind perturbations, respectively; $\theta^{'}$ is the potential temperature perturbation; $p^{'}$ is the pressure perturbation; $\bar{N}$, $\bar{\theta}$, $\bar{\rho}$, and c_s are Brunt–Vaisala frequency, potential temperature, density, and speed of sound, respectively, at the sea level; and x, y, and σ denote zonal, meridional, and vertical coordinate, respectively. Results from this calculation are shown in Figures 52, 53, and 54.

Figure 52 shows the evolution of total energy for each perturbed ensemble run for the entire inner domain (domain 3) by forecast hour. Both kinetic and potential energy increase in all ensemble runs for the first three hours and then decrease rapidly. The increases for the first three hours are noteworthy, as perturbations that are introduced are designed utilizing ESA to impact the forecast at 03Z. This result may be coincidental, but is worth noting for testing in future experiments where the perturbation could be introduced to affect forecast metrics at later forecast hours. These plots also reveal that the full data assimilation (DA1, DA2, and DAJ) introduce perturbations that cause the total energy to be approximately an order of magnitude higher. This is most likely due to the larger δx introduced by the assimilation process as compared to the perturbation method.

Figure 52 also reveals that the perturbations introduced at the upstream point (point 2) impact the total energy perturbation longer than the perturbations introduced at the downstream (point 1). Even though the initial total energy perturbation is smaller in runs perturbed at point 2, the decay in perturbation energy is slower for runs P2 and DA2 when compared to P1 and DA1. Point 2 is the upstream perturbation and changes upstream would take longer to propagate out of the domain. This is also seen in Figures 53 and 54. Figure 53 divides the inner domain into two parts, east and west, and shows the total energy perturbation in these two regions. The west calculation is the western three-fifths of domain 3 or roughly the mountainous portion of the domain. The east calculation is the eastern two-fifths of the domain or roughly the plains portion of the domain. Despite the eastern portion being one-fifth smaller, the total energy perturbation over the plains is larger for all runs, again indicating the larger impact of perturbations for the easterly point 1.

Figure 54 is the total energy perturbation for a 40 x 40 grid point box from the innermost domain centered over USAFA. The forecast metric *J*, that each of the perturbations are designed to impact at the three hour forecast, is centered in this box. These plots remain consistent with the previous discussion showing that the DA runs have a larger energy perturbation and the perturbations introduced at point 2 impact the energy perturbation for a longer period of time. The upstream perturbations (P2 and DA2) have a much longer impact in this calculation than any of the others presented. In fact, the energy perturbations remain larger than the initial condition perturbations for nine hours and don't start to precipitously drop off until after 12 hours into the forecast.

The total energy perturbation in the east for P2 (Figure 53) and the APE perturbation over USAFA for P2 (Figure 54) increases from the 15 to 18 hour forecast. This signifies a potential impact to the forecast out to 18 hours. This suggests that carefully selected and targeted observations when assimilated into the analysis can impact the ensemble mean forecast for at least 12 hours. The sharp drop after 12 hours may indicate a lack of impact beyond this point. However, a sharp cold front with a strong synoptic signal begins to impact the forecast region at this time. Although very strong and intense, the DSWS is a mesoscale feature with relatively small spatial and temporal scales. The cold front, supported by an upper-level trough and jet stream, represents a much larger spatial and temporal scale that dominates the smaller scales. This cold front is a dramatic regime shift and one expects convergence of all ensembles from a westerly DSWS regime into a synoptic cold frontal pattern no matter how big the perturbations that are introduced, or how strong the DSWS.

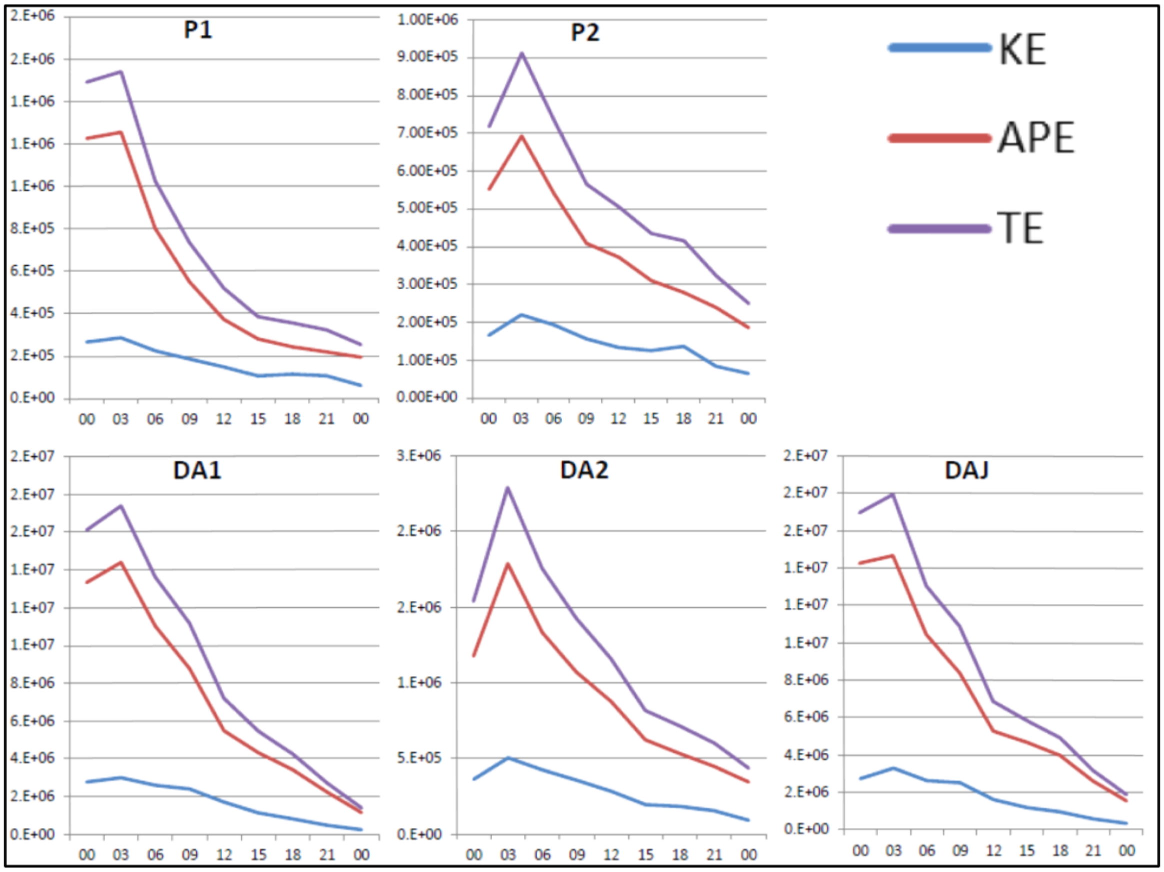

Figure 52. Kinetic, available potential, and total energy perturbation for domain 3 by forecast hour for each ensemble run from 00Z 30 December to 00Z 31 December 2008. Units for the vertical axis are Joules. The y-axis scales are different for each plot.

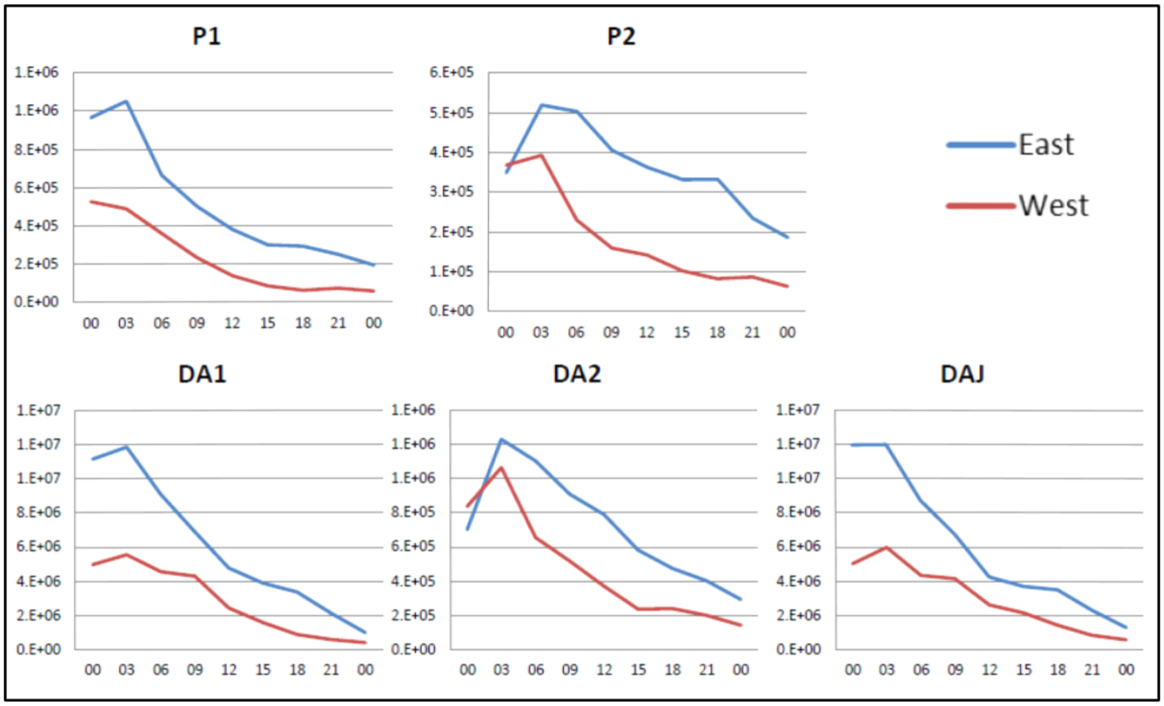

Figure 53. Total energy perturbation for domain 3 divided into the western and eastern portions of the domain by forecast hour for each ensemble run from 00Z 30 December to 00Z 31 December 2008. Units for the vertical axis are Joules. The y-axis scales are different for each plot.

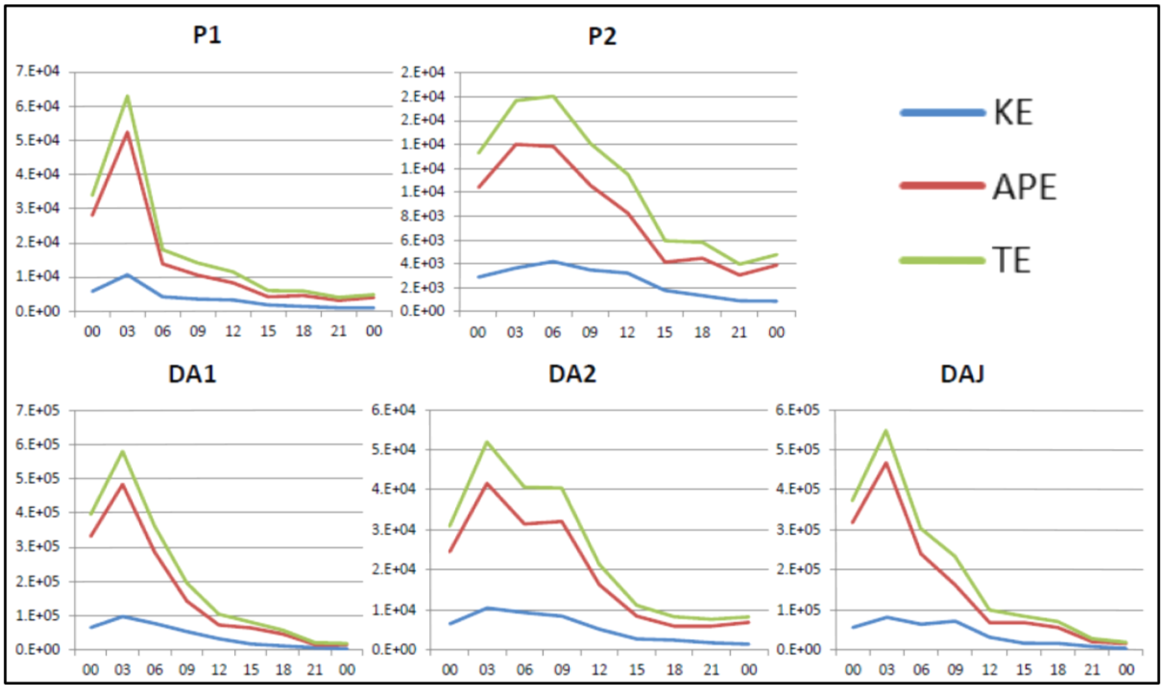

Figure 54. Kinetic, available potential, and total energy perturbation for a 40 grid point by 40 grid point box centered over USAFA from domain 3 by forecast hour for each ensemble run from 00Z 30 December to 00Z 31 December 2008. Units for the vertical axis are joules. The y-axis scales are different for each plot.

D. METHOD FOR TESTING LINEARITY WITH FEWER MEMBERS

The method used in this research for testing sensitivity involves: 1) creating and running a control ensemble run with 96 members (NP run); 2) performing an ESA calculation to select perturbation points; 3) perturbing the initial conditions and then re-running the entire ensemble (96 members) to determine if the change in the initial conditions ESA predicted actually changed the forecast metric in the same manner. This is sometimes referred to as a linearity test. This entire process is very time consuming and expensive. A method is tested to try and simplify this process and identify more quickly if a perturbation at a particular location will impact the forecast as predicted by ESA or not. The results obtained from the full method discussed in previous sections are used to verify if the same information can be gained by running just a few members rather than all 96 members in step 3 of this process. If a method is devised to test the potential impact of perturbation points, then more points can be tested in a timely and cheaper fashion and only points that impact the forecast can be used for assimilation (G. Hakim, personal communication, December 14, 2012).

The method tested involves rank ordering the *J* forecast metric by the member closest to the ensemble mean to the member farthest from the ensemble mean. This is done for the NP run at the forecast valid time for *J* (03Z). This allows us to identify which members are closest to the mean in terms of the forecast metric *J*. Once the rank order of the members is identified, this same rank order of the members is applied to each of the perturbation runs (P1, P2, DA1, DA2, DAJ) and the difference between the ensemble mean for the perturbation run and each individual member is calculated with members remaining in the original rank order. This difference is then summed and averaged for ensemble sizes of 1, 2, 3…etc., through 96 in the rank order previously determined. This calculation reproduces what the ensemble mean would be if a smaller number of ensembles members were used to test linearity. This calculation is shown graphically in Figure 55. The results from the DAJ run are omitted as they are almost identical to the DA1 results.

Figure 55 shows that a substantial number of members are needed for the ensemble mean of smaller sets of members to approximate the mean value of *J* for all 96 members in terms of the magnitude of change for the perturbed runs. The approximate magnitude of *J* for 96 members, starts to occur at around 60 members for the P1, DA1, and DAJ runs and doesn’t occur until greater than 80 members for the P2 and DA2 runs. This result suggests that for the phenomena modeled and the *J* chosen, it is difficult to capture the magnitude of the sensitivity of *J* in a perturbed run with significantly fewer members.

However, the direction of change (positive or negative) of the entire ensemble mean is predicted with far fewer members. The P1, DA1, and DAJ runs correctly predict the direction of change with as few as three members. The P2 and DA2 runs correctly predict the right direction with fewer than three members, but then predict the wrong direction until an ensemble of approximately 20 members is obtained. It is also important to note that P2 performed the worst in terms of the linearity tests of all the ESA results (see overview to this chapter) and would be the most likely perturbation point to discard and replace with another. These results suggest that although smaller number of ensemble members may not be useful in predicting the final magnitude of the change in *J* for the entire ensemble run, as few as three members may give insight to the final direction of change for the entire set. This may be useful in future work, allowing only a few hours to be spent testing potential perturbation points to determine if the forecast metric moves in the correct direction rather than days to weeks running the entire ensemble. If the forecast metric moves in the wrong direction, results from this method suggest that a new perturbation point might be a wiser choice before perturbing and running the full ensemble.

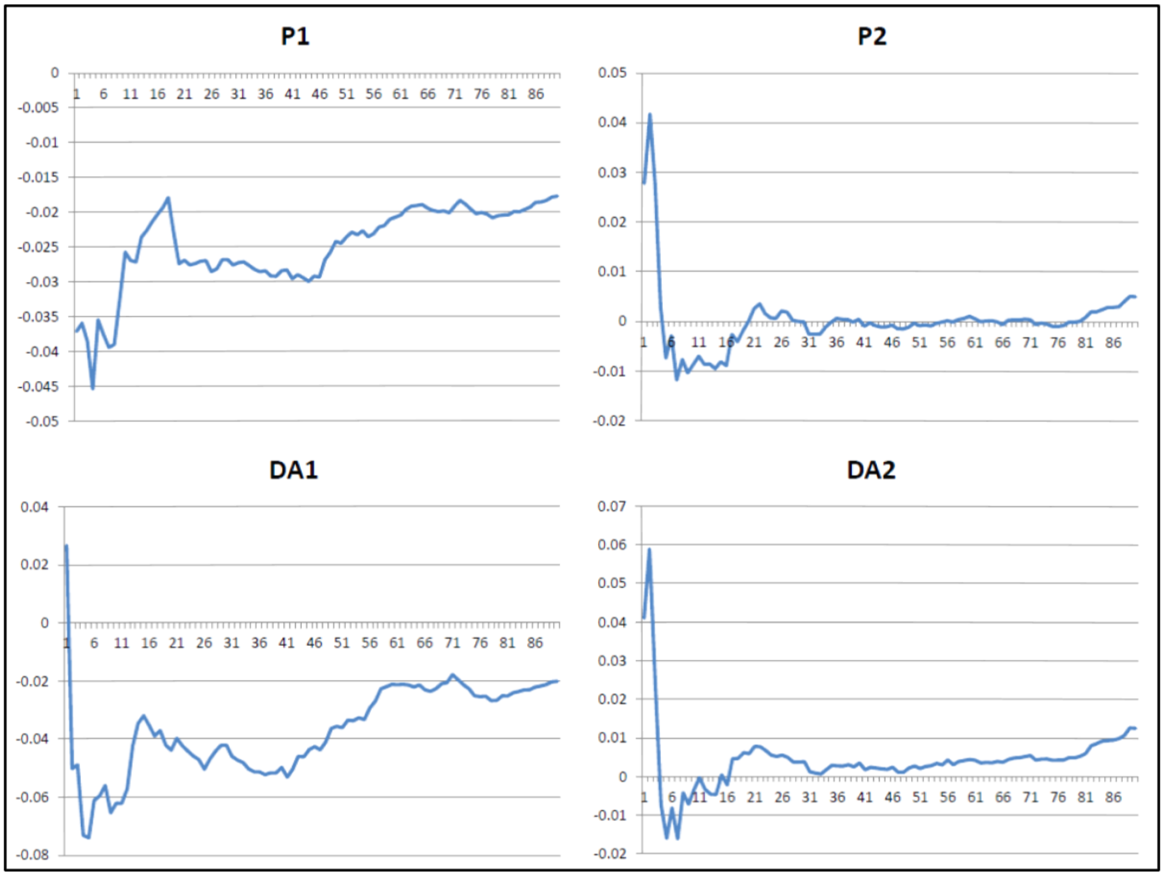

Figure 55. Summed differences of the forecast metric *J* between ensemble runs and the NP run (y-axis) for ranked ensemble sizes 1–90 (x-axis).

THIS PAGE INTENTIONALLY LEFT BLANK

V. OBSERVATIONAL, MODELING, AND FREQUENCY ANALYSIS OF FOURTEEN SEVERE DOWNSLOPE WINDSTORMS AT USAFA

A. OVERVIEW

Despite much research into the initiation and causes of severe DSWS over many decades, much of the theory is still based upon idealized terrain and two-dimensional simulations. While idealized two-dimensional simulations give great insight into what atmospheric parameters play a role in the development of these storms, they lack full explanations of how these theoretical principles play out in more realistic complex three-dimensional flows. The goal of the work done in this chapter is to determine whether the conditions and atmospheric features that caused the severe DSWS on 30 December 2008, and evaluated using ESA, are unique or not when put in context of other DSWS. The research aims to model, analyze, and classify the strongest DSWS recorded by the HWAS sensors at USAFA. This helps determine which of the downslope initiation factors hypothesized in the literature are most important at this location, which classification of storms are the strongest, and which have winds that propagate the farthest from the lee of the mountain slope.

B. BACKGROUND

An in-depth review of downslope winds, and overview of the historical research, is given in Chapter II. Durran (2003) summarizes and states that, “Significant downslope winds have been observed to develop in three basic situations: (1) when a standing mountain wave in a deep cross-mountain flow achieves sufficient amplitude to overturn and breakdown at some level in the troposphere, (2) when standing mountain waves break and dissipate at a critical level in a shallow cross-mountain flow, and (3) when there is sufficient static stability near mountain-top level in the cross-mountain flow to create high downslope winds even without wave breaking.” For the purposes of this research, type 1 from above will be referred to as wave breaking (WB). Type 2 events are most common during a bora and are not examined, as they are not found to be responsible for the strongest DSWS at USAFA. Type 3 storms, or the non-breaking cases, often occur when there is a strong stable layer near mountaintop level, below a much deeper layer of relatively weak upper-tropospheric stability (Durran 1986). These non-breaking, stability layered, less vertical type 3 cases are referred to as non-wave breaking (NWB) for this research.

Prototypical examples of vertically propagating breaking waves and stability layered non-breaking trapped waves are given in Durran 2003 for idealized isolated terrain and a two-dimensional model. The strong downslope wind caused by a vertically propagating breaking wave is characterized by a positive horizontal velocity perturbation of greater than 18 m s^{-1} (Figure 5 Durran 2003) and a maximum surface wind speed of greater than 28 m s^{-1} is noted. The prototypical example of a non-breaking trapped wave (Figure 6 Durran 2003) shows non-breaking waves lead to strong winds, but significantly weaker winds than the wave breaking case, with the positive horizontal velocity perturbation of only 12 m s^{-1} for this simulation along the lee slope.

These idealized cases have led to the popular notion that the strongest DSWS are almost always associated with vertically propagating wave breaking events. Evidence can be found in educational tools such as the popular COMET modules produced by University Corporation for Atmospheric Research (UCAR). The COMET module entitled “Mountain Waves and Downslope Winds,” states that strong downslope wind cases are usually associated with waves breaking aloft and that the strongest downslope winds develop directly beneath the region of flow reversal at the critical level in mature vertically propagating waves (METED/COMET cited 2013). While it is true that vertically propagating waves with a critical level and wave breaking often produce strong winds, the research presented in this chapter suggests that in the highly irregular and three-dimensional terrain upstream of USAFA, the strongest events recorded by the HWAS sensors are NWB. Winds from these NWB events on average extend farther to the east and away from the lee slope than vertically propagating WB events.

C. DATA AND METHODOLOGY

The severe DSWS that occurred on 30 December 2008 at USAFA, that is modeled and studied by the WRF ensemble runs for the ESA research presented in previous chapters, is the strongest and has the largest extent of strong winds ever recorded by the HWAS network. As noted in Chapter III, this storm is caused by a NWB trapped wave upstream of the Front Range over the higher terrain of the central Colorado Rockies. To understand, whether or not this type of NWB event is commonplace at USAFA, thirteen additional severe DSWS are identified using the HWAS database and deterministically modeled using WRF. The fourteen storms in total are chosen based upon the strongest winds observed at the various HWAS sensors. In some cases severe winds are observed, but only at a handful of sensors.

Date	# of HWAS Severe	Max Gust Rampart (kt)	Max Gust Community Center (kt)	Max Gust Airfield (kt)	Max Gust Pine Creek (kt)	Strength Score	Type	Upstream Wavelength (km)	Max Wind Model (kt)
3/6/2004	6	73	58	45	41	217	NWB	48.78	82
11/3/2005	12	71	70	63	63	267	NWB	42.74	74
4/15/2006	9	73	69	62	46	250	WB	26.25	74
6/7/2007	11	60	63	58	51	232	WB	15.50	66
10/2/2007	4	68	63	34	37	202	WB	34.13	47
1/5/2008	11	74	65	54	57	250	WB	26.25	74
12/18-19/2008	5	72	57	47	41	217	WB	26.25	74
12/30/2008	12	79	68	64	57	268	NWB	26.18	62
12/20/2010	10	62	56	57	53	228	NWB	42.74	66
11/12/2011	10	68	68	60	52	248	NWB	26.25	66
11/13/2011	4	77	52	49	43	221	WB	16.26	86
1/19/2012	10	73	66	53	54	246	NWB	48.78	82
2/21/2012	7	61	60	60	37	218	WB	14.84	54
2/23/2012	11	66	60	60	51	237	WB	42.74	78

Table 7. Table summarizing fourteen severe DSWS analyzed and modeled at USAFA. Six non-wave breaking (NWB) and eight wave breaking (WB) storms are shown.

Table 7 includes a list of these fourteen severe DSWS, and parameters describing these storms. In total, only two storms have ever produced severe winds at all twleve HWAS sensors and only eight storms have been observed at 10 or more sensors. Each

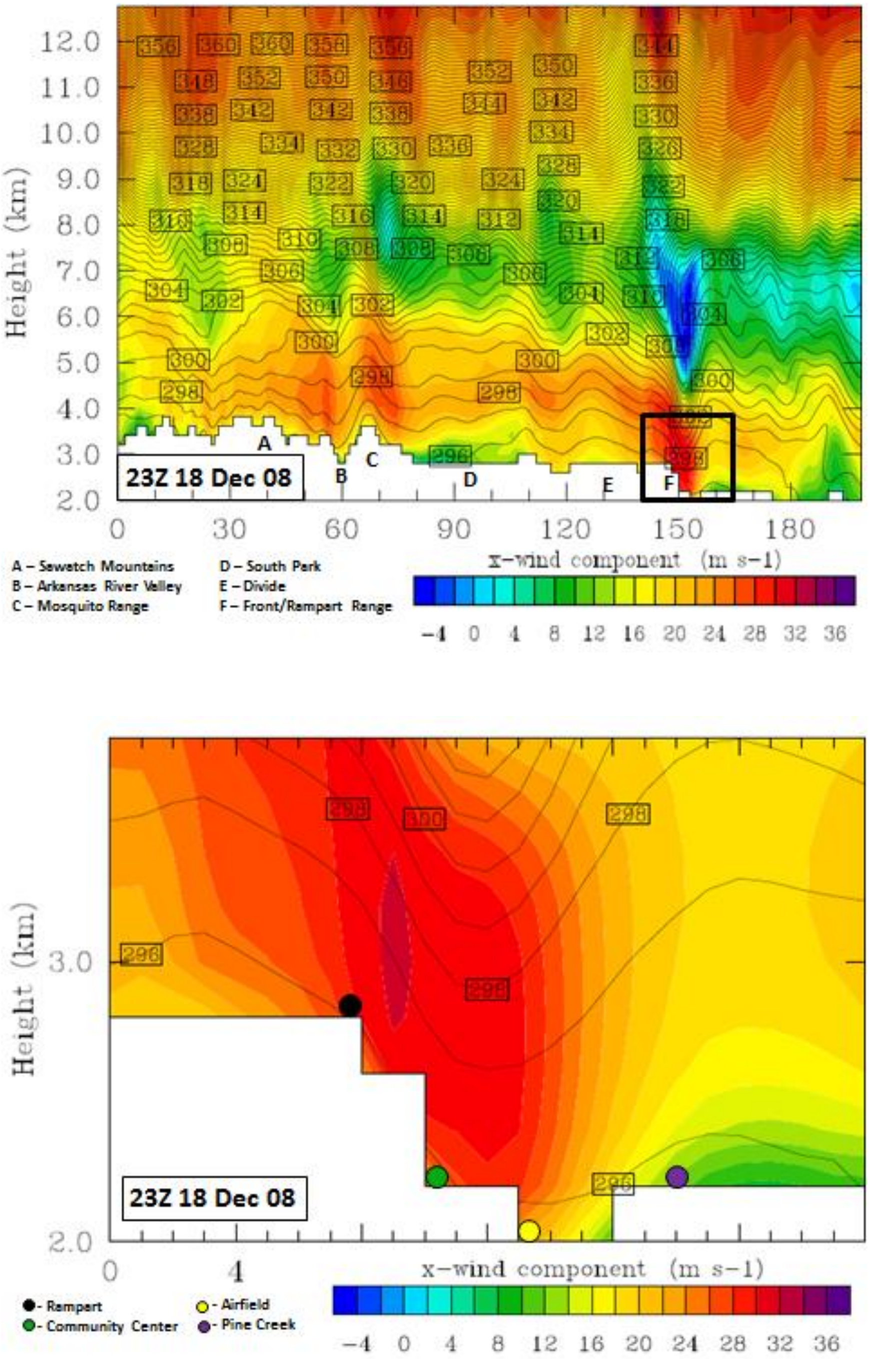

Figure 56. Cross section of *x*-wind component (shaded) and potential temperature (contoured) from west to east across Colorado (top) at the gridline of the Rampart sensor from the WRF deterministic run valid 23Z 18 December 2008. The black box indicates the area shown in the cross section in the bottom part of the figure. The horizontal axis is scaled to the number of grid points from the innermost domain with a resolution of 1.33 km. Approximate locations of four HWAS sensors are marked by circles.

of these eight storms are included in the set, as well as six other storms notable for their extreme winds at one or more of the HWAS sensors.

Single deterministic WRF-ARW runs are performed for each of these severe DSWS. The truth run from the 30 December 2008 storm is selected as the model of choice for that event. The configuration of the truth run (domains, resolution, physics packages, etc.) is used for the deterministic WRF runs (c.f. Chapter III, Figure 20, Table 1). The forecast is output at one hour intervals. Cross sections of *x*-wind component and potential temperature are plotted for each event at every forecast hour along the solid black line given in Figure 16. In addition, a subdomain is plotted at each forecast hour, showing more detail in the area given by the black box in Figure 56. Each event is analyzed hour by hour to determine the forecast time when the model predicts the strongest *x*-wind component in this box. The time and speed of the forecast maximum winds around USAFA is recorded. The speed of the maximum wind for each event as recorded by HWAS at the Rampart, Community Center, Airfield, and Pine Creek sensors, and forecast by the model in the zoomed in cross sections is given in Table 7.

These cross sections are analyzed and each storm is classified into one of two general categories: non-wave breaking (NWB) or wave breaking (WB) events. The primary criteria used to determine storm category is the existence of middle to upper-tropospheric self-induced critical layers, as evidenced by easterlies or negative *x*-wind components in the cross sections. If a self-induced critical layer is evident, suggesting a vertically propagating wave with wave-breaking, then the storm is categorized as wave breaking (WB). If no self-induced critical layer is found, then the storm is categorized as non-wave breaking (NWB). The categorization of each storm is given in Table 7. Six of the storms were categorized as non-wave breaking and eight of the storms were categorized as wave-breaking. As discussed, the most notable non-wave breaking storm was the 30 December 2008 event, used for the ESA portion of this research and depicted by the truth run shown in Appendix B. An example of a wave breaking storm is shown in Figure 56 and cross sections at the time of maximum winds are given in Appendix C.

The criterion used to identify NWB events is the lack of evidence in the model of a self-induced critical level. While the non-existence of a vertically propagating breaking wave does not automatically determine that a trapped wave exists, evidence suggests that the majority of the non-wave breaking events studied for this research, exhibit trapped behavior or properties. Note that the term “trapped” used here refers to trapping of wave energy upstream of the lee slopes and location of the severe DSWS, not trapped waves in the lee of the terrain. Trapped lee waves, rotor, flow separation, and flow reversal at the surface under the rotor are observed and suggested by both the surface HWAS data and the model simulations downstream of the Front Range for a period of time in almost every event, but are not used as a criteria for determining the type of storm causing the downslope winds.

D. RESULTS

1. Strength Score Analysis

A strength score is developed for downslope winds observed at USAFA. This score is the sum of the peak wind gusts observed during each storm by the Rampart, Community Center, Airfield, and Pine Creek HWAS sensors. These sensors are chosen as they are all roughly at the same latitude and extend in a line from west to east allowing for the assessment of the strength and distance from the lee slope the strong winds propagate. The exact location of these sensors is given in Figure 63 and Table 8 in Appendix A. The maximum gust values for each storm, at each sensor, and the summed strength score is given in Table 7.

The strength score reveals that the strongest winds recorded at each of these four sensors all occurred during a trapped event. The highest recorded gusts at the Rampart and Airfield sensors (79 and 64 kt) occurred during the 30 December 2008 NWB event and the highest recorded gusts at the Community Center and Pine Creek sensors (70 and 63 kt) occurred during the 03 November 2005 NWB event. These two events rank a close first and second in overall strength score with values of 268 and 267, respectively. Note that these two NWB events are the only two DSWS to record severe wind gusts (greater than 50 kt) at all twelve HWAS sensors. Overall, four of the highest six strength scores are produced by NWB events rather than vertically propagating WB events. In addition, the average strength score for NWB events is much higher than vertically propagating WB events with a score of 246 compared to 228.

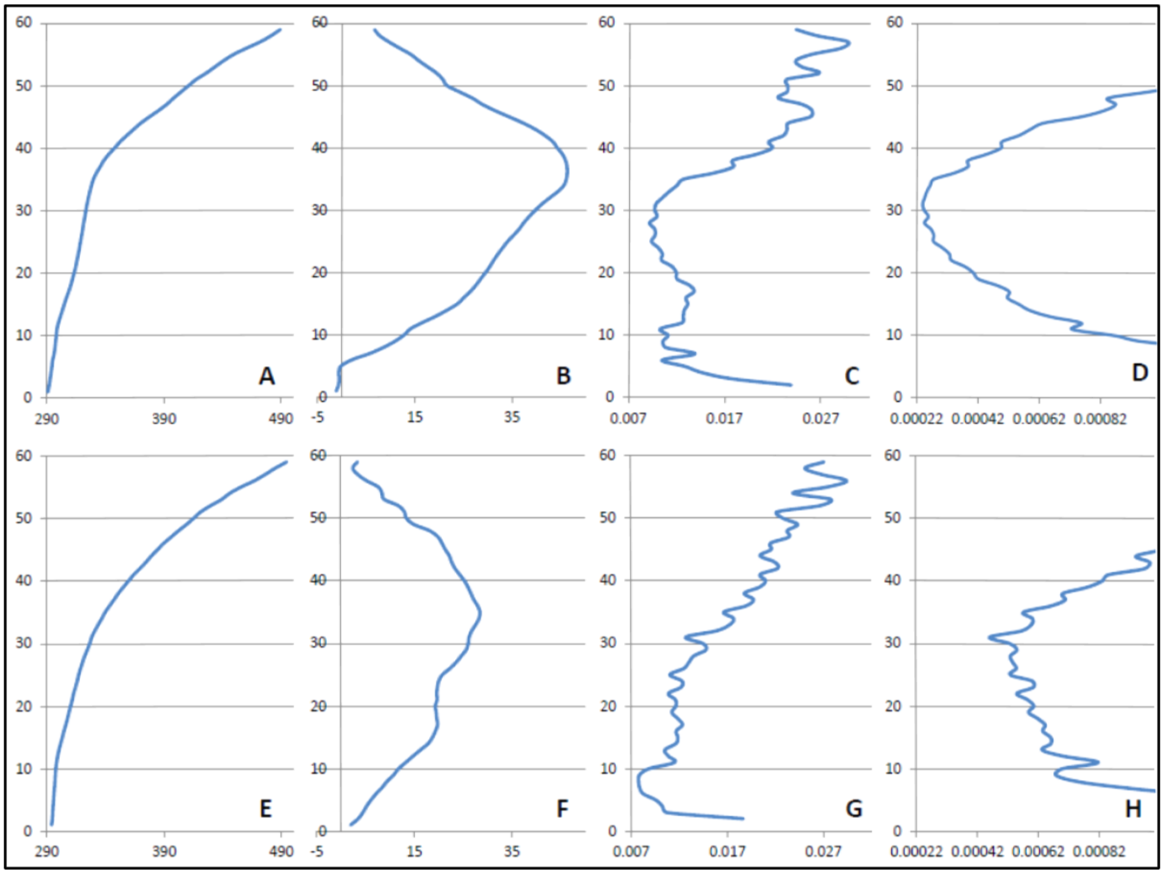

Figure 57. Composite vertical soundings by model level at Grand Junction, CO for all non-breaking events (top) and breaking events (bottom). Valid three hours prior to strongest winds at USAFA. Shown is Potential temperature (K) in plots a and e, *x*-wind component (m s^{-1}) in plots b and f, Brunt-Väisälä frequency in plots c and g, and Scorer parameter in plots d and h.

2. Composite Upstream Soundings

Composite soundings of all NWB and WB events are calculated at the upstream sounding location of Grand Junction and are shown in Figure 57. Composite soundings are valid three hours prior to the time of the strongest modeled winds at USAFA. These soundings show that NWB events are characterized by stability layering as revealed by potential temperature and the Brunt-Väisälä frequency. In the NWB composites, a stable layer is present as revealed by a relative maximum of Brunt-Väisälä frequency at model levels 12 to 18, which corresponds to an altitude of about 3500 – 5500 m MSL. In addition, the NWB events have stronger forward shear that inhibits wave breaking due to a much sharper increase in westerly winds with height, with an average maximum wind of 46 m s^{-1} centered at model level 35 (11 km MSL). These factors lead to a strong increase with height of the Scorer parameter in the lower and middle troposphere (Figure 57d) that is commonly associated with trapped waves. In contrast, the WB events have only one pronounced stable layer near the ground, winds that increase much slower with height, and a much weaker wind maximum of only 28 m s^{-1} at model level 34 (10.7 km MSL).

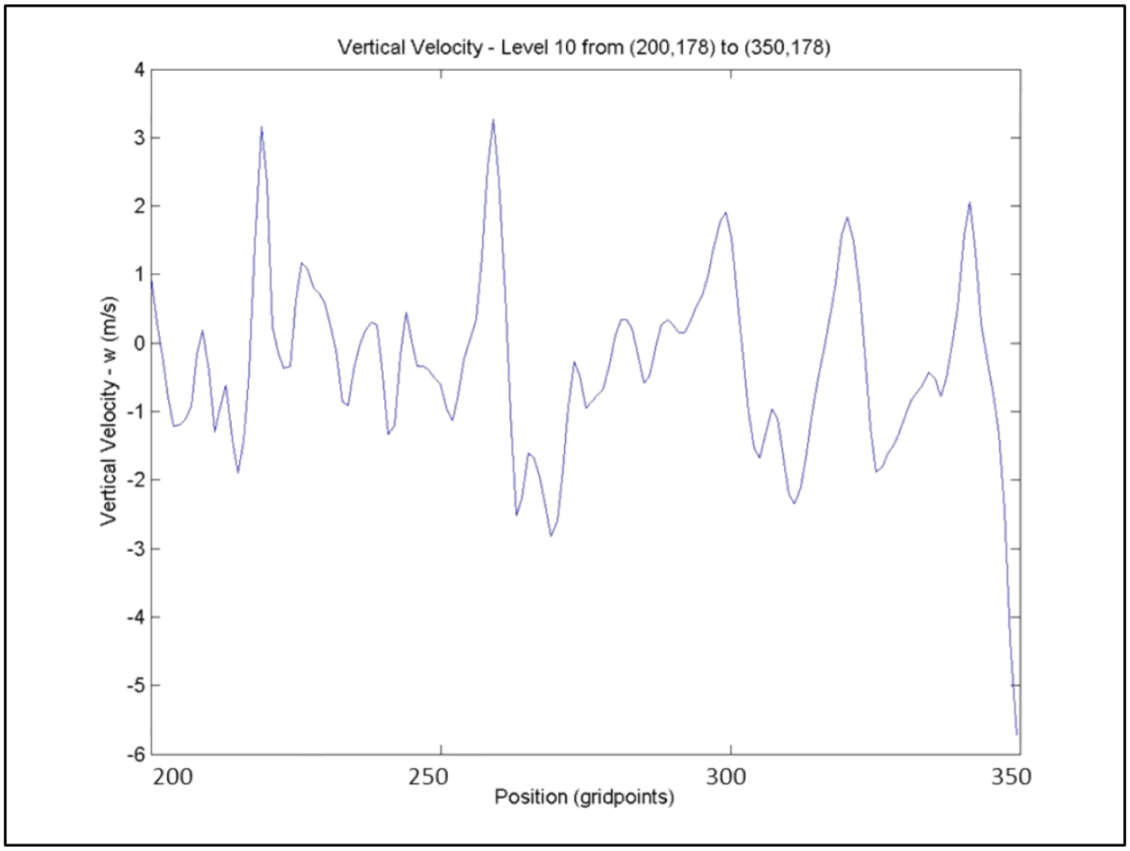

Figure 58. Upstream *z*-wind component at the gridline of the Rampart sensor during time of maximum winds at USAFA from model level 10 for the truth run valid 12Z December 2008.

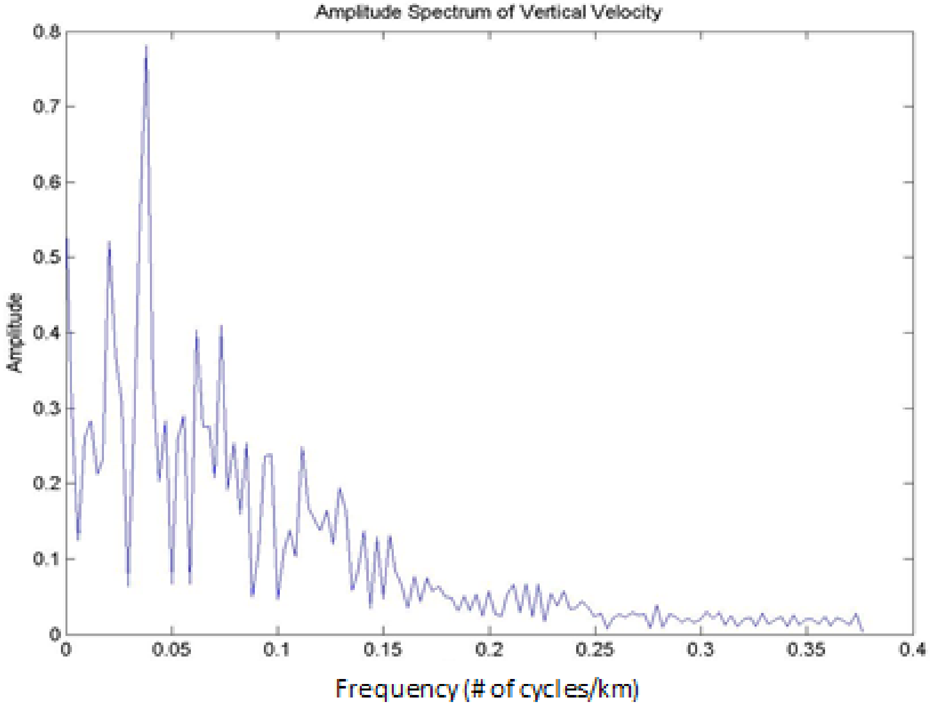

Figure 59. Frequency spectrum of upstream *z*-wind component during time of maximum winds at USAFA from model level 10 for the truth run valid 12Z December 2008.

3. Fourier Analysis

To access the upstream wavelength properties of NWB and WB events, and to compare these results to the dominant upstream terrain frequencies, a Fourier analysis is conducted of the upstream waves and terrain. The purpose of this analysis is to determine what role the wavelength of the terrain has in determining the type of gravity wave causing the DSWS and if wavelength varies between NWB and WB events.

To determine the dominant frequencies and wavelength of the upstream waves, a Fourier analysis of the upstream wave structures is performed on all fourteen wind events, by conducting a Fast Fourier Transform (FFT) of the *z*-wind component at model level 10 (approximately 1400 m AGL) from grid points 200 to 350 of domain 3 at the gridline of Rampart sensor at the hour of maximum winds in the model at USAFA. Since the data varies as a function of distance (km) rather than time, the FFT transforms the data into wave number space, giving frequencies with units of km^{-1} or the number of wave cycles per km. The wavelength with the largest amplitude in the frequency domain is given in Table 7 for each event. The *z*-wind component at the time of maximum winds at USAFA for the trapped event on 30 December 2008 from the truth run is given in Figure 58 and the upstream frequency domain for this event is given in Figure 59.

A Fourier analysis of the upstream terrain height, as resolved by the model, is also conducted by performing a FFT at the gridline of the Rampart sensor and for the same grid points as the wind analysis. A method is used that follows Young and Pielke (1983), where a linear trend is calculated in the terrain by the method of least squares and then subtracted from the terrain height. The resulting series is transformed into wavenumber space using a FFT and frequencies are given as the number of cycles per km. Figure 60 shows a plot of the frequency domain of the upstream terrain. The wavelength of each of the fourteen storms analyzed is depicted on the frequency plot as either a "*" for a NWB event or as a "#" for a WB event. For the strongest severe DSWS there are three distinct modes or frequencies that account for all of these storms, and each of the three modes correspond to dominant frequencies in the terrain spectrum. The three active modes correspond to a wavelength of 42.5 km, 26.2 km, and 14.8 km. The trapped events are confined to the longer two modes, and the vertical events are mostly confined to the shorter two modes.

These results are in contrast to previous work, showing that the wavelength of breaking events at Boulder, Colorado have a longer wavelength than the trapped non-breaking waves downstream (Klemp and Lilly 1975). Analysis here shows that the wavelength of the NWB events causing DSWS is on average longer than the WB events. Figure 61 reinforces this conclusion with the terrain frequency domain plotted against the composite NWB and WB frequency domains. This plot also shows the alignment of the composite NWB storms with the two longer wavelength active terrain modes, and the alignment of the composite WB storms with the two shorter wavelength active terrain modes. This plot also reveals that there are dominant terrain modes such as the one at 114 km that do not correspond to active modes for severe DSWS in the atmosphere.

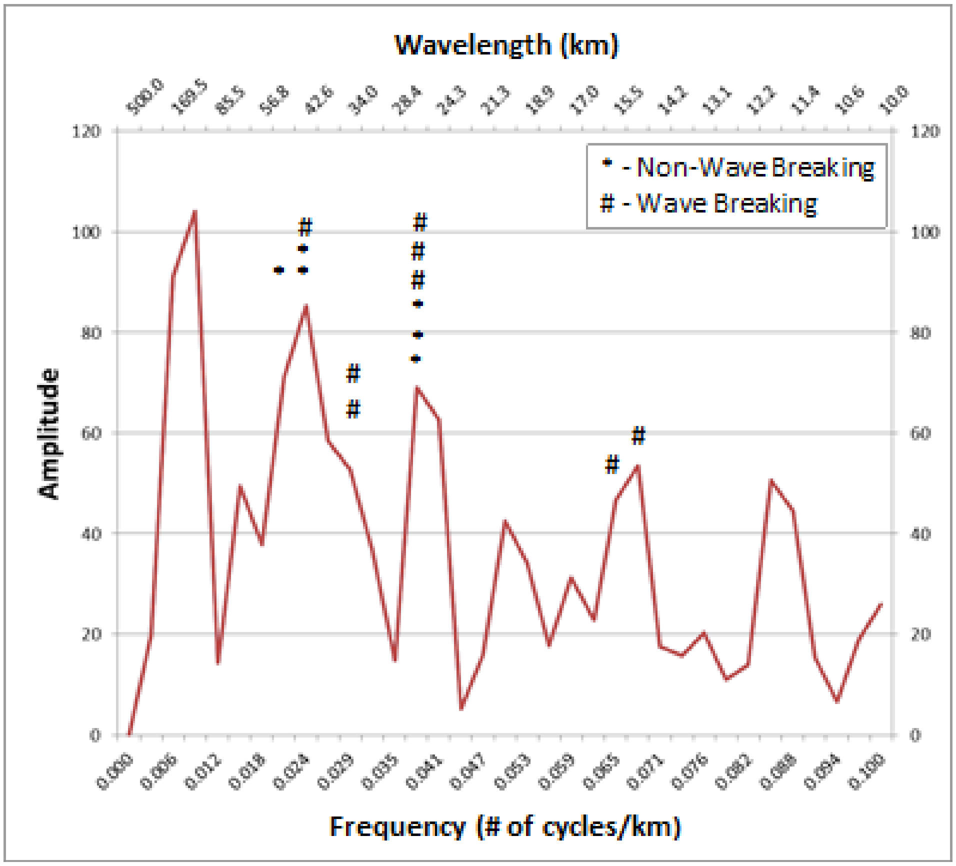

Figure 60. Frequency spectrum of upstream terrain overlaid with wavelength of the fourteen severe DSWS as given in Table 7. A “*” denotes the wavelength of a non-wave breaking event and a “#” denotes the wavelength of a wave breaking event.

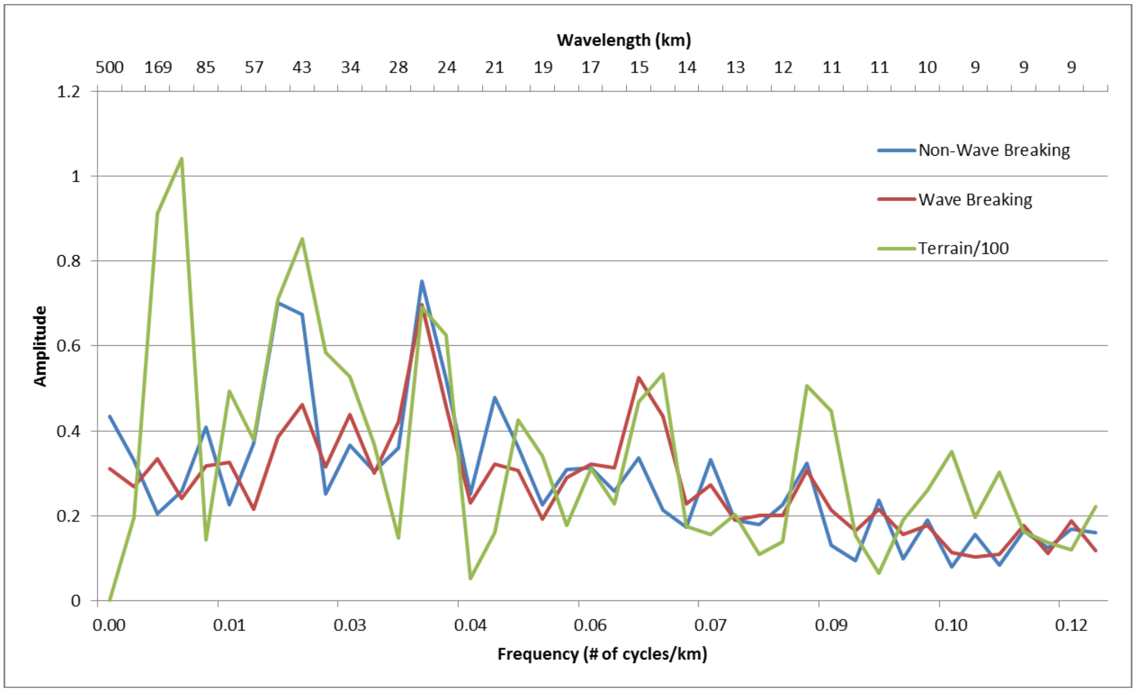

Figure 61. Frequency spectrum of upstream terrain (green) and composite frequency spectrums for the non-wave breaking (blue) and wave breaking (red) severe DSWS.

E. SUMMARY AND DISCUSSION

This chapter shows the strongest DSWS, both in magnitude and eastward propagation away from the mountains, are caused by NWB events far more often than WB events at USAFA. The majority of the NWB events exhibit trapped behavior or properties. This suggests that trapped waves, perturbed by the upstream terrain over central Colorado, propagate downstream across the elevated terrain west of the Rampart Range and play a significant role in the formation of severe DSWS at USAFA. This highlights the theory adopted by many that the strongest DSWS are caused by vertically propagating breaking waves. Much of this theory is derived from two-dimensional regular terrain and idealized simulations. Our research suggests that strong downslope winds in complex terrain may be caused by upstream wave trapping more often than previously thought, and that broader climatological classification studies at more locations may help clarify severe DSWS dynamics.

The 30 December 2008 severe DSWS that was caused by a NWB trapped wave was not only isolated to the irregular terrain around USAFA. As noted in Chapter II, this windstorm was widespread causing more than $7 million in damage in Colorado, making it the fourth most expensive windstorm in Colorado’s history. Cross sections taken from the truth run at Boulder, CO reveal that a NWB trapped wave is also responsible for the high winds and damage at that location which is characterized by more regular terrain and a continuous decent form the Continental Divide to the Eastern Plains. The highest wind gusts recorded in Boulder from this upstream trapped wave were 96 kt (Earth System Research Laboratory, cited 2013). This suggests that extremely strong NWB trapped events may play a more significant role at locations of both irregular and more idealized terrain.

This study highlights the differences in upstream atmospheric soundings that cause these two different types of storms as shown in the composite soundings from Grand Junction. The results from this study and the ability to determine a priori using observed and forecast upstream soundings should aid forecasters at USAFA and similar locations to develop forecast rules of thumbs that distinguish between NWB and WB events. This information can be used to help determine the likely hood that locations away from the base of the mountains will experience extreme threshold events.

The results from the Fourier analysis of these severe DSWS show that only certain wavelengths are excited in the strongest downslope wind events at USAFA. It remains to be seen if only strong events occur at these wavelengths or if weaker events also occur at these excitable modes. The question also remains about whether the terrain forces the atmospheric flow into these preferred wavelengths or if the forcing comes from the atmosphere, such that when certain parameters like stability, wind shear, and tropopause height come together, the atmospheric dynamics alone determine these preferred modes. It is possible that if the dynamics of the atmosphere produce a wave at a mode that is not preferred, when the flow interacts with the terrain, the flow is sheared, or there is destructive interference preventing the most extreme downslope wind events from occurring. A more in-depth analysis of both strong and weak storms could lead to the development of forecast tools based upon verification of NWP forecasts that use the wavelength or frequency as predicted by the model to determine the probability that a strong threshold level event that propagates away from the mountain slope is more likely to occur.

The goal of the analysis presented in this chapter is to determine whether the conditions and atmospheric features that caused the severe DSWS on 30 December 2008, and evaluated using ESA, are unique or not when put in context of other DSWS. The results presented in this chapter link the atmospheric structures found in NWB events to the structures successfully identified by ESA. ESA identified the sensitivity of a NWB DSWS at USAFA to a strong stable layer at model level 13 (2200 m AGL) at both upstream and downstream locations. The vertical profile of the ensemble mean upstream sensitivity location (Figure 26 bottom) is very close in proximity and structure to the composite sounding at Grand Junction, CO, produced from six NWB DSWS (Figure 57). The composite sounding (Figure 62) at the downstream sensitivity location (point 1) from the six NWB events shows a strong stable layer at model level 15 (2800 m AGL) as revealed by potential temperature and Brunt-Väisälä frequency. Results show that ESA successfully identified an atmospheric structure that is common in the majority of the strongest NWB DSWS at USAFA. This suggests that targeting observations at these locations prior to the onset of a non-breaking severe DSWS would impact and potentially improve forecasts of these phenomena in numerical models.

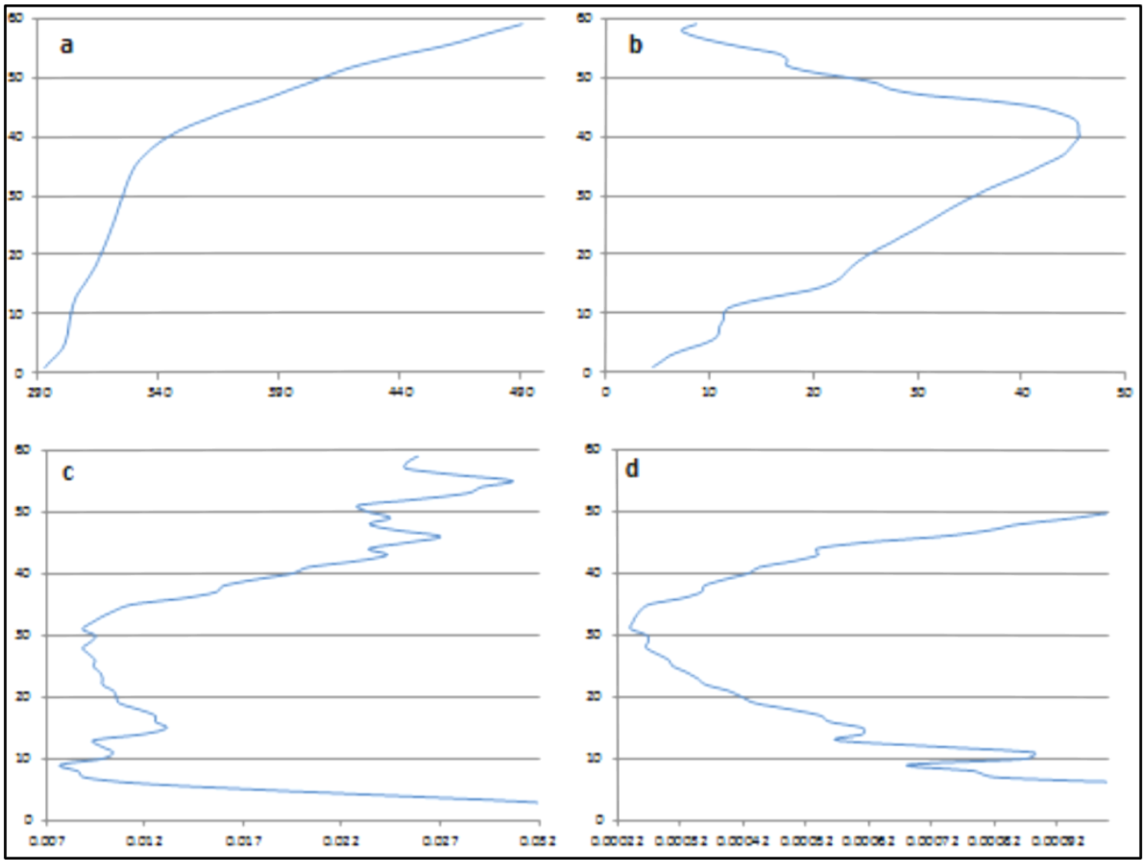

Figure 62. Composite vertical soundings by model level at downstream sensitivity location (point 1) for six non-breaking severe DSWS. Valid three hours prior to strongest winds at USAFA. Shown is a) potential temperature (K), b) *x*-wind component (m s^{-1}), c) Brunt-Väisälä frequency, and d) Scorer parameter.

THIS PAGE INTENTIONALLY LEFT BLANK

VI. CONCLUSIONS AND FUTURE WORK

A. SUMMARY

We present as primary and secondary goals: 1) to determine if a mesoscale ensemble and ESA is a useful analysis tool to determine the sensitivity of severe DSWS in complex terrain to initial conditions and assimilated observations, and 2) to provide context for the ESA case study with analysis of thirteen additional severe DSWS. ESA was utilized to quantify the sensitivity of a severe DSWS with respect to leeside conditioning in contrast to upstream synoptic conditions. This study aimed to determine if sensitivities can be used to reduce forecast uncertainty for a forecast metric utilizing ESA and a targeted network design. This study is motivated by the larger question of whether ESA can be useful tool in fine-scale, highly non-linear, high impact events.

These goals were accomplished by identifying and studying a severe DSWS on 30 December 2008 at USAFA, lee of the Rampart Range, just north of Colorado Springs, Colorado. A mesonet of twelve surface observations known as the High Wind Alert System, or HWAS, was utilized in identifying and understanding the spatial and temporal impacts of this strong severe DSWS that buffeted the local area with wind gusts topping out at 79 kt. A series of over 100 WRF-ARW single deterministic runs were performed to test the time step, vertical resolution, and physics' packages best suited to resolve this and other DSWS at this location. A final WRF configuration was set and used in conjunction with an Observing System Simulation Experiment (OSSE) to create a five day truth run for this event. Boundary conditions and soil conditions were updated every three hours with CFSR data for this truth run.

Next, the WRF ensemble system was created and conditioned by assimilating synthetic observations from the truth run that mimicked a network of rawinsonde and ASOS locations every three hours. An ensemble referred to as the NP run was created with 96 members and run from 00Z 30 December to 00Z 31 December for the duration of this event. Ensemble Sensitivity Analysis was performed with various forecast metrics on the NP run. A forecast metric (*J*) that is a modified Bulk Richardson number was settled upon and two points of strong sensitivity in the initial conditions (one upstream and one downstream) were identified from ESA. Five separate ensemble runs were generated (P1, P2, DA1, DA2, DAJ). The first two (P1 and P2) introduced separately a perturbation of potential temperature from the truth run at the downstream and upstream locations and the perturbation was spread utilizing linear regression of the analysis as sampled by the ensemble. The final three ensemble runs (DA1, DA2, DAJ) were generated by assimilating a temperature observation from the truth run at the downstream location, upstream location, and both locations simultaneously and performing full data assimilation using an Ensemble Kalman filter. The results from these experiments were used to access our research objectives.

B. OUTCOMES AND BROADER IMPLICATIONS

The most important outcomes of this research is demonstration of the utility of ESA and its capability of quantifying severe DSWS sensitivity. In varying degrees, ESA showed skill in identifying regions of initial condition sensitivity to a forecast metric J. Every experiment moved the ensemble mean for J in the correct direction as predicted by the sensitivity (dJ/dx) given in Table 2 and shown in Figure 24. In general, experiments at point 1 (downstream) had a larger actual δJ and impact on the forecast than experiments at point 2 (upstream) for both the perturbation experiment and data assimilation experiment. This was partially due to the larger δx introduced for DA1, and also showed that the perturbation associated with the downstream condition is more linearly related to the downslope winds three hours later.

The P1 ensemble run outperformed the other model runs by moving J over 48% toward the expected value as predicted by the ESA performed on the NP run as shown in Table 5. While the perturbations introduced were very small, even these small perturbations, identified by ESA, impacted the forecast metric J reasonably well showing the strong dependence of mountain waves on the initial conditions. The better performance by DAJ indicated a synergistic effect where the joint assimilation of points 1 and 2 is slightly better than assimilating at any of the single points alone.

Another outcome of this research is demonstrating that ESA can identify physical and dynamical structures in the atmosphere that play a role in the formation of a DSWS. ESA was able to identify traditional upstream sounding parameters, such as the strength of the near mountain top stable layer, as playing a role in the strength and structure of a DSWS. Most importantly, ESA shed new light on the impact of downstream structures, or leeside conditioning, that play a role in the formation of flow separation, leeside rotor, and convergence between the rotor's return flow and the downslope winds. In fact, observation assimilation that adjusted the strength and characteristics of the downstream air mass and stable layers had more impact on the forecast than assimilating upstream observations. Intuitively, this relationship makes sense. While a DSWS can only occur if the upstream terrain, flow characteristics, and forcing is adequate, once a wave is generated, the characteristics of that wave and flow will be modified by the environment it is flowing into. The results suggest that leeside conditioning is important if trying to determine the extent of westerly winds down the slope, the point of flow separation, and the strength, location, and structure of leeside rotors.

Another outcome of this research is highlighting the usefulness of a modified Bulk Richardson number in a less than traditional application. Traditionally, Bulk Richardson numbers are used on scales smaller than studied in this research to classify turbulent vertical motions and buoyancy forces. While there is definitely turbulence and vertical motion in the dynamic DSWS and lee wave rotor scenario, the modified Bulk Richardson number developed for this study proved well suited to capture the relevant physics and structures in the convergence zone between the downslope winds and leeside rotor in the vicinity of the flow separation. The success of ESA in this research can be directly attributed to the Bulk Richardson number being an appropriate metric to sample these features.

The extent to which sensitivities can be used to reduce forecast uncertainty is still unclear. This study showed that sensitivities from ESA certainly can affect the spread of an ensemble as demonstrated by changes in the standard deviation of the distribution. While this shows sensitivity to the initial conditions, it does not necessarily show a reduction in forecast uncertainty. The ensemble runs that verified best in terms of moving

J toward what ESA predicted had an increase in the standard deviation indicating possible increased uncertainty in the forecast. In general, perturbations introduced and observations assimilated upstream decreased the spread of the forecast metric increasing confidence in the forecast. Perturbations introduced or observations assimilated downstream increased the spread of the forecast metric decreasing confidence in the forecast. An explanation is proposed and supported by evidence that shows advection of regions of decreased spread downstream from the assimilation points leading to decreased spread from the upstream point and increased spread from the downstream point.

The modeling, composite, and Fourier analysis performed on fourteen severe DSWS showed that upstream non-breaking waves, that exhibit trapped behavior and properties, play a larger role in severe DSWS at USAFA than previously thought. This study showed that non-breaking waves are responsible for the strongest winds recorded by HWAS and a majority of the strongest DSWS that propagate away from the mountain slope and out over the plains despite the fact that severe wave breaking DSWS occur more frequently. The Fourier analysis revealed that all fourteen severe storms fall into one of three frequency modes that correspond to modes in the upstream terrain. This suggested that either the atmosphere must force itself into one of these wavelengths or the terrain must force the atmosphere into one of these wavelengths in order for the most severe downslope winds to occur at USAFA.

Results from the composite studies of fourteen severe DSWS link the atmospheric structures found in NWB events to the structures successfully identified by ESA. These results show that ESA successfully identified an atmospheric structure that is common in the majority of NWB DSWS at USAFA. This suggests that targeting observations at these locations prior to the onset of a non-breaking severe DSWS would impact and potentially improve forecasts of these phenomena in numerical models.

C. FUTURE WORK

Further study of the topics put forth in this research falls into two main areas: ESA testing and the further investigation into the initial conditions and physical structures that lead to strong DSWS, flow separation, and adjacent lee rotors in realistic complex terrain.

1. ESA Testing

ESA showed skill at identifying initial conditions that affected a forecast metric. However, the length of the forecast in this study was only three hours. Future studies should focus on identifying the length of time ESA is useful for highly mesoscale and complex phenomena. The total energy perturbation analysis performed on the ensemble runs in this study suggested that impacts were made to the forecast for at least 12 hours and 15–18 hours in isolated cases. The length of the impact may have been limited in this study due to an approaching cold front that changed the flow regime. Future studies may benefit from pushing back the initialization time for the ensemble runs in order to not be as close to the end of the downslope event. Doing so would allow for the testing of ESA with longer forecast times. Longer forecast times also may allow for a more complete assessment of the impact of ESA on ensemble spread over time, shedding more light on whether or not sensitivities can be used to reduce forecast uncertainty in an ensemble.

ESA was applied in this study to a non-wave breaking severe DSWS and found to be useful tool. Future research should be conducted utilizing ESA and WB events to determine if the same utility applies. Similar methods and linearity testing should be accomplished to address this unsettled question.

Additional insight utilizing the concepts of ESA could be gained by switching J and x in ESA and doing a reverse regression (G. Hakim, personal communication, December 12, 2012). Instead of calculating dJ/dx, perhaps calculating dx/dJ would add insight into how initial conditions (x) impact a forecast metric J. This would pose the question: if a certain J is wanted, how must x change in order to obtain the desired result? An experiment of this type could allow assessment of whether one sounding at a location is more relevant than ten surface observations in a different location.

2. Initial Condition Impacts on Downslope Windstorms

One of the largest impacts of this study is the assessment that the leeside conditioning plays an important role in the distance DSWS extend down the slope, the presence and location of flow separation, and location and strength of adjacent rotor's return flow. Insight into the role of leeside conditioning could be accomplished using a two-dimensional flow model with idealized terrain. This would allow for easy introduction of various downstream stability and wind profiles, and a fairly straightforward method for evaluating the general impact of the leeside environment. In addition, a study of this type could quantify the distance downstream perturbations to the leeside environment impact upstream downslope winds, flow separation, and rotor formation. Additionally, a study of this type could help determine if leeside conditioning downstream of the slope plays a larger role in determining the strength of a DSWS in non-wave breaking versus wave breaking cases.

Another experiment that could be conducted to assess the impact of assimilating leeside observations would be to assimilate the entire or smaller subset of the HWAS observations into an ensemble during the conditioning period. Ensemble runs at various event lead times and lengths could be run to quantify the impact of the HWAS observations on the forecast. This could be accomplished in conjunction with ESA predictions to access ESA's ability to predict the location of initial condition sensitivity. A study of this type would help quantify a mesonet's impact on modeling and forecast products for high impact events in complex terrain.

Additional investigation into the role of the height and structure of the tropopause on DSWS, flow separation, and leeside rotor formation is needed. Although all perturbations were introduced in the lower troposphere between 3 and 4 km in this study, large changes in the temperature and wind fields were seen at tropopause level. If a change in the lower troposphere caused changes at the tropopause then it is reasonable to assume that sensitivities exist at the tropopause level. Previous studies have noted this sensitivity, but much is left to be explored in this area, and ESA provides a good tool to assess the potential impact of tropopause height and structure on mountain wave phenomena.

Lastly, more research is needed to enhance our understanding of the role of complex terrain upstream of the DSWS location. Most idealized studies in the past introduce unperturbed flow upstream of regularly shaped terrain. In reality, flow is rarely unperturbed when it arrives in Colorado due to the multiple upstream mountain ranges in the intermountain west. Studies should be conducted that determine the wavelength or frequency of perturbed flow before it encounters the Rocky Mountains and how those frequencies relate to the frequencies of highest amplitude found by the Fourier Analysis in this study. It may be found that perturbations or waves already inherent in the upstream flow play an important role in determining the type and strength of DSWS in the lee of the Rocky Mountains and similar locations with multiple upstream mountain ranges.

THIS PAGE INTENTIONALLY LEFT BLANK

APPENDIX A

A. USAFA GEOGRAPHY

Appendix A follows Homan (2007).

USAFA lies at the base of the eastern slopes of the Front Range of the Rocky Mountains approximately 20 km northwest of Colorado Springs, Colorado. The Continental Divide runs north to south through Colorado and is 110 km to the northwest of USAFA and 135 km directly to the west (Figure 63). The average ridgeline elevation along the Continental Divide is 3600 m with several peaks greater than 4200 m. Although not entirely part of the Continental Divide, the Mosquito Range lies about 105 km to the west-northwest of USAFA with ridgelines of just over 3600 m and several peaks above 4200 m. The Tarryall and Kenosha Mountains lie even closer at 70–80 km to the northwest with several peaks in the 3600 to 3800 m range.

The local dominant feature around USAFA is the Rampart Range. It runs north to south along the western flank of USAFA and the surrounding areas. Pikes Peak (4300 m) is the dominant feature of the Rampart Range and is located approximately 21 km southwest of the USAFA Airfield. The average ridgeline of the Rampart Range directly adjacent to USAFA is about 2700 m with several peaks around 2900 m.

The USAFA Reservation is 18,500 acres and varies greatly in elevation both north to south and east to west. There are several ridges that extend west to east from the Rampart Range along USAFA, with their average elevations ranging from 2225 to 2000 m. Between these ridges are valleys that range in elevation from 2050 to 1950 m. The main cadet area (often referred to as the Terrazzo) where the dormitories and academic buildings are located is positioned on one of these ridges at 2212 m. The USAFA Airfield lies at the mouth of Pine and Douglas Valleys with elevations ranging from 1990 to 2005 m. Jack’s Valley, the main summertime training area lies on the north end of the USAFA Reservation and ranges in elevation from 2130 m to the west and 1980 m to the east. Monument Creek flows north to south along the eastern edge of USAFA and parallels Interstate 25 (I-25) and a set of railroad tracks from the northern boundary of USAFA to roughly where I-25 is adjacent to the stadium. At this point the creek and railroad tracks turn in a southwesterly direction and are west of the USAFA Airfield where the creek turns again roughly south and exits the USAFA Reservation just southwest of the South Gate. Monument Creek is the center of a valley that runs north to south with elevations increasing to the west and also to the east.

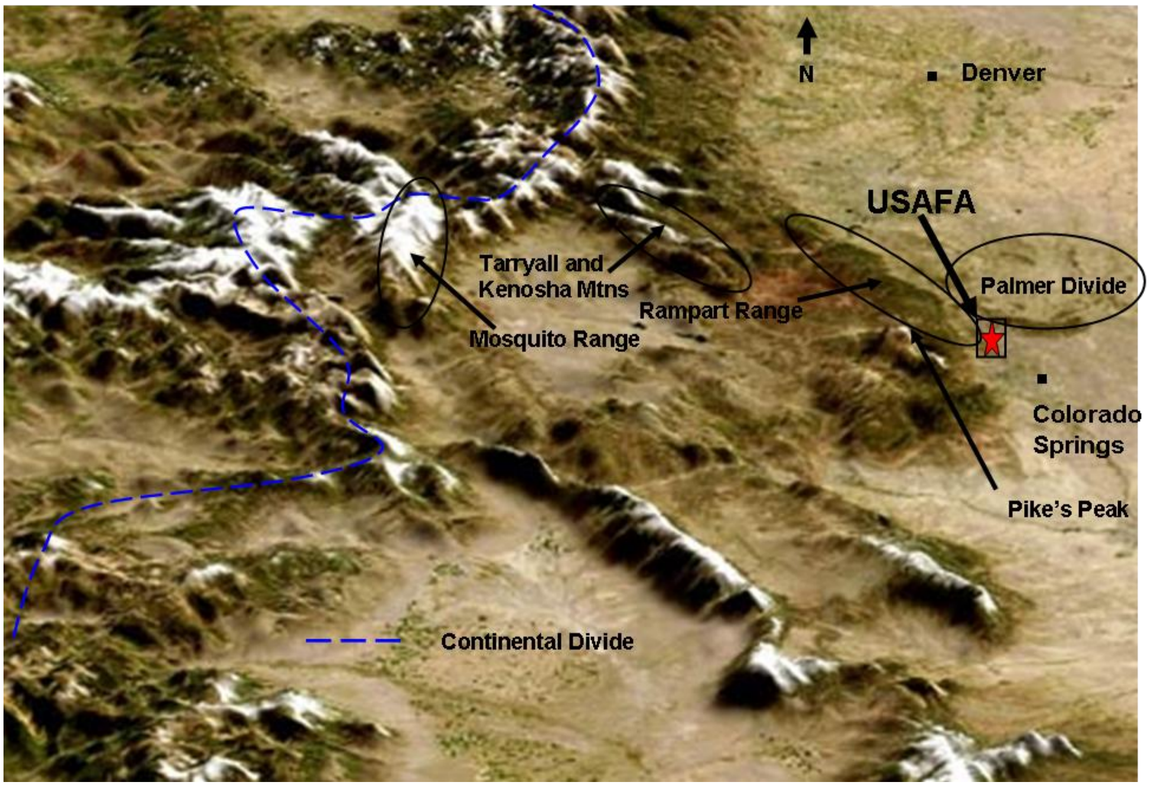

Figure 63. Image showing mountain ranges, terrain and geography of Colorado. Image taken after first snowfall in 2002. (After Descloitres, 2002).

Located about 18 km north of the USAFA Airfield and 13 km north of the cadet area is the crest of the Palmer/Monument Divide (sometimes referred to as the Palmer/Monument Ridge). This ridge extends east from the Rampart Range with an average elevation of 2280 m and maximum elevation above 2400 m. This ridge is the main geographical feature between Colorado Springs and Denver and measures north to south on average 45–55 km and runs from the Rampart Range 45–55 km east out onto the adjacent plains. Due to the Palmer Divide, elevations increase as you head north from

USAFA as well as to the east. The region directly 6–12 km to the east of USAFA on the Palmer Divide is known as the Black Forest due to its abundance of Ponderosa Pines with elevations of 1980 m to 2375 m. The terrain drops to the east of Black Forest; however, this drop is much more pronounced to the southeast and south of the Academy. The elevation at Limon, CO (87 km to the east-northeast) is 1635 m while at Pueblo, CO (69 km to the south-southeast) is 1440 m.

B. HIGH WIND ALERT SYSTEM (HWAS) DESCRIPTION

The twelve weather observation sensors that make up the HWAS network are strategically positioned at locations to provide an adequate sample of meteorological data and give a good representation of weather conditions around USAFA in the diverse terrain. A map of these sensors is provided in Figure 64, and the elevation and longitude/latitude positioning of each sensor is provided in Table 8. Nine of the sensors are located on the USAFA Reservation with the Rampart sensor located at the top of the Rampart Range ridgeline due west of USAFA in Pikes Peak National Forest. The Pine Creek sensor is located on a roof at a local school east of USAFA while the Lewis Palmer sensor (also on a roof at a local school) is north of USAFA. Both of these sensors are on the edge of the Palmer Divide and the terrain decreases in elevation from these sensors toward USAFA.

Sensor Name	Latitude	Longitude	Elevation (m)
Aardvark	39° 02’ 07” N	104° 50’ 39” W	2042.2
Airfield	38° 56’ 06” N	104° 49’ 30” W	1978.2
Command Post	39° 00’ 37” N	104° 53’ 11” W	2179.3
Community Center	38° 58’ 57” N	104° 52’ 29” W	2185.4
Lewis Palmer	39° 04’ 48” N	104° 51’ 16” W	2132.1
North Ridge	39° 01’ 33” N	104° 52’ 43” W	2183.9
Pine Creek	38° 59’ 12” N	104° 45’ 48” W	2126.0
Pine Valley	38° 58’ 13” N	104° 51’ 37” W	2026.9
Rampart	38° 59’ 13” N	104° 55’ 14” W	2840.8
South Gate	38° 56’ 56” N	104° 48’ 55” W	1953.8
South Ridge	38° 57’ 25” N	104° 50’ 51” W	2036.1
Stadium	38° 59’ 51” N	104° 50’ 55” W	2084.9

Table 8. HWAS sensors longitude/latitude and elevation.

HWAS sensors located on the USAFA Reservation are mostly located along west to east oriented ridgelines with a few exceptions. The Pine Valley sensor is on the rooftop of a school that is located in the largest west to east oriented valley on USAFA. The Airfield sensor is on the east side of Monument Creek and is located at the mouth of Pine Valley. This sensor is in an open field just west of the adjacent runways on the USAFA Airfield for the case studies in this research, but was moved to a location northwest of the runways in 2011. The Aardvark sensor lies along the eastern most extension of the Northridge. It is adjacent to an additional runway used for training and Monument Creek. When strong winds are present from the west, because this sensor is not in a west-east oriented valley but at the base of a ridgeline, this sensor is often spared the strongest winds and the recorded wind values are much lower than at other sensors. Instead, with its proximity to Monument Creek, it is in an ideal location to measure drainage flow from the north coming down the Palmer Divide. The only other sensor that is located on a platform that is on top of a building is the Command Post sensor which is located on top of Vandenberg Hall, a six-story tall cadet dormitory. This sensor has the greatest number of man-made obstructions around it of any of the sensors with several other buildings close by in all directions. It is the furthest west and closest to the steep slopes of the Rampart Range than any of the other sensors except for Rampart which lies at the atop of the Front Range.

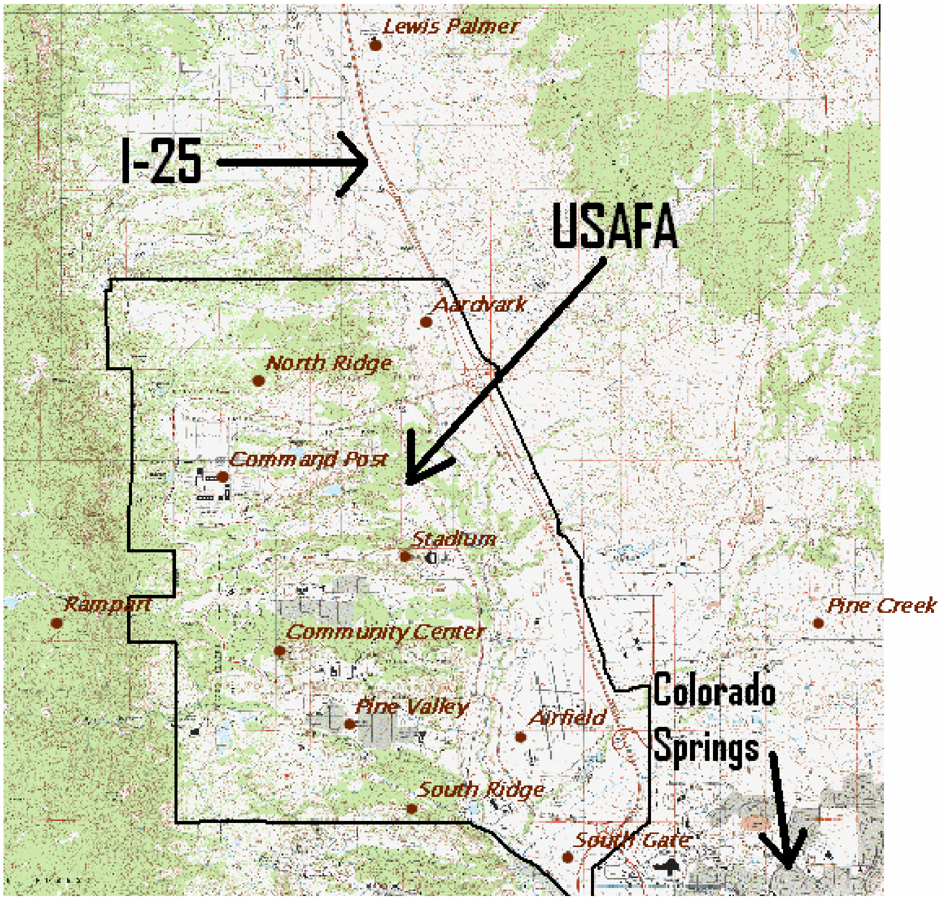

Figure 64. Map of locations of HWAS sensors. Green shaded regions indicate areas covered by forest.

THIS PAGE INTENTIONALLY LEFT BLANK

APPENDIX B

A. PERFECT MODEL—“TRUTH RUN” FIGURES

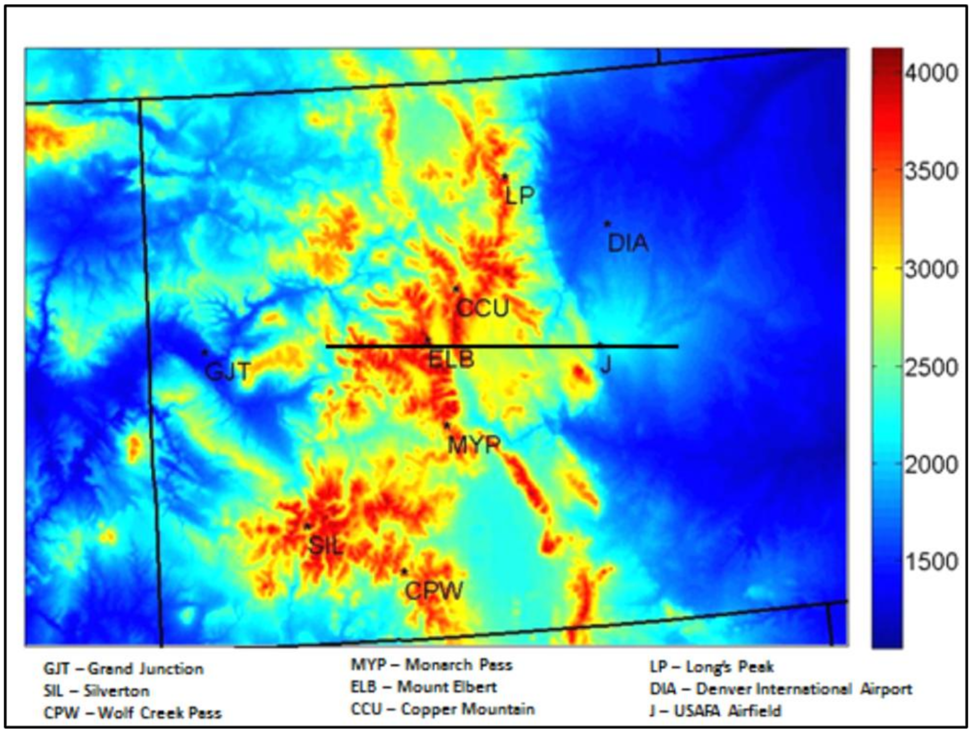

Figure 65. Terrain height in meters for innermost domain centered over Colorado. Solid black line indicates location of cross sections shown in upper plots of figures that follow at the gridline of the Rampart sensor.

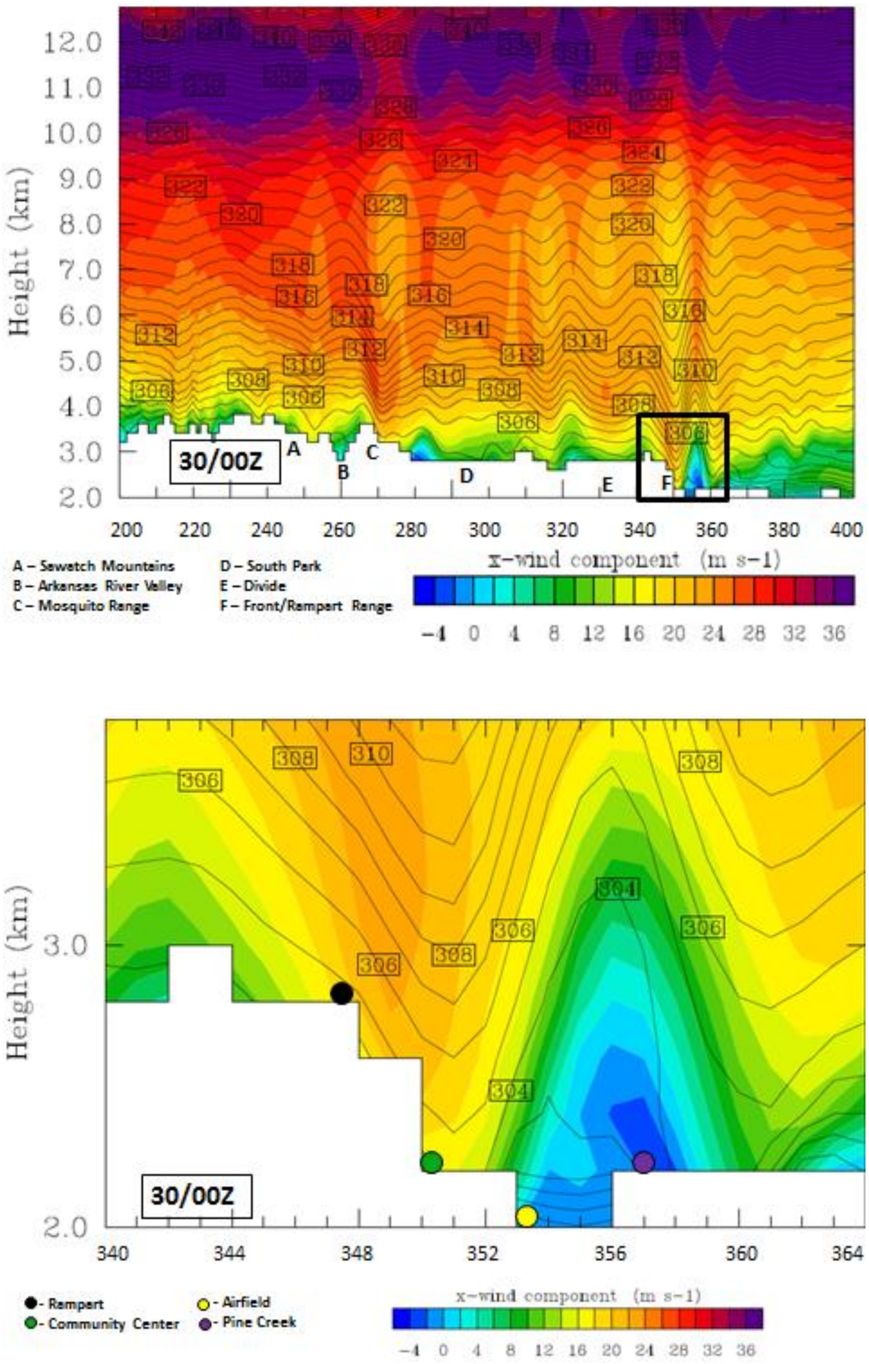

Figure 66. Top: Cross section of *x*-wind component (shaded) and potential temperature (contoured) from west to east along solid black line in previous figure for the 12/30/2008 00Z truth run. Black inset box indicates location of zoomed in cross section depicted at bottom half of figure. The horizontal axis is scaled to the number of grid points from the innermost domain with a resolution of 1.33 km. Approximate locations of four HWAS sensors are marked by circles.

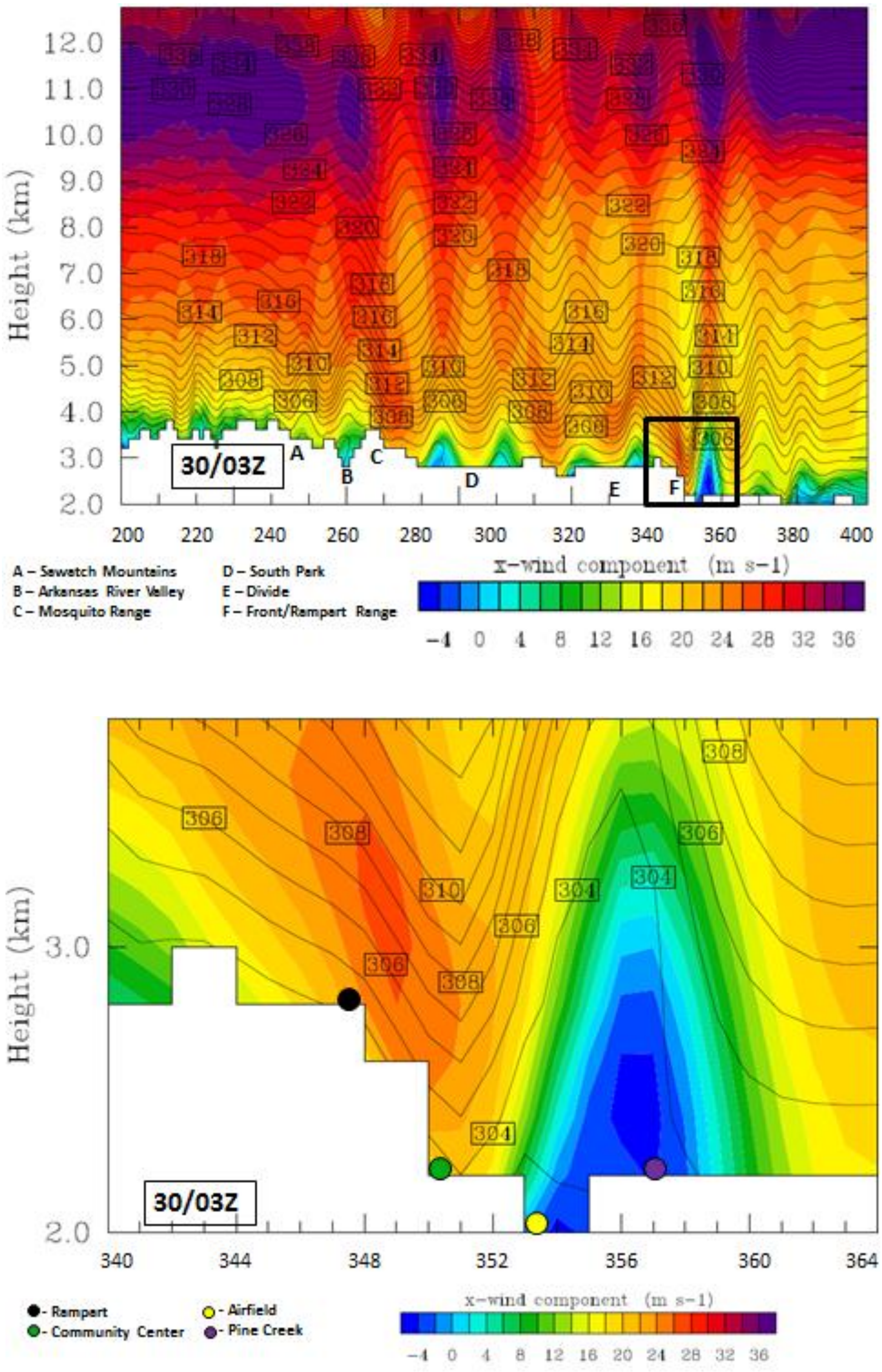

Figure 67. Truth run for 12/30/2008 03Z. Description follows previous figure.

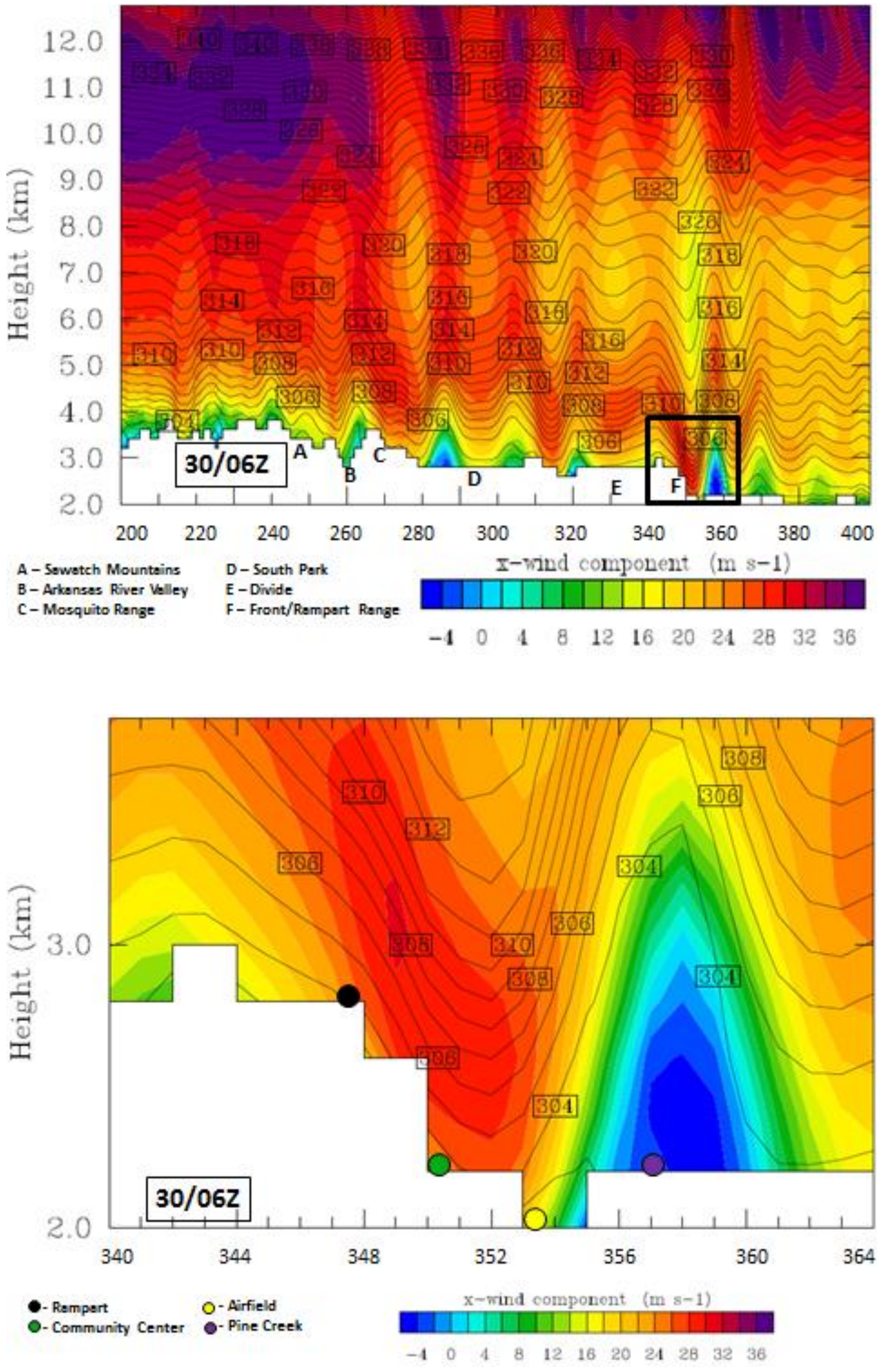

Figure 68. Truth run for 12/30/2008 06Z. Description follows previous figure.

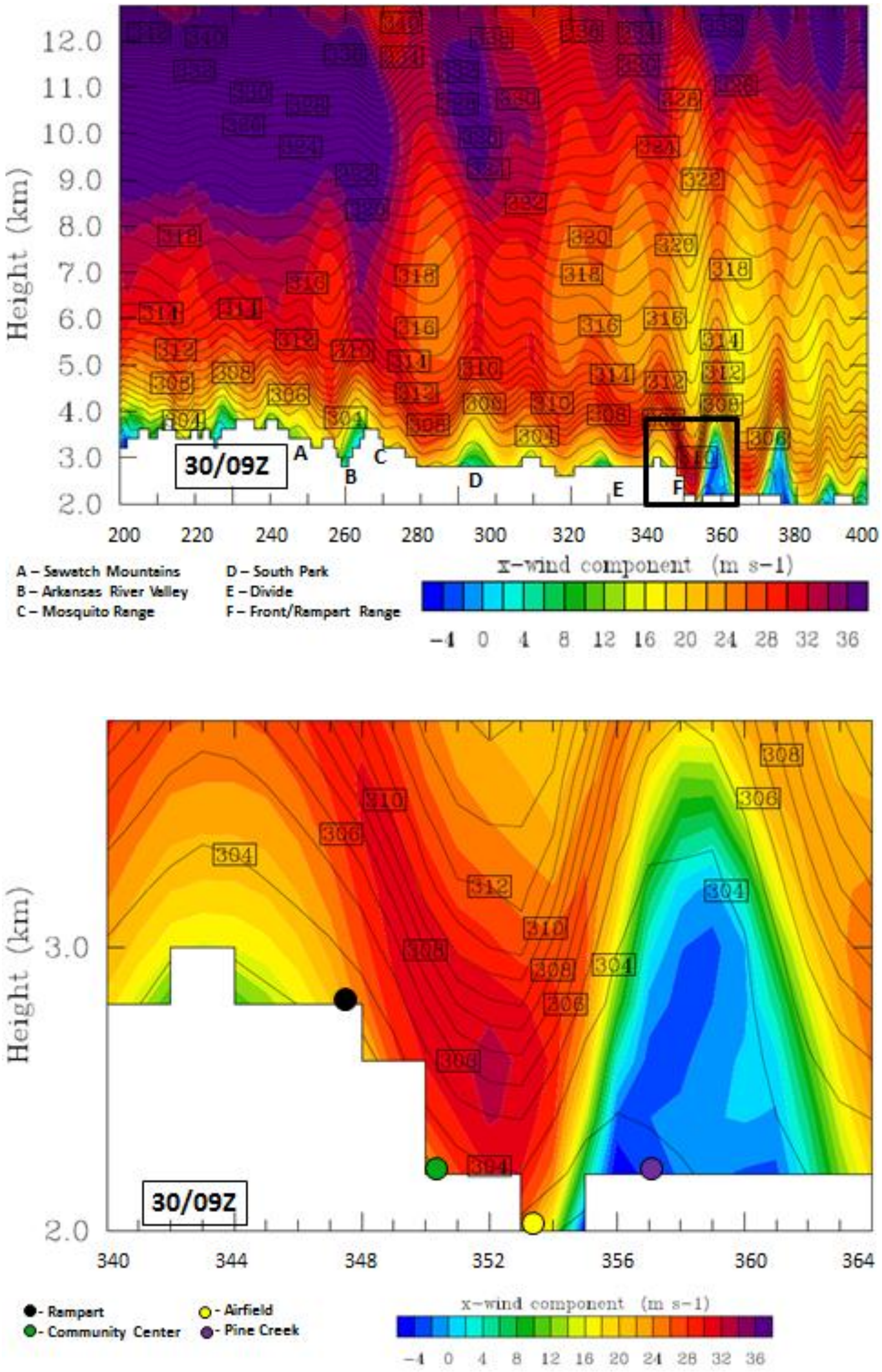

Figure 69. Truth run for 12/30/2008 09Z. Description follows previous figure.

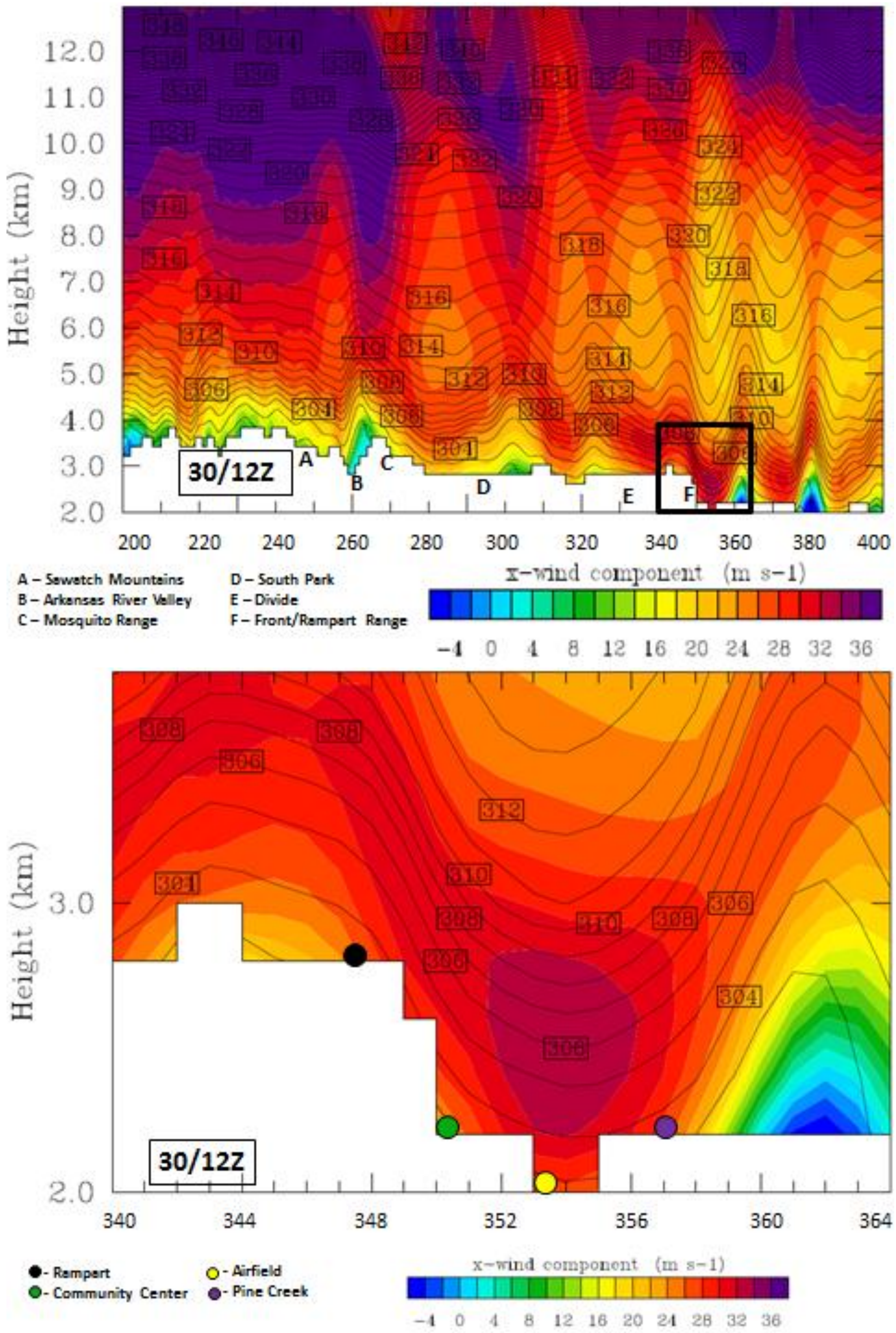

Figure 70. Truth run for 12/30/2008 12Z. Description follows previous figure.

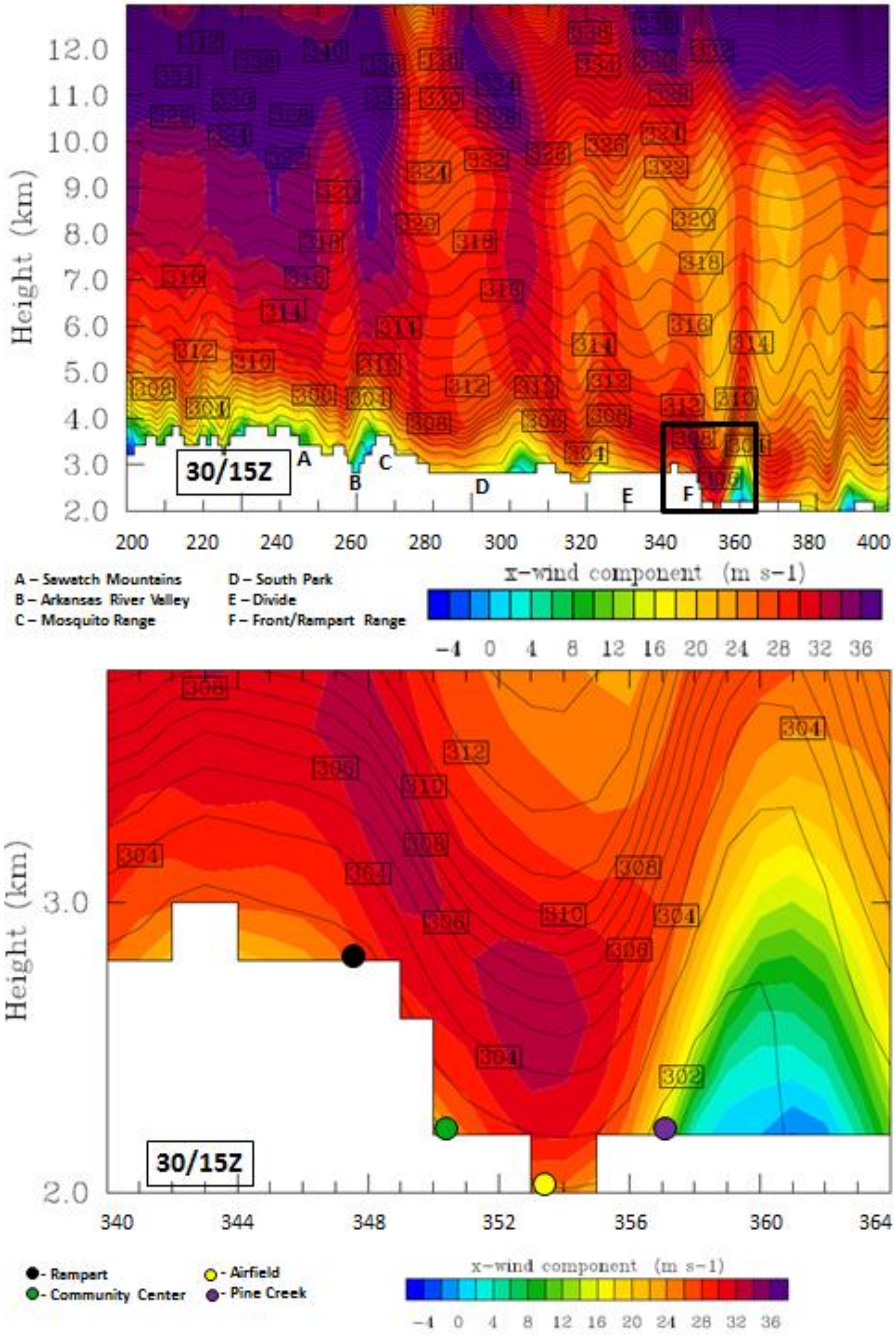

Figure 71. Truth run for 12/30/2008 15Z. Description follows previous figure.

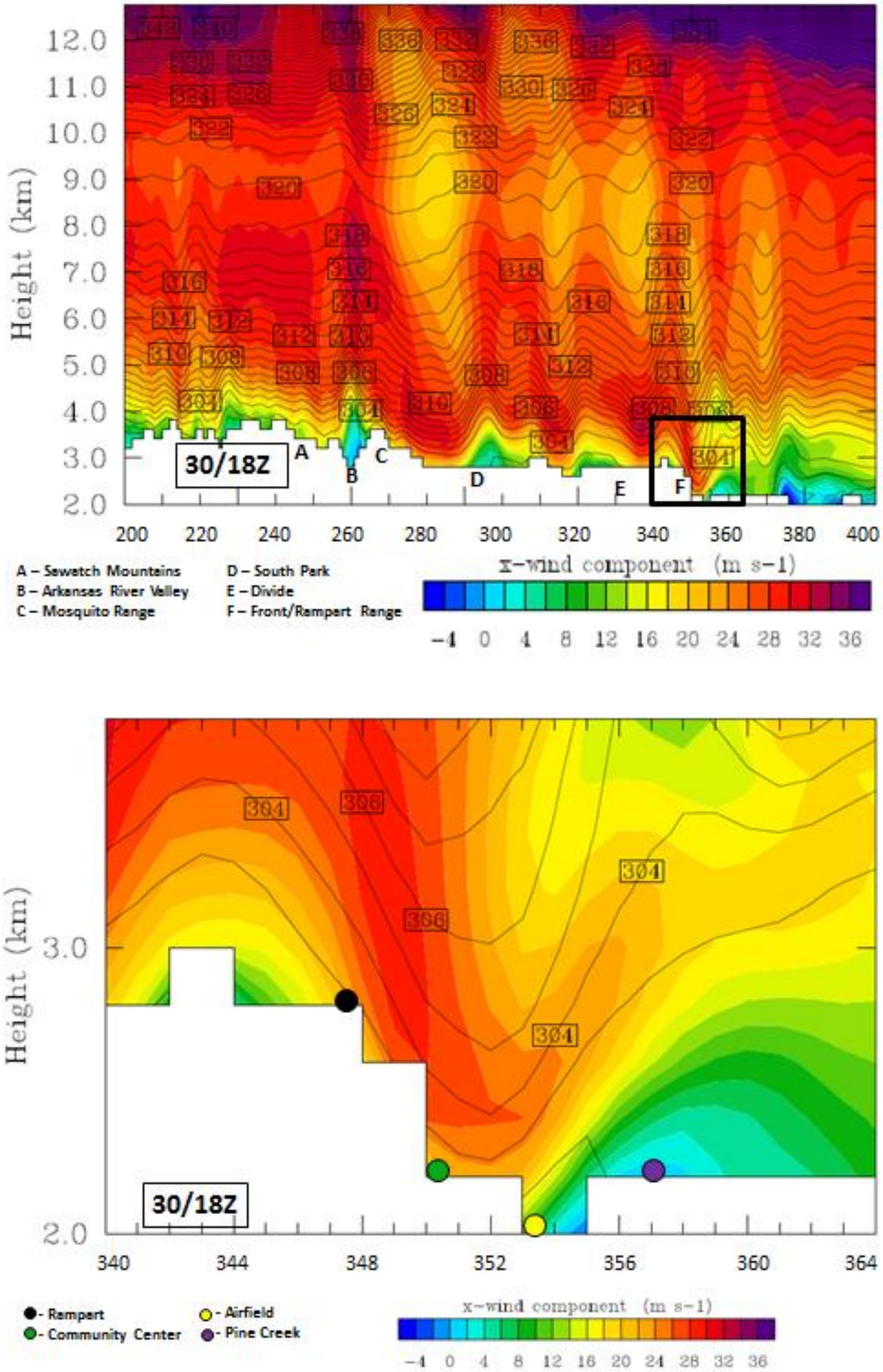

Figure 72. Truth run for 12/30/2008 18Z. Description follows previous figure.

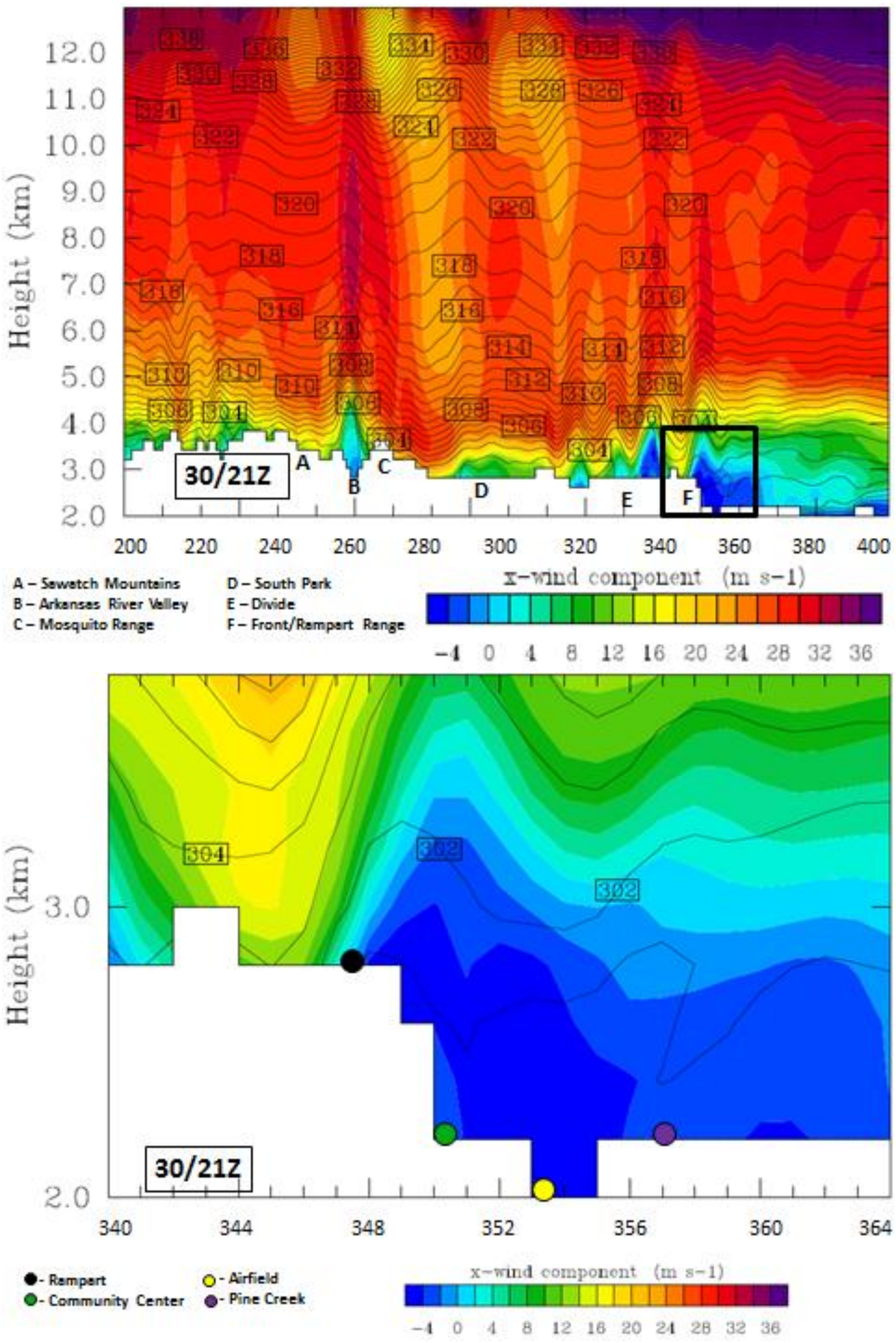

Figure 73. Truth run for 12/30/2008 21Z. Description follows previous figure.

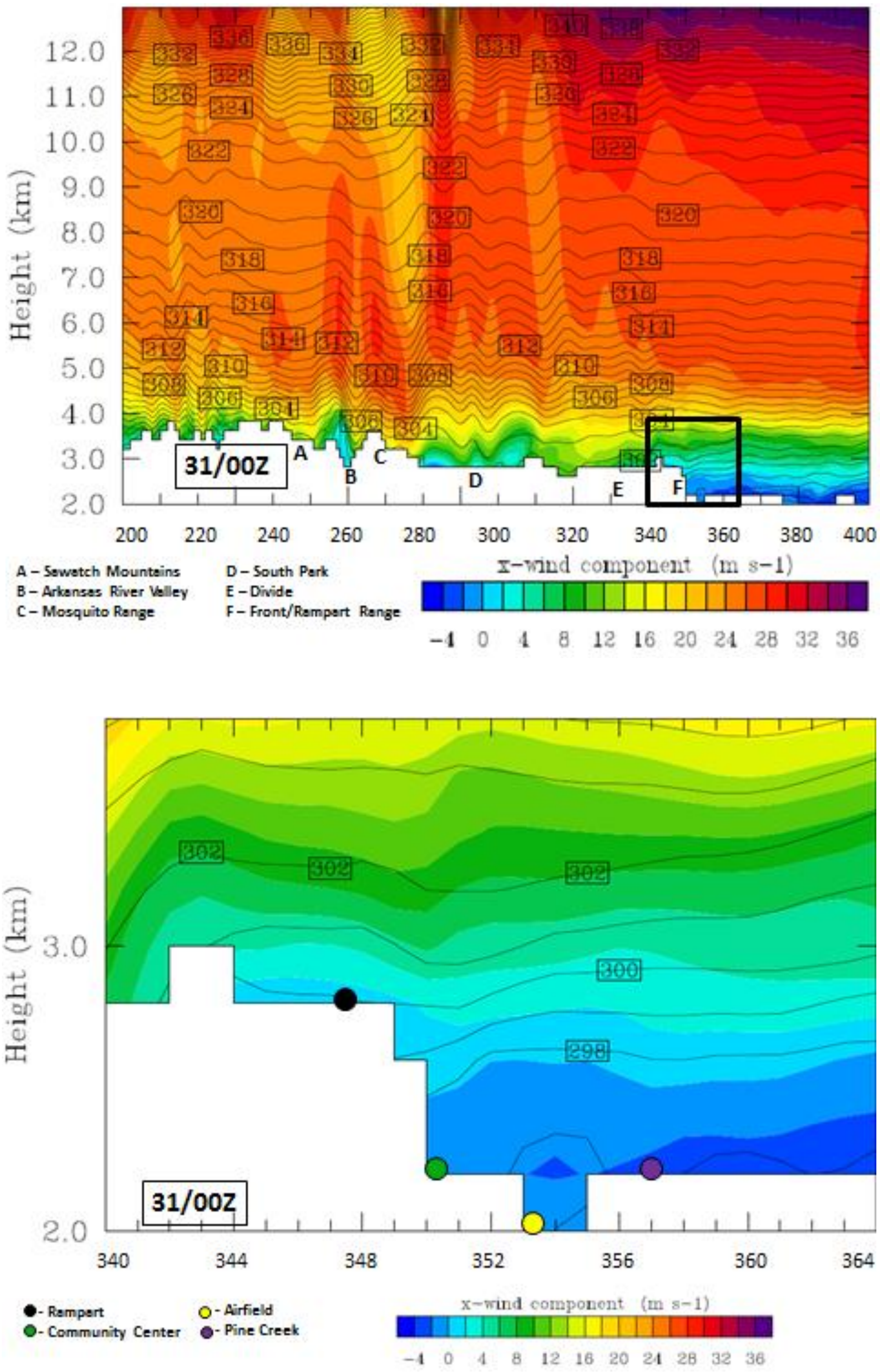

Figure 74. Truth run for 12/31/2008 00Z. Description follows previous figure.

APPENDIX C

A. FIGURES OF WRF MODEL RUNS FOR FOURTEEN SEVERE DOWNSLOPE WINDSTORMS AT USAFA

Appendix C contains cross sections for each of the fourteen severe DSWS for the case-study presented in Chapter V. The time of each cross section corresponds to the time of maximum winds as predicted by the model in the solid black box over USAFA shown in the top of each figure and shown in the zoomed-in cross section in the bottom of each figure. The figures are ordered with the six non-breaking events shown first and then the eight vertically propagating breaking wave events shown second. The times displayed in these figures are not necessarily the best example of larger scale trapping or wave-breaking used to classify each event, but rather correspond to the time of maximum winds lee of the Rampart Range at USAFA.

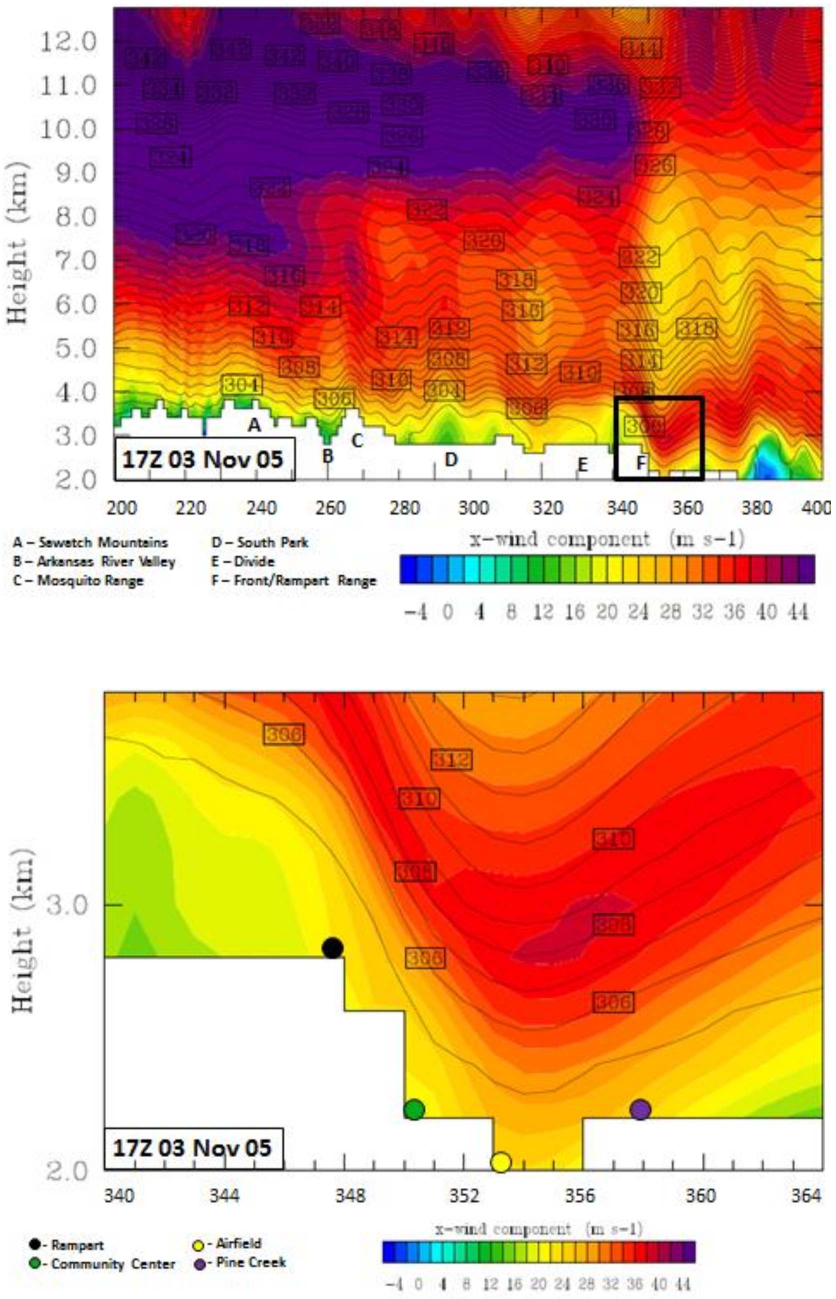

Figure 75. Top: Cross section from west to east as depicted by solid black line in Figure 16 for the 11/03/2005 17Z WRF run. Black inset box indicates location of zoomed in cross section depicted at bottom half of figure. The *x*-wind component is shaded in color and theta is contoured with solid black lines. The horizontal axis is scaled to the number of grid points from the innermost domain with a resolution of 1.33 km. Approximate locations of four HWAS sensors are marked by circles.

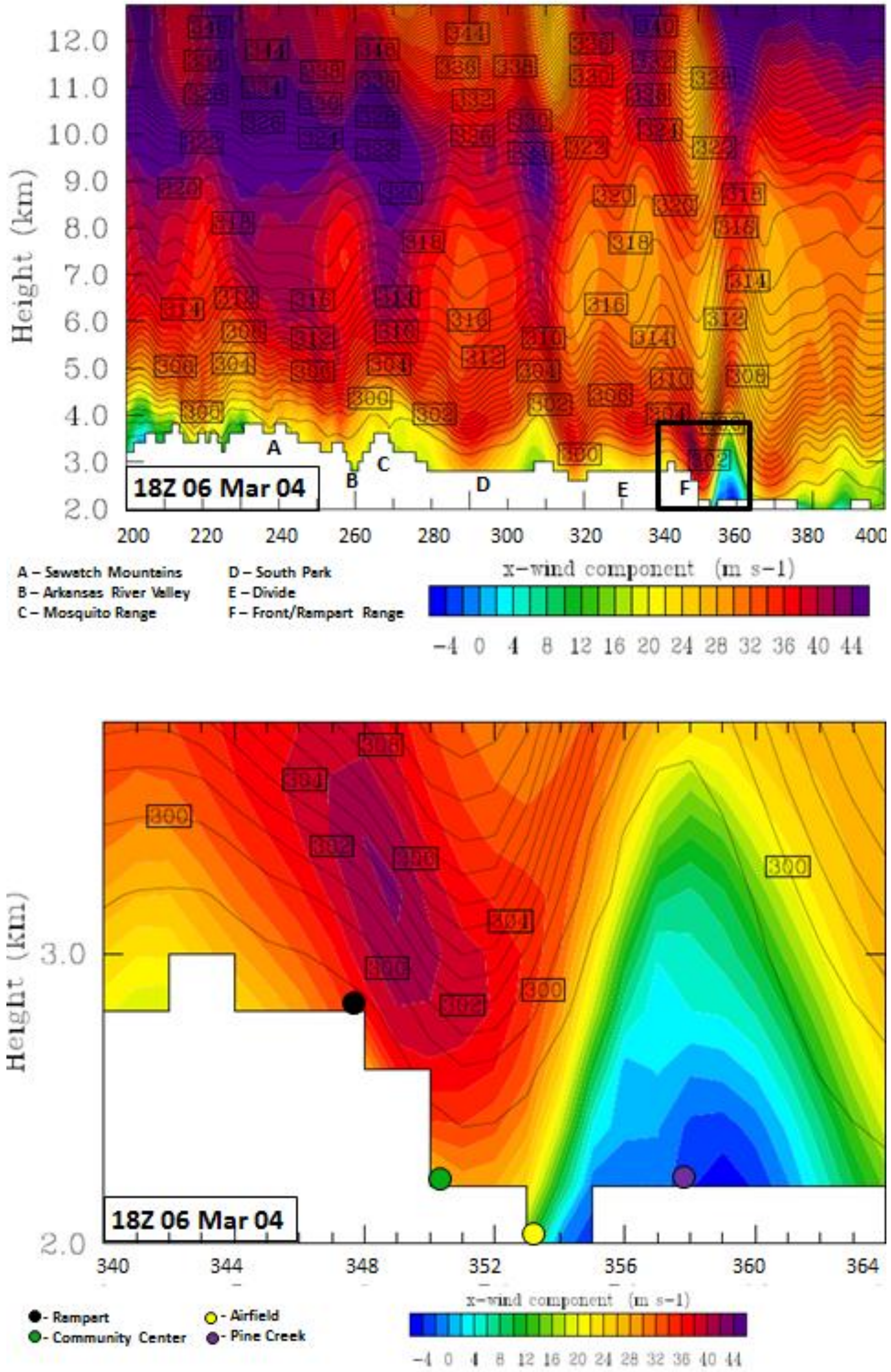

Figure 76. WRF run for 03/06/2004 18Z. Description follows previous figure.

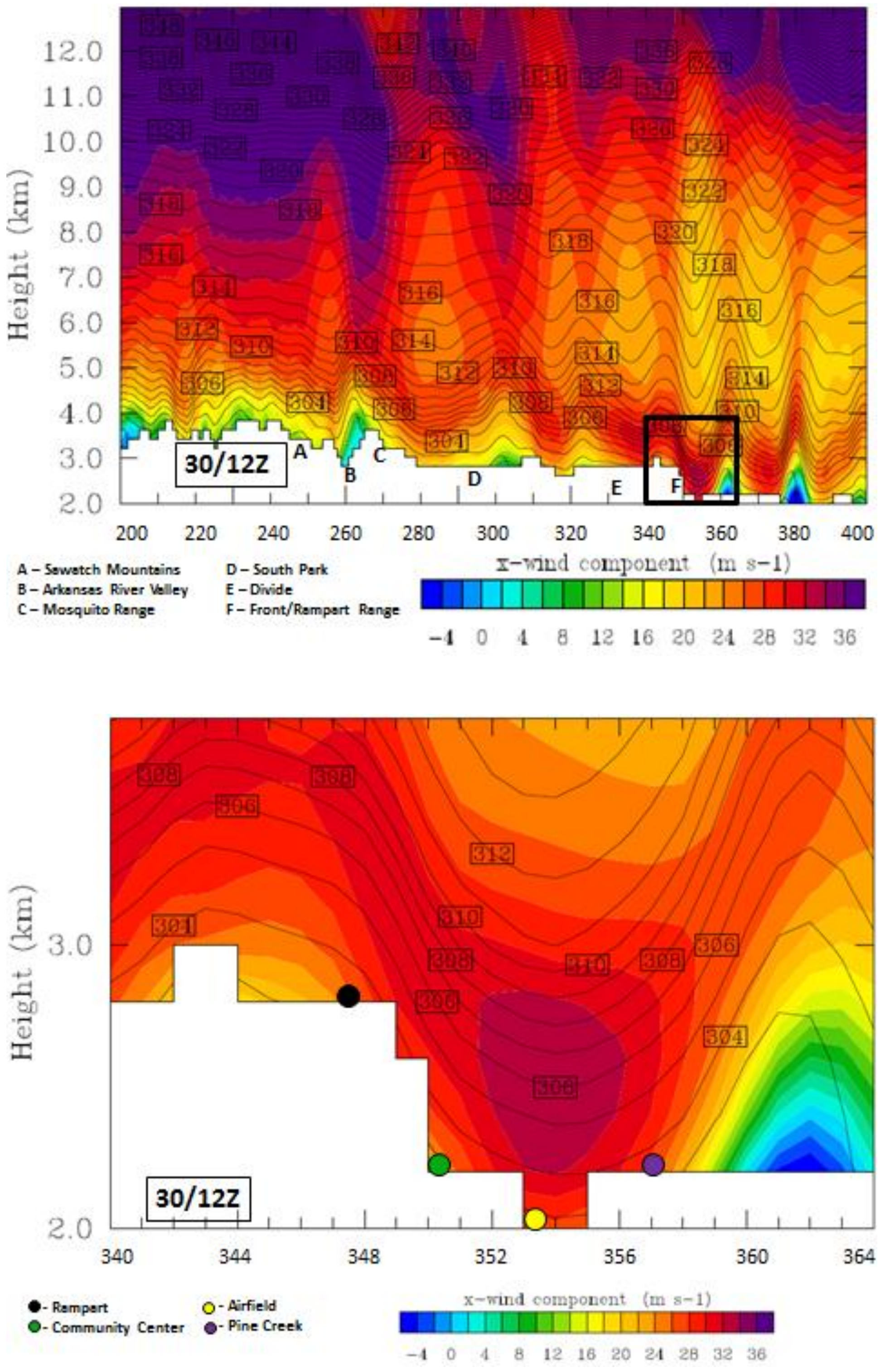

Figure 77. WRF truth run for 12/30/2008 12Z. Description follows previous figure.

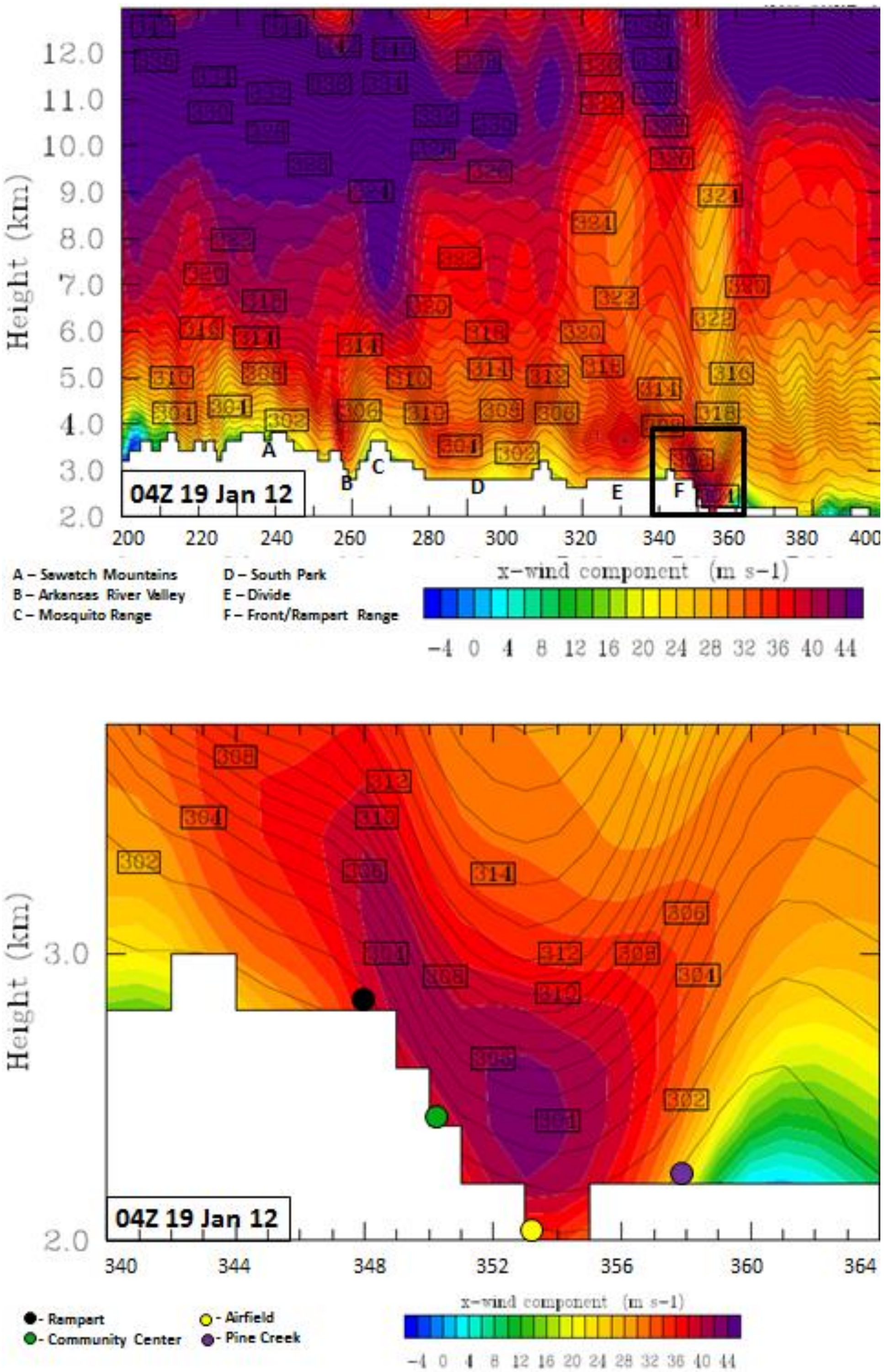

Figure 78. WRF run for 01/19/2012 04Z. Description follows previous figure.

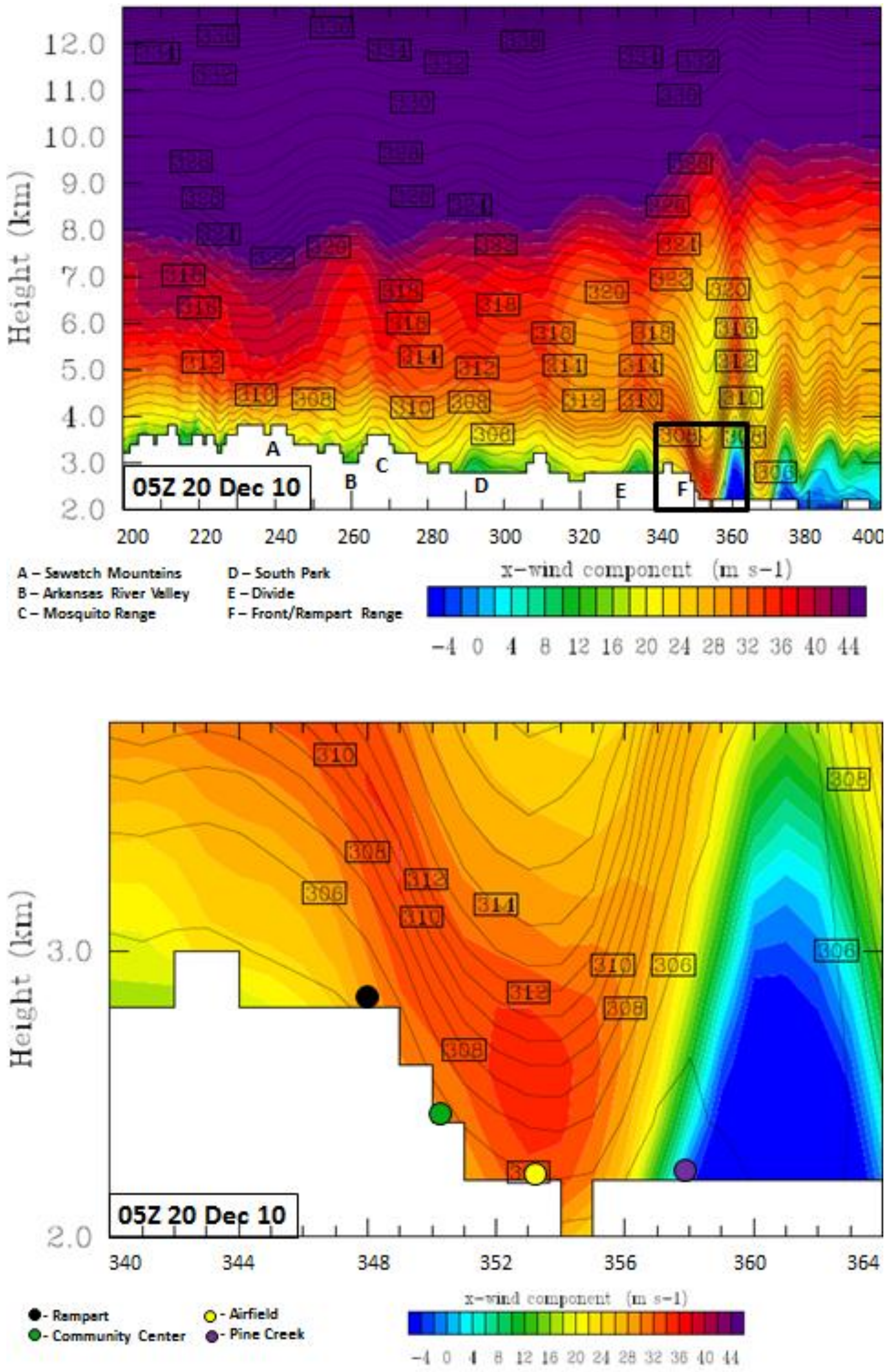

Figure 79. WRF run for 12/20/2010 05Z. Description follows previous figure.

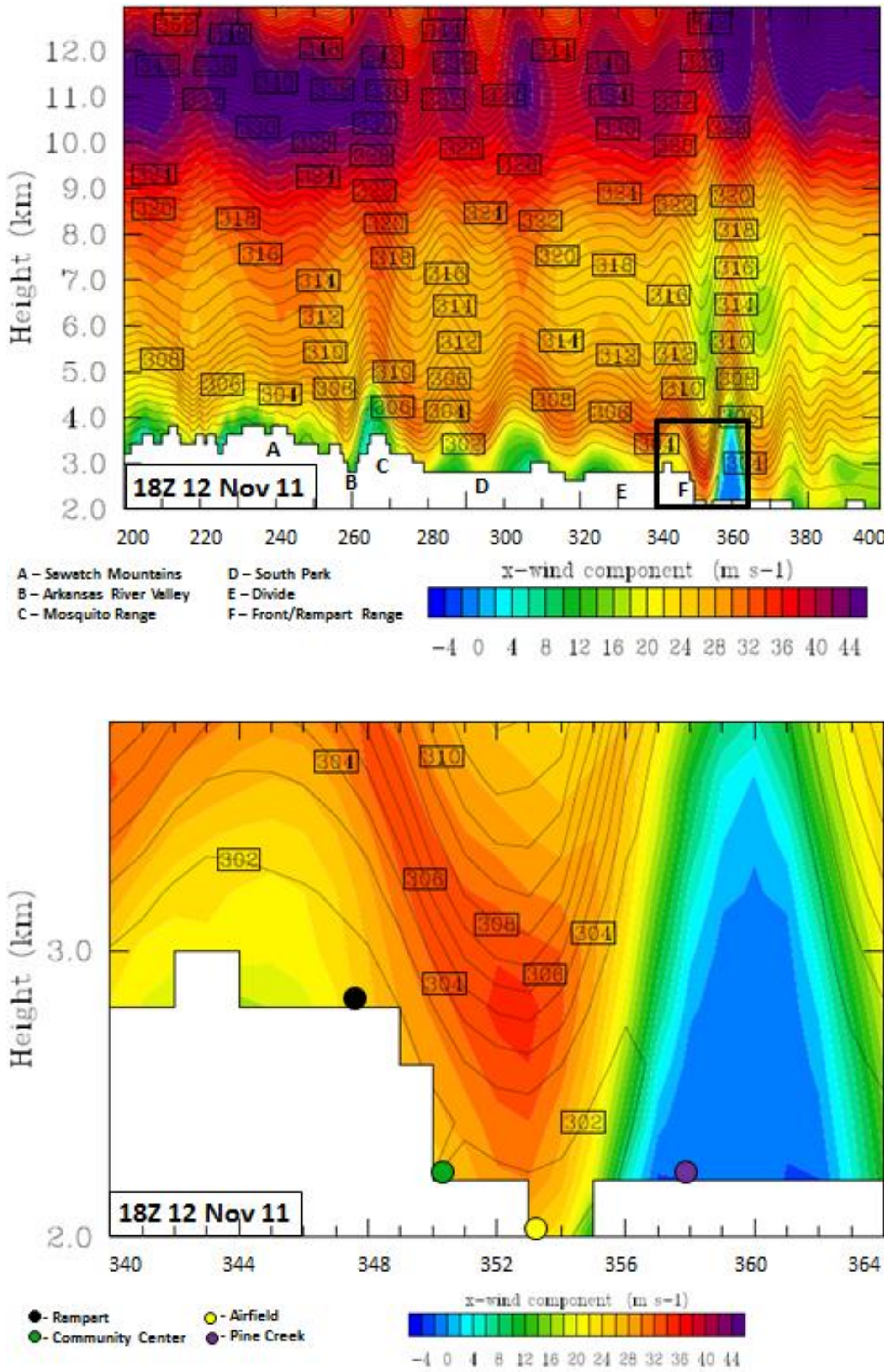

Figure 80. WRF run for 11/12/2011 18Z. Description follows previous figure.

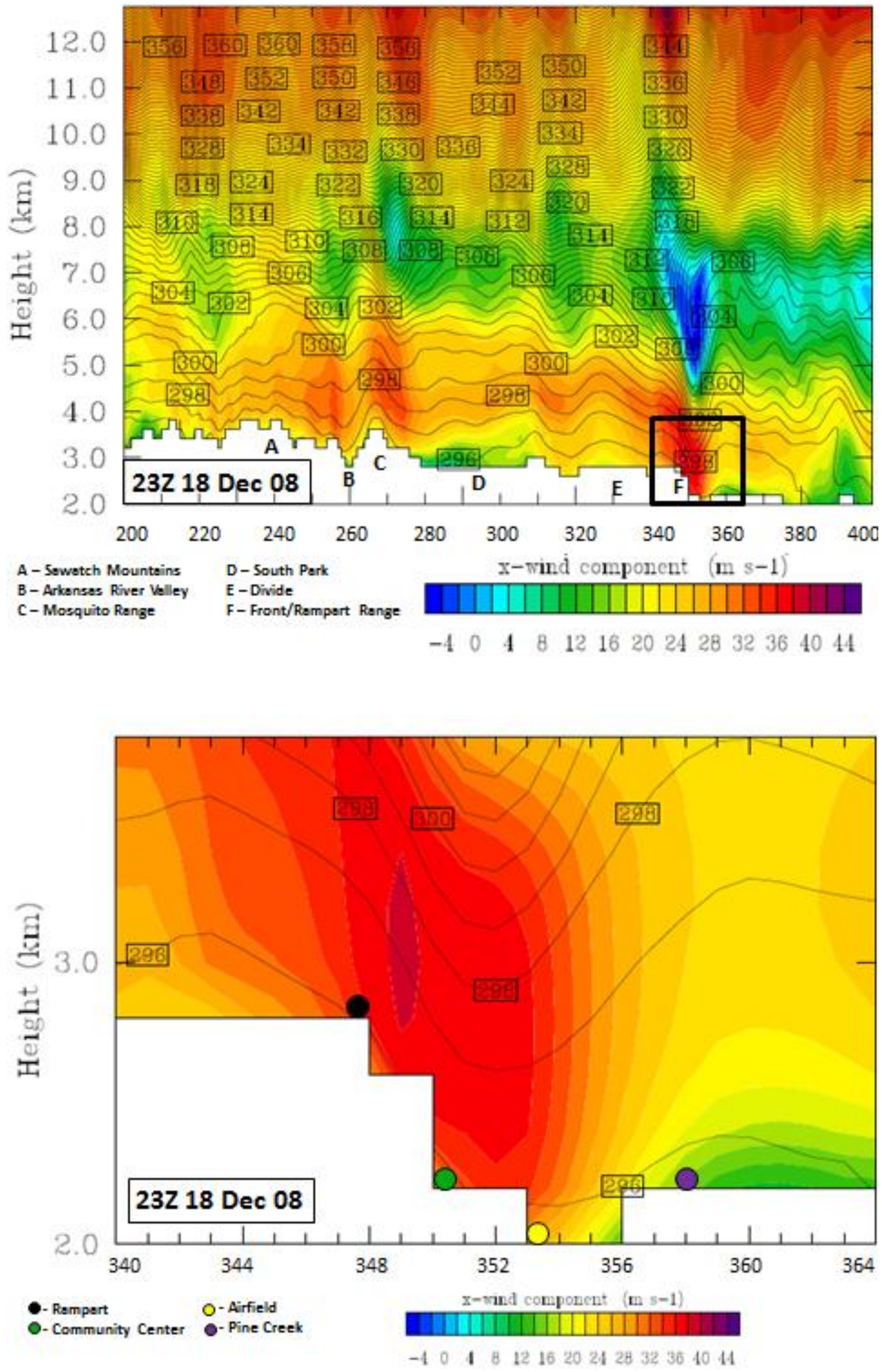

Figure 81. WRF run for 12/18/2008 23Z. Description follows previous figure.

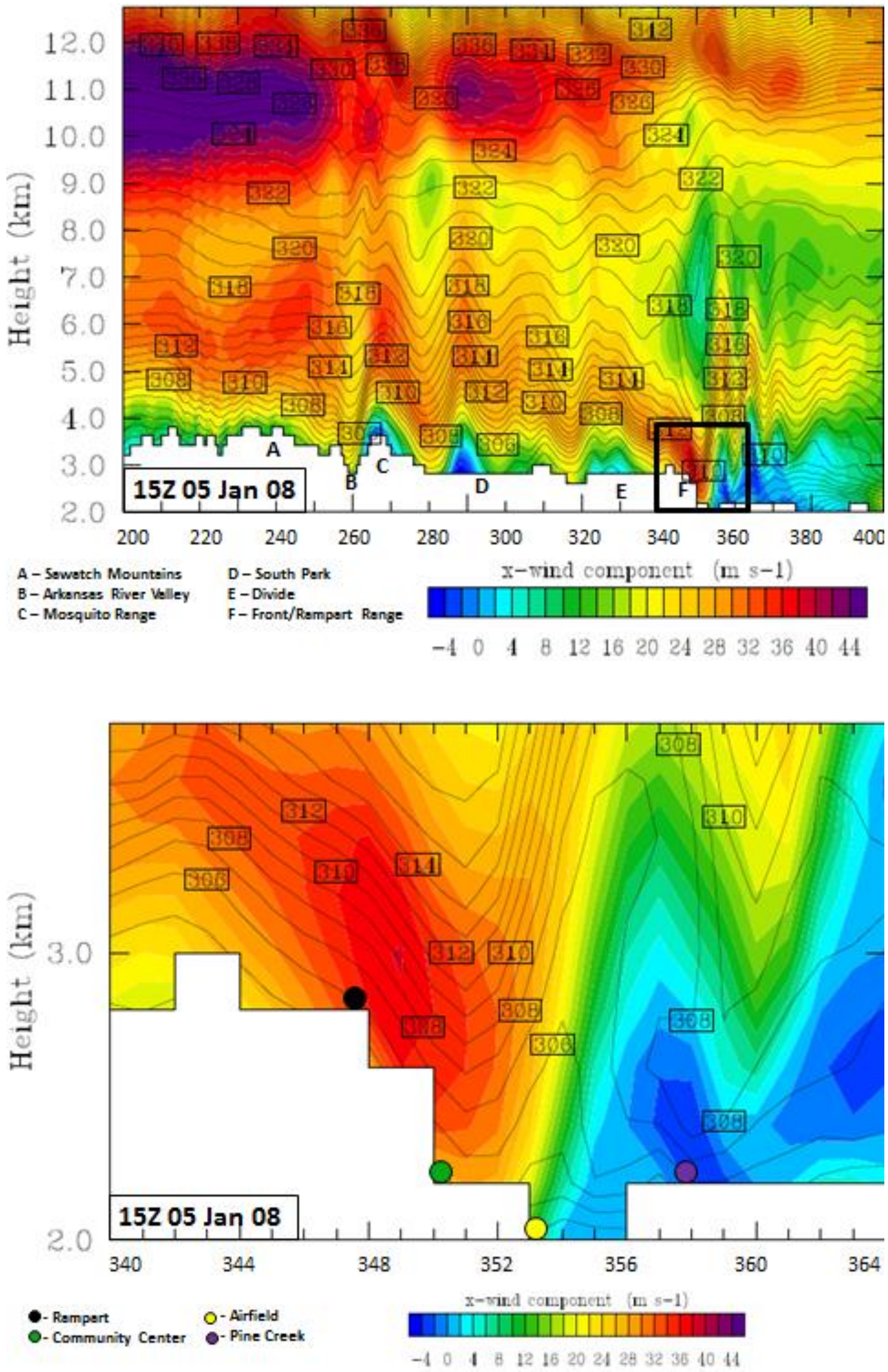

Figure 82. WRF run for 01/05/2008 15Z. Description follows previous figure.

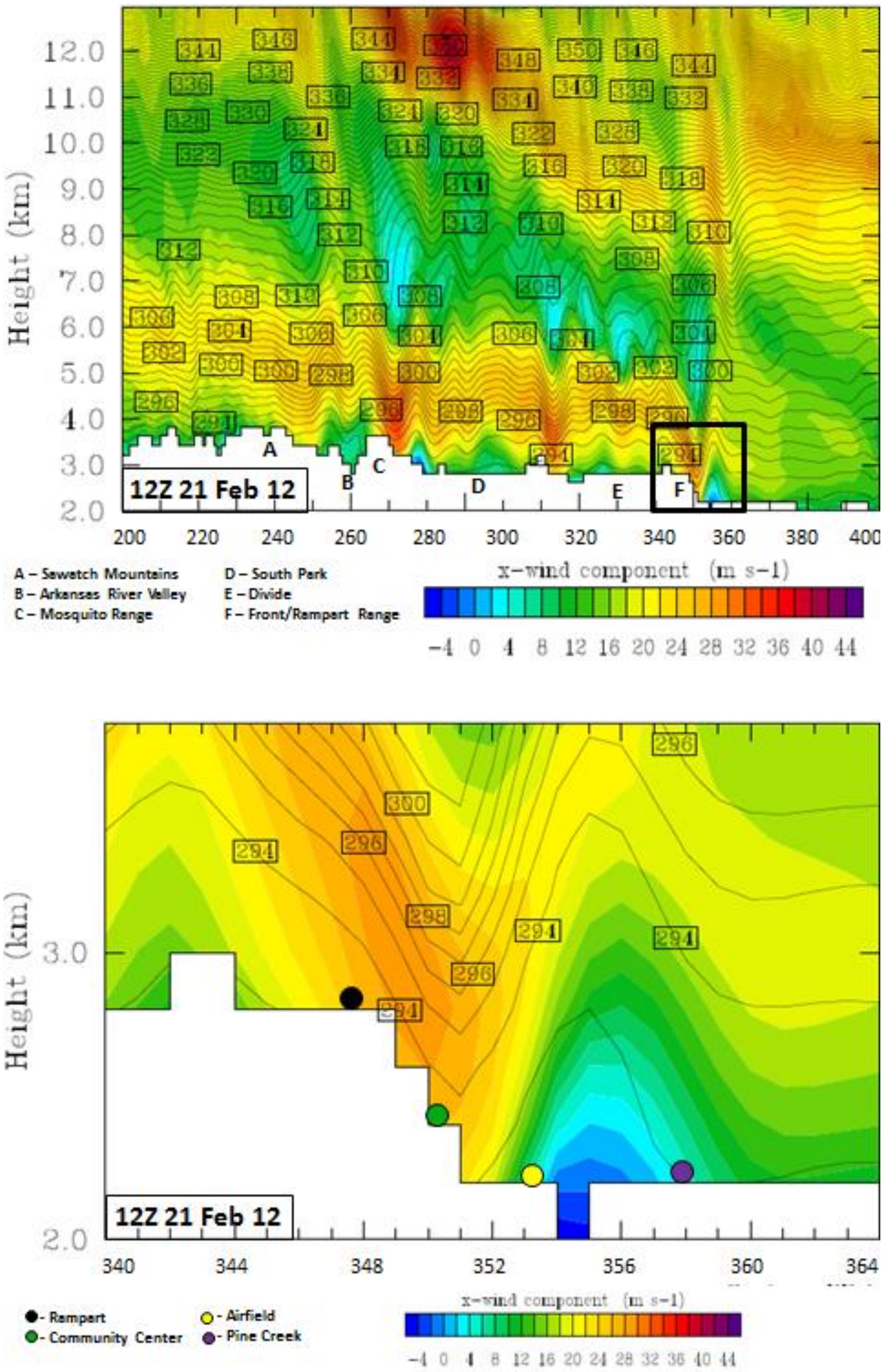

Figure 83. WRF run for 02/21/2012 12Z. Description follows previous figure.

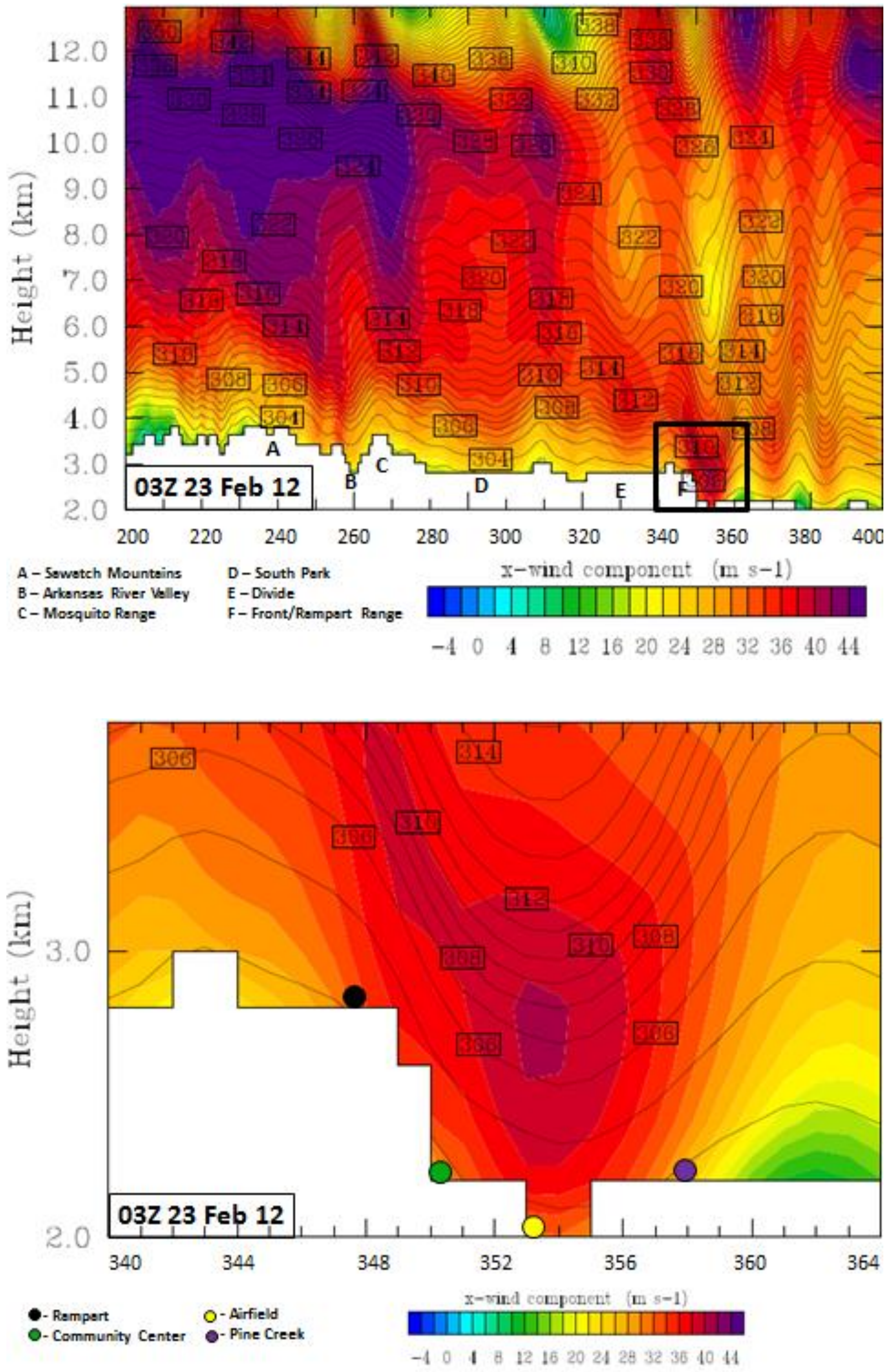

Figure 84. WRF run for 02/23/2012 03Z. Description follows previous figure.

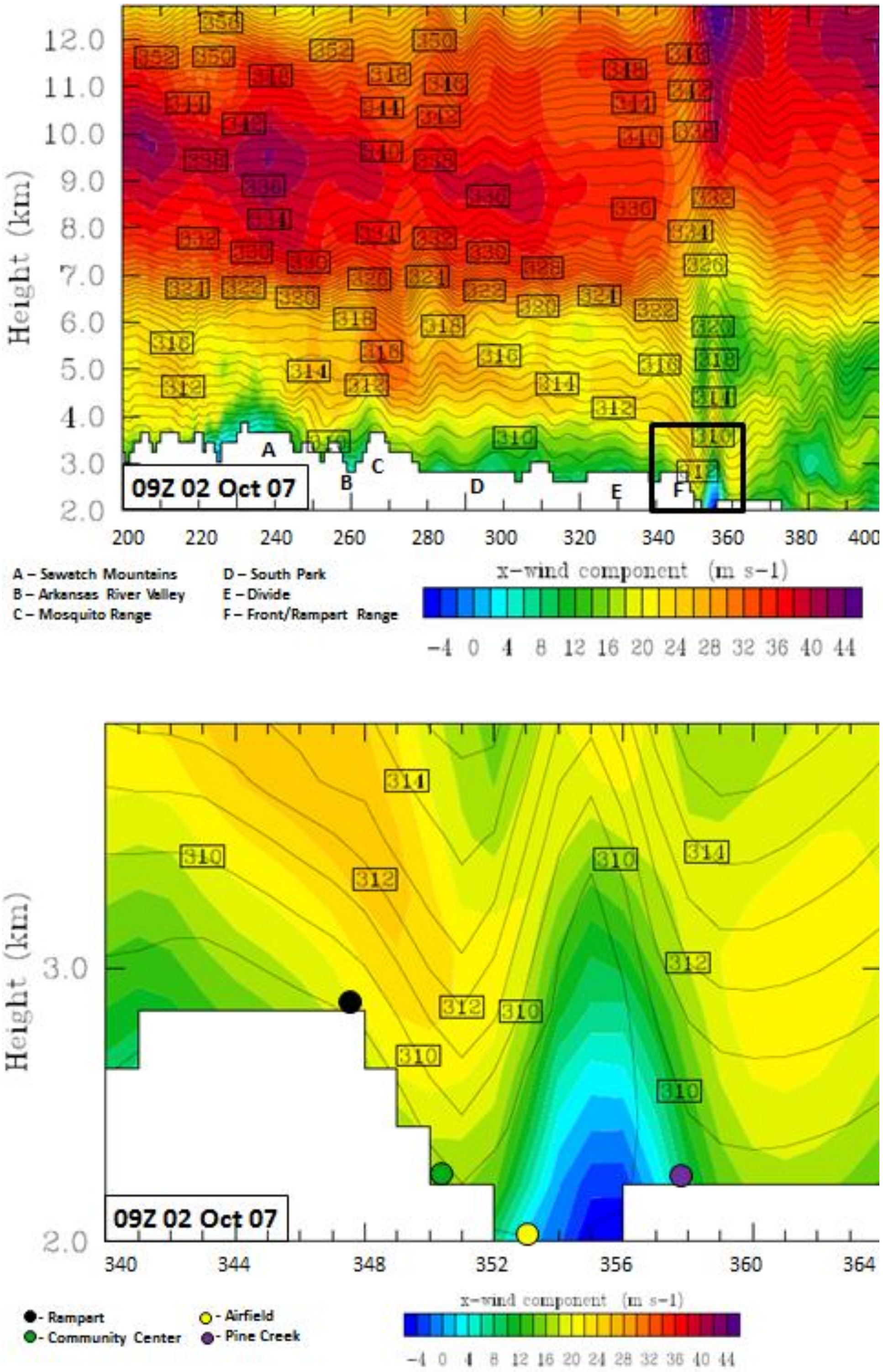

Figure 85. WRF run for 10/02/2007 09Z. Description follows previous figure.

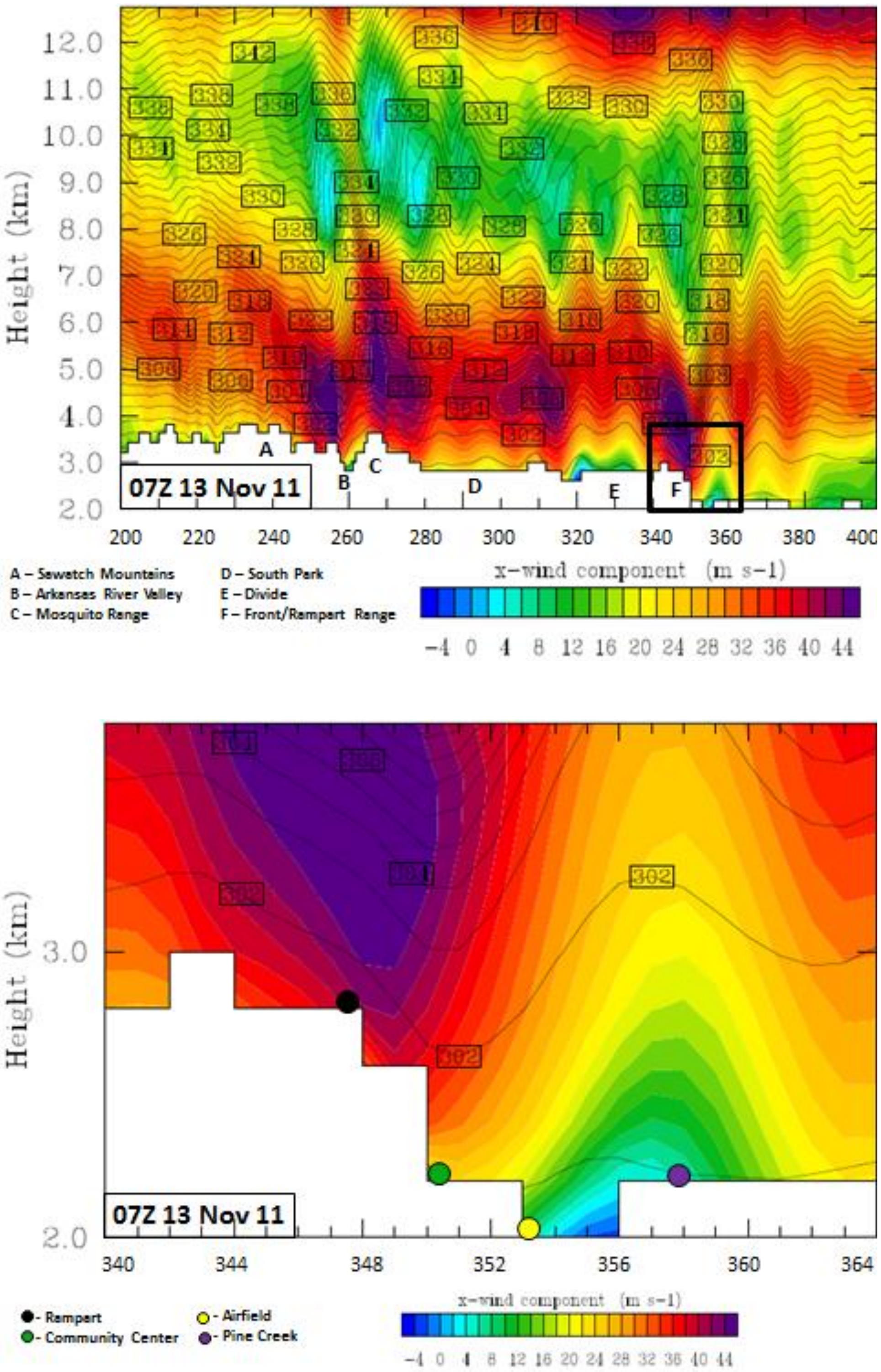

Figure 86. WRF run for 11/13/2011 07Z. Description follows previous figure.

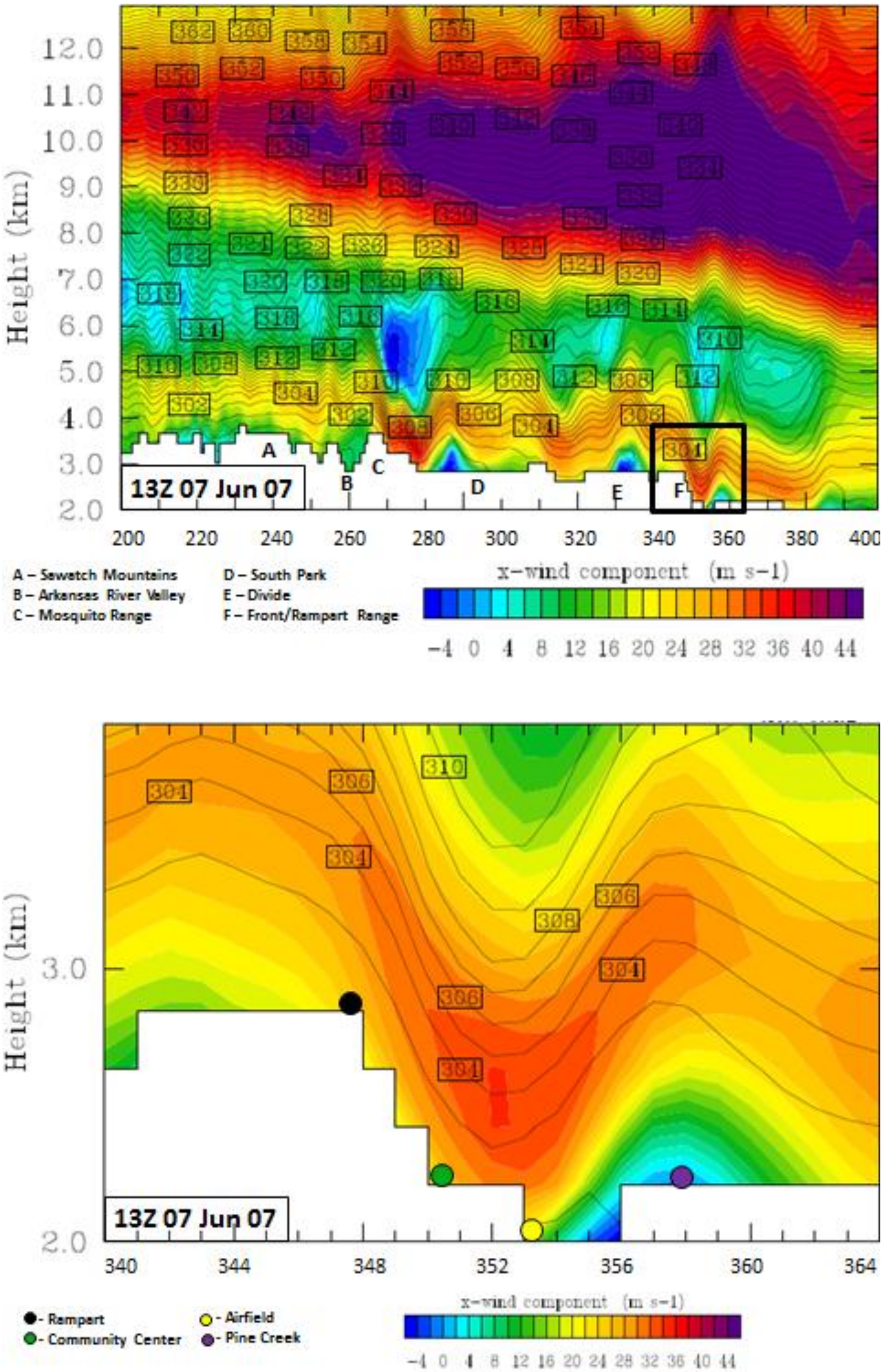

Figure 87. WRF run for 06/07/2007 13Z. Description follows previous figure.

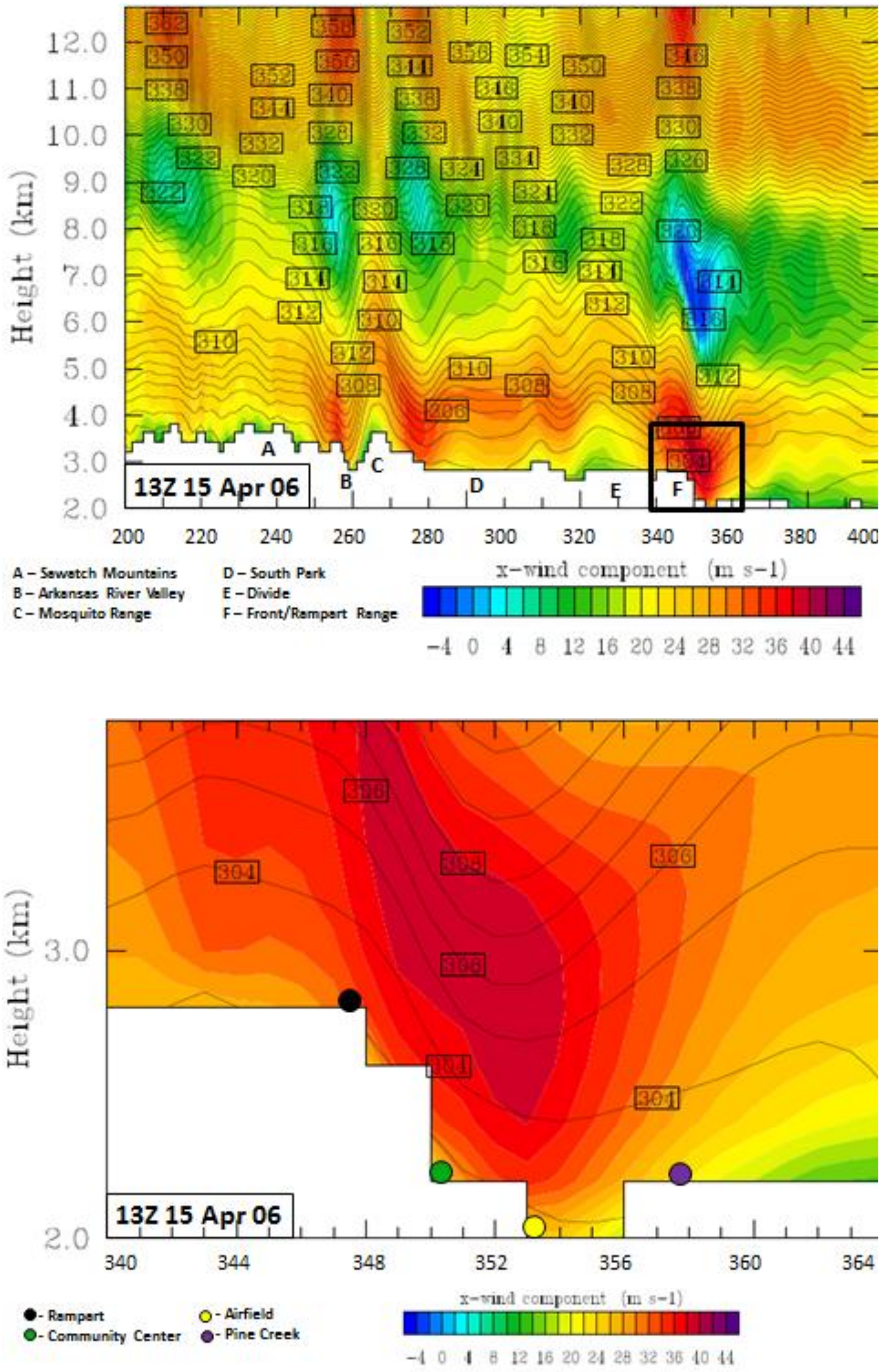

Figure 88. WRF run for 04/15/2006 13Z. Description follows previous figure.

THIS PAGE INTENTIONALLY LEFT BLANK

LIST OF REFERENCES

Aanenson, C. J. M., 1965: Gales in Yorkshire in February 1962. *Geophys. Mem*., **14**, 1–44.

Ancell, B., & Hakim, G., 2007: Comparing adjoint- and ensemble-sensitivity analysis with applications to observation targeting. *Mon. Wea. Rev.*, **135**, 4117–4134.

Anderson, J. L., 2003: A local least squares framework for ensemble filtering. *Mon. Wea. Rev.*, **131**, 634–642

Anderson, J., T. Hoar, K. Raeder, H. Liu, N. Collins, R. Torn, and A. Avellano, 2009: The data assimilation research testbed: A community facility. *Bull. Amer. Meteor. Soc.*, **90**, 1283–1296.

Berliner, L. M., Lu, Z.-Q., & Snyder, C., 1999: Statistical design for adaptive weather observations. *J. Atmos. Sci.*, **56**, 2536–2552.

Brinkman, W., 1974: Strong downslope winds at boulder, colorado. *Mon. Wea. Rev.*, **102**, 592–602.

Clark, T. L., and R. D. Farley, 1984: Severe DSWS calculations in two and three spatial dimensions using an elastic interactive grid nesting: A possible mechanism for gustiness. *J. Atmos. Sci*., **41**, 329–350.

Clark, T. L., and W. R. Peltier, 1977: On the evolution and stability of finite amplitude mountain waves. *J. Atmos. Sci*., **34**, 1715–1730.

Clark, T. L. and Peltier, W. R., 1984: Critical level reflection and resonant growth of nonlinear mountain waves. *J. Atmos. Sci.*, **41**, 3122–3134.

Descloitres, J., MODIS Land Rapid Response Team, cited March 2007. [Available online at http://www.14ers.com/images/ranges3db700x414.jpg.]

Doyle, J., Amerault, C., & Reynolds, C. A., 2007: Sensitivity analysis of mountain waves using an adjoint model. *Meteorologische Zeitschrift*, **16**, 607–620.

Doyle, J. D., and D. R. Durran, 2002: The dynamics of mountain-wave-induced rotors. *J. Atmos. Sci*., **59**, 186–201.

Durran, D.R., 1986: Another look at downslope winds. Part I: The development of analogs to supercritical flow in an infinitely deep, continuously stratified fluid. *J. Atmos. Sci.*, **43,** 2527–2543.

Durran, D. R., 1990: Mountain waves and downslope winds. Atmospheric Processes Over Complex Terrain. *Amer. Meteor. Soc*., **23**, 59–81.

Durran, D.R., 2003: Downslope winds. Encyclopedia of atmospheric sciences, 2003, Holton, J.R., J. Pyle and J.A. Curry eds. pp. 1161–1170, Elsevier Science Ltd.

Durran, D. R., and J. B. Klemp, 1987: Another look at downslope winds. Part II: Nonlinear amplification beneath wave-overturning layers. *J. Atmos. Sci*., **22,** 3402–3412.

Earth System Research Laboratory, cited July 2013: Boulder wind info. [Available online at ESRL : PSD : Boulder Wind Events.]

Eliassen, A., and E. Palm, 1960: On the transfer of energy in stationary mountain wave. *Geofis. Pub*., **22**, 1–23.

Gaspari, G., and S. E. Cohn, 1999: Construction of correlation functions in two and three dimensions. *Quarterly Journal of the Royal Meteorological Society*, **125**, 723–757.

Glickman, T. S., Ed., 2000: *Glossary of Meteorology*. 2d ed. Amer. Meteor. Soc., 855 pp.

Grimit, E. P., and C. F. Mass, 2007: Measuring the ensemble spread–error relationship with a probabilistic approach: Stochastic ensemble results. *Mon. Wea. Rev.*, **135**, 203–221.

Hakim, G., & Torn, R., 2008: Ensemble synoptic analysis. *Meteorological Monographs,* **33**, 147–161.

Hamill, T. M, cited 2013: Review of "covariance localization" in ensemble filters. [Available online at http://www.esrl.noaa.gov/psd/people/tom.hamill/CovLocal_BuenosAires_Hamill.ppt.]

Hertenstein, R. F., 2009: The influence of inversions on rotors. *Mon. Wea. Rev*., **137**, 433–446.

Hertenstein, R. F., and J. P. Kuettner, 2005: Rotor types associated with steep lee topography: Influence of the wind profile. *Tellus*, **57A**, 117–135.

Homan, P., 2007: Evaluation of high density surface observations in complex terrain and their contribution to the MM5 model. Naval Postgraduate School.

Holmboe, J., and H. Klieforth, 1957: Investigations of mountain lee waves and airflow over the Sierra Nevada. Final Rep. Contract AF19(604)-728, University of California ADNo. 133606, Department of Meteorology, University of California, Los Angeles, 290 pp.

Houghton, D. D., and E. Isaacson, 1968: Mountain winds. *Stud. Num. Anal*., **2,** 21–52.

Houtekamer, P. L., and Mitchell, H. L, 2001: A sequential Kalman Ensemble Filter for atmospheric data assimilation. *Mon. Wea. Rev.*, **129**, 123–137.

Jiang, Q., and Doyle, J., 2008: Diurnal variation of downslope winds in Owens Valley during the Sierra rotor experiment. *Mon. Wea. Rev.*, **136**, 3760–3780.

Jiang,Q., J. D. Doyle, S. Wang, and R. B. Smith, 2007: On boundary layer separation in the lee of mesoscale topography. *J. Atmos. Sci.*, **64**, 401–420.

Kalnay, E., 2009: *Atmospheric Modeling, Data Assimilation and Predictability*. 5th ed. Cambridge University Press, 341 pp.

Kim, H. M., and Jung, B. J., 2009: Influence of moist physics and norms on singular vectors for a tropical cyclone. *Mon. Wea. Rev.*, **137**, 525–543.

Klemp, J.B., and Lilly, D.R., 1975: The dynamics of wave-induced downslope winds. *J. Atmos. Sci.*, **32**, 320–339.

Kuettner, J., 1959: The rotor flow in the lee of mountains. GRD Res. Notes No. 6, Geophys. Res. Directorate, Air Force Cambridge Res. Center.

Lee, T., Rielke, R., Kessker, R., & Weaver, J., 1989: Influence of cold pools downstream of mountain barriers on downslope winds and flushing. *Mon. Wea. Rev.*, **117**, 2041–2058.

Lester, P. F., and Fingergut, 1974: Lower turbulent zones associated with mountain lee waves. *J. Appl. Meteor.*, **13**, 54–61.

Lilliefors, H. W., 1967: On the Kolmogorov-Smirnov test for normality with mean and variance unknown. Journal of the American Statistical Association. **62**, 399–402.

Lorenz, Edward N., 1963: Deterministic nonperiodic flow. *J. Atmos. Sci.*, **20**, 130–141.

Lorenz, E. N., 1969: The predictability of a flow which contains many scales of motion. *Tellus*, **21**, 289–307.

Lorenz, E., Emanuel, K., 1998: Optimal sites for supplementary weather observations: simulation with a small model. *J. Atmos. Sci*., **55**, 399–414.

Long, R. R., 1953a: Some aspects of the flow of stratified fluids. I. A theoretical investigation. *Tellus*, **5**, 42–58.

METED/COMET Program, cited July 2013: Mountain Waves and Downslope Winds [http://www.meted.ucar.edu/mesoprim/mtnwave/print.htm.]

Oard, Michael J., 1993: A method for predicting Chinook winds east of the Montana Rockies. *Wea. Forecasting*, **8**, 166–180.

Peltier, W. R. and T. L. Clark, 1979: The evolution and stability of finite amplitude mountain waves II: Surface wave drag and severe DSWS. *J. Atmos. Sci*., **36**, 1498–1529.

Pielke, R.A., 1985: The use of mesoscale numerical models to assess wind distribution and boundary layer structure in complex terrain. *Bound.-Layer Meteor*., **31**, 217–231.

Reinecke, P., and Durran, D., 2008: Estimating topographic blocking using a Froude number when the static stability is non-uniform. *J. Atmos. Sci.*, **65**, 1035–1048

Reinecke, P., and Durran, D., 2009: Initial-condition sensitivities and the predictability of downslope winds. *J. Atmos. Sci*., **66**, 3401–3418.

Rocky Mountain Insurance Information Association, cited January 2009: Tuesday's gusts blow in Colorado's fourth most expensive windstorm. [Available online at http://www.rmiia.org/News_room/catastrophe_news/2009_01_02_Colorado_Wind.asp.]

Saha, et al., 2010: The NCEP Climate Forecast System Reanalysis. *Bull. Amer. Meteor. Soc.*, **91**, 1015–1057.

Skamarock, W.C., J. B. Klemp, J. Dudhia, D. O. Gill, D. M. Barker, M. G. Duda, X. Huang, W. Wang, and J. G. Powers, 2008: A description of the advanced research WRF version 3. NCAR Tech. Note, NCAR/TN-475+STR, 113 pp.

Scorer, R.S., and H. Klieforth, 1959: Theory of mountain waves of large amplitude. *Quart. J. Roy. Meteor. Soc*., **85**, 131–143.

Smith, R. B., 1977: The steepening of hydrostatic mountain waves. *J. Atmos. Sci*., **34,** 1634–1654.

Snyder, C., 1996: Summary of an informal workshop on adaptive observations and FASTEX. *Bull. Amer. Meteor. Soc.*, **77**, 953–961.

Stull, R. B., 1988: *An Introduction to Boundary Layer Meteorology*. Kluwer Academic Publishers, 666.

Torn, R., 2010: Ensemble-based sensitivity analysis applied to African easterly waves. *Weather and Forecasting*, ***25***, 61–78.

Torn, R., & Hakim, G., 2008: Ensemble-based sensitivity analysis. *Mon. Wea. Rev.*, **136**, 663–677.

Torn, R., and Hakim, G., 2009: Initial condition sensitivity of Western Pacific extratropical transitions determined using ensemble-based sensitivity analysis. *Mon. Wea. Rev.*, ***137***, 3388–3406.

Torn, R., G. Hakim and C. Snyder, 2006: Boundary conditions for limited-area ensemble Kalman filters. *Mon. Wea. Rev*., **134**, 2490–2502.

The Weather Research and Forecasting Model (WRF), cited 2013: WRF Model Users Page. [Available online at http://wrf-model.org/users/users.php.]

Vosper, S. B., 2004: Inversion effects on mountain lee waves. *Quart. J. Roy. Meteor. Soc*., **130**, 1723–1748.

Vosper, S. G., P. F. Sheridan, and A. R. Brown, 2006: Flow separation and rotor formation beneath two-dimensional trapped lee waves. *Quart. J. Roy. Meteor. Soc*., **132**, 2415–2438.

Wilks, D. S., 2006: *Statistical methods in the atmospheric sciences*. 2nd ed. Academic Press, 627 pp.

Young, G., and Pielke, R., 1983: Application of terrain height variance spectra to mesoscale modeling. *J. Atmos. Sci*., **40**, 2555–2560.

Zou, X., F. Vandenberghe, M. Pondeca, and Y.-H. Kuo, 1997: Introduction to adjoint techniques and the MM5 adjoint modeling system. NCAR Tech. Note NCAR/TN-435STR, 110 pp.

THIS PAGE INTENTIONALLY LEFT BLANK

INITIAL DISTRIBUTION LIST

1. Defense Technical Information Center
   Ft. Belvoir, Virginia

2. Dudley Knox Library
   Naval Postgraduate School
   Monterey, California